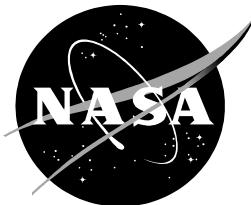


Haystack and HAX Radar Measurements of the Orbital Debris Environment; 2003

Orbital Debris Program Office
Human Exploration Science Office
Astromaterials Research and Exploration Science Directorate

C. L. Stokely, J. L. Foster, Jr., E. G. Stansbery,
J. R. Benbrook, Q. Juarez

November 2006



National Aeronautics and
Space Administration

Lyndon B. Johnson Space Center
Houston, Texas 77058

**Haystack and HAX Radar Measurements
of the
Orbital Debris Environment
2003**

JSC-62815

C.L. Stokely¹, J. L. Foster, Jr.², E. G. Stansbery³
J. R. Benbrook⁴, Q. Juarez⁴

¹ESCG/Barrios Technology, Inc.
2200 Space Park Dr., Ste. 400
Houston, TX 77058

²Science Applications International Corporation, Inc.
2450 NASA Pkwy
Houston, TX 77058

³National Aeronautics and Space Administration
Johnson Space Center
Houston, TX 77058

⁴ESCG/Jacobs-Sverdrup, Inc.
2224 Bay Area Blvd, Box 7
Houston, TX 77058

November 2006

Executive Summary

The continual monitoring of the low Earth orbit (LEO) environment using highly sensitive radars is essential for an accurate characterization of the dynamic debris environment. This environment is continually changing or evolving since there are new debris sources and debris loss mechanisms that are dependent on the dynamic space environment. Such radar data are used to supplement, update, and validate existing orbital debris models [1]. Orbital debris models are used for risk analysis of space operations, shielding design of spacecraft for protection from impacts with space debris, debris mitigation studies and policies, and long term projections for future population growth of space debris [2].

NASA has been utilizing radar observations of the debris environment for over a decade from the MIT Lincoln Laboratory (MIT/LL) Long Range Imaging Radar (known as the Haystack radar) and the smaller nearby Haystack Auxiliary Radar (HAX). Both of these systems are highly sensitive radars that operate in a fixed staring mode to statistically sample orbital debris in the LEO environment. The Haystack and HAX radars are, respectively, X-band and Ku-band monopulse tracking radars collocated in Tyngsboro, Massachusetts at a latitude of 42.6°. The HAX radar has a shorter wavelength but because of its smaller diameter, it has a larger radar detection volume than Haystack. HAX is not as sensitive as Haystack but its larger detection area allows it to collect increased statistics for larger debris objects. Each of these radars is ideally suited to measure debris within a specific size region. The Haystack radar generally measures from less than 1 cm to several meters. The HAX radar generally measures from 2 cm to several meters. These overlapping size regions allow a continuous measurement of debris with diameters from less than 1 cm to several meters. As a calibration benchmark, the count rate or "flux" of pieces with size 10 cm detected by Haystack and HAX is shown to agree with the number of objects in the USSPACECOM catalog. During the 2003 fiscal year, October 2002 to September 2003, all Haystack and HAX radar data were collected at 75° elevation, pointing East.

Some of the data are seen to group into families that can sometimes be associated with individual breakups or groups of breakups. A new technique for identifying breakup fragments was employed, allowing for identification of debris from the nuclear powered SNAPSHOT satellite.

Immediately before the start of fiscal year 2003, 1 October 2002, MIT/LL changed their Processing and Control System (PACS), used for debris detection and near real time processing. This entailed replacing the analog components of their processing system with digital components along with accompanying software adjustments. After the transition, anomalous debris data was identified in early 2005 by the NASA Orbital Debris Program Office, revealing errors in the PACS. These errors reduced the capability of the Haystack radar to detect debris less than 1 cm, and the HAX radar to detect debris less than 4 cm for data recorded between July 2002 and July 2005. The errors in the PACS were identified and corrected by MIT/LL before the FY2006 debris observations began in November 2005. Despite the limitations of the radars imposed by the PACS errors, the excellent statistics provided by 633.3 hours of Haystack data and 541.8 hours of HAX data during FY2003 have greatly helped in characterizing the small debris environment.

Haystack and HAX have shown that the debris environment is dynamic and can change rapidly. Therefore, continued monitoring, or at least, frequent, periodic sampling of the debris environment to sizes below 1 cm should be continued.

Table of Contents

1.0	Introduction.....	1
2.0	Background	1
3.0	Radars and Radar Processing	2
3.1	Radar Description	2
3.2	Data Collection.....	4
3.3	ODAS Processing	6
3.4	Noise Floor Shape Factor	9
3.5	Calibration	10
3.6	PP/OP Channel Cross-talk.....	11
3.7	Data Quality	12
3.8	Detection Validation	12
3.9	SNR versus Time	13
3.10	Voltage Ratio.....	13
3.11	Offset Angles.....	14
3.12	Inclination Estimation	15
3.13	Integrated Signal to Noise and False Alarms	19
4.0	The NASA Size Estimation Model	20
5.0	Data Overview	23
5.1	Description of Data Collected.....	23
5.2	Comparison of Derived Parameters for Cataloged Objects	25
6.0	Results.....	28
6.1	Measurement Summary.....	28
6.2	Polarization Measurements.....	36
7.0	Breakups	39
7.1	SNAPSHOT Historical Background	44
7.2	SSN Observations.....	46
7.3	SNAPSHOT Debris Population Estimation	48
8.0	Conclusions	49
	References.....	49

List of Tables

Table 1.	Debris Mode Operating Parameters	5
Table 2.	The NASA SEM curve $x=g(z)$ in the Mie resonance region.....	21
Table 3.	Haystack FY2003 Data Summary.....	23
Table 4.	HAX FY2003 Data Summary	23

List of Figures

Figure 3.1-1. An engineering blueprint of the Haystack radar, supporting pedestal, and radome. Note that English units are used.....	3
Figure 3.3-1. An overview of the data collection and analysis.....	7
Figure 3.3-2. Histograms of SNR for Haystack in FY2002 and FY2003.....	8
Figure 3.3-3. Histograms of SNR for HAX in FY2002 and FY2003.....	8
Figure 3.4-1. Noise floor with digital filter of the PP sum channel, OP sum channel, PP Traverse difference channel, and PP Elevation difference channel.....	9
Figure 3.4-2. Noise floor with analog filter of the PP sum channel, OP sum channel, PP Traverse difference channel, and PP Elevation difference channel.....	10
Figure 3.6-1. Distribution of PP and OP integrated signal-to-noise ratios of accepted detections for Haystack.....	12
Figure 3.9-1. ODAS figure of the measured RCS as an object traverses the beam. For a mainlobe detection, the RCS should map as an approximately Gaussian-shaped pattern. The uncorrected signal is indicated by the squares. The triangles show the RCS corrected for beam loss.....	13
Figure 3.10-1. An ODAS figure of the monopulse voltage ratios, indicating that a target is crossing the beam from left-to-right in azimuth (traverse) and top-to-bottom in elevation. A square \square data point indicates an elevation voltage ratio and a triangle Δ indicates a traverse voltage ratio.....	14
Figure 3.11-1. A ODAS detection plot showing an object passing through the mainlobe of the beam. The offset angles determined from the data fit and those estimated from the voltage ratios are nearly the same. Triangles are measured points, pulses (+) are the fitted trajectory and circles are fitted data. The inner circle represents the half-power point of the beam; the outer circle represents the first null.....	15
Figure 3.12-1. The signal-to-noise ratio of the principal polarization radar return signal versus the inclination determined using the Doppler measurement assuming circular orbits.....	16
Figure 3.12-2. The signal-to-noise ratio of the principal polarization radar return signal versus inclination determined using the monopulse system.....	16
Figure 3.12-3. Altitude vs. Range Rate for FY2003 Haystack data collected at a 75° elevation angle with an overlay of calculated inclination assuming circular orbits.....	18
Figure 3.12-4. Altitude vs. Range Rate for FY2003 HAX data collected at a 75° elevation angle with an overlay of calculated inclination assuming circular orbits.....	18
Figure 3.13-1. Distribution of integrated signal-to-noise ratios of all detections for Haystack and HAX. The steep line at the left of the figure is the theoretical false alarm rate....	19
Figure 4.0-1. Results of RCS-to-Physical size measurements on 39 “representative” debris objects over the frequency range 2.0 – 18 GHz (15 – 1.67 cm wavelength). Each point represents an average RCS for a single object measured at a single frequency over many orientations. The oscillating line is the radar cross section for a spherical conductor while the smooth line is the polynomial fit to the data.	22
Figure 5.1-1. Altitude vs. size estimated from the NASA SEM for Haystack detections.....	24
Figure 5.1-2. Altitude vs. size estimated from the NASA SEM for HAX detections.....	24
Figure 5.1-3. Approximate size limits vs. altitude for Haystack and HAX for WFC4 in the 75° East stare mode.....	25
Figure 5.2-1. Comparison of Haystack-derived size and SSN-reported size for those Haystack 75° East detections collected in FY2003 that correlate to catalogued objects.....	26

Figure 5.2-2. Comparison of HAX-derived size and SSN-reported size for those HAX 75° East FY2003 detections that correlate with cataloged objects.....	26
Figure 5.2-3. Comparison of the Doppler inclination derived from Haystack data with the cataloged inclination for correlated targets in the 75° East FY2003 data.....	27
Figure 5.2-4. Comparison of the Doppler inclination derived from HAX data with the cataloged inclination for correlated targets in the 75° East FY2003 data.....	28
Figure 6.1-1. Flux of 1 cm debris for Haystack 75° East measurements for 2003 with 100 km altitude bins.....	30
Figure 6.1-2. Flux of 1 cm debris for HAX 75° East measurements for 2003 with 50 km altitude bins.....	30
Figure 6.1-3. Size distributions at 400, 500, 600, and 700 km for fluxes for FY2003 Haystack and HAX 75° East measurements.....	31
Figure 6.1-4. Size distributions at 800, 900, 1000, and 1100 km for fluxes for FY2003 Haystack and HAX 75° East measurements.....	32
Figure 6.1-5. Size distributions at 1200, 1300, 1400, and 1500 km for fluxes for FY2003 Haystack and HAX 75° East measurements.....	33
Figure 6.1-6. Size distributions at 1600 and 1700 km for fluxes for FY2003 Haystack 75° East measurements.....	34
Figure 6.1-7 and Figure 6.1-8. Doppler Inclination histogram for FY2003 Haystack 75° East measurements. Altitude histogram for detections with Doppler Inclination between 62° to 68°.....	34
Figure 6.1-9 and Figure 6.1-10. Altitude histogram for detections with Doppler Inclination between 68° to 74°. Altitude histogram for detections with Doppler Inclination between 80° to 86°.....	35
Figure 6.1-11 and Figure 6.1-12. Altitude histogram for detections with Doppler Inclination between 88° to 94°. Altitude histogram for detections with Doppler Inclination between 95° to 103°.....	35
Figure 6.2-1. The altitude versus Doppler inclination for debris with highly polarized return signals, <i>i.e.</i> , polarization greater than 0.84.....	37
Figure 6.2-2. The altitude versus Doppler inclination for all debris.....	37
Figure 6.2-3. Cumulative count rate of NaK debris versus RCS for several fiscal years.....	38
Figure 7.0-1. The altitude versus Doppler inclination for FY2003 Haystack detections.....	40
Figure 7.0-2. Day vs. hour for altitudes from 1200 km to 1400 km in the Doppler inclination band from 89° to 94°.....	41
Figure 7.0-3. Observation of the debris plane of SNAPSHOT passing radar beam in year 2003, day 107, at 2:53 am UCT.....	42
Figure 7.0-4. SEM size distribution for catalogued SNAPSHOT debris cloud candidate.....	43
Figure 7.0-5. Size distribution of Haystack detections determined to be SNAPSHOT debris....	43
Figure 7.0-6. Altitude histogram for SNAPSHOT debris candidates.....	44
Figure 7.1-1. Configuration of the SNAPSHOT/Agena D payload and the three pieces of operational debris left on orbit (nose fairing and 2-piece heat shield).....	45
Figure 7.2-1. Orbit period for SNAPSHOT (SSN 1314) and associated cataloged debris.....	47
Figure 7.2-2. Area-to-mass histogram of cataloged SNAPSHOT debris.....	47
Figure 7.2-3. Gabbard diagram of all SNAPSHOT debris tracked in May 2006 including both cataloged and analyst objects.....	48

List of Acronyms

AZ	Azimuth
A/D	Analog-to-Digital
COBE	Cosmic Background Explorer
CW	Continuous Wave
dB	Decibels
dBsm	Square meters measured in decibels
DECR	Debris Environment Characterization Radar
EL	Elevation
EMI	Electromagnetic Interference
FFT	Fast Fourier Transform
GMT	Greenwich Mean Time
HAX	Haystack Auxiliary radar
HV	High Voltage
ISS	International Space Station
JSC	Johnson Space Center
LDEF	Long Duration Exposure Facility
LEO	Low Earth Orbit
LRIR	Long Range Imaging Radar - (Haystack Radar)
MIT/LL	Massachusetts Institute of Technology/Lincoln Laboratory
NaK	Sodium-Potassium
NASA	National Aeronautics and Space Administration
NCI	Non-Coherent Integration or Non-Coherently Integrated
ODAS	Orbital Debris Analysis System
ODERACS	Orbital DEbris RAdar Calibration Spheres
OP	Orthogonal Polarization
ORDEM	Orbital Debris Engineering Model
PACS	Processing and Control System
PP	Principal Polarization
RCS	Radar Cross Section (usually in dBsm)
RF	Radio Frequency
RMS	Root Mean Square
RORSAT	Radar Ocean Reconnaissance SATellites
RTG	Radio-isotope Thermoelectric Generators
SECOR	(Geodetic) Sequential Collation of Range
SEM	Size Estimation Model
SSEM	Statistical Size Estimation Model
SNR	Signal-to-Noise Ratio
SSN	U.S. Space Surveillance Network
STS	Space Transportation System (Space Shuttle)
TLE	Two Line Element set

TR	Traverse
USSPACECOM	U.S. Space Command
UTC	Coordinated Universal Time
WFC	Waveform Code
WGS	World Geodetic System

1.0 Introduction

This document provides the results of observations of the orbital debris environment using the MIT/LL Long Range Imaging Radar (LRIR), or “Haystack,” and the Haystack Auxiliary (HAX) radars over the period from October 2002 through September 2003, fiscal year 2003 (FY2003).

The FY2003 data were taken with a redesigned data acquisition system in which large segments of the real time processing have been converted from analog to digital. The system supports longer transmitted pulses and faster pulse repetition rates, providing enhanced detection capability. The transmitted pulse has been extended from 1.024 ms to 1.638 ms. The range window of the radar has been extended from 900 km to 1580 km.

All of the 633.3 hours of Haystack data and the 541.8 hours of HAX data were taken in the 75° East stare mode. The long data collection time provides the best orbital debris statistics ever obtained at this excellent observation angle. This observation angle represents a compromise between Doppler inclination resolution and slant range to an altitude.

Breakup clouds in the debris population are apparent because of the statistics. The large population of debris between 850-1000 km altitude in an inclination band centered near 65° inclination was identified in 1995 [3, 4, 5, 6] as small spherical droplets of eutectic sodium-potassium (NaK) coolant. This NaK coolant leaked from fast neutron reactors that separated from the Russian Radar Ocean Reconnaissance SATellites (RORSATs) at the end of their useful lifetime.

Analysis of the Haystack data has revealed evidence of a near-circular debris ring in a polar orbit with altitudes ranging from 1270 km to 1330 km. This debris ring appears twice each day to the radar, corresponding to viewing of two sides of the ring. Most of the debris ring candidates are smaller than 4 cm. The altitude, inclination, and radar observation times of the debris ring correspond to the orbit plane of the nuclear powered SNAPSHOT satellite (International ID: 1965-027A; U.S. Space Command Satellite ID:1314), commonly referred to as Ops 4682. The SNAPSHOT satellite is well known for shedding pieces of debris with more than 50 catalogued debris pieces.

2.0 Background

As space activity has increased, orbital debris has become an increasingly important issue. By the mid-1970s it was realized that orbital debris poses a hazard to orbiting operational satellites and space vehicles. The concern of the National Aeronautics and Space Administration (NASA) of properly estimating the risk to operational, planned, and proposed space vehicles resulted in the creation of the NASA Orbital Debris Program in 1979. The February 2003 Space Shuttle Columbia accident, resulting from a hole in the leading edge of a wing, highlighted concerns regarding protection of manned spacecraft from hypervelocity debris impacts. A hypervelocity impact generally implies a relative speed between a projectile and a target of at least several kilometers per second. The precise definition of a hypervelocity impact is outside of the scope of this report.

Prior to 1990, measurements of the orbital debris environment came mainly from two separate sources. Data on the large objects were maintained by the U.S. Space Surveillance Network (SSN), which tracks space objects and maintains a catalog of orbital elements for each tracked object. The smallest detectable debris size (nominally about 10 cm) was limited, in part, by the 68 cm wavelength of the majority of the SSN radars. Data on debris less than 1 mm in size came from spacecraft surfaces returned to Earth, such as the Space Transportation System

(STS) windows and the Long Duration Exposure (LDEF) satellite [7, 8, 9, 10, 11]. Information regarding debris in the size range between 1 mm and 10 cm had been interpolated from these two sources. The planned Space Station Freedom, which evolved into the present International Space Station (ISS), created an urgent need for a better understanding of the orbital debris environment at space station altitudes in the size regime of 1 cm to 10 cm in low Earth environment (LEO), especially given the large size of the ISS and the long duration of exposure to the orbital debris environment [12]. In response to this need, NASA proposed building its own Debris Environment Characterization Radar (DECR) specifically for orbital debris research. The U.S. Department of Defense proposed instead that NASA use the Haystack radar located near Tyngsboro, Massachusetts, for orbital debris measurements. NASA became party to a memorandum of agreement with the United States Space Command (USSPACECOM) by which Haystack was to provide orbital debris data for NASA. Data collection for this project began in October 1990. As part of the memorandum, NASA funded the construction of the HAX radar, in close proximity to the Haystack facility. The HAX radar began supplementing the Haystack data in March 1994.

NASA has been using Haystack since October 1990 and HAX since March 1994 to characterize the debris environment in size, altitude, and inclination. Results from previous measurements have been published in JSC-27436 [3], JSC-28744 [13], JSC-28744A [13], JSC-28744B [13], JSC-32213 [14], JSC-32213 Appendix A [15], JSC-32213 Appendix B [16], JSC-26655 [17], JSC-26655 Appendix A [18], JSC-27842 [19], JSC-27971 [20], JSC-49875 [21] and the references therein included. A detailed description of the data collection and data analysis techniques are presented in Appendix A of JSC-26655. An overview of the data collection and analysis will be included in the current report.

The NASA Orbital Debris Program has conducted two independent reviews using experts on radar and statistics. The first panel of experts made recommendations regarding processing and analysis [22]. The second panel examined NASA's statistical treatment of the data and its use in characterizing the debris environment [23]. Each group commended NASA for its efforts and found NASA procedures and conclusions to be sound.

In addition, NASA conducted space flight experiments in 1994 and 1995, Orbital DEbris RAdar Calibration Spheres (ODERACS) [24], to investigate Haystack's calibration and validate the processing at NASA Johnson Space Center (JSC). In summary, the ODERACS experiments showed that the Haystack radar is calibrated within nominal limits, with measured RCS values accurate to ± 1.5 dB. The ODERACS experiments prompted several changes to the processing steps and the software to correct errors, improve accuracy, and remove biases in the data. JSC-26655 Appendix A [18] documents the revised processing and analysis steps.

3.0 Radars and Radar Processing

3.1 Radar Description

The Haystack and HAX radars are high power, right circularly polarized, amplitude sensing monopulse tracking radars with very high sensitivity. High power radars are required for orbital debris observations since the observation time for a single debris piece is generally limited to less than 1 second and most debris is small (<10 cm), returning radar signals with low SNR. The Haystack radar operates in the X-band and the HAX radar operates in the Ku-band. To detect debris, a pulsed continuous wave (CW) single frequency waveform is used.

Both Haystack and HAX radars utilize a Cassegrain configuration, with the radar signal reflected by the hyperbolic subreflector onto the parabolic reflecting surface. Haystack and HAX are

collocated in Tyngsboro, Massachusetts with longitude, latitude, and elevation of the radar's Cassegrain focus:

Haystack: Latitude: 42.623287 N ; Longitude: 288.511846 E ; Elevation: 115.69 m
 HAX: Latitude: 42.622835 N ; Longitude: 288.511709 E ; Elevation: 101.11 m

assuming an Earth radius of 6378.135 km. These coordinates and Earth radius are from the 1984 World Geodetic System (WGS84).

Figure 3.1-1 is an engineering diagram of the Haystack antenna and its protective radome. The following descriptions focus on Haystack rather than HAX since Haystack provides the majority of the small debris data. The 36.6 m parabolic main reflector is a solid aluminum surface shell composed of 96 light, stiff aluminum panel sections. The RMS deviation from a perfect paraboloid is 0.25 mm. Haystack's operating efficiency at 10 GHz (3 cm wavelength) is 35%, corresponding to a gain of 67.23 dB with a 0.058° half-power beamwidth.

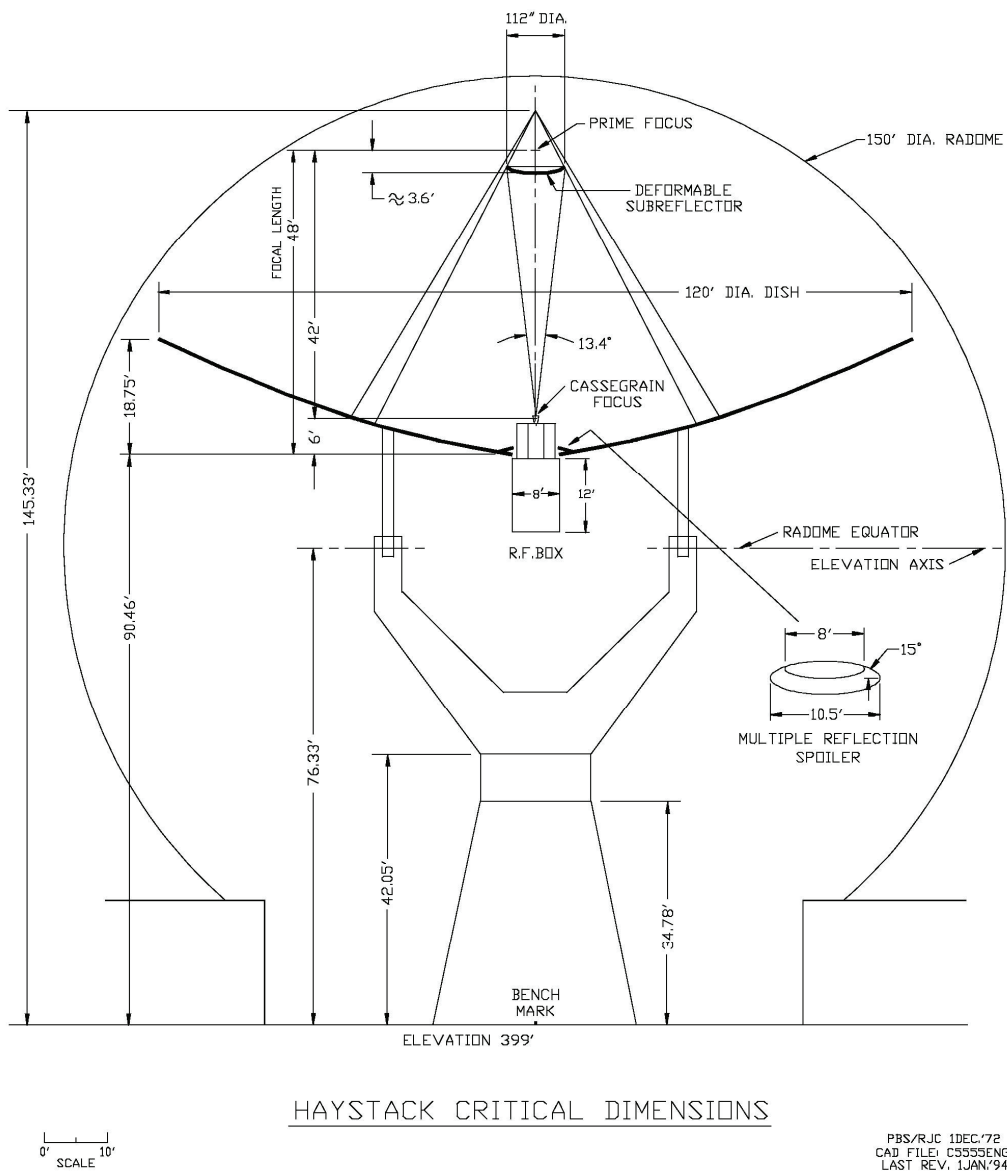


Figure 3.1-1. An engineering blueprint of the Haystack radar, supporting pedestal, and radome. Note that English units are used.

The approximately hyperbolic-shaped 2.84 m wide subreflector is composed of fiber-reinforced plastic with a set of nineteen computer controlled actuators. These actuators precisely control the subreflector's surface (deformable along 6 axis) to compensate for residual errors in the primary surface, and can focus, translate, and tilt the subreflector. Astigmatism and other gravitational deformations of the main reflector are compensated by a combination of computer-controlled subreflector deformation and thermal control of the main reflector. The subreflector is slightly defocused and adjusted to provide a parabolic illumination taper, resulting in reduced sidelobes compared to an untapered system. The first, second, and third sidelobes reduce the two-way measurement of RCS by approximately -41 dB, -49 dB, and -55 dB. A perfectly focused untapered parabolic radar should have sidelobes at -35 dB, -48 dB, and -56 dB.

The 45.7 m rigid radome provides protection from snow, ice, wind loading, and direct radiation from the sun. The benefits of providing environmental control with this radome more than compensate for any signal attenuation from its use. It is composed of 932 triangular membranes of 0.6 mm thickness hydrophobic laminated Tedlar-coated dacron cloth, which has minimal signal loss at the frequencies of operation. The dacron cloth, called Esscolam from L-3 Communications (formerly ESSCO), has a very low signal transmission loss across the frequencies of operation and has a good ability to shed water. The triangular membranes are supported by a lightweight aluminum frame structure. The radome uses irregular triangular tile patterns to spoil the symmetry of the radome in order to reduce radome chamber resonances from standing waves.

Haystack's pointing accuracy is ~1.5 millidegrees during stable thermal conditions (e.g., winter nights) as determined using naturally occurring astronomical maser sources. Summer daytime pointing is more variable due to thermal gradients across the antenna structure. The slew rate of Haystack is 2°/second and slew rate acceleration is 1.8°/second² with full sky coverage. Haystack's beam width is too narrow and its slew rate acceleration is insufficient for stare and chase observations of (generally low SNR) debris.

Haystack utilizes a high power X-band monopulse tracking feed that transmits right-hand circular polarization and receives both right- and left-hand circular polarization. The multi-mode feed uses a multiflared horn design, operating like an amplitude-sensing monopulse four horn feed, a very demanding and unfeasible physical space requirement [25].

The HAX radar is configured as a scaled-down version of the Haystack radar. HAX's 12.2 m parabolic main reflector deviates from a perfect paraboloid by 0.46 mm RMS. HAX's operating efficiency at 16.7 GHz (1.8 cm wavelength) is 51%, corresponding to a gain of 63.64 dB with a half-power beamwidth of 0.10°. HAX's pointing accuracy is ~2.0 millidegrees during stable thermal conditions. The HAX radar is tapered such that the first sidelobe reduces the two-way measurement of RCS by approximately -38 dB. The slew rate of HAX is 10°/second with full sky coverage. HAX utilizes the same type of feed design but its wavelength is shorter (Ku-band, 1.8 cm wavelength) and emits less power than Haystack.

3.2 Data Collection

For debris observations, both radars are operated in a staring, or "beam park," mode in which the antenna is pointed at a specified elevation and azimuth and remains there while debris objects randomly pass through the field-of-view. This operational mode provides a fixed detection volume important to the measurement of the debris flux, or number of objects detected per unit area per unit time. By operating the radar in a stare mode and not tracking detected debris objects, a precise measurement of the object's orbit is sacrificed. However, by examining the signals from the monopulse angle channels operating in an open-loop mode,

position in the radar beam for each pulse can be determined. From this path through the beam, orbital elements are deduced with moderate accuracy.

The operating parameters for the Haystack and HAX radars during the debris measurements are shown in Table 1. FY2003 marked the introduction of a new waveform, designated waveform code 4 (WFC 4) for both Haystack and HAX, which increases the pulse duration and energy on target by 60% over the waveforms used in previous years. With WFC 4, the single pulse signal-to-noise (SNR) values on a 0 dBsm (1.0 m^2) target at 1000 km range are 59.2 dB and 40.56 dB for Haystack and HAX, respectively. With Haystack, objects smaller than 1 cm diameter can be observed throughout the range window.

Table 1. Debris Mode Operating Parameters

Operating Parameter	HAX	Hay
Peak power (kW)	50	250
Transmitter Frequency (GHz)	16.7	10.0
Transmitter Wavelength (cm)	1.8	3.0
Antenna Diameter (m)	12.2	36.6
Antenna Beam Width (deg)	0.10	0.058
Antenna Gain (dB)	63.64	67.23
System temperature (K)	161	186
Total System losses (dB)	4.5	3.9
Waveform Code	4	4
Range Gates	16	16
Intermediate Frequency Bandwidth (KHz)	1000	1000
Independent Range/Doppler Samples	12126	12126
FFT Size	2048	2048
Number of non-coherent integrated pulses used for detection	16	16
Pulse width (msec)	1.6384	1.6384
Pulse repetition frequency (Hz)	60	60
Receiver window (msec)	12.126	12.126
Single Pulse SNR on 0 dBm ² target at 10 ³ km (dB)	40.56	59.2
Average Power (kW)	4.89	24.5
Doppler Extent (km/second)	± 4.5	± 7.5

Immediately before the start of fiscal year 2003, 1 October 2002, MIT/LL upgraded their Processing and Control System (PACS), used for debris detection and near real time processing. This entailed replacing the analog components of their processing system with digital components along with accompanying software adjustments.

The PACS has been programmed to record data in a buffer which is saved only when the integrated signal exceeds a predetermined threshold above system noise. In this way, many hours of debris observation can be performed without using an impractical amount of recording medium.

For Haystack real-time signal processing, of the six signals that are produced by the monopulse receiver network, the following four channels are processed in the radar: PP sum, OP sum, PP traverse difference, and PP elevation difference. The OP traverse difference and OP elevation difference channels are terminated. Data from all four channels are coherently converted to 60 ± 10 MHz intermediate frequency, further bandpass filtered to 20 MHz bandwidth using a switchable bank of digital SAW (surface acoustic wave) filters centered at 60 MHz, further down-converted to 10.0 ± 10.0 MHz, and then digitized at a rate of 40 MHz in accord with Nyquist's theorem using a 12-bit A/D digitizer. This data is then decimated by 32, resulting in

data collected at a 1.25 MHz rate. The digitized signals are decimated to match the bandwidth of each particular waveform. The SAW filter discards about 20% of the upper bandwidth of the 1.25 MHz data, resulting in data collected at approximately 1.0 MHz rate. Further processing demodulates the signal and develops digital in-phase (I) and quadrature-phase (Q) signals. This process produces single channel I and Q signals that are always correctly balanced. Using about a 40% range gate overlap between adjacent gates, the I and Q samples are fast Fourier transformed (FFT) to the frequency domain. Complex FFT data for each channel are sent to a memory buffer containing data for the previous 12 to 20 pulses. To minimize the archiving of data with no detections, a noncoherent 16-pulse running sum of the PP sum channel data is maintained, and only when a threshold is exceeded are the spectral data for all four channels permanently recorded to tape. The recording threshold is intentionally set lower than allowed in subsequent processing to ensure that no usable data are missed. Moreover, several pulses before and after a declared detection event are recorded to ensure no useful data are missed.

3.3 ODAS Processing

Orbital debris data from the radars recorded by the PACS are transferred to NASA JSC via high density 8 mm magnetic tapes. The data are processed at JSC using the Orbital Debris Analysis System (ODAS) that is now hosted on a Hewlett Packard Itanium computer operated by a NASA contractor team. An overview of the processing is shown in Figure 3.3-1.

The ODAS software computes the signal strength, signal-to-noise ratio (SNR), traverse (TR) and elevation (EL) voltage ratios (difference value normalized by the sum value), range, and range rate. Other parameters are derived from these measurements. MIT/LL sends JSC digitized frequency domain data which is sampled at 1.25 MHz. When ODAS finds a detection candidate, the data from this range gate and the two adjacent range gates are converted to the time domain. ODAS then concatenates these three range gates and performs a matched filter (a convolution, *i.e.* cross-correlation, of the received signal with a replica transmitted signal) detection to determine the range, range-rate, and amplitude. This amplitude is ultimately used in determining the RCS.

For an orbiting object passing through the radar field-of-view, the key step in the data processing is determining the location of a debris object in the radar beam for each radar pulse. From these locations, the motion of the object through the beam can be recreated and used to estimate orbital elements. Also, the signal strength can be augmented by the relative antenna gain determined by the antenna beam-pattern calibration discussed below. Thus, the returned signal strength can be estimated as if the object were at the center of the radar beam. The radar cross section (RCS) is determined by applying the absolute radar calibration, antenna beam shape, and the range to the object. The reported RCS is an average of several beam shape corrected RCS measurements over the beam width using a SNR weighting in the averaging. This ensures that low SNR RCS data do not corrupt the average RCS measurement.

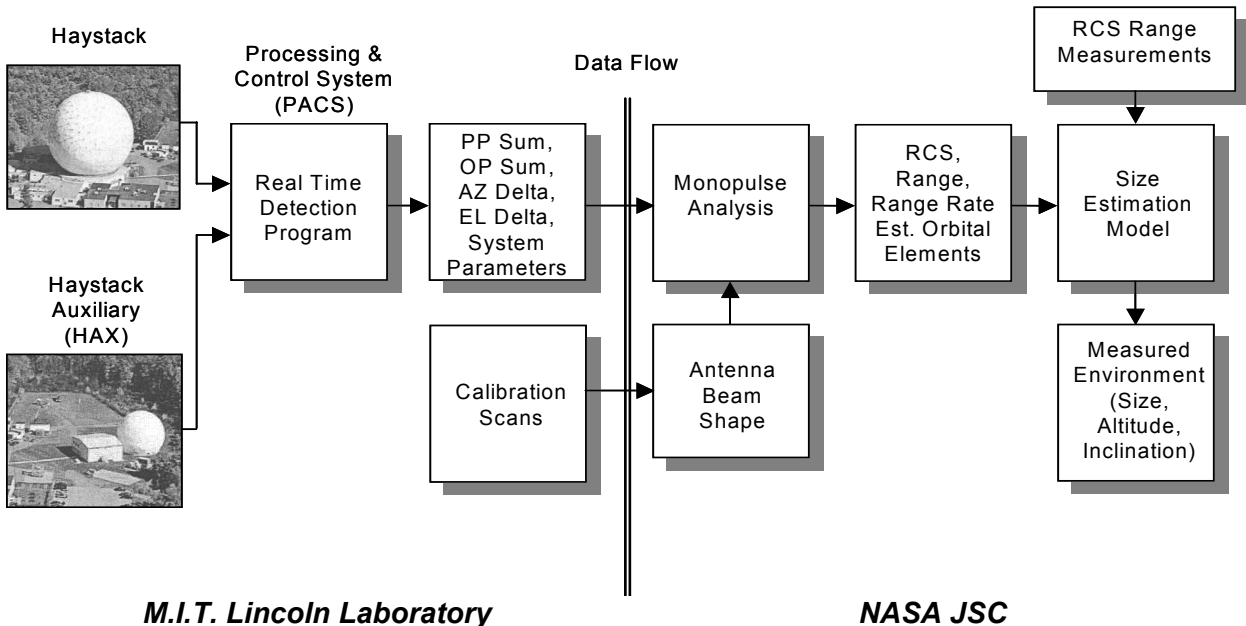


Figure 3.3-1. An overview of the data collection and analysis.

After the transition at MIT/LL to the all digital system in FY2003, anomalous debris data was identified for both Haystack and HAX in early 2005 by the NASA Orbital Debris Program Office, revealing errors in the PACS. Figure 3.3-2 and Figure 3.3-3 are histograms of SNR for Haystack and HAX in FY2002 and FY2003 both pointing at 75° East. The large number of counts for SNR near 5.5 dB are expected since below about 6 dB marks the rapid onset of false alarms. However, an anomalous drop in the number of detection in SNR histogram is evident between the onset of false alarms and SNR below 10 dB. Based on a thorough analysis of correlating debris sizes with SNR values, it can conservatively stated that these errors reduced the capability of the Haystack radar to detect debris less than 1 cm, and the HAX radar to detect debris less than 4 cm, for all data recorded during FY2003. Some subsets of the data appear to exhibit a +1.5 dB to +2.0 dB bias in the measured RCS. It is unclear if the SNR issues are the cause of this in tandem with difficulties encountered in the FY2003 radar calibrations. Despite the limitations of the radars imposed by the PACS errors, the excellent statistics provided by 633.3 hours of Haystack data and 541.8 hours of HAX data during FY2003 have greatly helped in characterizing the small debris environment.

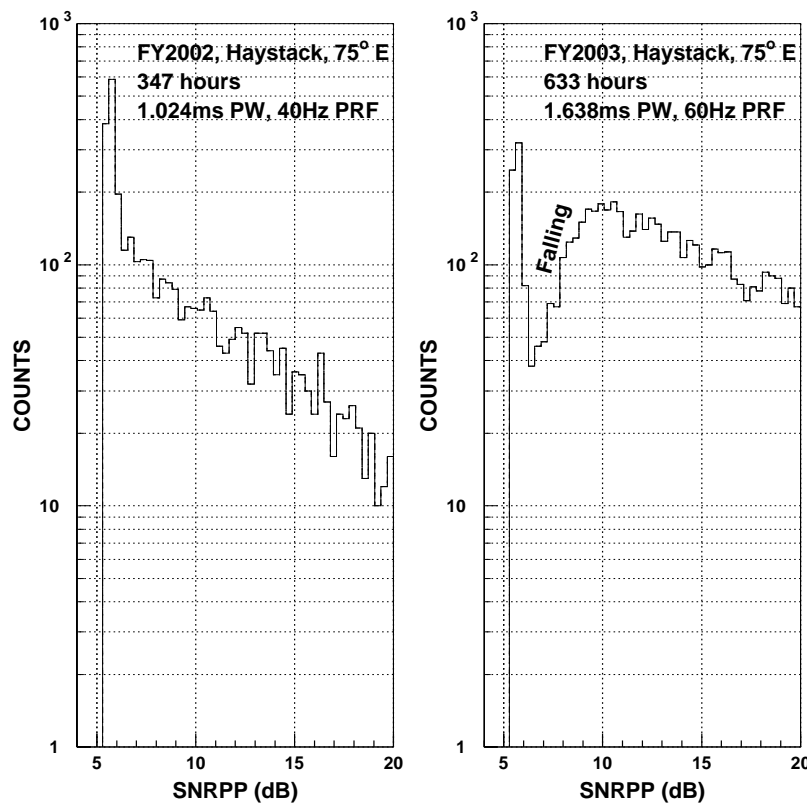


Figure 3.3-2. Histograms of SNR for Haystack in FY2002 and FY2003.

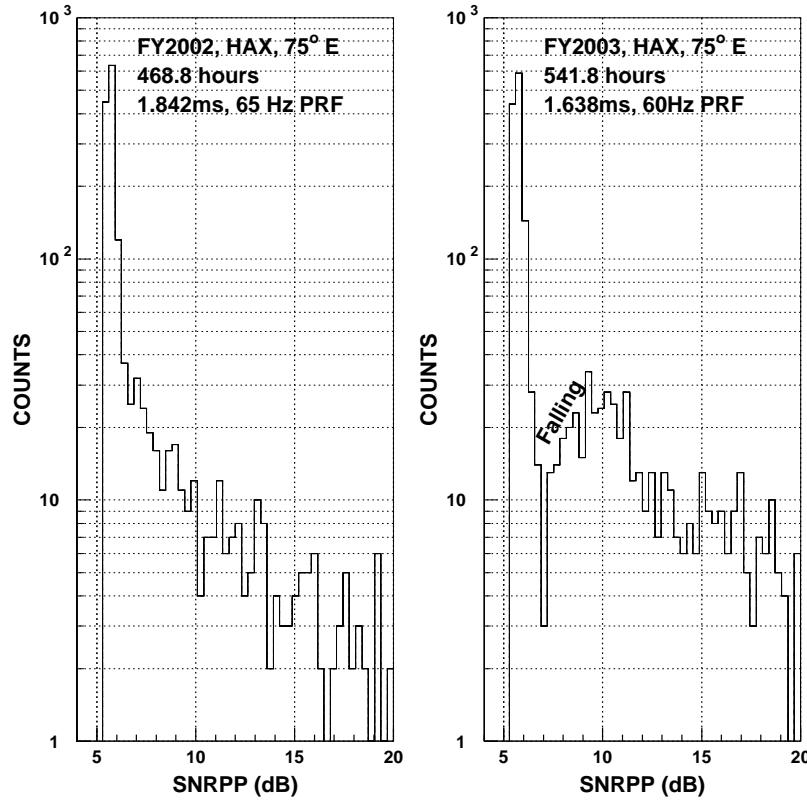


Figure 3.3-3. Histograms of SNR for HAX in FY2002 and FY2003.

3.4 Noise Floor Shape Factor

ODAS utilizes a “shape factor” to represent the noise floor of all the Doppler cells for a range gate and are subtracted from the signal emerging from the intermediate frequency bandwidth filter. A shape factor is a set of empirically derived unitless scalars specific to each Doppler cell that are used to normalize the detection data’s Doppler cells to the same gain. The SAW bandpass filters are the hardware filters that produce the uneven noise floor that is compensated for in the ODAS processing [26].

Figure 3.4-1 shows the 2048 channel WFC 4 shape factor associated with the new digital bandpass filters. Figure 3.4-2 shows the shape factor for the analog bandpass filters with the previous Haystack and HAX electronics. The data taken with the new digital filter shows a noticeable improvement in monopulse beam position scatter. For the analog filter, the shape factor spans the entire Doppler width, 1 MHz. The shape factor for the digital filter spans about 80% of the entire 1.25 MHz Doppler width, defined by the plateau evident in the figure. The resulting Doppler width for the digital filter is approximately 1 MHz. The spike in the center Doppler cell in Figures 3.4-1 and 3.4-2 originate from zero velocity clutter at the radar.

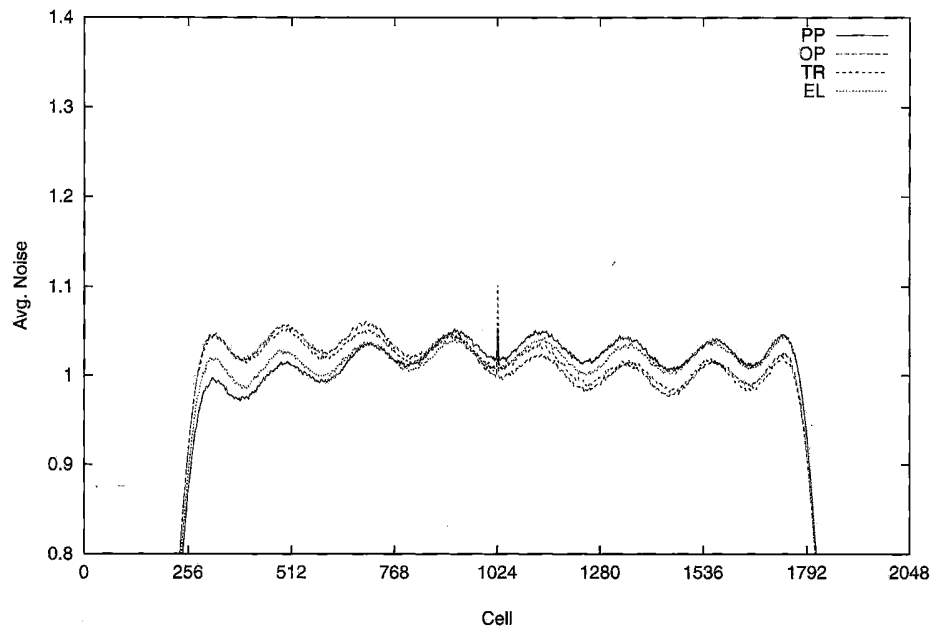


Figure 3.4-1. Noise floor with digital filter of the PP sum channel, OP sum channel, PP Traverse difference channel, and PP Elevation difference channel.

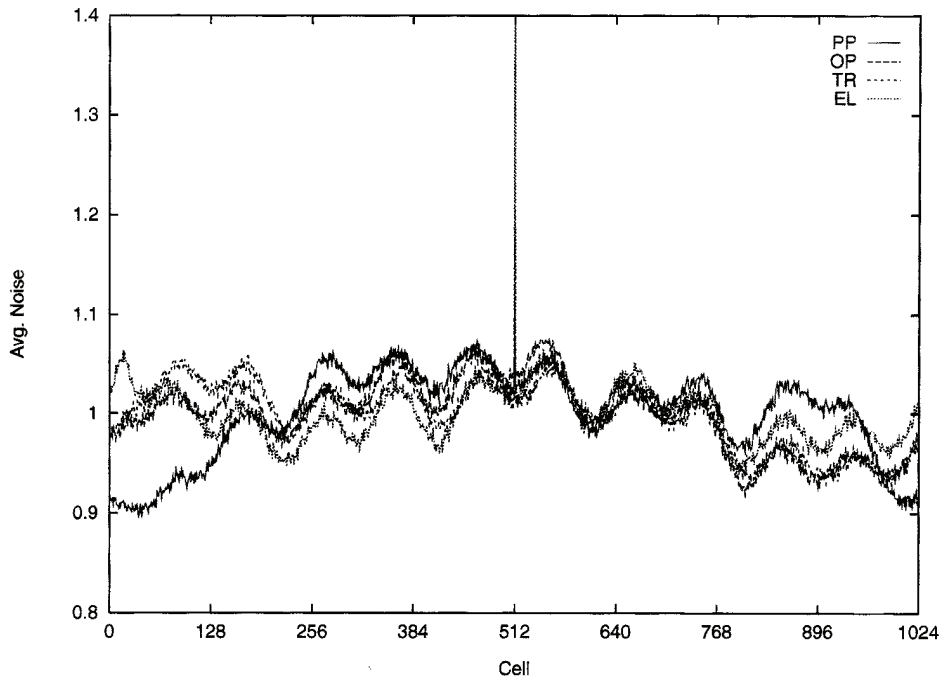


Figure 3.4-2. Noise floor with analog filter of the PP sum channel, OP sum channel, PP Traverse difference channel, and PP Elevation difference channel.

3.5 Calibration

Calibration of the radar is a major concern for debris data collection. Two types of recurring calibrations are performed using orbiting calibration spheres of known size. The first is an absolute calibration performed by tracking a sphere at the center of the radar beam. Second, the relative sensitivity of the remainder of the antenna pattern is measured by scanning the antenna around the location of the sphere as it moves across the sky in orbit. The first determines the system gain and the second determines the antenna beam pattern.

Several times each day as part of the calibration sphere scans, the Haystack radar measures the RCS of the calibration sphere to calculate a "system sensitivity constant," used to maintain the system calibration. The Haystack radar tracks the difference between the calibration constant being used and the one currently measured. If the measured constant drifts sufficiently far away from the currently "used" value they adjust the constant. The new value is typically the average of the measured values from the past several days. The data tapes recorded at the Haystack facility contain only the averaged constant which remains unchanged for a few days.

The antenna beam shape pattern is determined by initially tracking a calibration sphere satellite to calculate a state vector; the radar antenna then executes a spiral scan around the target to measure the beam shape. Only signals with sufficient SNR (>12 dB) are used by ODAS to ensure an accurate beam shape estimate. The antenna beam pattern is carefully monitored since the largest uncertainties in RCS estimation originate from the beam shape correction procedure [22, 23].

In addition to the recurring calibration, NASA undertook an experiment to validate the data collection, analysis, and recurring calibration techniques. To remedy concerns regarding the several orders of magnitude difference in RCS between a calibration sphere and small debris objects, NASA deployed six small calibration spheres from the Space Shuttle in February 1994

to provide additional calibration targets for Haystack debris measurements. The experiment, ODERACS [24], released two 5.08 cm, two 10.16 cm, and two 15.24 cm diameter metal spheres. To validate the collection, analysis, and calibration techniques, these small spheres flew through the Haystack field-of-view and the data was processed exactly like debris data. Results indicate that the radar and processing system provide the correct RCS to within ± 1.5 dB.

Spheres only return circularly polarized radar energy in the primary polarization (PP). MIT/LL injects test signals into the receiver pre-amplifiers that are used for the OP calibration constant. In order to calibrate the orthogonal polarization (OP) channel, NASA flew ODERACS II in February 1995, which released one each of the three sized spheres released during ODERACS, plus three dipoles. Two of the dipoles were 13.348 cm in length while the third dipole was 4.420 cm long. Dipoles return radar energy in both polarizations equally. An absolute calibration of the OP channel was obtained by calibrating the PP channel with one of the spheres and then performing a relative calibration of OP/PP using one of the dipoles. ODERACS II validated the signal injection calibration procedure [24].

The new waveform and digital filter beginning in FY2003 were accompanied by a transition to standardized software. The program controlling the calibration scans was not included in the new software suite for Haystack. The replacement calibration scan code produced irregular and incomplete spiral scans of the one-way half power (-3 dB) width of the beam. Within ODAS, the RCS in the PP polarization is modeled as a parabolic surface over the (mainlobe) angle offset domain. With incomplete data over large regions of the gain surface, the parabolic fits are not well constrained and can result in unphysical estimates of the gain surface. In some cases with incomplete spiral scans, these polynomial functions would rapidly diverge outside of the fitted data. To remedy these problems, several spiral calibration scans were concatenated to ensure the necessary coverage over the 3 dB width of the beam.

3.6 PP/OP Channel Cross-talk

Figure 3.6-1 shows the distribution of PP and OP integrated signal-to-noise ratios of accepted detections for Haystack. There are two distinct groups of detections, one for which the PP and OP integrated SNRs are about equal, and a group for which SNR is dominated by the PP signal but which shows an OP SNR component above approximately 20 dB PP SNR. The behavior of the OP SNR component is consistent with -20 dB crosstalk between the PP and OP channels. Additionally, Haystack has observed -20 dB crosstalk between PP and OP channels for measured RCS values using various calibration spheres [27].

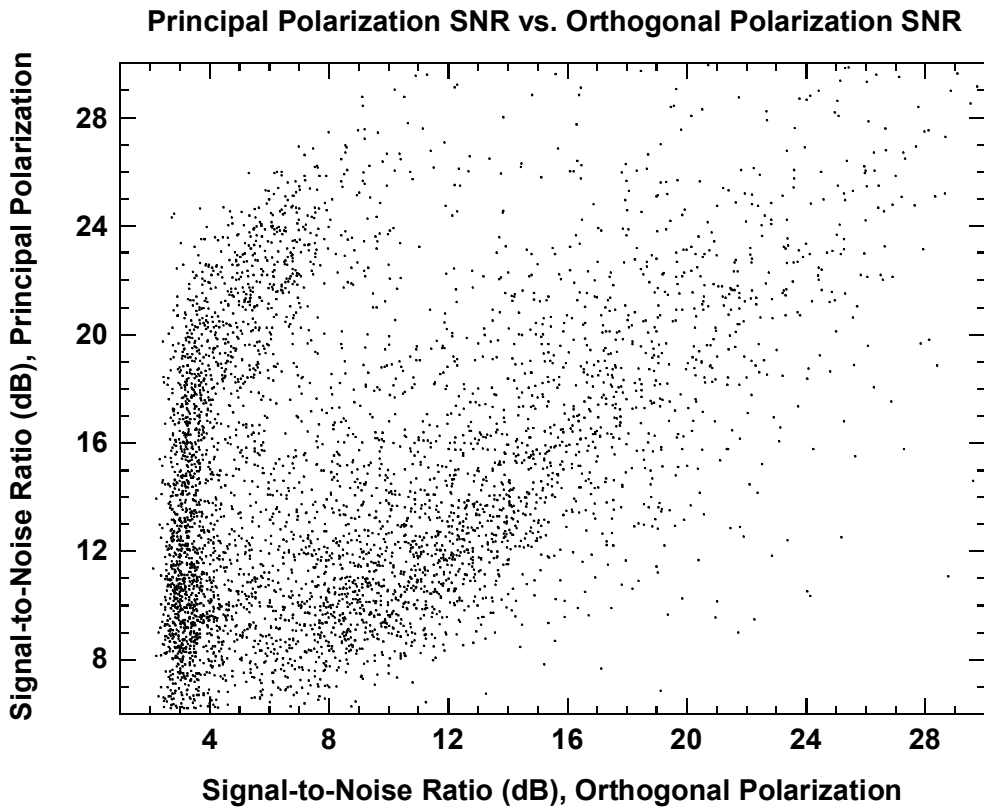


Figure 3.6-1. Distribution of PP and OP integrated signal-to-noise ratios of accepted detections for Haystack.

3.7 Data Quality

The Haystack data have been examined in a number of ways to ensure the highest quality of the reported results. To validate the data, the monopulse phase, voltage ratios, SNR, and uncorrected RCS measurements are manually inspected for each detection. Additionally, a summary list of parameters is gathered for each detection, including time of the detection, integrated SNR, slant range, range rate, derived inclination, and derived size. Distribution plots are made of many of the parameters as well as scatter plots of each parameter versus all of the other parameters. In the 1994 Haystack report [17], use of these plots resulted in the detection of several problems such as use of incorrect calibration constants and subtle shifts in the noise floor. All of the data included has been examined in this manner and any problems found were resolved.

3.8 Detection Validation

Because errors in estimating the RCS of small objects rapidly increase outside the nominal radar beamwidth, only objects that pass within the 3 dB (one-way) beamwidth of the radar are accepted for analysis [22, 23]. The criteria that are used to determine whether detections pass through the 3 dB beamwidth of the radar comes from analyzing several plots generated by the ODAS software: the SNR versus time, the elevation and traverse voltage ratio versus time, and a polar plot of the measured and estimated offset angles, *i.e.* the path through the radar beam. Attention is given during the data analysis to identify and remove large objects passing through the radar beam sidelobes that appear to be a valid detection of a small object.

3.9 SNR versus Time

The shape of the SNR distribution of a detection event is a key indication of a mainlobe detection. Theoretically, as a non-scintillating object traverses the mainlobe, a Gaussian shaped SNR distribution should be observed. Figure 3.9-1 illustrates such a mainlobe event (in the PP SNR channel). Multiple peaks in the SNR distribution may indicate that the object is rapidly tumbling. Gaps in the SNR distribution can indicate passage between lobes across a null of the radar beam. Multiple peaks with gaps may be an indication of a sidelobe detection which never goes through the mainlobe of the beam. Also, the duration of the detection can provide evidence of a sidelobe detection by making basic assumptions about the orbital speed given a detected altitude.

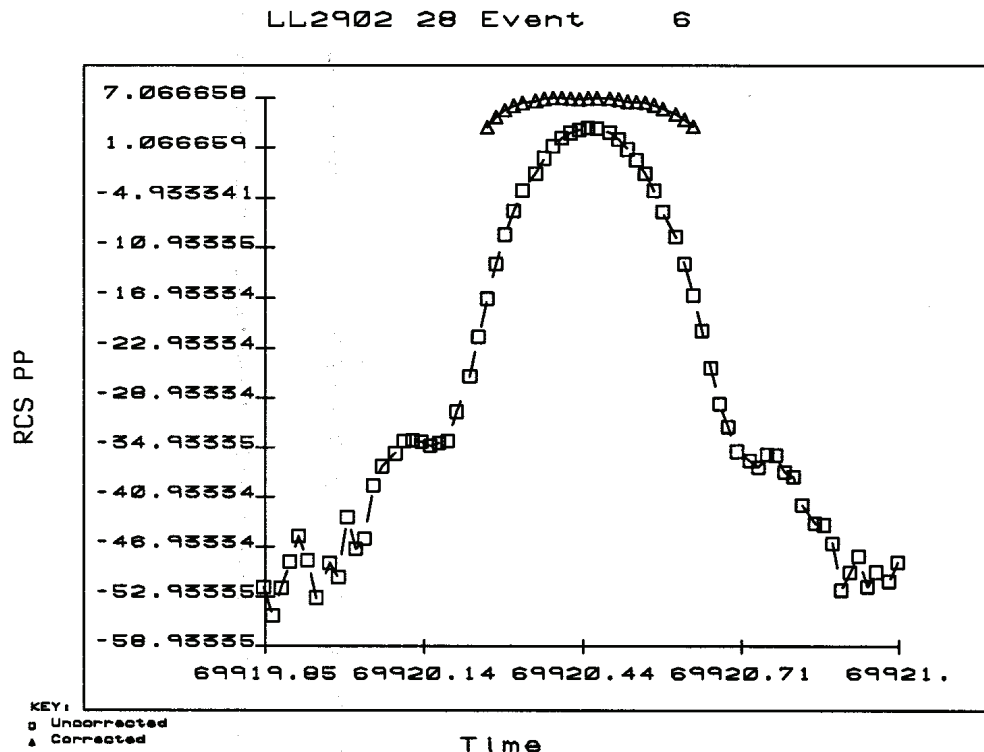


Figure 3.9-1. ODAS figure of the measured RCS as an object traverses the beam. For a mainlobe detection, the RCS should map as an approximately Gaussian-shaped pattern. The uncorrected signal is indicated by the squares. The triangles show the RCS corrected for beam loss.

3.10 Voltage Ratio

The voltage ratio plot, in Figure 3.10-1 shows a target crossing the beam from left-to-right indicated by a rising traverse voltage ratio. A voltage ratio of zero in azimuth or elevation indicates that the object is at the center of the beam in that coordinate. The voltage ratios for traverse motion (triangles) change in time from positive to negative values indicate that the object exhibits horizontal motion across the field of the radar. The voltage ratio for elevation changes from positive to negative indicate that the elevation is descending as the object crosses the beam. The nonlinearity in voltage ratios away from the beam center (voltage ratio ~ 0) is readily apparent. The maximum and minimum voltages correspond to the nulls in the beam diffraction pattern. The voltage ratios behavior in the first sidelobe resembles that through the center of the beam. Motion through a sidelobe can be indistinguishable from motion through the mainlobe of the beam if only the voltage ratio plots are considered.

LL2902 28 Event 6

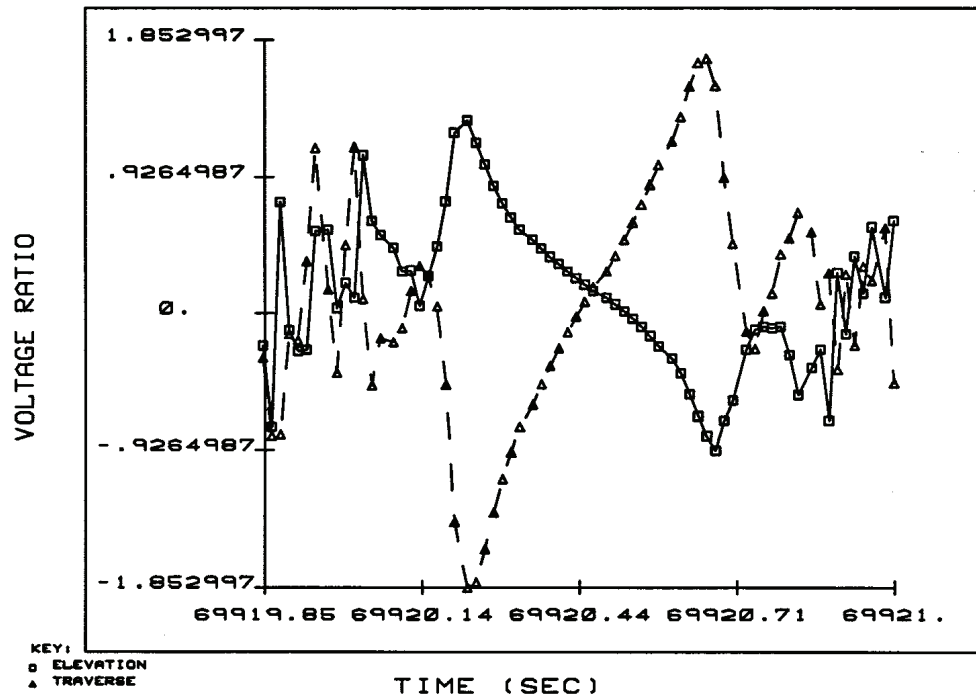


Figure 3.10-1. An ODAS figure of the monopulse voltage ratios, indicating that a target is crossing the beam from left-to-right in azimuth (traverse) and top-to-bottom in elevation. A square □ data point indicates an elevation voltage ratio and a triangle △ indicates a traverse voltage ratio.

3.11 Offset Angles

The measured offset angles are transformed from the voltage ratio using the radar calibration mapping. A straight-line path of the object through the beam is assumed for the linear fit of measured offset angle points. Figure 3.11-1 shows a mainlobe detection passing through the beam.

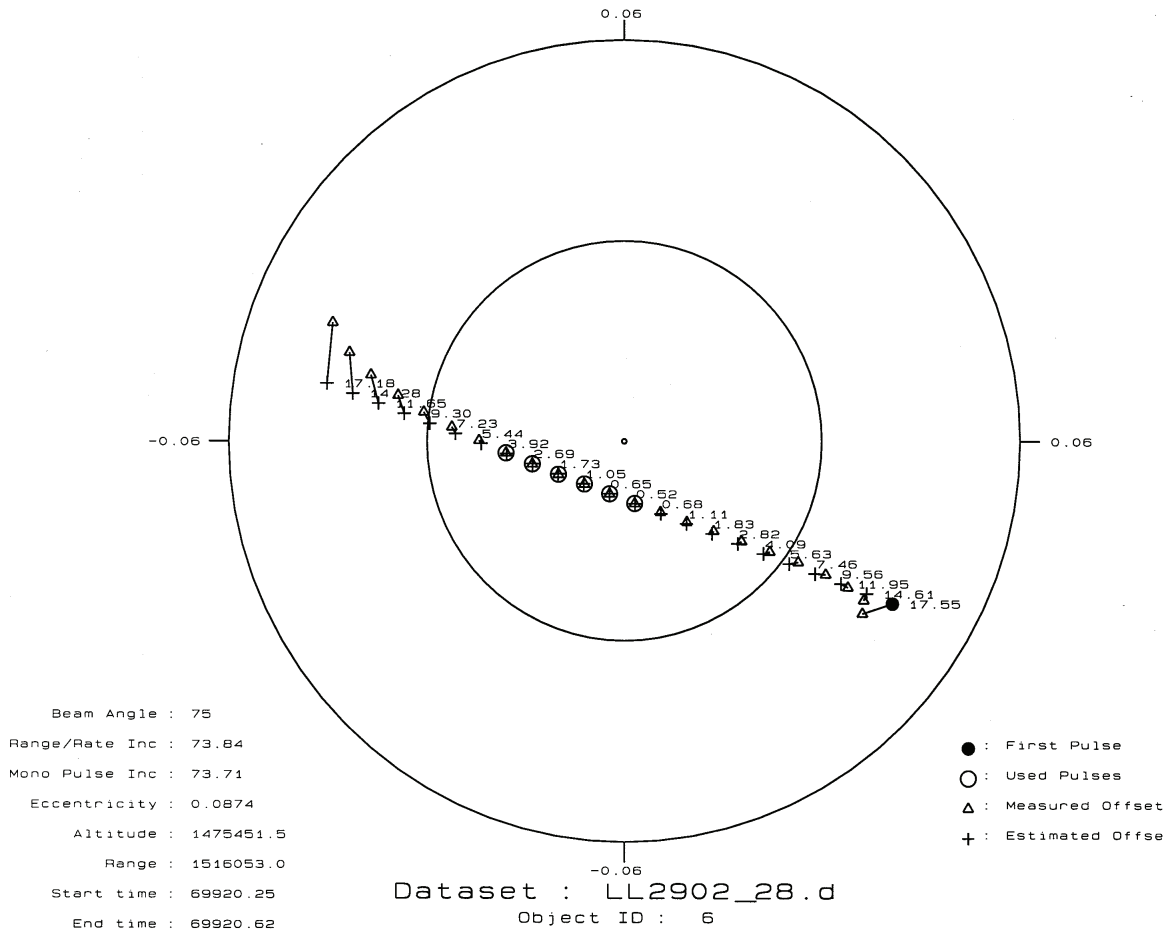


Figure 3.11-1. A ODAS detection plot showing an object passing through the mainlobe of the beam. The offset angles determined from the data fit and those estimated from the voltage ratios are nearly the same. Triangles are measured points, pulses (+) are the fitted trajectory and circles are fitted data. The inner circle represents the half-power point of the beam; the outer circle represents the first null.

3.12 Inclination Estimation

There are two methods of determining the orbital inclination of an object detected by the Haystack or HAX radars in the staring mode. In the “monopulse method,” the time history of the position of the object through the beam is determined from the open loop monopulse azimuth and elevation voltage ratios which are converted into direction and angular velocity across the beam. The direction and angular velocity along with the range, range rate, and time are transformed into the classic orbital elements including inclination. Inclination derived from this method will be referred to as the monopulse inclination. For objects with very large SNR values, this is the preferred method; however a relatively small amount of measurement noise quickly degrades velocity determination and the derived values of inclination and eccentricity become invalid. It was shown in previous Haystack reports that orbital inclination could also be estimated from range rate information if circular orbits are assumed. Inclination derived by this method will be referred to as Doppler inclination. Depending on where in the orbit an object is detected, the Doppler inclination may be invalid for objects with appreciable eccentricity. Statistically, Doppler inclination values have proven to be more reliable than monopulse values. Figure 3.12-1 and Figure 3.12-2 illustrate how the Doppler inclination and monopulse inclination depend on the SNR. The Doppler inclination is used in this report unless otherwise noted.

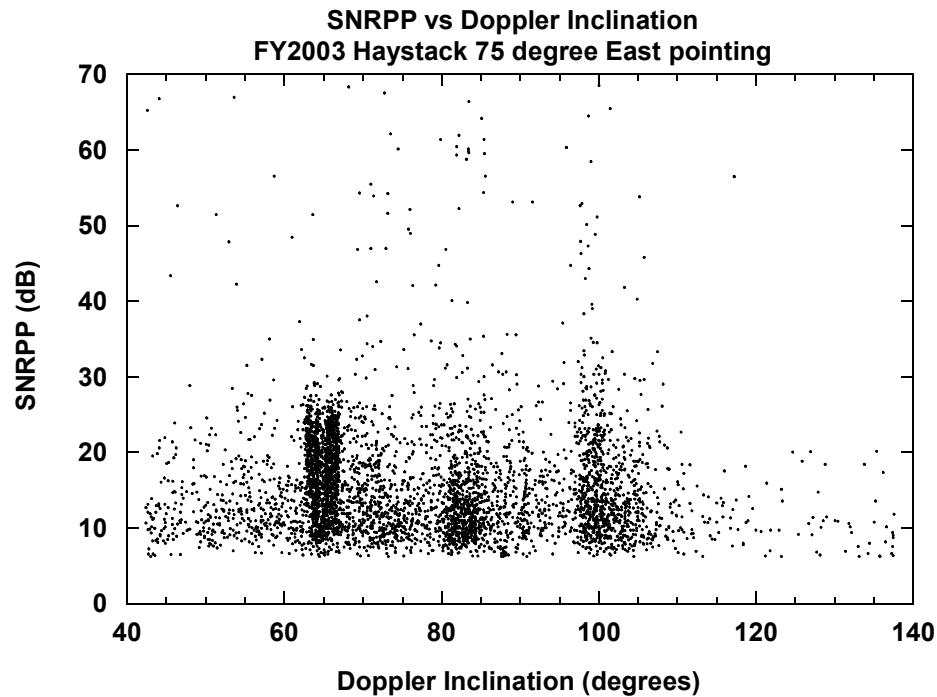


Figure 3.12-1. The signal-to-noise ratio of the principal polarization radar return signal versus the inclination determined using the Doppler measurement assuming circular orbits.

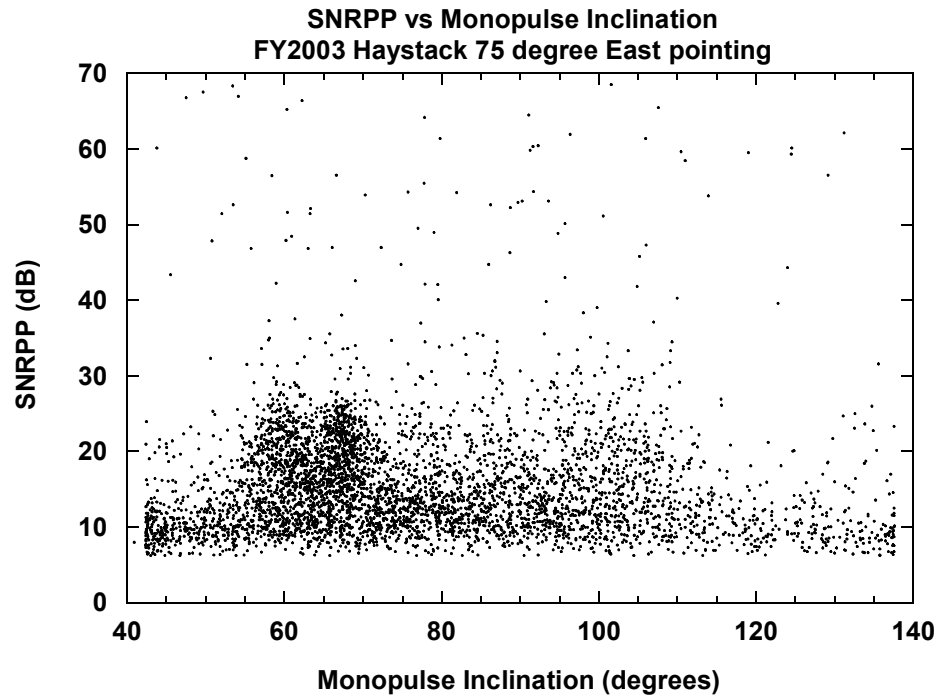


Figure 3.12-2. The signal-to-noise ratio of the principal polarization radar return signal versus inclination determined using the monopulse system.

Since 1994, NASA has collected data using a 75° elevation, 90° azimuth staring angle, referred to in this report as 75° East data. The angle between the orbit and the radar beam is sufficiently different from 90° that the Doppler range rate measurement can identify the orbital inclination with minor ambiguity in the resulting values. Orbits on ascending (traveling South to North)

passes will have slightly different range rates than orbits with the same inclination, but on descending (traveling North to South) passes. At 75°, the ambiguity is small enough that an inclination valid to about a degree can be obtained by averaging the two possible inclinations. Using this beam position, prograde and retrograde orbits have very different range rates. Figure 3.12-3 and Figure 3.12-4 show the relationship between range rate and inclination for this staring angle assuming circular orbits for Haystack and HAX, respectively. As elevation angle decreases, Doppler range rate increases but so does the inclination ambiguity and the slant range to an altitude (thus adversely affecting the sensitivity of the radar at that altitude). The 75° East data represents a compromise between the Doppler resolution, inclination ambiguity, and the slant range for detection of an object.

The points in Figure 3.12-3 and Figure 3.12-4 constitute a scatter plot of altitude versus range rate for the 75° East staring data taken in FY2003. The curves in this figure depict an overlay of the inclination calculated from the range rate assuming circular orbits. Note that orbits with inclinations less than about 40° and greater than about 140° are not seen by the radar (located near 40° N latitude) with 75° East pointing. It should be noted that much of the apparent structure in Figure 3.12-3 and Figure 3.12-4 can be described by circular orbits. This does not mean that there are no eccentric orbits in the data. In fact, those objects which have very high range rates beyond the 43° to 137° inclination overlay are either noise pulses, debris in eccentric orbits, or meteors. The radar has not detected a sufficient number of objects in highly eccentric orbits to give a structure that can be identified.

The improvement in inclination estimation afforded by the Doppler method now allows “families” of debris objects to be defined and studied separately. While it is impossible to say whether an individual detection is in a particular family because of the uncertainty in its eccentricity, the data in Figure 3.12-3 and Figure 3.12-4 show detections clumping into distinct families defined by limits of inclination and altitude. This indicates that extracting the data by choosing a narrow range of orbital parameters should minimize the number of “interlopers” and insures that the large majority of the extracted detections are of objects in the target family.

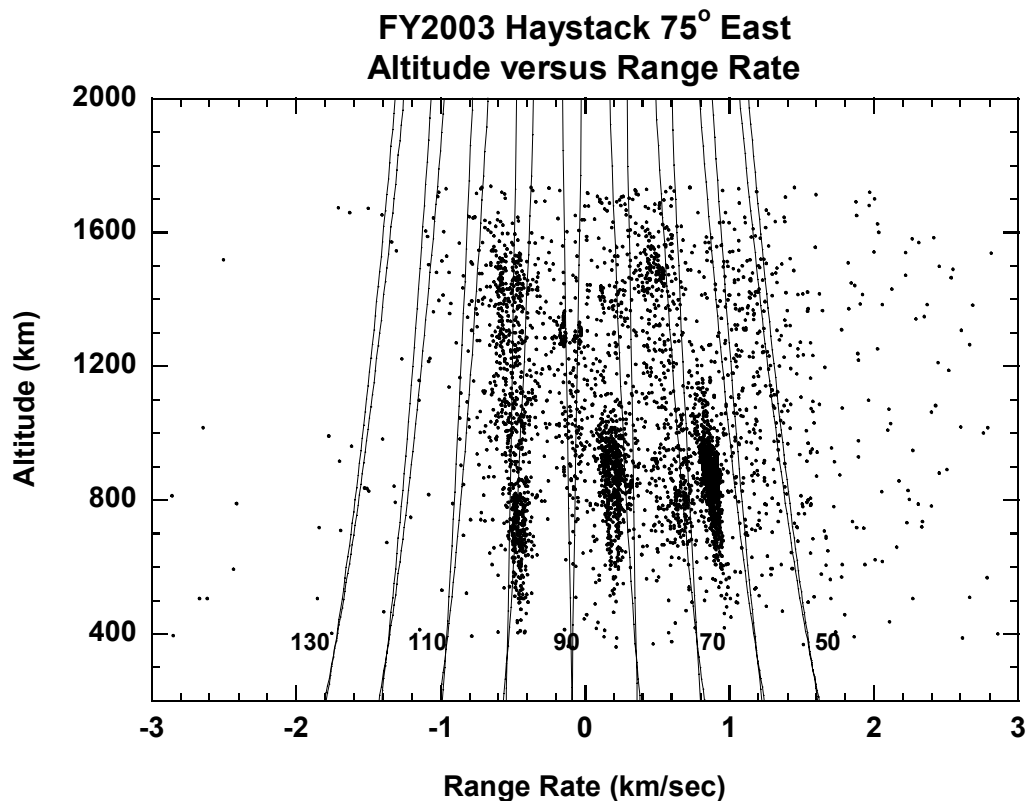


Figure 3.12-3. Altitude vs. Range Rate for FY2003 Haystack data collected at a 75° elevation angle with an overlay of calculated inclination assuming circular orbits.

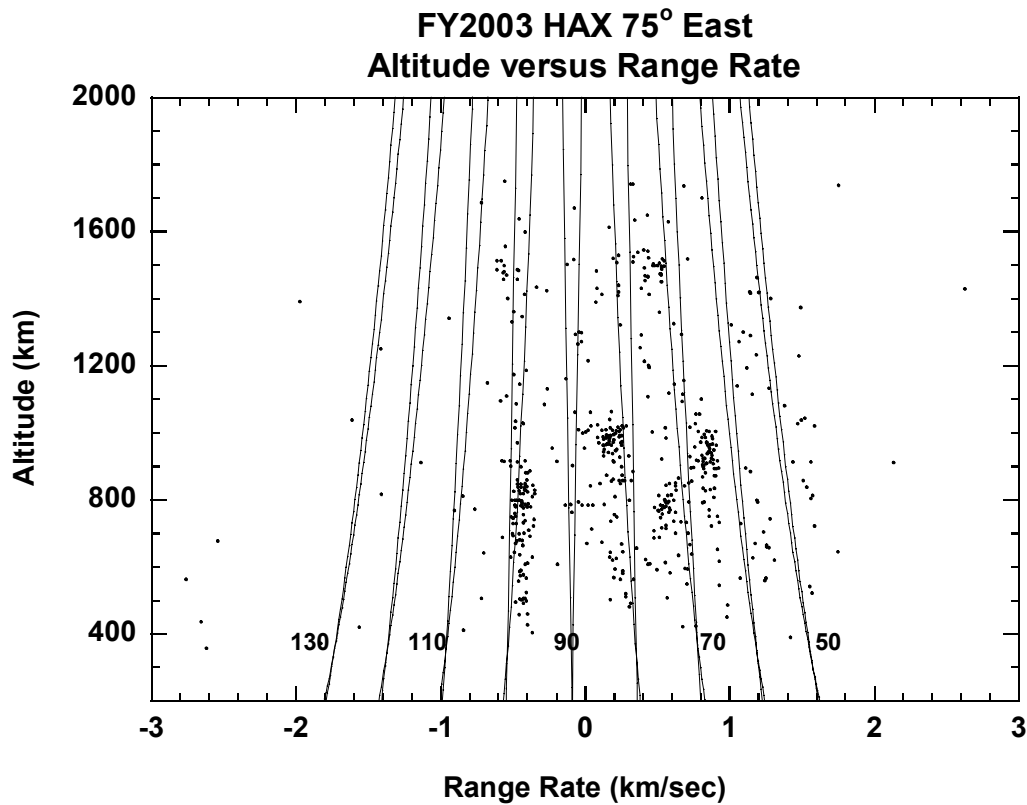


Figure 3.12-4. Altitude vs. Range Rate for FY2003 HAX data collected at a 75° elevation angle with an overlay of calculated inclination assuming circular orbits.

3.13 Integrated Signal to Noise and False Alarms

It is important to understand the statistics of false alarms and detection probability for the detection process used by Haystack and HAX. Figure 3.13-1 shows the distribution of the integrated SNR of all detections determined valid by PACS at MIT/LL for both Haystack and HAX. The theoretical distribution [28, 29] of false alarms for a small SNR is also shown. The false alarm rate is calculated using a program developed by Blake*.

During ODAS processing at JSC, the incoherently integrated 16-pulse SNR threshold is set so that the false alarm rate is 0.1 per hour of data collection for Haystack and 0.01 per hour for HAX. The SNR threshold for 0.1 false alarms per hour is 5.521 dB and the threshold for 0.01 false alarms per hour is 5.749 dB.

The low SNR discrepancy discussed in section 3.3 above indicates that some data with low SNR has been excluded. Moreover, the agreement between the theoretical false curve and the experimental observations is not in near-perfect agreement. MIT/LL's explanation was that their SNR acceptance threshold effectively was higher than originally expected as a result of a software error in their dual data buffering system. This problem was in addition to quantization errors in their new digital system. The end result is a measured false alarm rate lower than theoretical estimates. The conclusions presented in this report are believed to still be valid despite overestimating the false alarm rate and excluding some near-threshold detections.

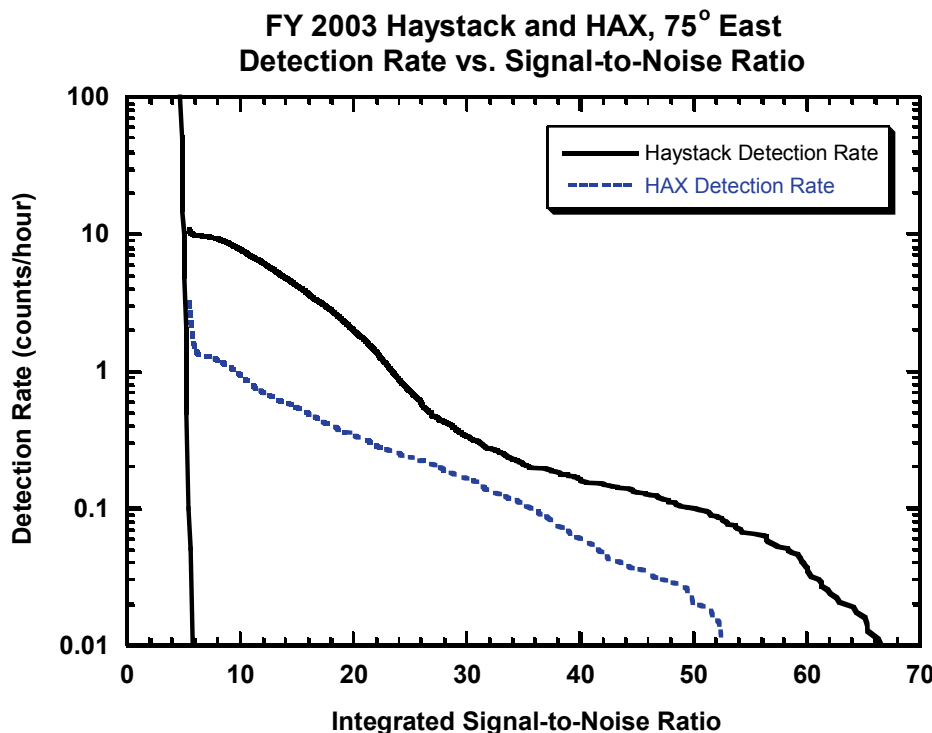


Figure 3.13-1. Distribution of integrated signal-to-noise ratios of all detections for Haystack and HAX. The steep line at the left of the figure is the theoretical false alarm rate.

* The ODAS SNR thresholds are determined using this program. In addition to false alarm rates, this program determines the probability of detection for noncoherently integrated pulses for the 5 Swerling scintillation cases.

4.0 The NASA Size Estimation Model

A separate study was done by XonTech, Inc. to develop a Size Estimation Model (SEM) to relate RCS to physical size. "Representative" debris objects were selected from two hypervelocity impacts of simulated satellites conducted at the Arnold Engineering Development Corporation by the U.S. Department of Defense [30, 31]. Some artificial debris-like objects were also included in the sample to represent better the postulated orbital debris environment. The RCS values of these 39 debris objects were measured at a controlled RCS radar range operated by the System Planning Corporation. The RCSs of these objects were measured over 4 radar frequency bands (2.5647-3.9111 GHz, 4.116-7.986 GHz, 8.1544-12.7684 GHz, and 12.924-17.538 GHz) with eight steps in the band of the lowest frequency and 16 steps in the band for the other three, and with hundreds of source-object orientations [23, 32, 33]. These frequencies, S-, C-, X-, and Ku-band, respectively, were chosen since they represent radar frequencies often used for orbital debris observations.

The characteristic length of an object is defined as the average of the largest dimensions for an object measured along three orthogonal axes. The first axis was chosen to coincide with the largest dimension, the second axis to coincide with the largest dimension in a plane orthogonal to the first axis, and the third axis to be orthogonal to the first two axes. In this report, the characteristic length of an object is referred to as size or diameter.

Consistent with the Maxwell's equations of electromagnetics, radar data from different wavelengths can be compared by normalizing the size by the wavelength of the measuring frequency and the RCS by the wavelength squared. This results in a size parameter $x=\text{size}/\text{wavelength}$ and a RCS parameter $z=\text{RCS}/\text{wavelength}^2$. No divergences from the scaling law invariances were observed from the analysis of the radar data by XonTech, but this may be a consequence of the limited size range chosen for the 39 pieces. Figure 4.0-1 shows the relationship between the measured RCS parameter and the object's physical size parameter. Each of the 2072 points on this plot is a weighted average for a single object over hundreds of different orientations at a single frequency. The data was weighted to account for nonuniform sampling of the object orientations as the data was collected [30, 31, 32, 33].

From this plot a scaling curve (smooth solid line) was developed which represents the mean of the measured RCS for each size/wavelength. For debris sizes much smaller or larger than the radar wavelength, the scaling curve approaches the Rayleigh or optics region curves, as expected. Between the Rayleigh and optics region curves is the Mie resonance region that results in an enhanced RCS measurement on average for a given size. In the resonance region, the scaling curve deviates from the optical curve (not shown) such that for a given RCS, the object is smaller in characteristic length than it would have been interpreted to be by using the optical approximation. The scaling curve may be expressed as:

$$x = \sqrt{\frac{4z}{\pi}}, \text{ for } z > 5, \text{ Optical Regime}$$

$$x = \sqrt[6]{\frac{4z}{9\pi^5}}, \text{ for } z < 0.03, \text{ Rayleigh Regime}$$

$$x = g(z), \text{ in between, Mie Resonance Regime}$$

where $z=\text{RCS}/\lambda$, $x=\text{diameter}/\lambda$, and λ is wavelength. In the above equations, the quantity z is assumed to not be expressed in dB. The smooth function $g(z)$ is expressed by 23 points in Table 2.

Table 2. The NASA SEM curve $x=g(z)$ in the Mie resonance region.

$x=\text{diameter}/\lambda$	$z=\text{RCS}/\lambda^2$
0.10997	0.001220
0.11685	0.001735
0.12444	0.002468
0.13302	0.003511
0.14256	0.004993
0.15256	0.007102
0.16220	0.01010
0.17138	0.01437
0.18039	0.02044
0.18982	0.02907
0.20014	0.04135
0.21237	0.05881
0.22902	0.08365
0.25574	0.1190
0.30537	0.1692
0.42028	0.2407
0.56287	0.3424
0.71108	0.4870
0.86714	0.6927
1.0529	0.9852
1.2790	1.401
1.5661	1.993
1.8975	2.835

Note that most of the debris for Haystack is in the Rayleigh region, which allows size estimates that are relatively insensitive to errors in the RCS measurements.

For comparison, the oscillating RCS-to-size curve for a spherical conductor is shown in the figure. The NASA SEM is not applicable to estimate sizes of spherical conductors (such as NaK droplets) in the Mie Resonance region. The oscillations result from constructive and destructive interference of electromagnetically induced waves on the surface of the conducting sphere. The estimation of debris sizes of highly polarized objects is discussed further in section 6.2.

The size-to-RCS curve for a spherical conductor is expressed theoretically as:

$$z = \frac{1}{\pi} \left| \sum_{n=1}^{\infty} (-1)^n \left(n + \frac{1}{2} \right) (b_n - a_n) \right|^2$$

where the coefficients a_n and b_n are

$$a_n = \frac{j_n(2\pi x)}{h_n^{(2)}(2\pi x)}$$

$$b_n = \frac{2\pi x \cdot j_{n-1}(2\pi x) - n \cdot j_n(2\pi x)}{2\pi x \cdot h_{n-1}^{(2)}(2\pi x) - n \cdot h_n^{(2)}(2\pi x)}$$

Where $h_n^{(2)}(x) = j_n(x) - i \cdot y_n(x)$, in which $j_n(x)$ and $y_n(x)$ are the spherical Bessel functions of the first and second kinds, respectively [34].

Further work has shown that the size implied by a single valued smooth RCS-to-size curve in Figure 4.0-1 needs to be adjusted slightly. This is because for any given size there is a distribution of RCS values, not necessarily symmetric about a mean or median RCS value. Sometimes an object will appear to be larger than the mean value and sometimes it will appear to be smaller. The radars measure a number of similar RCS values. Of these, some will be smaller objects which appear bigger, some will be objects that appear to be the correct size, and some will be larger objects which appear to look smaller. Because the SEM is a simple model for one-to-one RCS-to-size mapping, it does not provide an uncertainty estimate for the derived size distribution, nor does it take into account the specific distribution of RCS values for a given size. To improve the original NASA SEM, a Statistical Size Estimation Model (SSEM) has been developed [35]. The SSEM is based on the expectation maximization theorem clarified and further developed by Vardi and Lee [36]. The SSEM utilizes conditional probability distributions of RCS given a size, which were an outcome of the analysis done by XonTech of the RCS radar range measurements.

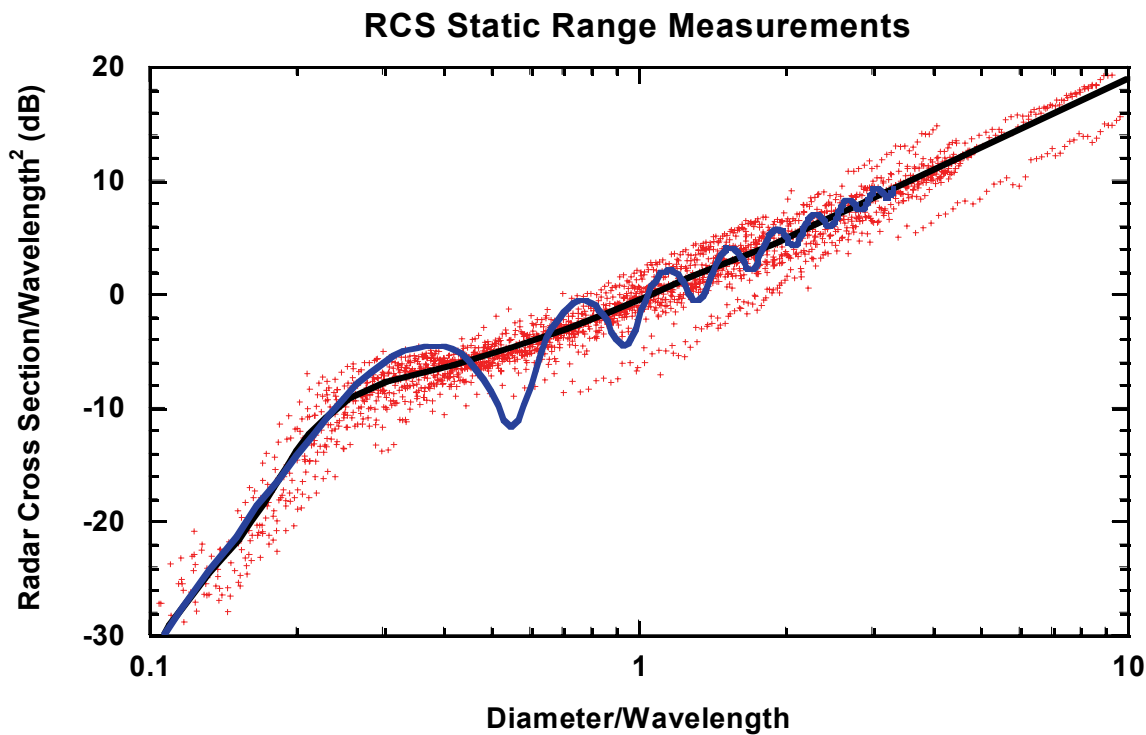


Figure 4.0-1. Results of RCS-to-Physical size measurements on 39 “representative” debris objects over the frequency range 2.0 – 18 GHz (15 – 1.67 cm wavelength). Each point represents an average RCS for a single object measured at a single frequency over many orientations. The oscillating line is the radar cross section for a spherical conductor while the smooth line is the polynomial fit to the data.

5.0 Data Overview

5.1 Description of Data Collected

For the collection year FY2003, all data were collected at 75° elevation, 90° azimuth (East looking). Table 3 and Table 4 show the number of hours data collected for each radar.

Table 3. Haystack FY2003 Data Summary

Altitude Window (km)	Range Window (km)	Usable Altitude Window (km)	Usable Range Window (km)	Hours	Det>5.5 dB INTSNR*	FA < 0.1/hr Detections (INTSNR*> 5.521dB)	Valid Detections (within range window)
302.77	312.33	351	352	633.3	6830	6209	4611**
1837.05	1885.29	1787	1835				

* 16 pulse non-coherent average

** sidelobe, noise and arcing removed

Table 4. HAX FY2003 Data Summary

Altitude Window (km)	Range Window (km)	Usable Altitude Window (km)	Usable Range Window (km)	Hours	Det>5.5 dB INTSNR*	FA < 0.01/hr Detections (INTSNR*> 5.749dB)	Valid Detections (within range window)
302.77	312.33	351	352	541.8	1926	1550	543**
1837.05	1885.29	1787	1835				

* 16 pulse non-coherent average

** sidelobe, noise and arcing removed

During ODAS processing at JSC, the incoherently integrated 16-pulse SNR threshold is set so that the false alarm rate is 0.1 per hour of data collection for Haystack and 0.01 per hour for HAX. With these false alarm rates, about 1% of Haystack's detections are expected to be false alarms; less than 1% of HAX's detections are expected to be false alarms.

The range window for Haystack and HAX WFC 4 in the 75° East stare mode extends from an altitude slightly over 300 km to slightly beyond 1800 km. This is a significantly larger range window than used in the past. For debris objects at altitudes slightly above the maximum and slightly below the minimum altitude, only part of their reflected radar energy is detected in the receive window by Haystack. If these objects have low SNR they can be indistinguishable from objects exactly at the maximum or minimum altitude, but will appear to be smaller than they actually are because only part of the reflected energy is detected. To eliminate this problem, all detections in the first and last 50 km of range are not reported in the flux versus altitude calculations. This leaves an effective range window of about 1450 km for Haystack and HAX with WFC 4.

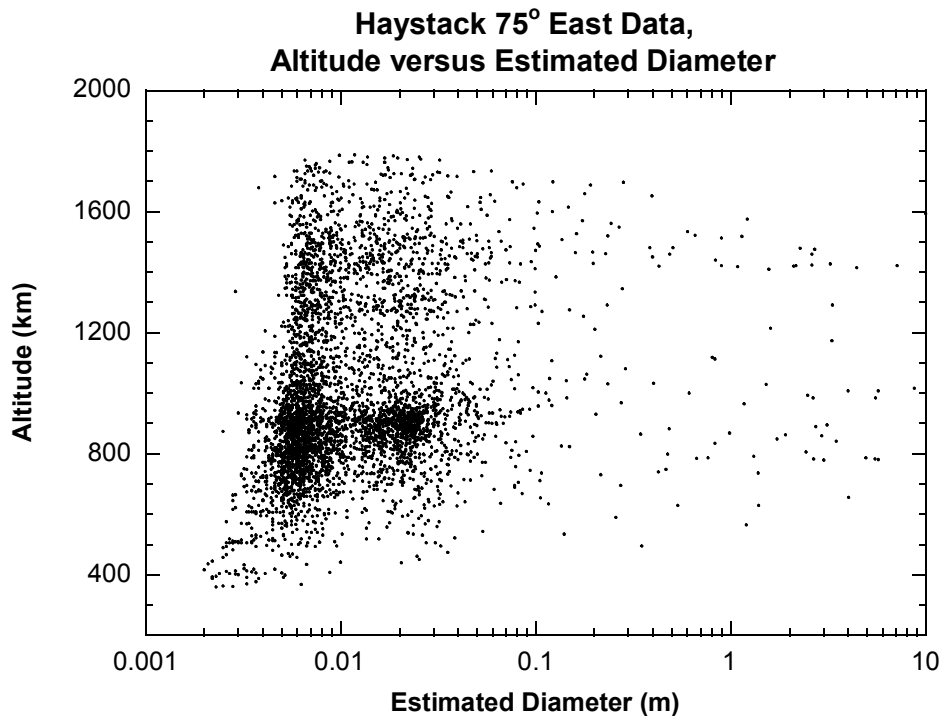


Figure 5.1-1. Altitude vs. size estimated from the NASA SEM for Haystack detections.

Figure 5.1-1 shows altitude versus size for the FY2003 Haystack data. Figure 5.1-2 shows altitude versus size for the FY2003 HAX data. Figure 5.1-3 shows the approximate size limits for data from the two radars as a function of altitude. For WFC 4, essentially the entire range window of Haystack is in the Rayleigh region with RCS proportional to the 6th power of diameter, while the range window for HAX is almost entirely in the optical region with RCS approximately proportional to diameter squared.

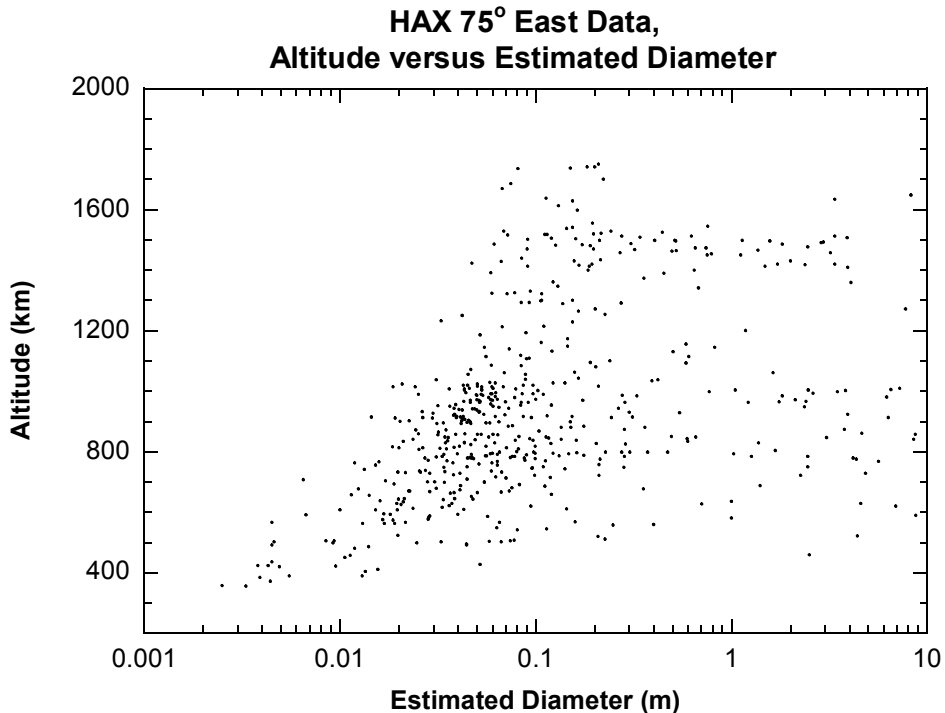


Figure 5.1-2. Altitude vs. size estimated from the NASA SEM for HAX detections.

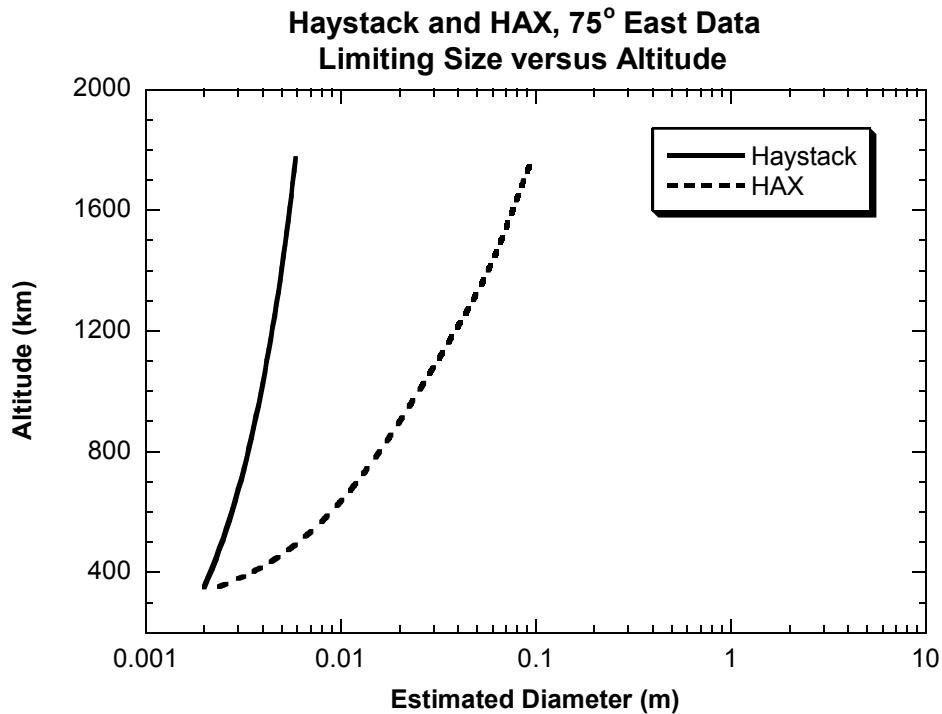


Figure 5.1-3. Approximate size limits vs. altitude for Haystack and HAX for WFC4 in the 75° East stare mode.

5.2 Comparison of Derived Parameters for Cataloged Objects

In the course of collecting staring data, some objects in the SSN catalog pass through the Haystack or HAX field-of-view. Comparisons between the catalog-derived parameters and the Haystack- and HAX-derived parameters are made to help validate the ODAS results. In making the comparisons, however, it must be remembered that the data are collected with different instruments with different objectives in mind. The SSN sensors concentrate on obtaining metric observations, position, and velocity from which orbital elements can be calculated or updated. Historically, the SSN has been less interested in the size of objects. SSN size estimates are reported in the "RCS Catalog" and historically have come primarily from tracking by the Eglin FPS-85 (68 cm wavelength) radar, although additional radars have been recently included. A study [37] found that the reported sizes of objects varied from catalog to catalog, and that for comparisons with optical measurements, more consistent results were obtained by averaging the sizes reported in many different RCS catalogs. In the debris studies, the Haystack data are being used to statistically characterize the debris environment and the size or orbit of an individual object is not critical so long as the distribution of sizes or orbits is representative of the environment.

Figure 5.2-1 and Figure 5.2-2 show a comparison of diameters for cataloged objects which appear in the Haystack and HAX data. SSN sizes and Haystack and HAX sizes are deduced from the NASA SEM. Those objects denoted with (\bullet) are identified as being detected in the mainlobe of the antenna beam. The solid line in the figure represents an exact match in size. The (Δ) sign indicates an object that was identified as being detected in a sidelobe. The dashed line (---) represents a match in size for objects that pass through one of Haystack's sidelobes, but are identified as passing through the mainlobe. Monopulse data from a sidelobe can cause a false indication of a mainlobe detection and produce a very low estimate of the detected object's diameter. For Haystack, the first, second, and third sidelobes reduce the two-way measurement of RCS by approximately -41 dB, -49 dB, and -55 dB. The behavior of the

Haystack sizes less than approximately 0.7 cm (for a 3 cm Haystack wavelength) occurs because of the transition from the optical regime to the Rayleigh regime for Haystack measurements. For HAX, the first sidelobe reduces the two-way measurement of RCS by approximately -38 dB.

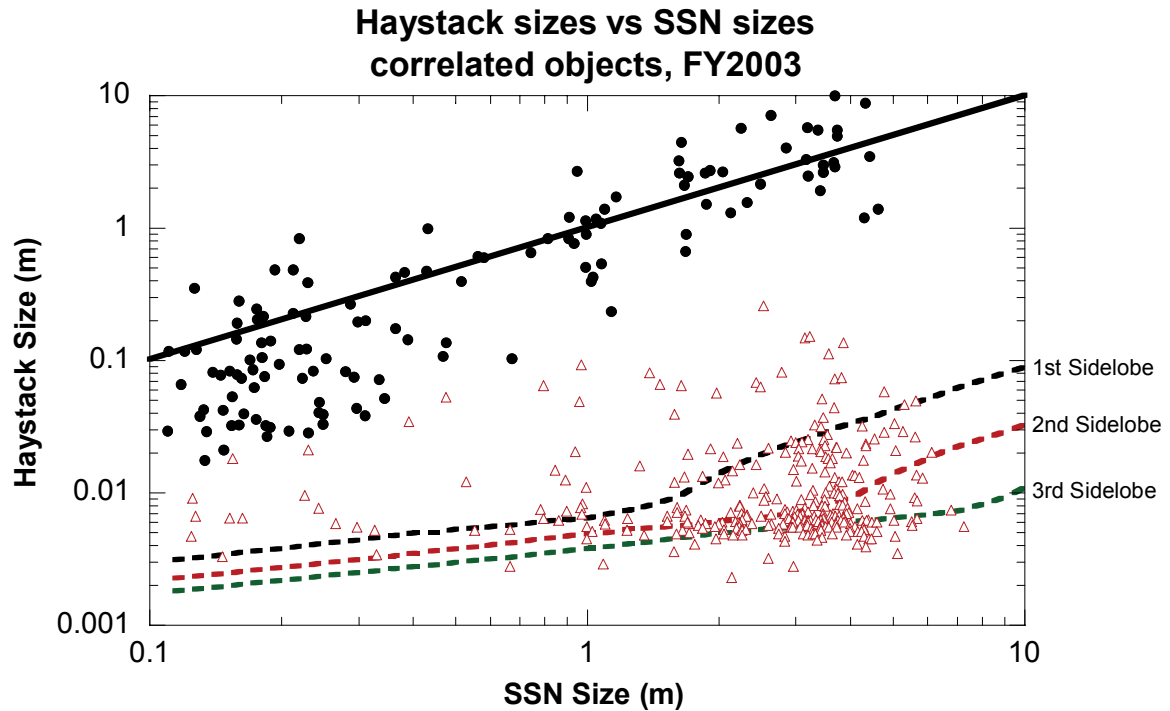


Figure 5.2-1. Comparison of Haystack-derived size and SSN-reported size for those Haystack 75° East detections collected in FY2003 that correlate to cataloged objects.

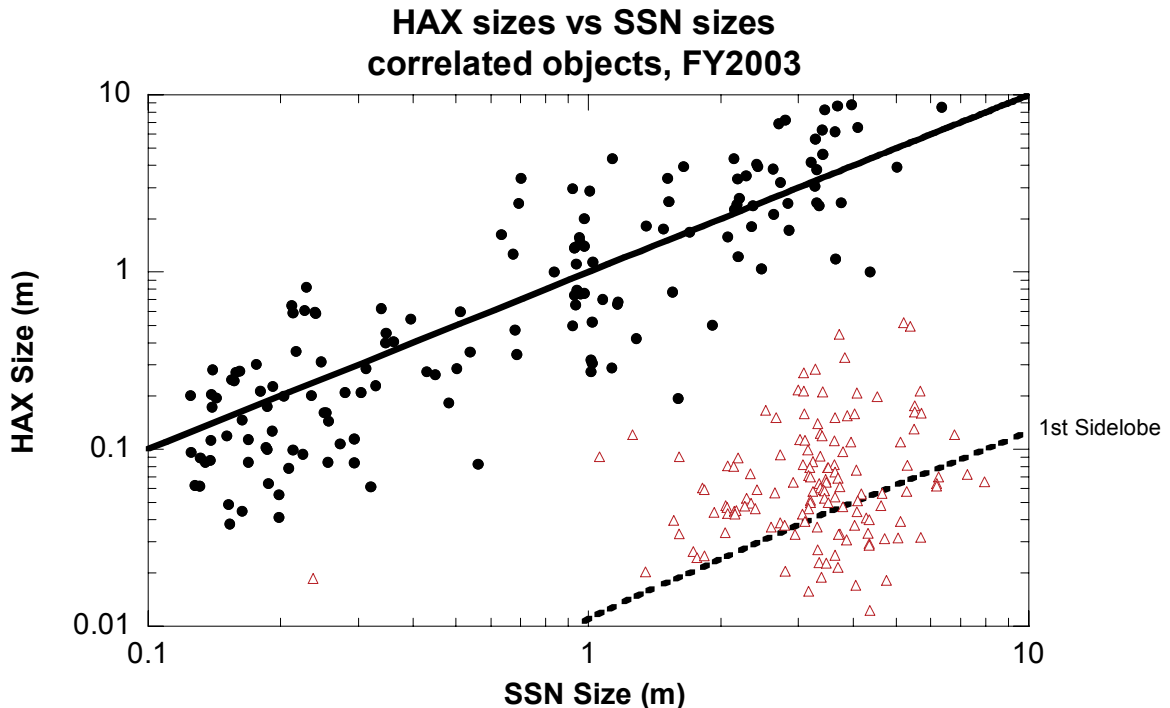


Figure 5.2-2. Comparison of HAX-derived size and SSN-reported size for those HAX 75° East FY2003 detections that correlate with cataloged objects.

In cases where all indicators point to a mainlobe detection but the size estimate is less than 12% of the Elgin size, the detections were arbitrarily identified as sidelobe detections. Figure 5.2-1 and Figure 5.2-2 include detections that were identified as sidelobe detections from the behavior of the monopulse voltage ratios, phase, SNR, and uncorrected RCS data. An invalid size is most likely due to a sidelobe detection, which was identified (see following section) from the ODAS plots. It is also possible an optimal selection of data was not used by the software to estimate size because the estimated offsets angles were poorly fit. Other plausible, but less likely explanations are that: 1) the object was not the catalogued object it was thought to be; or, 2) the orientation of the object during the very short interval during beam passage gave an anomalously low size.

Ignoring sidelobe detections and misidentified correlations, the sizes from the two data sources are in good agreement for large objects, but for small objects, sizes calculated from Haystack are smaller than those from Eglin [37]. In June 1993, the Air Force conducted a two-week debris test during which the Millstone radar tracked some small (10 - 50 cm) debris objects that were also tracked by Eglin. In most cases, Millstone also saw the object as smaller than Eglin. The explanation [38] provided by MIT/LL, which operates Millstone, was that the software at Eglin will only accept individual radar returns which pass a preset threshold when computing an average size. At Millstone, as long as the object is being tracked, all of the radar returns are averaged. Therefore, Eglin calculates an erroneously large size because it is not using the smallest returns when computing the average RCS. This discrepancy will be greater for smaller objects.

Figure 5.2-3 and Figure 5.2-4 compare the Doppler inclination derived from Haystack and HAX data with the catalogued inclination for correlated targets in the FY2003, 75° East data. Most points lie on or near the dotted line that represents a one-to-one match of the SSN catalog inclination values and the Doppler inclination values. The figure shows there is good correlation between Haystack and SSN inclinations.

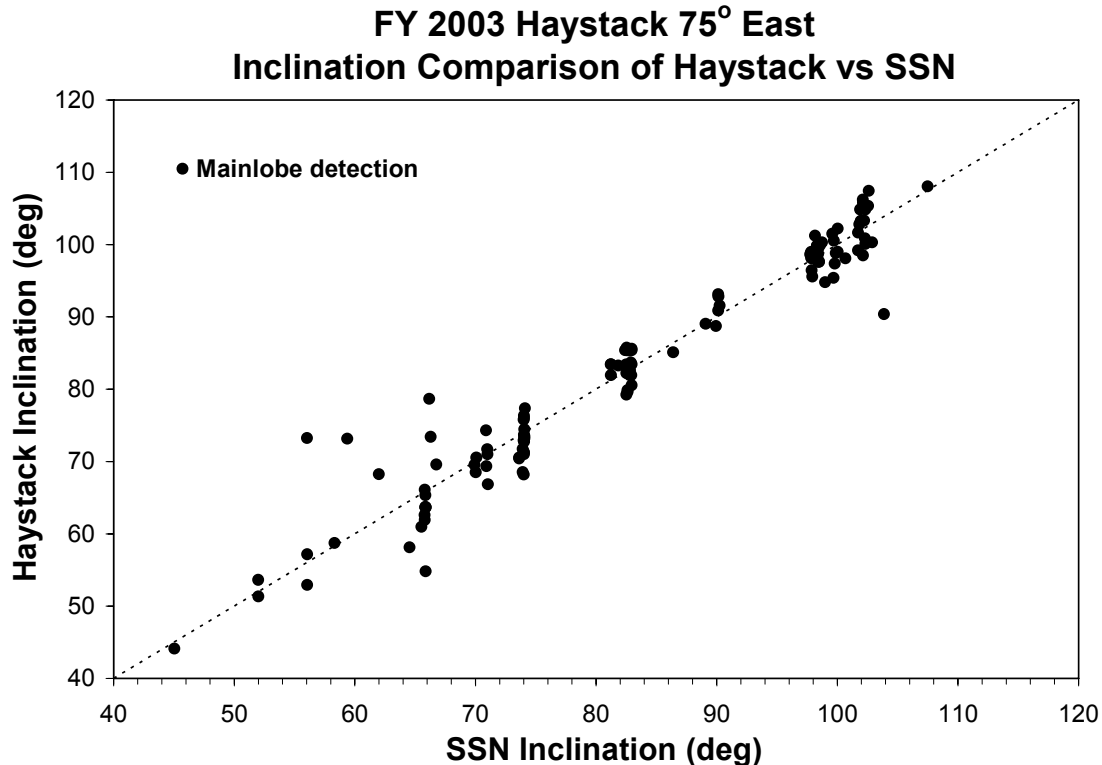


Figure 5.2-3. Comparison of the Doppler inclination derived from Haystack data with the catalogued inclination for correlated targets in the 75° East FY2003 data.

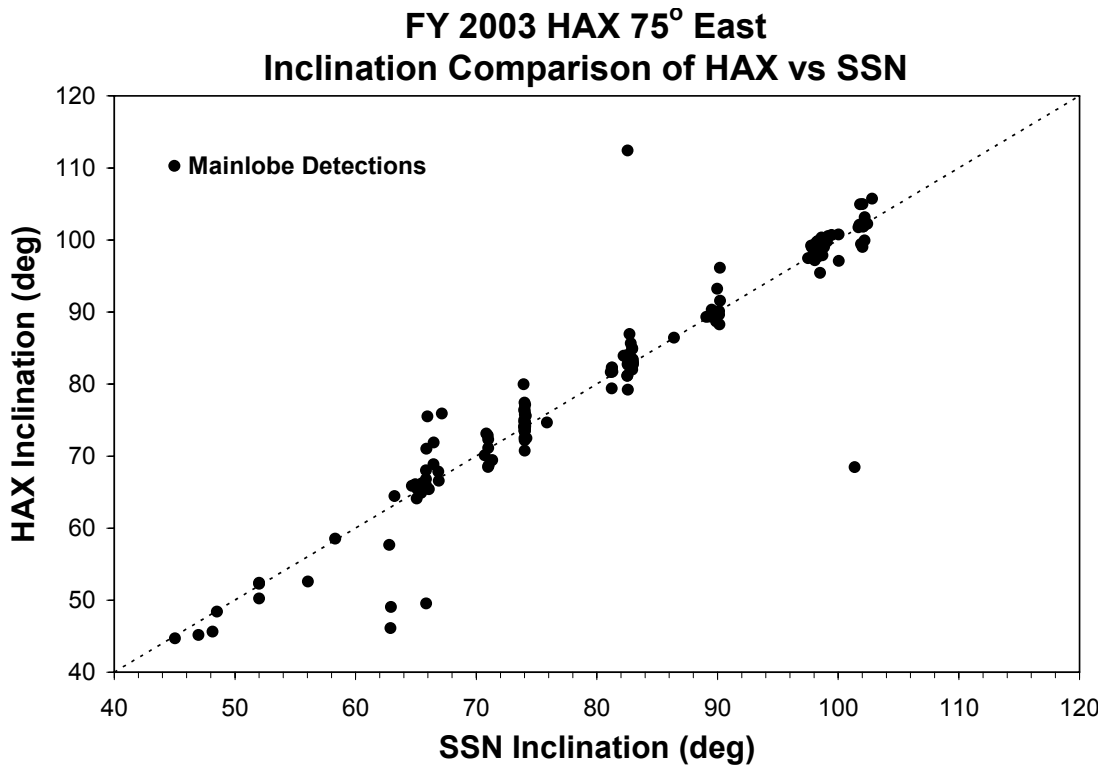


Figure 5.2-4. Comparison of the Doppler inclination derived from HAX data with the cataloged inclination for correlated targets in the 75° East FY2003 data.

6.0 Results

6.1 Measurement Summary

This report discusses Haystack and HAX data collected during fiscal year 2003, from 1 October 2002 to 30 September 2003. All of the data were collected in a fixed staring mode at 75° elevation and 90° azimuth with WFC 4, a CW 1.6384 millisecond pulse, at a pulse repetition frequency of 60 Hz. Due to the increased range extent of Haystack and HAX radars from improvements in the PACS at MIT/LL that were completed at the end of FY2002, this data covers an altitude range that previously required combining data from smaller altitude ranges. Since the number of debris observation hours at the Haystack and HAX radars is limited, the increased range extent in the FY2003 data results in the best orbital debris statistics ever obtained in a single year. Unfortunately, errors in the PACS reduced the sensitivity of Haystack to detect debris with diameters less than approximately 1 cm and that of HAX to detect debris with diameters less than approximately 4 cm.

Table 3 and Table 4 in section 5.1 summarize the data collection for the FY2003 time period. The range window of both Haystack and HAX extends from 312 km to 1885 km. For 75° East pointing, the altitude window for both of these radars extends from 303 km to 1837 km. As described in section 5.1, the first 50 km and the last 50 km within this range window are ignored. Excluding these data near the ends of the range window, the effective range window of each radar is 352 km to 1835 km and the effective altitude window is 351 km to 1787 km.

The risk analysis associated with orbital debris generally starts with cumulative debris fluxes, with the flux area defined by the conic frustum area of the cone using the 3 dB radar beamwidth between the altitudes of interest. The cumulative flux quoted in this paper is commonly referred

to as the surface area flux, which relates to the cross sectional flux through the relation $\text{flux}_c = \text{flux}_s \cdot \pi$.

Figure 6.1-1 and Figure 6.1-2 show the 1 cm (cumulative) flux for Haystack in 75° East stare as a function of altitude with 100 km and 50 km altitude bins. HAX data is not shown since HAX is not efficiently detecting debris down to 1 cm diameter. The solid lines represent a size estimation model [35] statistical flux of 1 cm objects and the error bars are those associated with the SSEM. The errors assume Poisson statistics and do not incorporate any systematic errors or biases

Figure 6.1-3 through Figure 6.1-6 show Haystack and HAX 75° East size distribution measurements in 100 km bins from 400 km to 1700 km for Haystack and HAX. As a benchmark, the flux of 10 cm objects from the USSPACECOM catalogue at the beginning, middle and end of FY2003 are also shown. As expected, both Haystack and HAX show a rolloff in sensitivity at small sizes due to a decreased detection probability. Assuming Poisson statistics underestimates the errors since a debris swarm observed by the radar can bias the flux measurement, particularly for larger sizes since the number of observations of large objects can be very small. This may explain some of the discrepancies between fluxes observed by Haystack, HAX, and the catalogued population.

A histogram of Doppler inclination for Haystack-detected debris is shown in Figure 6.1-7. There are five inclination regions that are populated: 65°, 70°, 83°, 90°, and 100°. The altitude histograms for each of these regions are shown in Figure 6.1-9 through Figure 6.1-12. Objects at 65° (62° to 68°) are spread between 700 km to 1100 km peaked at 900 km; objects at 70° (68° to 74°) are at 800 km and 1450 km; objects at 83° (80° to 86°) are at 900 km and 1500 km; objects at 90° (88° to 94°) are at 900 km with a small population near 1300 km; objects at sun-synchronous orbits near 98° (95° to 103°) show populations between 700 km to 1000 km and 1300 km to 1600 km.

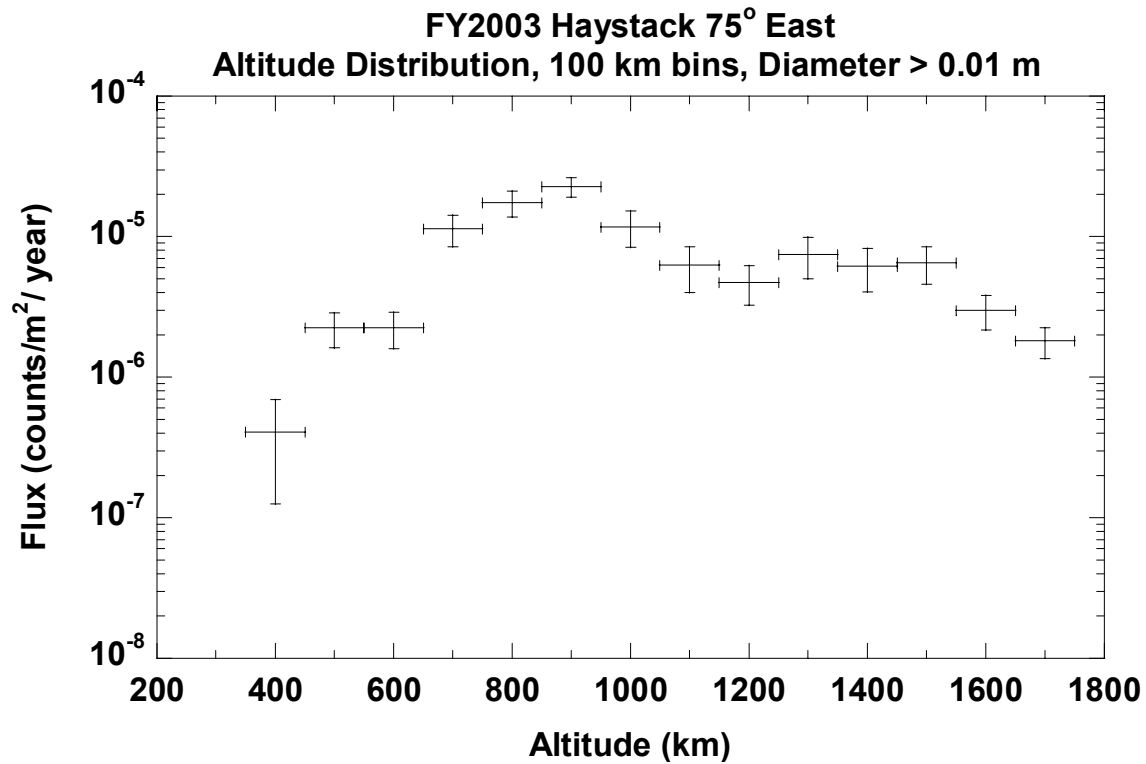


Figure 6.1-1. Flux of 1 cm debris for Haystack 75° East measurements for 2003 with 100 km altitude bins.

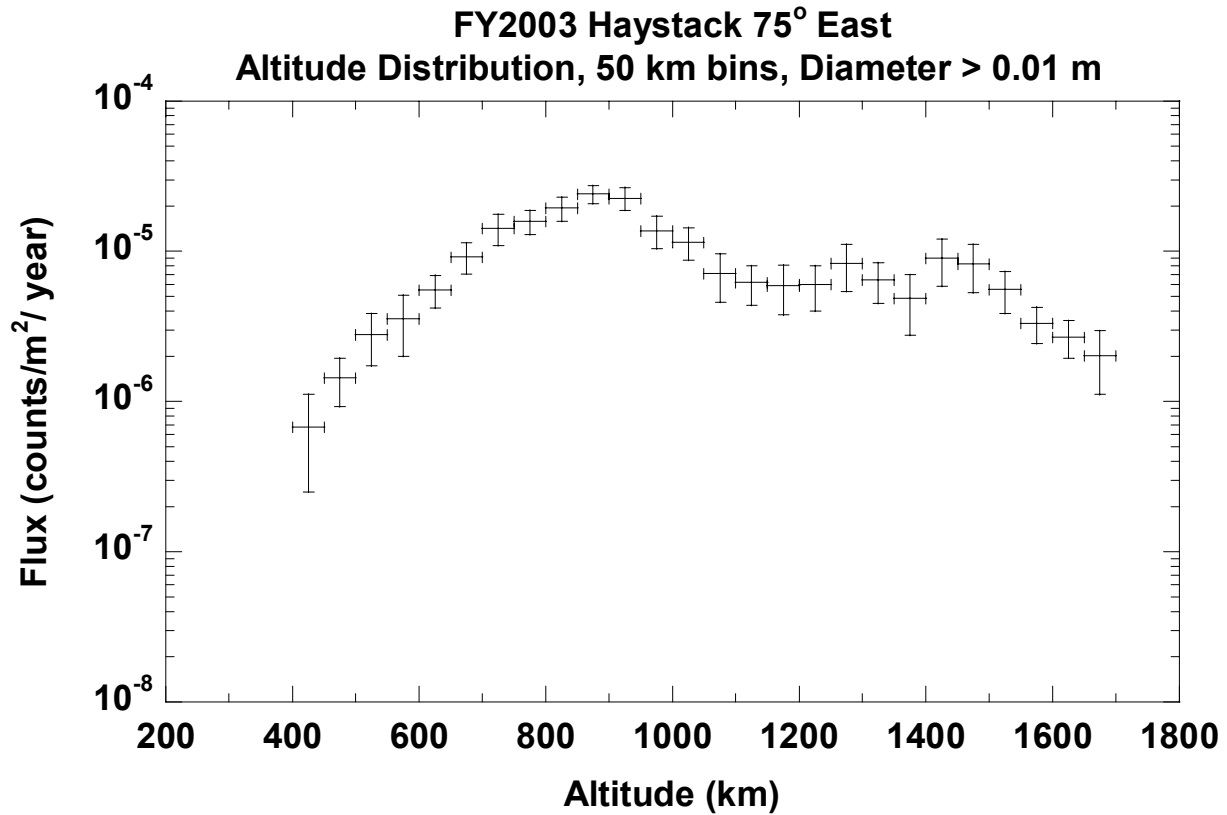


Figure 6.1-2. Flux of 1 cm debris for HAX 75° East measurements for 2003 with 50 km altitude bins.

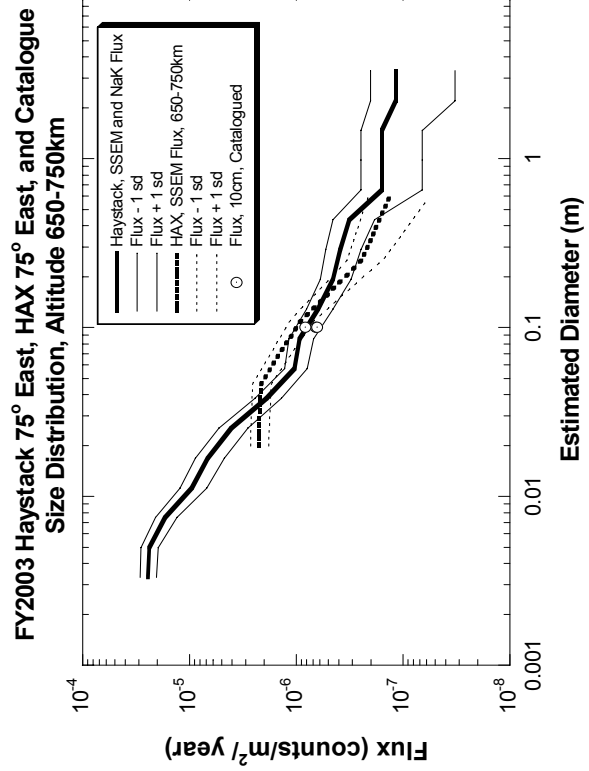
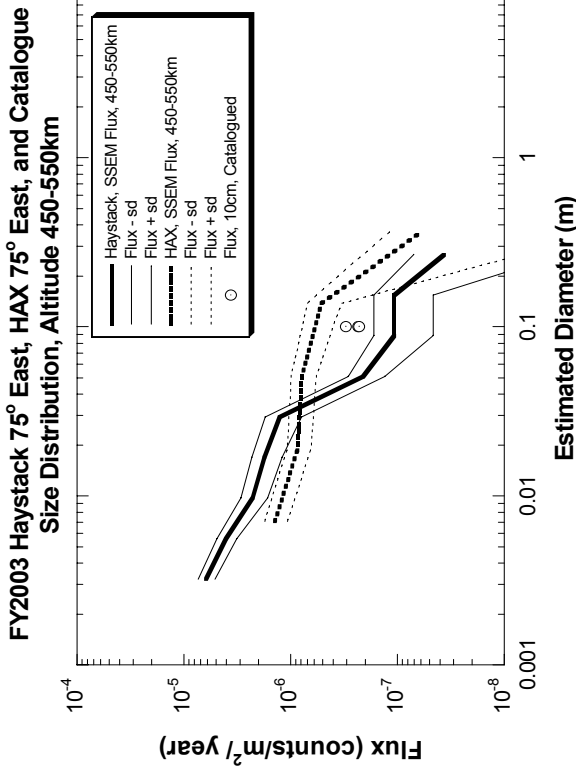
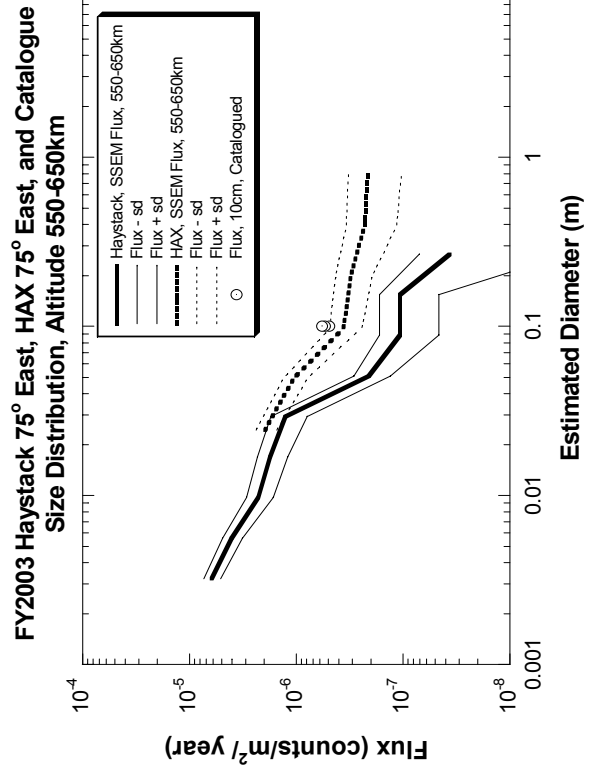
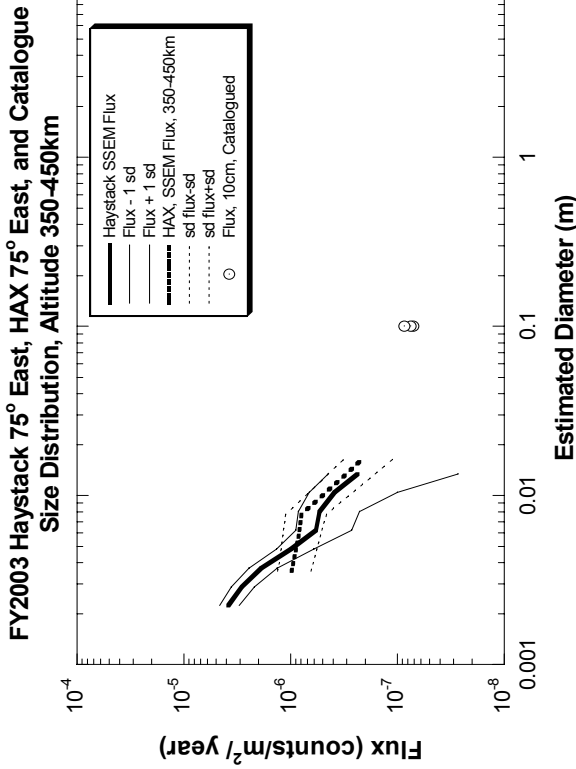


Figure 6.1-3. Size distributions at 400, 500, 600, and 700 km for fluxes for FY2003 Haystack and HAX 75° East measurements.

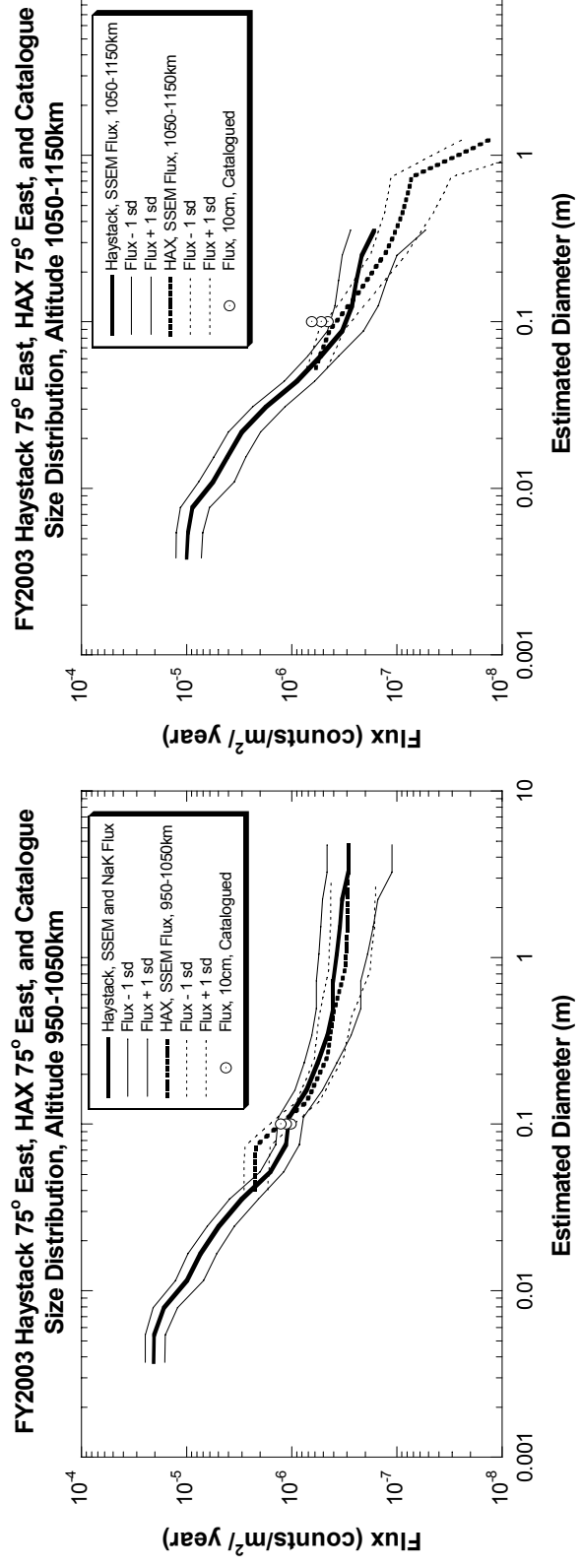
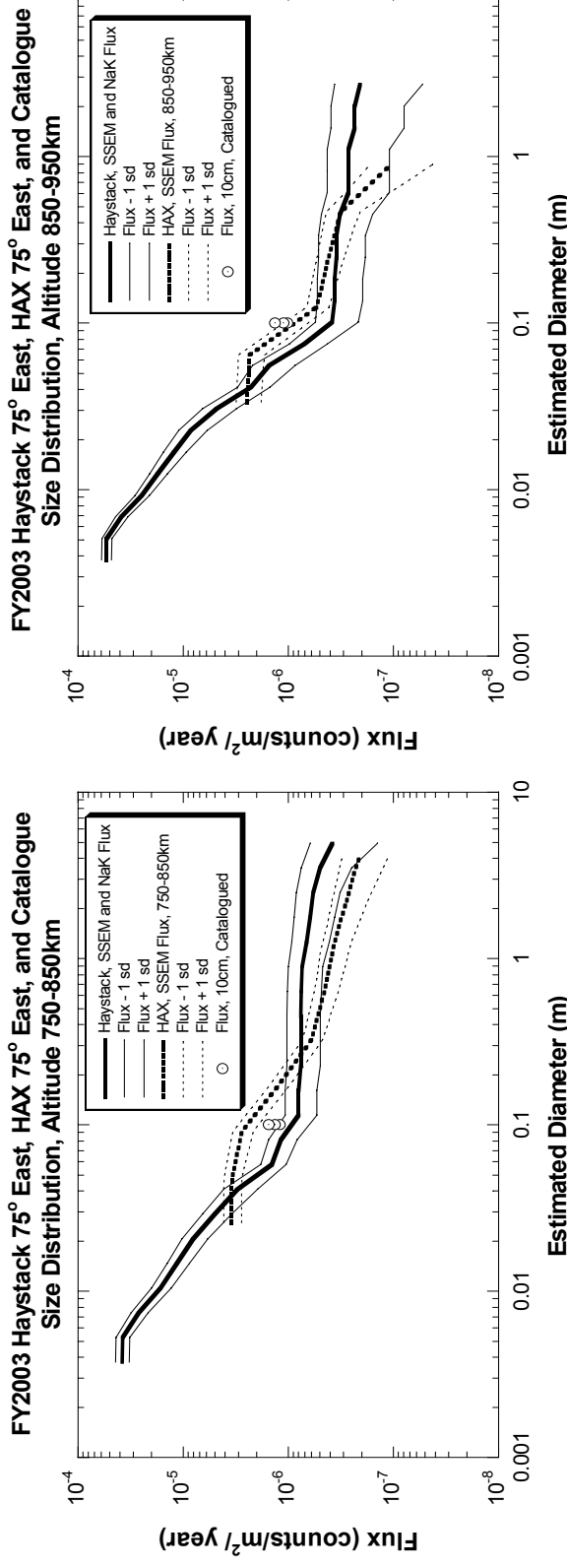


Figure 6.1-4. Size distributions at 800, 900, 1000, and 1100 km for fluxes for FY2003 Haystack and HAX 75° East measurements.

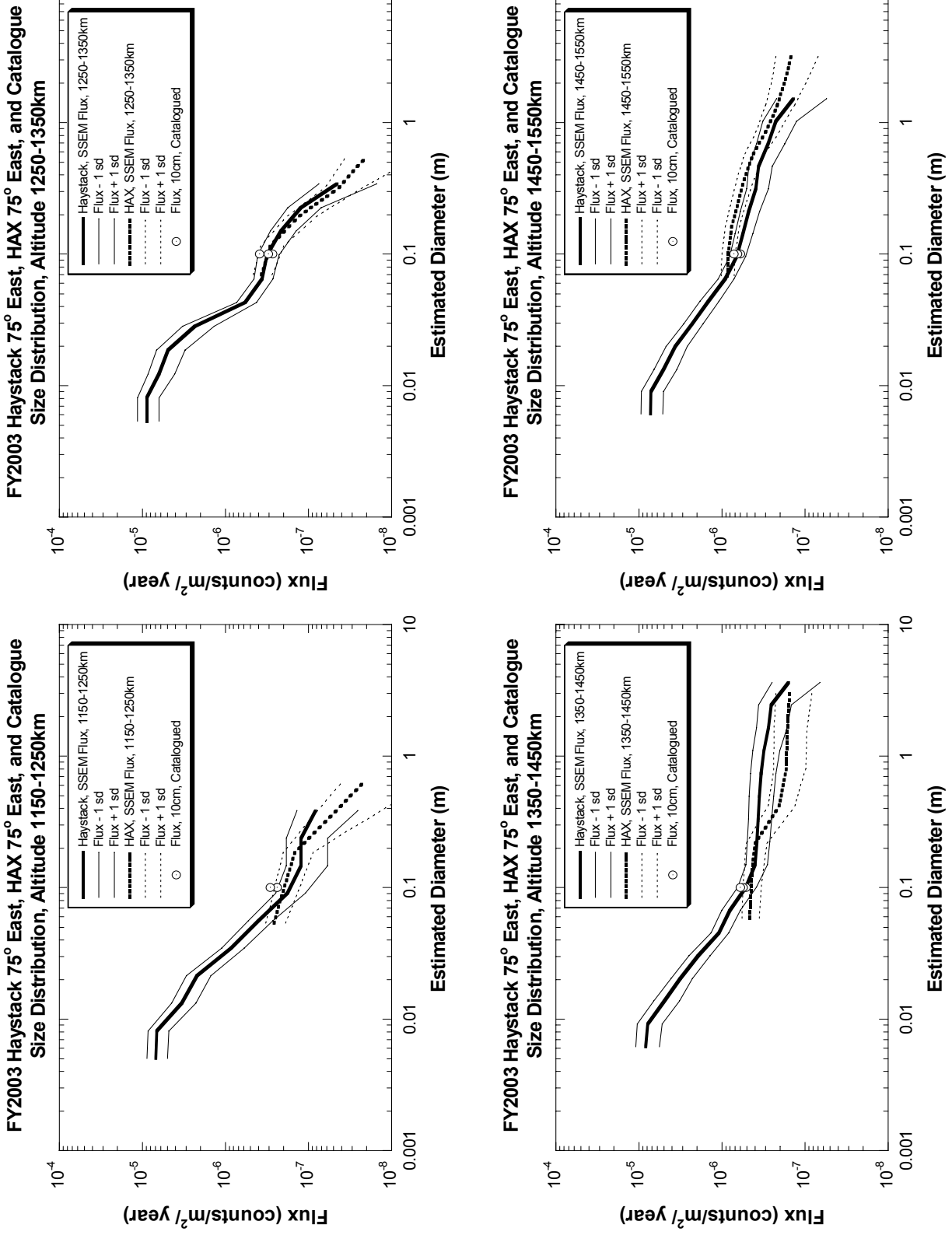


Figure 6.1-5. Size distributions at 1200, 1300, 1400, and 1500 km for fluxes for FY2003 Haystack and HAX 75° East measurements.

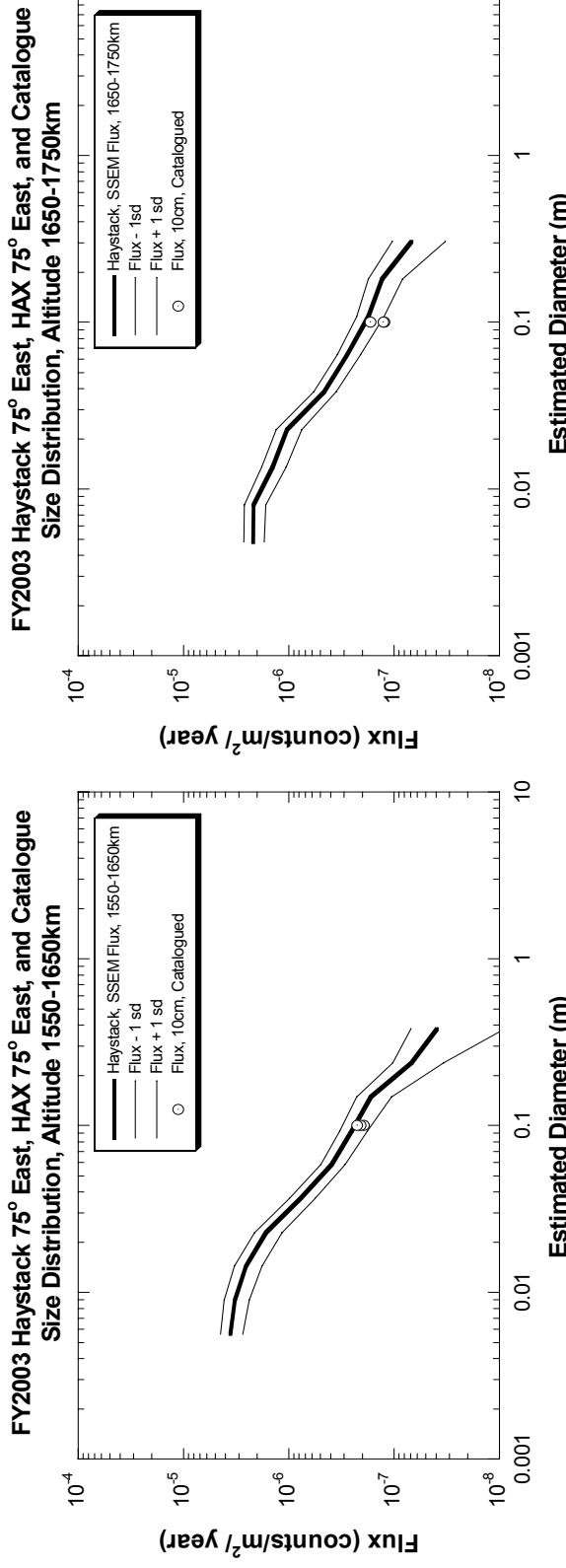


Figure 6.1-6. Size distributions at 1600 and 1700 km for fluxes for FY2003 Haystack 75° East measurements.

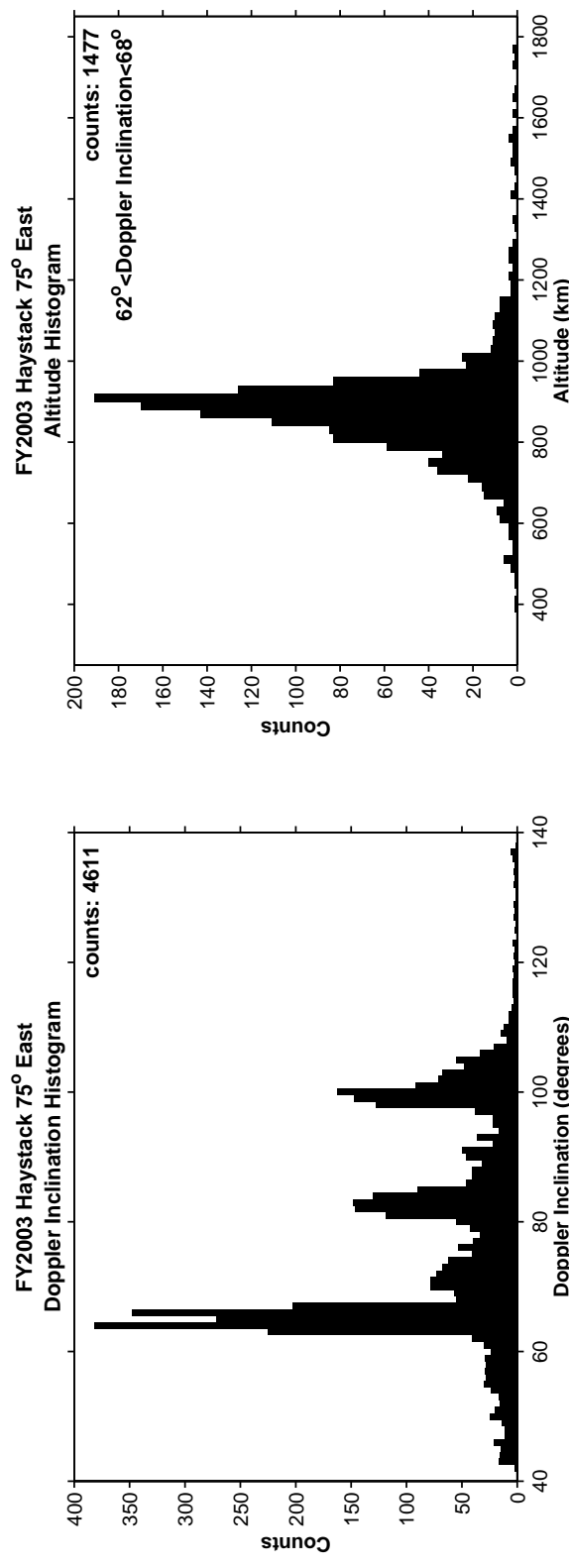


Figure 6.1-7 and Figure 6.1-8. Doppler Inclination histogram for FY2003 Haystack 75° East measurements. Altitude histogram for detections with Doppler Inclination between 62° to 68°.

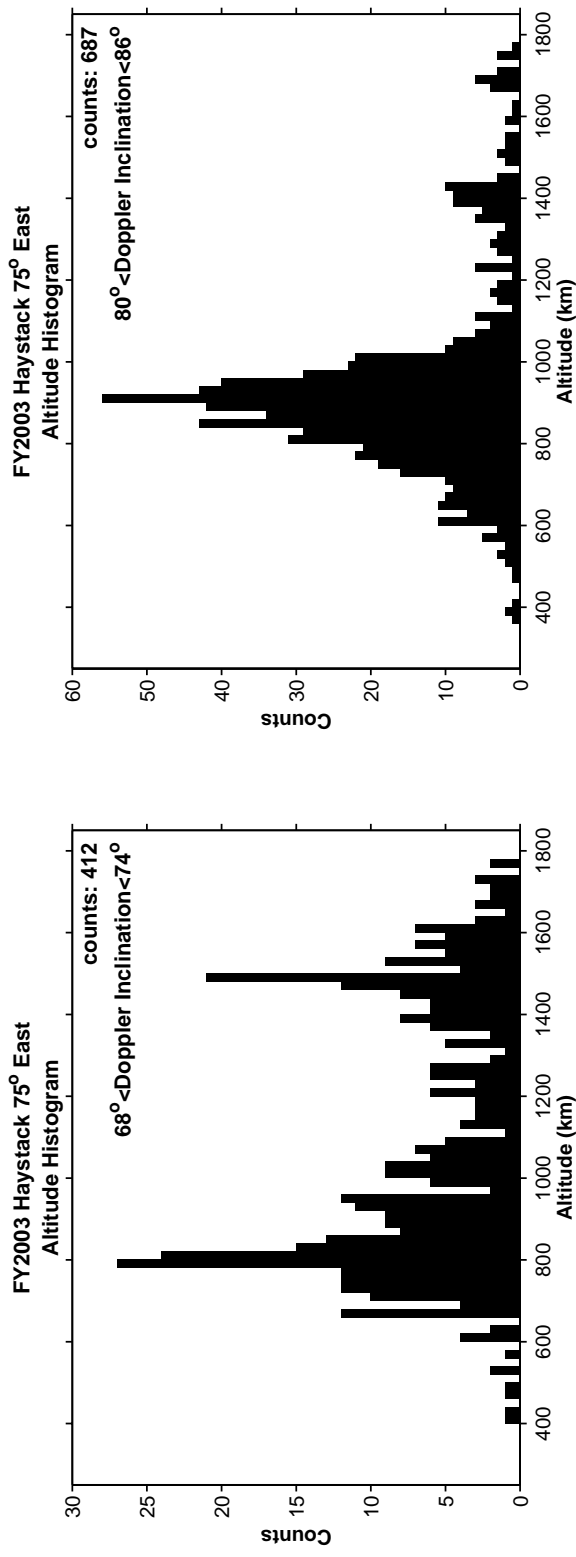


Figure 6.1-9 and Figure 6.1-10. Altitude histogram for detections with Doppler Inclination between 68° to 74° . Altitude histogram for detections with Doppler Inclination between 80° to 86° .

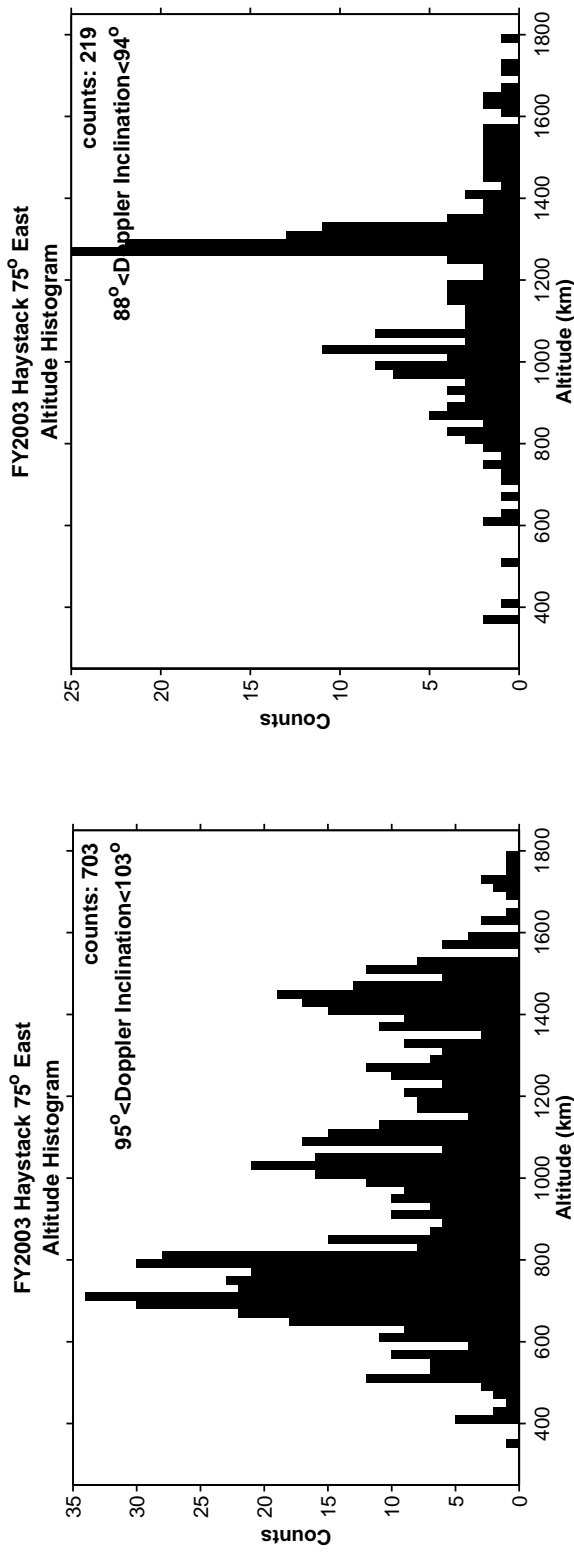


Figure 6.1-11 and Figure 6.1-12. Altitude histogram for detections with Doppler Inclination between 88° to 94° . Altitude histogram for detections with Doppler Inclination between 95° to 103° .

6.2 Polarization Measurements

The transmitted beam of Haystack and HAX is right circularly polarized. The left circularly polarized part of the return signal is referred to as the principal polarization (PP) component. The right circularly polarized portion of the return signal is referred to as the orthogonal polarization (OP) component. Polarization, P , measured as

$$P = \frac{RCS_{PP} - RCS_{OP}}{RCS_{PP} + RCS_{OP}}$$

contains information about the target, possibly indicating if it is spherically shaped*. A target with a polarization near +1 is consistent with a spherical conductor. The measured polarization should not be an artifact of system noise since one expects the same noise level in both the PP and OP channels. This definition of polarization (also known as the Mott polarization) differs slightly from that used in previous radar reports. To ensure consistency with previous years with this new definition, objects with a polarization greater than 0.84 will be referred to as highly polarized. It is assumed that a majority of highly polarized radar return signals are for debris that are spherical or spherical-like.

Figure 6.2-1 shows a figure of altitude versus Doppler inclination for all debris with highly polarized return signals. For comparison, Figure 6.2-2 shows a figure of altitude versus Doppler inclination for all debris. Among debris with highly polarized radar returns, there are three primary inclination regions that are populated: 65° , 83° , and 98° . The highly polarized targets near 65° inclination between 700 km to 1000 km altitude have been identified as spherical eutectic NaK coolant from ejected cores of Russian RORSATs. As in Reference 10, those debris objects with an altitude between 700 km to 1000 km, Doppler inclination between 62° and 68° , and with a measured polarization in excess of 0.84 are assumed to be NaK debris. The groups of objects in Figure 6.2-1 near inclinations of 83° and 98° have not been attributed to a single source such as coolant from an ejected core. Objects at 83° are predominately distributed between 600 km to 1000 km. Highly polarized sun-synchronous objects near 98° are distributed between 500 km to 1600 km with a concentration of debris near 750 km.

* This is not true for linearly polarized radar signals.

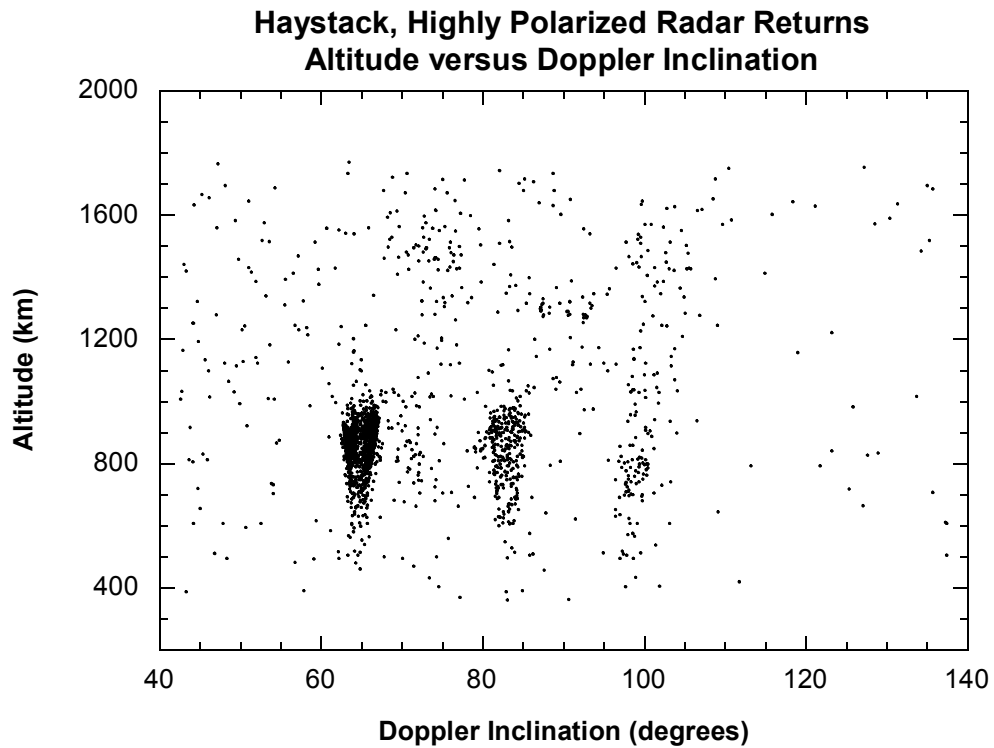


Figure 6.2-1. The altitude versus Doppler inclination for debris with highly polarized return signals, *i.e.*, polarization greater than 0.84.

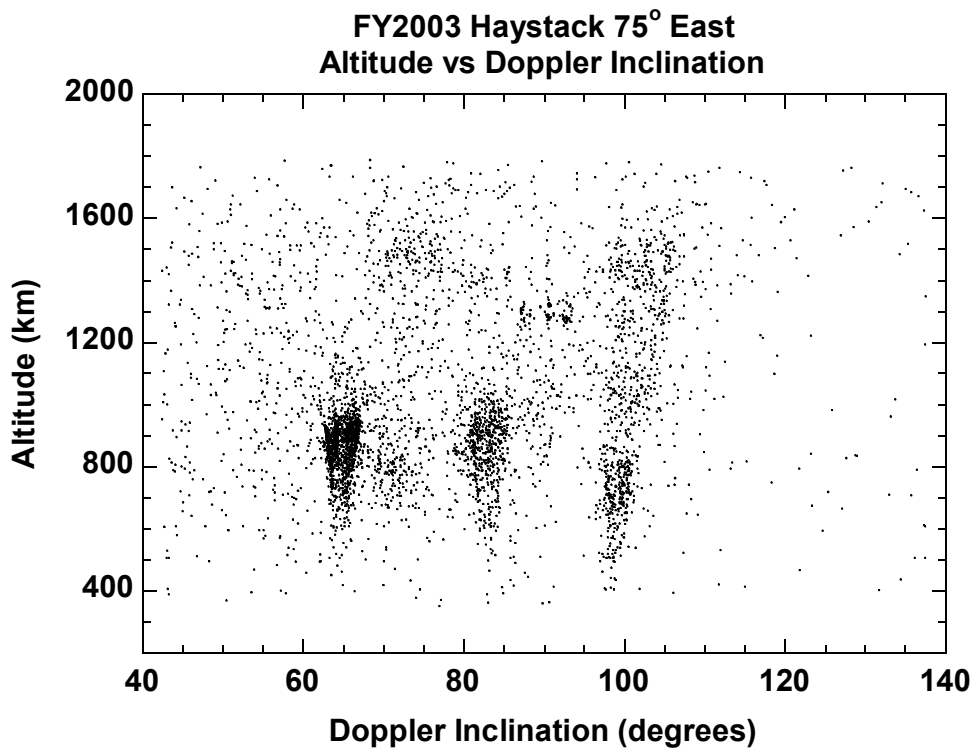


Figure 6.2-2. The altitude versus Doppler inclination for all debris.

The cumulative detection rate of NaK debris versus RCS from fiscal years 2000 through 2003 are shown in Figure 6.2-3. The NaK population is unique since there are no new sources of this debris. Moreover, no appreciable fraction of NaK debris is being lost to reentry. The year to year stability of this population is confirmed in Figure 6.2-3 for fiscal years 2000, 2001, and 2002. However, the data for FY2003 indicate a lower detection rate than in previous years for the debris with a smaller RCS. Also, there appears to be RCS bias of + 2 dB compared to previous years. These differences are most likely attributable to the problems encountered in the PACS all-digital system as discussed in section 3.3.

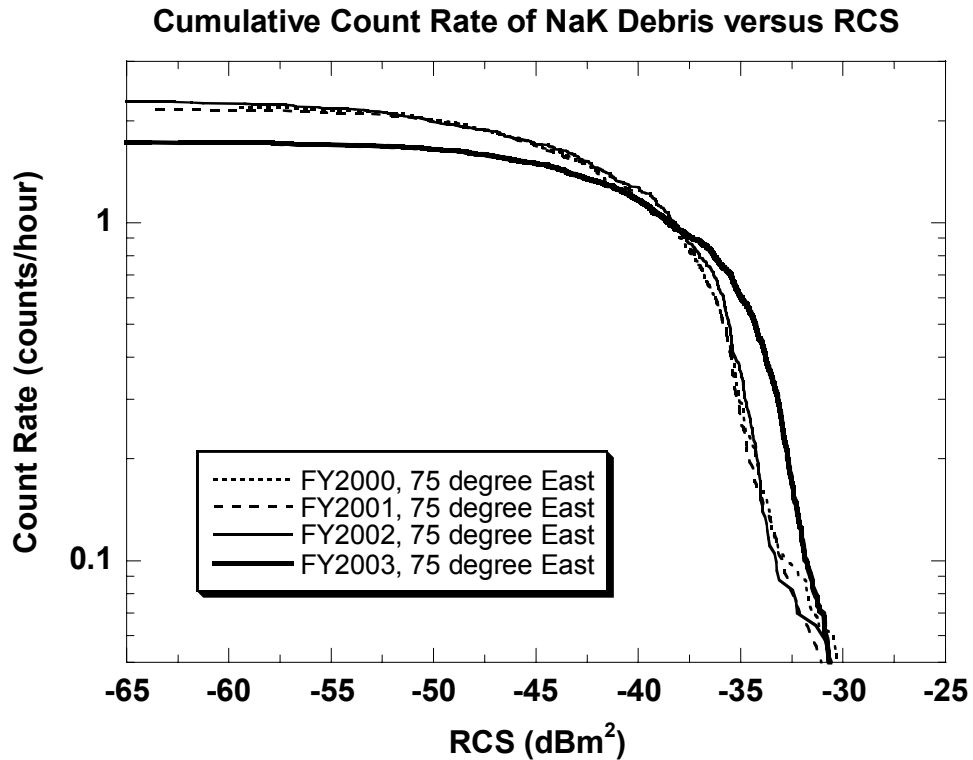


Figure 6.2-3. Cumulative count rate of NaK debris versus RCS for several fiscal years.

For the cumulative flux versus diameter given in the previous section, the size distributions for NaK debris and the non-NaK debris were treated separately. The non-NaK size distribution was determined using the SSEM. The cumulative fluxes for these distributions were then added directly to the cumulative fluxes from the SSEM. The error bars shown are those from the SSEM.

A + 2 dB bias does not critically affect the estimate of much of the non-NaK debris since much of the debris is in the Rayleigh region. Within the Rayleigh region, errors in RCS measurements do not significantly change size estimates. The bias does however affect size estimates for non-NaK debris in the Mie and optical region. No correction is made for this bias for non-NaK flux estimates.

Determining the size distribution of the NaK population is complicated since multiple disparate sizes are possible for a given RCS in the Mie resonance region. Figure 4.0-1 illustrates this phenomenon. For example, if the Haystack radar (3 cm wavelength) observes a NaK candidate with a RCS of -40 dBm², three distinct sizes are possible: 0.74 cm, 1.54 cm, and 1.76 cm. Since the SSEM requires smooth probability density distributions relating size and RCS, the statistical methodology of the SSEM is not appropriate for determining the size distribution of the NaK population.

From a previous analysis [21], the cumulative NaK population was determined to be:

$$N(d) = \frac{D \cdot E \cdot F \cdot d^a \cdot d^b \cdot [1 - \exp(-(d - d_0)^2 / (2 \cdot s^2))]}{D + E \cdot d^a + F \cdot d^b}$$

with $D = 4844.949$, $E = 0.070929$, $F = 0.02936787$, $a = -1.103482$, $b = -2.936787$, $d_0 = 0.058321$, $s = 0.00613216$, with $0.005 \text{ m} < d < 0.0583 \text{ m}$. Attempts to derive the FY2003 NaK population using techniques from the previous analysis failed since those fits are very sensitive to the shape of the RCS distribution. Since the population is believed to be stable and well understood based on the previous analysis [21], the FY2003 NaK population for each of the altitude bins is estimated using this population estimate. This FY2003 population distribution curve is scaled according the number of NaK detections determined at each altitude window. There are limitations to this that originate from detection inefficiencies encountered in FY2003 for debris with smaller RCS returns.

7.0 Breakups

The SSN identifies breakups from observations of large fragments which it can track with a predominantly UHF (330 - 1000 MHz) tracking network. There is often much detailed information available on the parent body and the time of the breakup. The orbit characteristics of an explosion cloud or breakup cloud vary greatly, depending on the orbit of the parent body, the precise breakup time, and on the energy the event imparts to the fragments.

Haystack data has been used in the past to examine families of objects from individual breakups or families of objects that can be isolated in altitude and inclination [12, 39]. This is possible because for some time after a breakup, the debris cloud particles can remain grouped together in similar orbit planes. The cloud will be visible to the radar for a short time, twice each day, as the plane moves through the field-of-view. There should be a unique three-dimensional pattern in observation time, range, and range-rate identifying the cloud. Eventually through differing rates of precession of the right ascension of ascending node of the debris clouds, the observation time becomes distributed so that event identification becomes much more difficult.

After a breakup event, the fragments distribute themselves around the orbit while the right ascension of ascending node Ω of the fragments slowly disperses. With the dispersal of the right ascension, the association of the fragment with the orbital plane is lost. The precession of the right ascension of ascending node is given by

$$\Delta\Omega = -0.584^\circ \left(\frac{R_\oplus}{p} \right)^2 \cos(\theta_{inc})$$

per orbit, where θ_{inc} is the inclination, R_\oplus stands for the Earth radius of 6378 km, and $p=a(1-e^2)$ is the semi-latus rectum, with semimajor axis a and eccentricity e [40]. For a circular orbit, the semi-latus rectum p is equal to the sum of the Earth's radius, R_\oplus , and the altitude of the satellite. Because $d\Omega/dt$ is proportional to $\cos(\theta_{inc})$, objects in a debris cloud (with a distribution in altitude) at 90° orbital inclination do not precess. Debris near 90° inclination will therefore remain time correlated with the orbital plane of the parent body for a very long time.

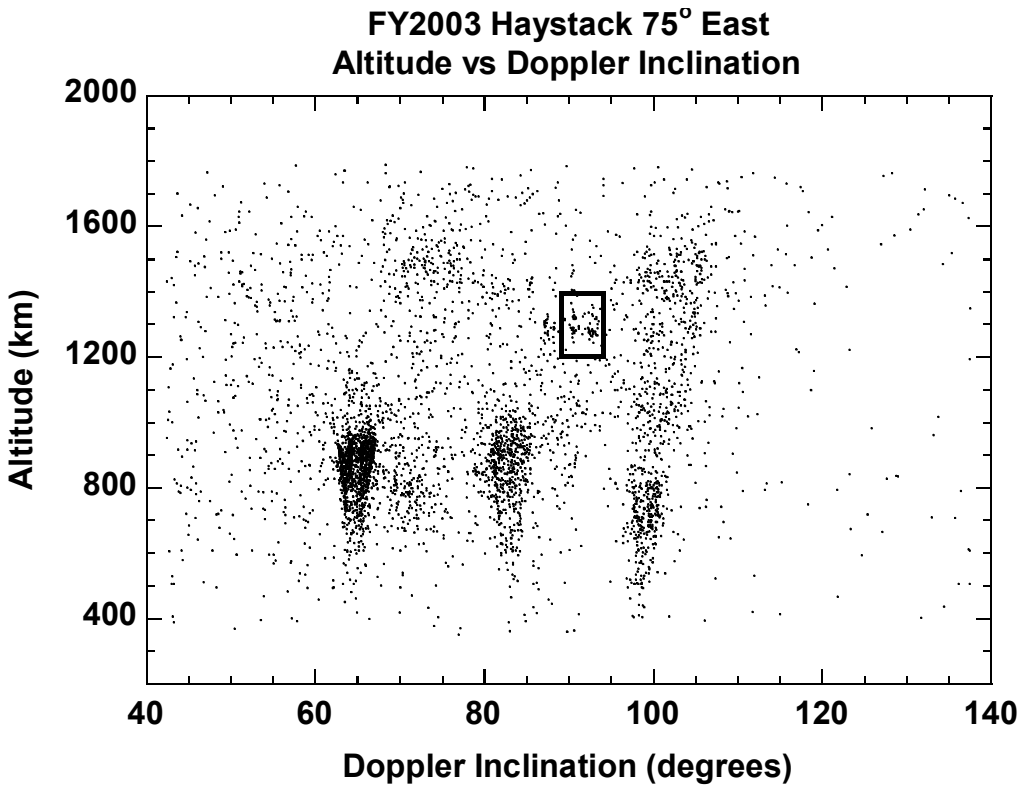


Figure 7.0-1. The altitude versus Doppler inclination for FY2003 Haystack detections.

Apparent in Figure 7.0-1 are distinct debris groupings at Doppler inclinations near 65° , 83° , and 98° . A concentration of detections near 1300 km altitude and 90° inclination is also evident. This region is highlighted with a box extending from 1200 km to 1400 km altitude and Doppler inclination from 89° to 94° .

A plot of day (of the year) versus the time-of-day of detections is shown in Figure 7.0-2. The small dots are all detections to indicate when the radar was actually collecting data. The large dots are within the box in Figure 7.0-1, 1200 km to 1400 km altitude and 89° to 94° Doppler inclination. The shaded areas are a guide to indicate roughly when the radar was acquiring data. As shown in the figure, the radar has about 8 hours of down time each day with the exception of a 24 hour campaign conducted on 20-21 January 2003.

Notice the clear correlations of the large dots, with a linear relationship between the day of year and the time-of-day for some of the data. This is evidence of debris in an orbit plane. Lines are shown in Figure 7.0-2 are separated by approximately 12 hours. This is a consequence of viewing the orbit plane twice each day by the radar. This corresponds to viewing two sides of the debris ring. The slope of the line indicates the debris orbit plane is being observed 238 seconds earlier each day. The radar observation times are in UTC, or GMT (Greenwich Mean Time), which are not a good time reference for use in the analysis of this problem. Sidereal time is better for this type of analysis when one accounts for the rotation of the Earth and the motion of the Earth around the sun. With this consideration, the observation time of an orbit plane at 90° should be 235.9 seconds earlier each day. The slope of the line in Figure 7.0-2 indicates that observations are 238 seconds earlier each day.

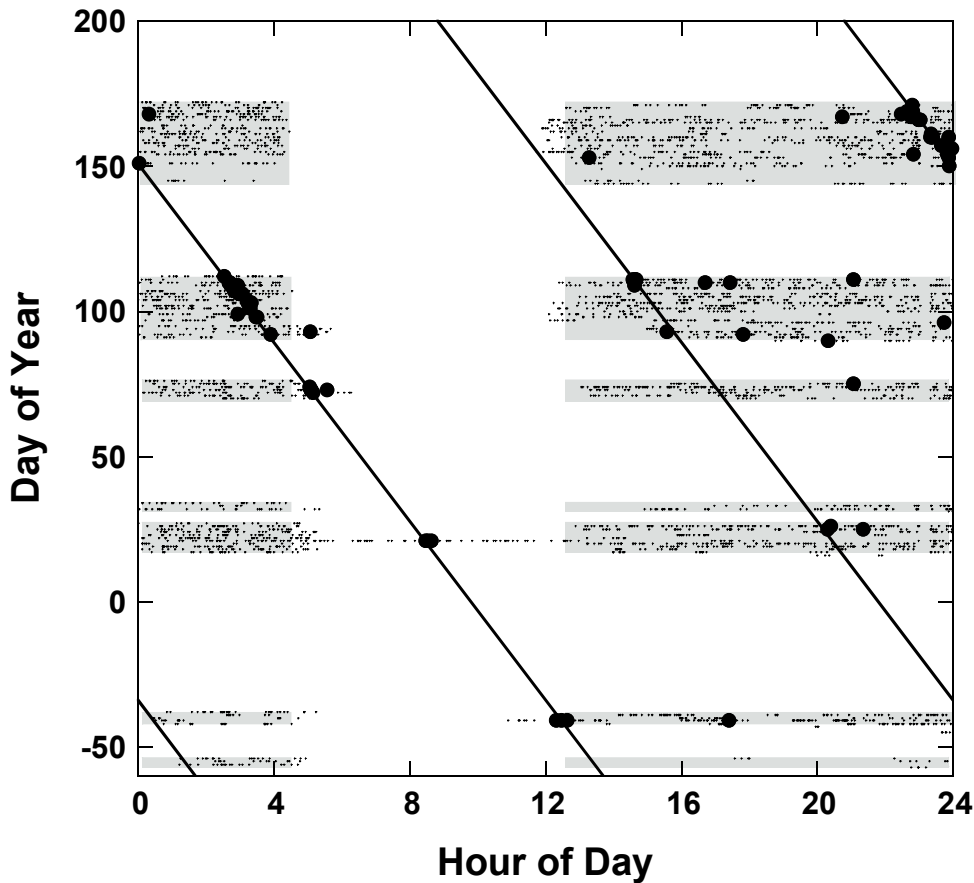


Figure 7.0-2. Day vs. hour for altitudes from 1200 km to 1400 km in the Doppler inclination band from 89° to 94° .

Analyses of these patterns in observation time, range, and range rate have identified 63 good debris candidates released from the polar orbiting SNAPSHOT satellite (International Designator: 1965-027A). This debris has been correlated with the orbit plane of the SNAPSHOT satellite using SATRAK and the appropriate two line element (TLE) sets provided by the SSN. Figure 7.0-3 shows the orbit plane of the SNAPSHOT satellite intersecting the 75° East pointing Haystack radar beam when a debris piece was observed. The satellite in the figure is on the other side of the Earth. The radar beam width is exaggerated as a visual aid.



Figure 7.0-3. Observation of the debris plane of SNAPSHOT passing radar beam in year 2003, day 107, at 2:53 am UCT.

The debris cloud associated with the SNAPSHOT satellite at an orbital inclination of 90.1° should still be intact even after many years of releasing objects. The SNAPSHOT satellite is a well known nuclear powered satellite launched in 1965 to a near circular 1300 km orbit with an inclination of 90.3° . This satellite began releasing debris in 1979 with new pieces being discovered and cataloged over the years. Fifty-one objects are still being tracked by the U.S. SSN.

For these debris, the size and altitude histograms are shown in Figure 7.0-4, Figure 7.0-5, and Figure 7.0-6. Some of the pieces are very large but were not identified by ODAS as being correlated with a tracked object. The altitude histogram indicates two separate distributions. Interestingly, the center of these two distributions separately match the known apogee and perigee of the SNAPSHOT parent body. Identifying SNAPSHOT debris in previous years is not readily possible since the radar rarely sampled altitudes between 1270 km to 1320 km.

This satellite is not in the breakup catalog. It is in the *History of On-orbit Satellite Fragmentations* [41] as an anomalous event since there has not been an explosion or a collision.

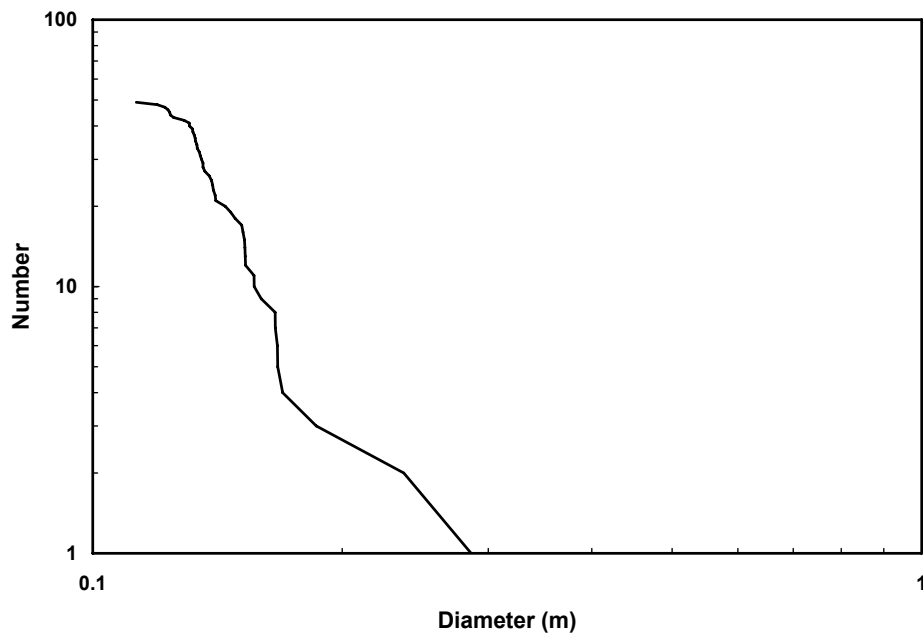


Figure 7.0-4. SEM size distribution for catalogued SNAPSHOT debris cloud candidate.

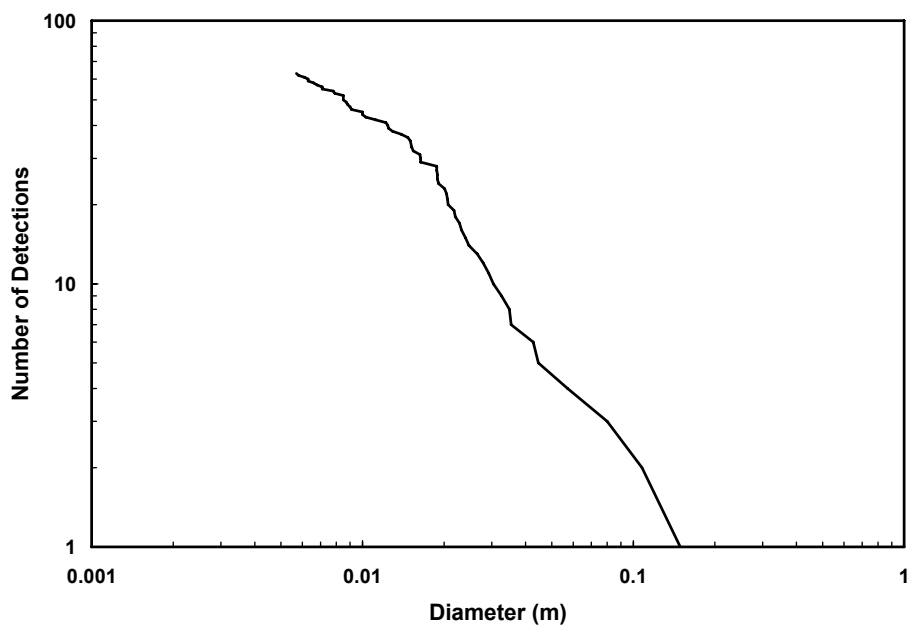


Figure 7.0-5. Size distribution of Haystack detections determined to be SNAPSHOT debris.

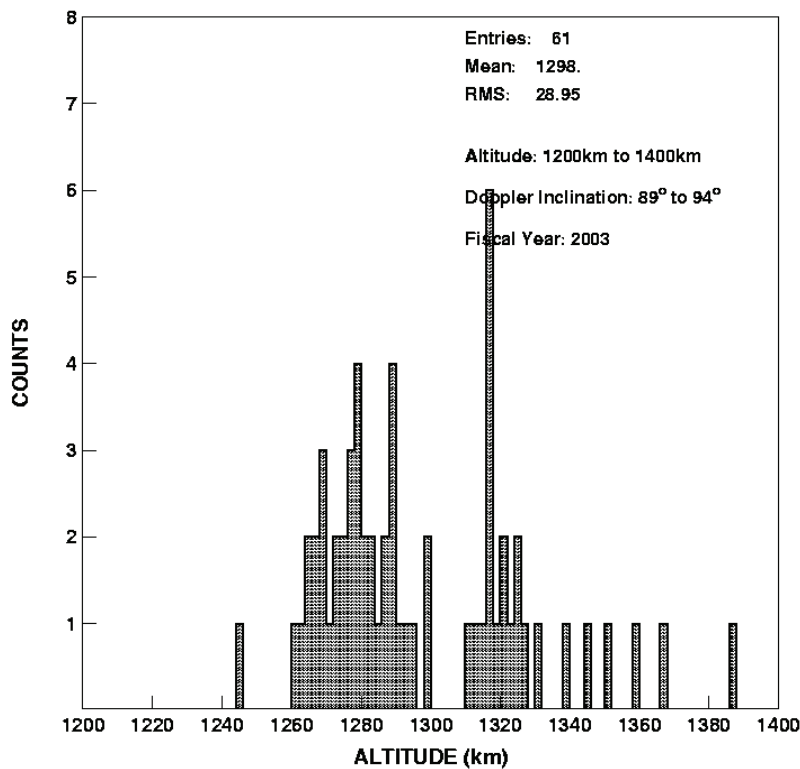


Figure 7.0-6. Altitude histogram for SNAPSHOT debris candidates.

7.1 SNAPSHOT Historical Background

The SNAPSHOT satellite was the first, and so far only, launch of a U.S. nuclear reactor into space. (All other nuclear power sources launched by the U.S. have been Radioisotope Thermoelectric Generators, or RTGs.) The payload, also known as SNAP-10A (System for Nuclear Auxiliary Power), was launched on 3 April 1965 on an Atlas/Agena D rocket from Vandenberg Air Force Base. The payload, by design, remained attached to the Agena D upper stage (see Figure 7.1-1). It was launched into a near-circular polar orbit with an inclination of 90.3° and a mean altitude near 1300 km. The Agena also housed a small experimental cesium ion thruster and a secondary payload, SECOR-4 (SEquential COllation of Range), which was deployed after the Agena reached its orbit.

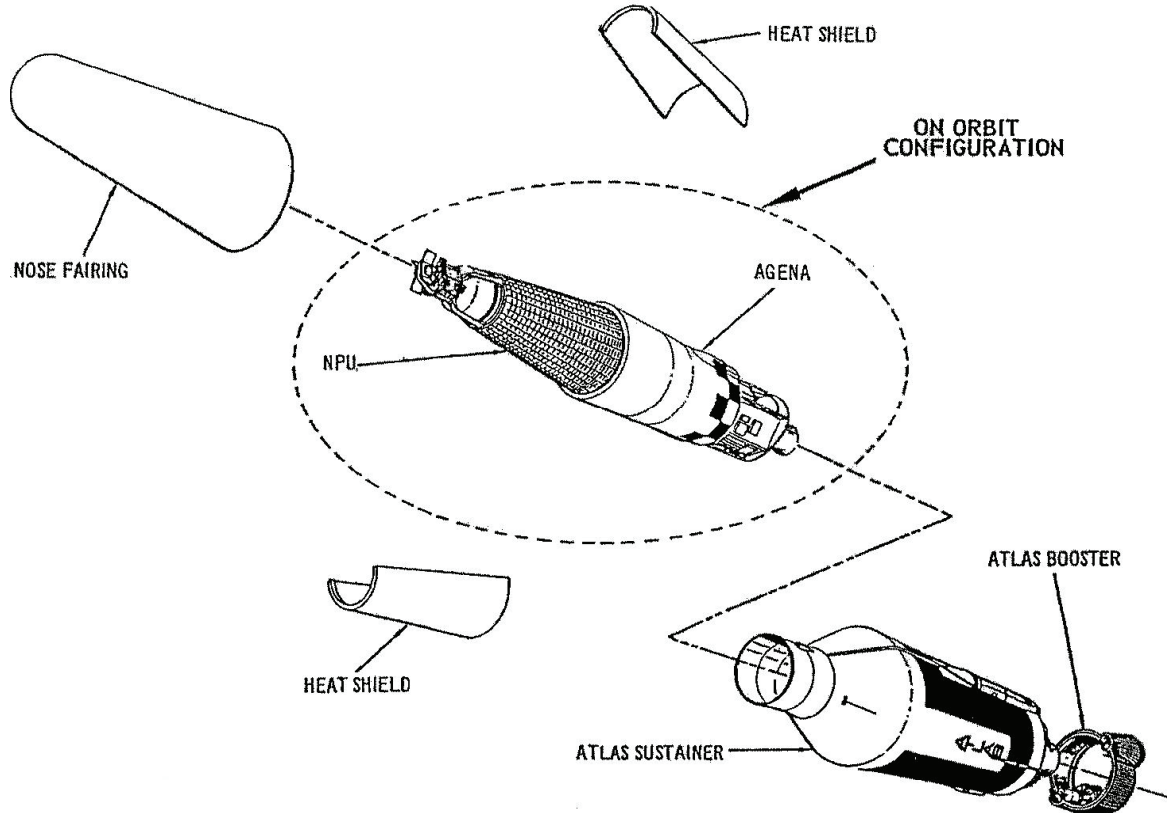


Figure 7.1-1. Configuration of the SNAPSHOT/Agena D payload and the three pieces of operational debris left on orbit (nose fairing and 2-piece heat shield).

At launch, the reactor was dormant. It was activated only after ground tracking and telemetry stations verified its orbit. After the reactor was activated, a two-piece heat shield was released from the conically shaped radiators. The reactor started and operated normally for 43 days. Then, unexpectedly, all ground command and telemetry contact with the vehicle was lost. Two days later the telemetry system came back on and functioned for four days providing partial data on the status of the spacecraft. The telemetry indicated "that some of the on-board safety shutdown devices ... had activated" and that the reactor was shut down [42].

The ion thruster also had problems. The ion engine was supposed to be operated using batteries for about 1 hour and then the batteries were to be charged for approximately 15 hours using power generated by the SNAP reactor. However, "flight data indicated a significant number of high voltage (HV) breakdowns, and this apparently caused sufficient electromagnetic interference (EMI) to induce false horizon sensor signals leading to severe attitude perturbations of the spacecraft" [39].

Sometime prior to 1980, but after more than 10 years in space, the SNAPSHOT/Agena combination began shedding debris at irregular intervals [41, 43]. This phenomenon is different from a classic breakup of an on-orbit satellite. In a classic breakup, a single energetic event occurs which produces numerous pieces and imparts some delta velocity (Δv) to them so that they disperse in altitude and (to a lesser degree) inclination from the parent satellite. In the case of SNAPSHOT, small numbers of debris have separated from the parent at very low Δv on at least seven separate occasions [41]. SNAPSHOT is not unique in terms of shedding pieces in this manner. The SEASAT payload, which is also attached to an Agena rocket body, has experienced several shedding events and the COsmic Background Explorer (COBE) has experienced at least 12 such events.

In 1985, after two Soviet satellites with nuclear power supplies reentered the Earth's atmosphere, the U.S. Air Force attempted to determine the cause of the SNAPSHOT debris. In an unclassified report with a classified appendix, the Air Force concluded that "based on data in the classified appendix, there appears to be several extraneous objects associate with the rear of the payload/rocket body structure" [44]. In other words, the debris appears to be coming from the Agena rocket rather than the SNAP-10A reactor.

It should be noted that SNAP-10A reactor design is similar to the Bouk nuclear reactors which powered some Soviet Radar RORSATs in that both used liquid metal NaK in heat transfer loops. It was standard procedure for a time to eject the nuclear core from the Bouk reactors into a higher disposal orbit. The ejection apparently breached the heat transfer loops and the NaK leaked out in spherical droplets at low relative velocities [3, 45]. This does not appear to be the source of the SNAPSHOT debris. Very few of the RORSAT NaK droplets are large enough to be seen and cataloged by the U.S. SSN whereas over 50 SNAPSHOT debris have been cataloged. Also, the liquid metal forms into spheres when released. Conducting spheres have a highly polarized radar return from circularly polarized radars such as Haystack. This is true of RORSAT debris, but is not from SNAPSHOT debris. Finally, the core of the SNAP-10A reactor was not ejected.

7.2 SSN Observations

The U.S. Department of Defense operates a worldwide network of radar and optical sensors for tracking Earth satellites (including payloads, rocket bodies, and debris) of the size 5-10 cm and larger. Tracked objects are maintained in two lists. Objects in the official catalog are given, along with their international designator, a sequential number starting with satellite number 1, the Sputnik 1 rocket body. Currently there are over 29,000 objects in the regular catalog including more than 19,000 objects which have reentered the Earth's atmosphere or have left Earth orbit. There are many objects which are tracked by the SSN but which have not yet been included in the regular catalog. This includes many small debris fragments. These objects are maintained in an "Analyst" list using numbers from 80,000 to 89,999. Objects in the analyst catalog are often transient in that they are discovered, tracked, identified, and then transferred to the regular catalog. The number in the analyst catalog is then reused.

In addition to the SNAPSHOT payload (U.S. Satellite Number 1314) and the SECOR-4 satellite (U.S. Satellite Number 1315), the SSN cataloged three debris objects within about 2 months of the launch (U.S. Satellite Numbers 1316, 1389, and 1399). U.S. Satellite Number 1399 was either initially or subsequently misidentified as originating from SNAPSHOT. The other two objects are likely the two piece heat shield released after reactor activation.

The first piece of debris (U.S. Satellite Number 11631) associated with the shedding events was cataloged near the end of November 1979. Since that time, 50 additional pieces have been included in the regular catalog. Figure 7.2-1 shows the orbital period history for all of the cataloged debris associated with SNAPSHOT from 1975 to 2006. From this plot, it is obvious that a great deal of cross tagging of observations has occurred over the years as evidenced in the discontinuities in individual orbital histories. Many of the debris objects have similar decay profiles from atmospheric drag. The effects of periods of high solar activity (circa years 1990 and 2001) and low solar activity (circa years 1986 and 1997) are evident in this figure by looking at the rate of change of orbital period. Several debris were added to the catalog near the beginning of 1988. Several of these pieces had orbital periods shorter than pieces cataloged in 1979. It is likely that at least one of the debris cataloged in 1988 was shed from SNAPSHOT prior to the first recognized shedding event. Hence, the first shedding event probably occurred prior to November 1979.

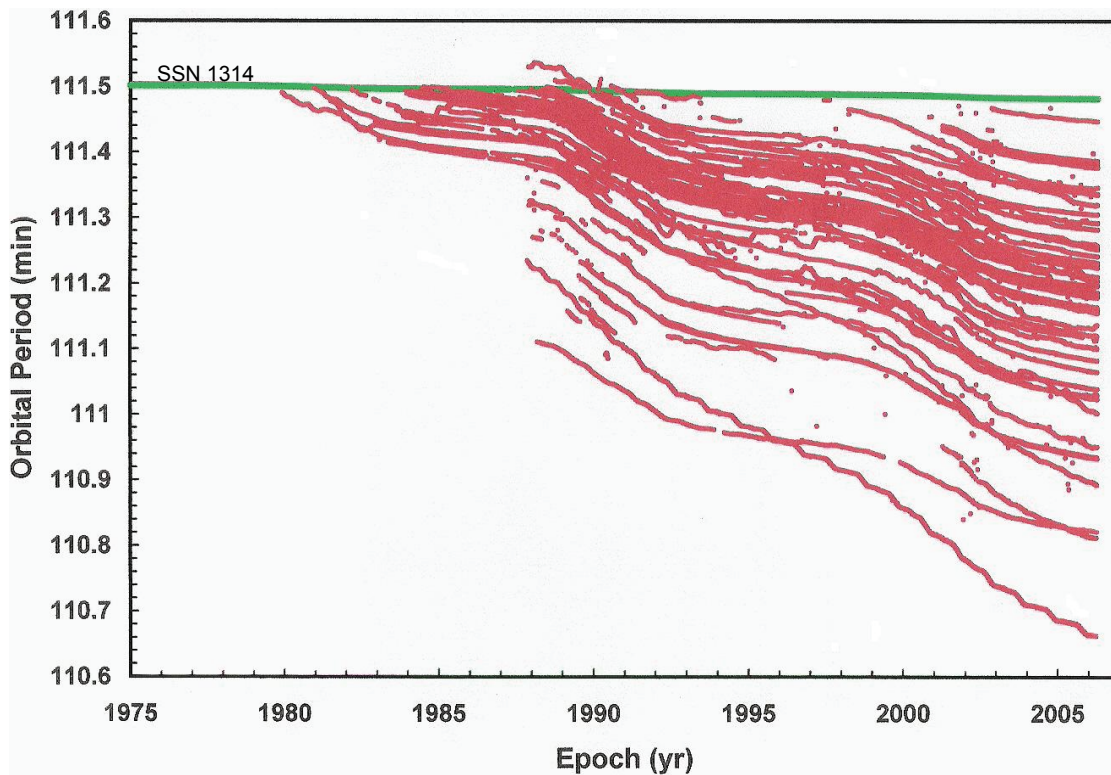


Figure 7.2-1. Orbit period for SNAPSHOT (U.S. Satellite Number 1314) and associated cataloged debris.

The orbital element history of each of the cataloged SNAPSHOT debris was used with NASA's Prop3D orbit propagator [46] curve fit the decay rate to estimate an effective area-to-mass ratio (assuming a coefficient of drag of 2.2). Most of the debris show an area-to-mass of between 0.1 – 0.2 m²/kg as shown in Figure 7.2-2.

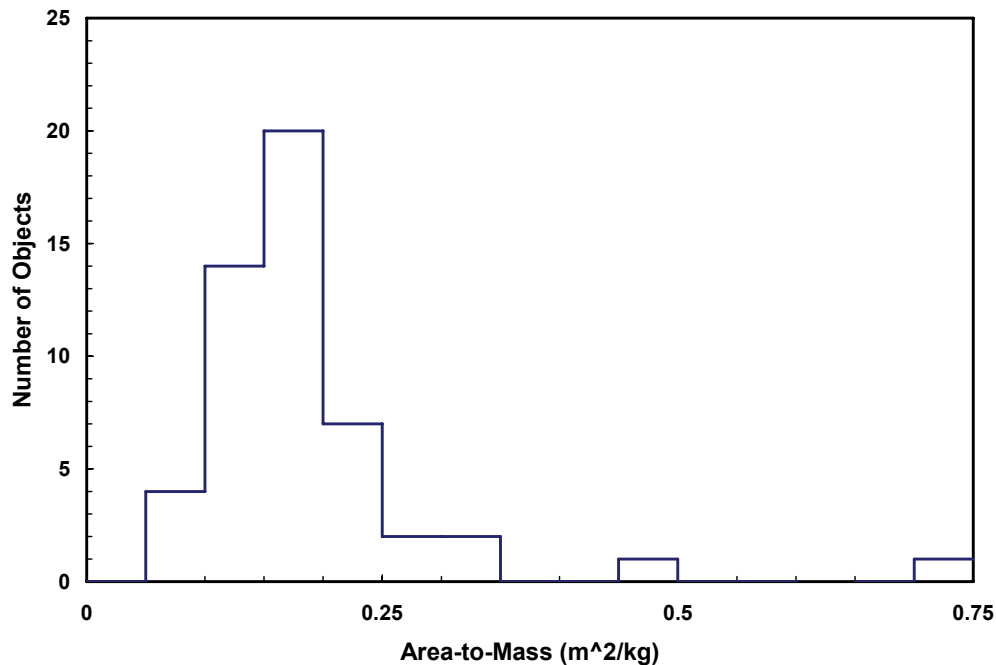


Figure 7.2-2. Area-to-mass histogram of cataloged SNAPSHOT debris.

In addition to the 51 SNAPSHOT debris in the regular catalog, in May 2006 the SSN was tracking about 100 analyst objects in orbits which indicate that they also originated from SNAPSHOT. No size information is available for analyst objects, however. Figure 7.2-3 shows the Gabbard diagram for both the analyst and regular cataloged objects and indicates that debris is not released energetically.

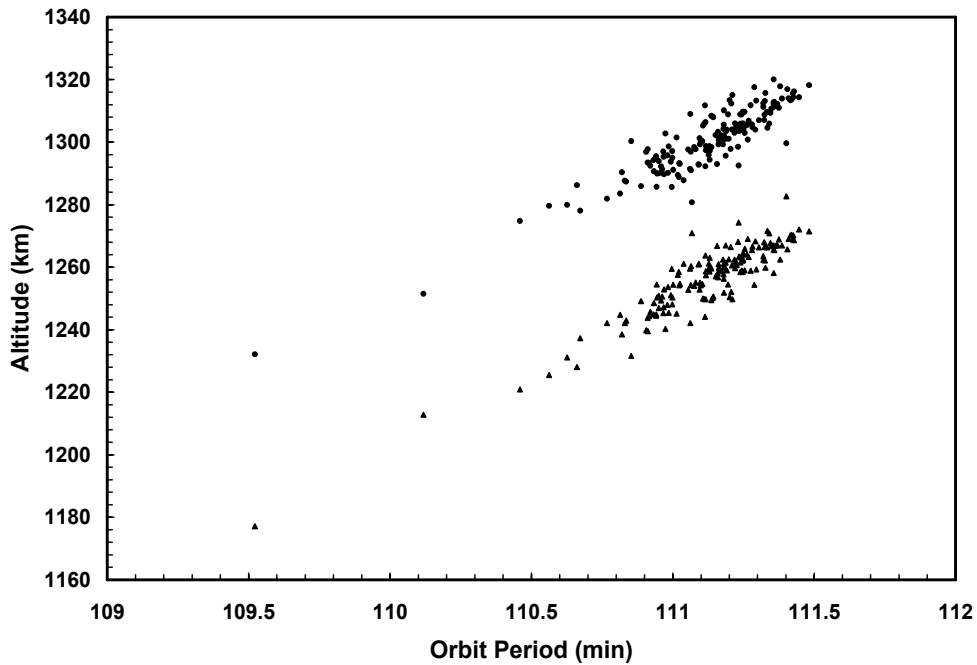


Figure 7.2-3. Gabbard diagram of all SNAPSHOT debris tracked in May 2006 including both cataloged and analyst objects.

7.3 SNAPSHOT Debris Population Estimation

The simplest method to estimate the population of SNAPSHOT is to simply ratio the total number of objects detected by Haystack with the number of catalogued objects. Since three of the 63 detections were catalogued debris then Haystack detected 20 times the catalogued population (about 50 objects) giving a total population of about 1000 objects larger than 5 mm diameter.

The number of three catalogued detections, however, has a large associated uncertainty due to the statistics of small numbers. In order to estimate a more expected catalogued detection rate, a series of simulations was run using the SATRAK software package. SATRAK can be used to determine when a satellite is in the field-of-view of a ground based sensor and is certified to produce the same answers as software in the SSN's Cheyenne Mountain Operations Center [47]. SATRAK was run using the orbital elements for the catalogued SNAPSHOT debris and a 1° field-of-view simulated radar beam at Haystack's location and pointing angles. The simulation was run for 5 continuous days radar time. This corresponds to 10 SNAPSHOT plane crossings. This process was repeated for 20 different 5 day intervals in FY 2003. An average of 4.2 catalogued detections per 10 plane crossings. Using the data presented in Figure 7.0-1, Haystack observed 55 plane crossings during 2003. If Haystack had a 1° field-of-view, then it should have detected 23.1 catalogued SNAPSHOT debris. However, since Haystack's beamwidth is 0.058° that number should be adjusted by the ratio of 0.058 to 1, giving an expected number of detections of 1.3.

The estimate of population at 5 mm diameter has additional problems, however. As the debris size approaches the threshold of detection for Haystack, the probability of detection drops. In other words, not every 5 mm debris object passing within Haystack's field-of-view will be detected. There is also the issue of the error discussed in section 3.3 which increased the number of missed detections for small particles. Therefore, the estimate of 1000 objects larger than 5 mm is a lower limit and the actual number may be several times larger.

A more reliable number would be the estimate of the 1 cm and larger population. Haystack detected about 45 objects in this size range. Using 1.3 as the number of detected cataloged objects provides an estimate of approximately 1700 pieces 1 cm and larger of the total number of SNAPSHOT debris in orbit.

8.0 Conclusions

The FY2003 Haystack and HAX orbital debris measurements described in this report provide a wealth of information on the small debris environment. The extremely good statistics in the data are unique in orbital debris measurements. The size distribution of detected objects can give insight into the type of breakup and provide data for improved breakup models.

Haystack and HAX data have been the key sources of information for the development of NASA's orbital debris models. Continued monitoring of the environment in the size ranges efficiently measured by Haystack and HAX is needed to continue the validation and refinement of these models.

References

1. Liou, J.-C. et al., NASA/TP - 2000 – 210780, *The New NASA Orbital Debris Engineering Model ORDEM 2000*, May 2000.
2. Kessler, D. J., Zhang, J., Matney, M. J., Eichler, P., Reynolds, R.. C., Anz-Meador, P. D., & Stansbery, E. G. *A Computer Based Orbital Debris Environment Model for Spacecraft Design and Observations in Low Earth Orbit*. NASA Technical Memorandum 104825, 1996.
3. Stansbery, E. G., et al., *Haystack Radar Measurements of the Orbital Debris Environment; 1990-1994*, NASA/JSC Publication JSC-27436, Houston, TX, April 20, 1996.
4. Goldstein, R. M., & Randolph, L. W. *Rings of Earth*. IEEE Trans. on Microwave Theory and Techniques, Vol. 40, No. 6, June 1992.
5. Kessler, D. J., M. J. Matney, R.C. Reynolds, R.P. Bernhard, E. G. Stansbery, N.L. Johnson, A.E. Potter and P.D. Anz-Meador. *A Search for a Previously Unknown Source of Orbital Debris: The Possibility of a Coolant Leak in Radar Ocean Reconnaissance Satellites*. JSC-27737 February 1997.
6. Grinberg, E. I., et al., *Interaction of Space Debris with Liquid Metal Circuit of RORSAT Satellites*. Proceedings of Second European conference on Space Debris, Darmstadt, March 1977, (ESA SP-393, May 1997).
7. Levine, A.S. (Ed.), 1991. LDEF – 69 months in space: The first post-retrieval symposium, NASA CP-3134.

8. Levine, A.S. (Ed.), 1991. LDEF – 69 months in space: The second post-retrieval symposium, NASA CP-3194.
9. Levine, A.S. (Ed.), 1991. LDEF – 69 months in space: The third post-retrieval symposium, NASA CP-3275.
10. Hyde, J.L., et al. *As-Flown Shuttle Orbiter Meteoroid/Orbital Debris Assessment. Phase I – Shuttle/Mir Missions.* STS-71, 76, 79, 81, 84, 86, 89 & 91. JSC-28768 January 2000.
11. Hyde, J.L., et al. *As-Flown Shuttle Orbiter Meteoroid/Orbital Debris Assessment. Phase I – Shuttle/Mir Missions.* STS-50, 56, 72, 73, 75, 77, 80, 85, 87, 88, 94, 95 & 96. JSC-29070 September 2000.
12. *Space Station Program Natural Environment Definition for Design.* SSP 30425 Revision A., June 1991.
13. Settecerri, T. J., Stansbery, E. G., Hebert, T. J.; *Radar Measurements of the Orbital Debris Environment: Haystack and HAX Radars October 1990 – October 1998;* NASA/JSC Publications JSC-28744, JSC-27844A, JSC-27844B; Houston TX, October 1999.
14. Stansbery, E. G., et al., *Characterization of the Orbital Debris Environment Using the Haystack Radar,* NASA/JSC Publication JSC-32213, Houston, TX, April 24, 1992.
15. Stansbery, E. G., et al., *Characterization of the Orbital Debris Environment using the Haystack Radar,* NASA/JSC Publication JSC-32213 Appendix A, Houston, TX, March 12, 1993.
16. Tracy, T. E., Armitage, P., & Stansbery, E. G. *Characterization of the Orbital Debris Environment Using the Haystack Radar – Debris Streams.* JSC-32213, Appendix B, March 12, 1993.
17. Stansbery, E. G., et al., *Haystack Measurements of the Orbital Debris,* NASA/JSC Publication JSC-26655, Houston, TX, May 20, 1994.
18. Stansbery, E. G., et al., *Haystack Measurements of the Orbital Debris,* NASA/JSC Publication JSC-26655 Appendix A, Houston, TX, May 20, 1994.
19. Settecerri, T. J., et al., *Haystack Radar Measurements of the Orbital Debris Environment; 1994-1996,* NASA/JSC Publication JSC-27842, Houston, TX, May 1997.
20. Settecerri, T. J., et al., Measurements of the Orbital Debris Environment: Comparison of the Haystack Radar and HAX Radars, NASA/JSC Publication JSC-27971, Houston, TX, August 1997.
21. Foster, J.L., et al, *Haystack and HAX Radar Measurements of the Orbital Debris Environment; 1999-2002,* NASA/JSC Publication JSC-49875, Houston, TX, October 2003.
22. Barton, D. K., et al., *Orbital Debris Radar Technology Peer Review,* Final Report, NASA/JSC Publication, Houston, TX, March 1992.
23. Barton, D. K., et al., *Final Report of the Haystack Orbital Debris Data Review Panel,* NASA/JSC Technical Memorandum 4809, Houston, TX, February 1998.

24. Cress, G. H., et al., Orbital Debris Radar Calibration Spheres, Radar and Optical Ground Based Measurements, NASA/JSC Publication JSC-27241, Houston, TX, June 1996.
25. Goudey, K.R. and Sciambi, Jr. A.F. *High Power X-Band Monopulse Tracking Feed for the Lincoln Laboratory Long-Range Imaging Radar* IEEE Transactions on Microwave Theory and Techniques, Vol. MTT-26, No. 5, May 1978.
26. O'Dea, B. *Noise Floor Investigation Report*, Northrop-Grumman, Internal Memorandum, August 2005.
27. Rosenberg, F.D. *Radar Characterization of RORSAT Coolant Spheres and their Potential Use for Calibration & Validation of Debris Tracking Sensors*. MIT/LL Project Report STK-264. November 2003.
28. Meyer, D. P. and Mayer, H. A., *Radar Target Detection: Handbook of Theory and Practice*, Appendix A-8, Academic Press, Inc., San Diego, CA, 1973.
29. Blake, L.V. *A FORTRAN Computer Program to Calculate Range of a Pulse Radar*. NRL Report 7448. August 28, 1972.
30. Dalquist, C. and Bohannon, G. *Physical Descriptions of Debris Objects Used in Static RCS Measurements*. XonTech Report 910555-1978. August 1991.
31. Bohannon, G., Caampued, T., and Young, N. *First Order RCS Statistics of Hypervelocity Impact Fragments*. XonTech Report 940128-BE-2305. April, 1994.
32. Everett, R., Caampued, T., and Chu, J. *Summary of Data Processing of September 1990 SPC Debris Data*. XonTech Report 910147-1937, March 1991.
33. Everett, R., Dalquist, C., and Caampued, T. *Summary of Processing of January 1991 SPC Debris Data*. XonTech Report 9100393-1965, July 1991.
34. Knott, E.F., et al. *Radar Cross Section*, Artech House, Boston, MA, 1993.
35. Xu, Y.-I and C.L. Stokely. *A Statistical Size Estimation Model for Haystack and HAX Radar Detections*, 56th International Astronautical Congress, Fukuoka, Japan, 2005.
36. Vardi, Y., and Lee, D., "From Image Deblurring to Optical Investments: Maximum Likelihood Solutions for Positive Linear Inverse Problems," J. R. Statist. Soc. B 55, pp. 569-612, 1993.
37. Henize, K. G., Anz-Meador, P. D., and Tracy, T. E. *A Study of Systematic Effects in Eglin (AN/FPS-85) RCS Data*. *Proceedings of the 1993 Space Surveillance Workshop*. M.I.T. Lincoln Laboratory Project Report STK-206, Vol. 1. 30 March - 1 April 1993.
38. Banner, G. P., M.I.T. Lincoln Laboratory, Private Communication. 1993.
39. Sovey, J. S., Rawlin, V. K., and Patterson, M. J. "Ion Propulsion Development Projects in U.S.: Space Electric Rocket Test I to Deep Space 1." J. of Propulsion & Power. Vol. 17, No3, pp. 517-526. May-June, 2001.
40. Montenbruck, O., et al. *Satellite Orbits*, Springer-Verlag, New York, NY, 2000.

41. Whitlock, D. O. *History of On-Orbit Satellite Fragmentations, 13th Edition.* JSC-62530. NASA, Johnson Space Center, Houston, TX, May, 2004.
42. Wilson, R. F., Dieckamp, H. M., and Cockeram, D. J. "SNAP 10A Design, Development, and Flight Test." AIAA Paper No. 65-467. Presented at the AIAA Second Annual Meeting, San Francisco, CA, July 26-29, 1965.
43. Johnson, N. L. "Environmentally-Induced Debris Sources." PEDAS1-B1.4-0020-02. Presented at the World Space Congress, Houston, TX, 2002.
44. DeVere, G. T. *Investigations of Certain Anomalies Associated with Object 1314, A US Nuclear Powered Satellite.* Technical Memorandum 85-S-001, Headquarters NORAD/ADCOM, DCS/Plans, March 1985 (Appendix TM-85-001A, Secret).
45. Sidharan, R. et al., "Radar and Optical Characterization of an Anomalous Orbital Debris Population." J. Spacecraft and Rockets. Vol. 36, No. 5, pp. 719-725. Sept.-Oct., 1999.
46. Whitlock, D. O. and Johnson, N. L. "Modeling and Monitoring the Decay of NASA Satellites." 4th European Conference on Space Debris. 18-20 April, 2005.
47. Grissom, W. and Guy, R. P. *SATRAK Operator's Guide, V 6.0.* Technical Report CS99-ITTS-001. Headquarters Space Warfare Center/AE, Schriever AFB, CO, 2002.

REPORT DOCUMENTATION PAGE
*Form Approved
OMB No. 0704-0188*

The public reporting burden for this collection of information is estimated to average 1 hour per response, including the time for reviewing instructions, searching existing data sources, gathering and maintaining the data needed, and completing and reviewing the collection of information. Send comments regarding this burden estimate or any other aspect of this collection of information, including suggestions for reducing this burden, to Department of Defense, Washington Headquarters Services, Directorate for Information Operations and Reports (0704-0188), 1215 Jefferson Davis Highway, Suite 1204, Arlington, VA 22202-4302. Respondents should be aware that notwithstanding any other provision of law, no person shall be subject to any penalty for failing to comply with a collection of information if it does not display a currently valid OMB control number.

PLEASE DO NOT RETURN YOUR FORM TO THE ABOVE ADDRESS.

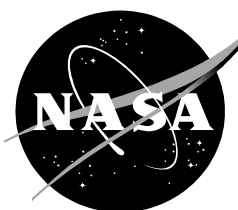
1. REPORT DATE (DD-MM-YYYY) 27-11-2006			2. REPORT TYPE NASA JSC Report		3. DATES COVERED (From - To) Oct 2002-Nov 2006	
4. TITLE AND SUBTITLE Haystack and HAX Radar Measurements of the Orbital Debris Environment; 2003			5a. CONTRACT NUMBER			
			5b. GRANT NUMBER			
			5c. PROGRAM ELEMENT NUMBER			
6. AUTHOR(S) Stokely, Christopher, L.*; Foster, John, L., Jr.**; Stansbery, Eugene, G.***; Benbrook, James, R.****; Juarez, Quanette, L.*****			5d. PROJECT NUMBER			
			5e. TASK NUMBER			
			5f. WORK UNIT NUMBER			
7. PERFORMING ORGANIZATION NAME(S) AND ADDRESS(ES) Lyndon B. Johnson Space Center National Aeronautics and Space Administration 2101 NASA Parkway Houston, TX 77058-3696				8. PERFORMING ORGANIZATION REPORT NUMBER JSC-62815		
9. SPONSORING/MONITORING AGENCY NAME(S) AND ADDRESS(ES) National Aeronautics and Space Administration Washington, D.C. 20546-0001				10. SPONSORING/MONITOR'S ACRONYM(S) NASA		
				11. SPONSORING/MONITORING REPORT NUMBER JSC-62815		
12. DISTRIBUTION/AVAILABILITY STATEMENT Available from the NASA Center for AeroSpace Information (CASI) 7121 Standard Hanover, MD 21076-1320						
13. SUPPLEMENTARY NOTES *ESCG/Barrios Technology, Inc.; **Science Applications International Corporation, Inc.; ***National Aeronautics and Space Administration; ****ESCG/Jacobs-Sverdrup, Inc.						
14. ABSTRACT NASA has been utilizing radar observations of the debris environment for over a decade from the MIT Lincoln Laboratory (MIT/LL) Haystack Radar and the smaller nearby Haystack Auxiliary Radar (HAX). Both of these systems are highly sensitive radars that operate in a fixed staring mode to statistically sample orbital debris in the LEO environment. The Haystack radar generally measures from less than 1 cm to several meters. The HAX radar generally measures from 2 cm to several meters. These overlapping size regions allow a continuous measurement of debris with diameters from less than 1 cm to several meters. As a calibration benchmark, the count rate or "flux" of pieces with size 10 cm detected by Haystack and HAX is shown to agree with the number of objects in the USSPACECOM catalog. During the 2003 fiscal year, October 2002 to September 2003, all Haystack and HAX radar data were collected at 75° elevation, pointing East. Some of the data are seen to group into families that can sometimes be associated with individual breakups or groups of breakups. A new technique for identifying breakup fragments was employed, allowing for identification of debris from the nuclear powered SNAPSHOT satellite.						
15. SUBJECT TERMS Orbital Debris; Space Debris; Radar; LEO; Low Earth Orbit; Measurements; Haystack; HAX; SNAPSHOT satellite; RORSAT; sodium-potassium; NaK						
16. SECURITY CLASSIFICATION OF: a. REPORT Unclassified			17. LIMITATION OF ABSTRACT UU	18. NUMBER OF PAGES 64	19b. NAME OF RESPONSIBLE PERSON Eugene G. Stansbery 19b. TELEPHONE NUMBER (Include area code) (281) 483-8417	

Haystack and HAX Radar Measurements of the Orbital Debris Environment; 2003 Appendix A

Orbital Debris Program Office
Human Exploration Science Office
Astromaterials Research and Exploration Science Directorate

C. L. Stokely, J. L. Foster, Jr., E. G. Stansbery,
J. R. Benbrook, Q. Juarez

November 2006



National Aeronautics and
Space Administration

Lyndon B. Johnson Space Center
Houston, Texas 77058

**Haystack and HAX Radar Measurements
of the
Orbital Debris Environment
2003
Appendix A**

JSC-62815A

C.L. Stokely¹, J. L. Foster, Jr.², E. G. Stansbery³
J. R. Benbrook⁴, Q. Juarez⁴

¹ESCG/Barrios Technology, Inc.
2200 Space Park Dr., Ste. 400
Houston, TX 77058

²Science Applications International Corporation, Inc.
2450 NASA Pkwy
Houston, TX 77058

³National Aeronautics and Space Administration
Johnson Space Center
Houston, TX 77058

⁴ESCG/Jacobs-Sverdrup, Inc.
2224 Bay Area Blvd, Box 7
Houston, TX 77058

November 2006

List of Tables

Table 1. Haystack FY2003 Data Summary.....	1
Table 2. HAX FY2003 Data Summary	1
Table 3. Debris Mode Operating Parameters	2

List of Figures

Figure 1. Detection Rate versus Integrated SNR for Haystack and HAX.	3
Figure 2. RCS parameter versus Size Parameter used in the NASA SEM.	4
Figure 3. Haystack Size versus SSN Size with Mainlobe and Sidelobes illustrated.	5
Figure 4. Haystack Size versus SSN Size with Mainlobe and Sidelobes Illustrated.....	6
Figure 5. Haystack Inclination versus SSN Inclination.....	7
Figure 6. HAX Inclination versus SSN Inclination.....	8
Figure 7. Haystack Altitude Histogram.....	9
Figure 8. Haystack Altitude Histogram for Catalogued Objects.....	10
Figure 9. Haystack Altitude Histogram for RORSAT NaK Debris.....	11
Figure 10. Haystack Altitude Histogram for Debris excluding RORSAT NaK Debris.....	12
Figure 11. Haystack Altitude versus Diameter.....	13
Figure 12. HAX Altitude versus Diameter.....	14
Figure 13. Haystack and HAX Minimum Detectable Diameter versus Altitude.....	15
Figure 14. Haystack Range Rate Histogram.	16
Figure 15. Haystack Range Rate Histogram for Catalogued Objects.....	17
Figure 16. Haystack Range Rate Histogram for RORSAT NaK Debris.....	18
Figure 17. Haystack Range Rate Histogram excluding RORSAT NaK Debris.....	19
Figure 18. Haystack Range Rate versus Doppler Inclination.	20
Figure 19. Haystack Altitude versus Doppler Inclination.....	21
Figure 20. Haystack Altitude versus Monopulse Inclination.....	22
Figure 21. Haystack Flux versus Altitude in 50 km bins for debris with diameter > 0.01 m.	23
Figure 22. Haystack Flux versus Altitude in 100 km bins for debris with diameter > 0.01 m.	24
Figure 23. Haystack, HAX, and the 10 cm Catalogue Flux versus Diameter for 350-450 km Altitude.	25
Figure 24. Haystack, HAX, and the 10 cm Catalogue Flux versus Diameter for 450-550 km Altitude.	26
Figure 25. Haystack, HAX, and the 10 cm Catalogue Flux versus Diameter for 550-650 km Altitude.	27
Figure 26. Haystack, HAX, and the 10 cm Catalogue Flux versus Diameter for 650-750 km Altitude.	28
Figure 27. Haystack, HAX, and the 10 cm Catalogue Flux versus Diameter for 750-850 km Altitude.	29
Figure 28. Haystack, HAX, and the 10 cm Catalogue Flux versus Diameter for 850-950 km Altitude.	30
Figure 29. Haystack, HAX, and the 10 cm Catalogue Flux versus Diameter for 950-1050 km Altitude.	31
Figure 30. Haystack, HAX, and the 10 cm Catalogue Flux versus Diameter for 1050-1150 km Altitude.	32
Figure 31. Haystack, HAX, and the 10 cm Catalogue Flux versus Diameter for 1150-1250 km Altitude.	33
Figure 32. Haystack, HAX, and the 10 cm Catalogue Flux versus Diameter for 1250-1350 km Altitude.	34

Figure 33. Haystack, HAX, and the 10 cm Catalogue Flux versus Diameter for 1350-1450 km Altitude	35
Figure 34. Haystack, HAX, and the 10 cm Catalogue Flux versus Diameter for 1450-1550 km Altitude	36
Figure 35. Haystack, HAX, and the 10 cm Catalogue Flux versus Diameter for 1550-1650 km Altitude	37
Figure 36. Haystack, HAX, and the 10 cm Catalogue Flux versus Diameter for 1650-1750 km Altitude	38
Figure 37. Haystack Doppler Inclination Histogram	39
Figure 38. Haystack Altitude Histogram for Debris with Doppler Inclination between 62° and 68°	40
Figure 39. Haystack Altitude Histogram for Debris with Doppler Inclination between 68° and 74°	41
Figure 40. Haystack Altitude Histogram for Debris with Doppler Inclination between 80° and 86°	42
Figure 41. Haystack Altitude Histogram for Debris with Doppler Inclination between 88° and 94°	43
Figure 42. Haystack Altitude Histogram for Debris with Doppler Inclination between 95° and 103°	44
Figure 43. Haystack Diameter Histogram	45
Figure 44. Haystack Diameter Histogram for Catalogued Objects	46
Figure 45. Haystack Diameter Histogram for RORSAT NaK Debris	47
Figure 46. Haystack Diameter Histogram for Debris excluding RORSAT NaK Debris	48
Figure 47. Haystack Diameter versus Doppler Inclination	49
Figure 48. Haystack Doppler Inclination versus Monopulse Inclination	50
Figure 49. Haystack Orthogonal Polarization RCS versus Principal Polarization RCS	51
Figure 50. Haystack Principal Polarization RCS Histogram	52
Figure 51. Haystack Orthogonal Polarization Histogram	53
Figure 52. Haystack Doppler Inclination Histogram	54
Figure 53. Haystack Doppler Inclination Histogram for Catalogued Objects	55
Figure 54. Haystack Doppler Inclination Histogram for RORSAT NaK	56
Figure 55. Haystack Doppler Inclination Histogram excluding RORSAT NaK Debris	57
Figure 56. Haystack Eccentricity Histogram	58
Figure 57. Haystack Eccentricity Histogram for Catalogued Objects	59
Figure 58. Haystack Eccentricity Histogram for RORSAT NaK	60
Figure 59. Haystack Eccentricity Histogram excluding RORSAT NaK Debris	61
Figure 60. Haystack Principal Polarization SNR versus Eccentricity	62
Figure 61. Haystack Orthogonal Polarization SNR versus Eccentricity	63
Figure 62. Haystack Hour of Day of Detection Histogram	64
Figure 63. Haystack Hour of Day of Detection Histogram for Catalogued Objects	65
Figure 64. Haystack Hour of Day of Detection Histogram for RORSAT NaK Debris	66
Figure 65. Haystack Hour of Day of Detection Histogram excluding RORSAT NaK Debris	67
Figure 66. Haystack Doppler Inclination versus Time of Detection	68
Figure 67. Haystack Daily Time of Detection versus Time of Year of Detection	69
Figure 68. Haystack Monopulse Inclination Histogram	70
Figure 69. Haystack Monopulse Inclination Histogram for Catalogued Objects	71
Figure 70. Haystack Monopulse Inclination Histogram for RORSAT NaK	72
Figure 71. Haystack Monopulse Inclination Histogram excluding RORSAT NaK Debris	73
Figure 72. Haystack Altitude versus Doppler Inclination for Highly Polarized Radar Returns ..	74
Figure 73. Haystack Radar Return Signal Polarization versus Altitude	75
Figure 74. Haystack Radar Return Signal Polarization versus Doppler Inclination	76

Figure 75. Haystack Principal Polarization SNR Histogram. Minimum SNR threshold is higher than shown in the radar report	77
Figure 76. Haystack Orthogonal Polarization SNR Histogram.	78
Figure 77. Haystack Principal Polarization SNR versus Orthogonal Polarization SNR.	79
Figure 78. Haystack Principal Polarization SNR versus Doppler Inclination.....	80
Figure 79. Haystack Principal Polarization SNR versus Monopulse Inclination.....	81
Figure 80. Haystack Principal Polarization SNR versus Range Rate.	82
Figure 81. Haystack Orthogonal Polarization SNR versus Doppler Inclination.	83
Figure 82. Haystack Orthogonal Polarization SNR versus Monopulse Inclination.....	84
Figure 83. Haystack Orthogonal Polarization SNR versus Range Rate.	85
Figure 84. Haystack Principal Polarization SNR versus Polarization.	86
Figure 85. Haystack Orthogonal Polarization SNR versus Polarization.....	87
Figure 86. Histogram of Haystack Observation Schedule throughout the Year.....	88
Figure 87. Histogram of Haystack Observation Schedule throughout the Year of Catalogued Objects.	89
Figure 88. Histogram of Haystack Observation Schedule throughout the Year of RORSAT NaK Debris.	90
Figure 89. Histogram of Haystack Observation Schedule throughout the Year of Debris excluding RORSAT NaK Debris.	91
Figure 90. Haystack Polarization versus Observation throughout the Year.....	92
Figure 91. Haystack Principal Polarization SNR versus Hour of Day of Detection.....	93
Figure 92. Haystack Orthogonal Polarization SNR versus Hour of Day of Detection.....	94
Figure 93. Haystack Altitude versus Hour of Day of Detection.	95
Figure 94. Haystack Altitude versus Observation Schedule throughout the Year.	96
Figure 95. Haystack Diameter versus Observation Schedule throughout the Year.....	97
Figure 96. Haystack Doppler Inclination versus Observation Schedule throughout the Year....	98
Figure 97. Haystack Principal Polarization SNR versus Observation Schedule throughout the Year.....	99
Figure 98. Haystack Orthogonal Polarization versus Observation Schedule throughout the Year.....	100
Figure 99. Haystack Range Rate versus Observation Schedule throughout the Year.	101
Figure 100. Haystack Radar Return Signal Polarization versus Observation Schedule throughout the Year.....	102
Figure 101. Haystack Range versus Observation Schedule throughout the Year.....	103
Figure 102. Haystack Monopulse Inclination versus Observation Schedule throughout the Year.	104
Figure 103. HAX Altitude Histogram.	105
Figure 104. HAX Altitude Histogram of Catalogued Objects.	106
Figure 105. HAX Altitude Histogram of RORSAT NaK Debris.....	107
Figure 106. HAX Altitude Histogram excluding RORSAT NaK Debris.....	108
Figure 107. HAX Range Rate Histogram.	109
Figure 108. HAX Range Rate Histogram for Catalogued Objects.	110
Figure 109. HAX Range Rate Histogram for RORSAT NaK Debris.	111
Figure 110. HAX Range Rate Histogram excluding RORSAT NaK Debris.	112
Figure 111. HAX Altitude versus Doppler Inclination.	113
Figure 112. HAX Altitude versus Monopulse Inclination.	114
Figure 113. HAX Range Rate versus Doppler Inclination.	115
Figure 114. HAX Diameter Histogram.	116
Figure 115. HAX Diameter Histogram for Catalogued Objects > 10 cm.....	117
Figure 116. HAX Diameter Histogram for RORSAT NaK Debris.	118
Figure 117. HAX Diameter Histogram excluding RORSAT NaK Debris.	119

Figure 118. HAX Diameter versus Doppler Inclination.....	120
Figure 119. HAX Doppler Inclination Histogram.....	121
Figure 120. HAX Doppler Inclination Histogram for Catalogued Objects.....	122
Figure 121. HAX Doppler Inclination Histogram for RORSAT NaK Debris.....	123
Figure 122. HAX Doppler Inclination Histogram excluding RORSAT NaK Debris.....	124
Figure 123. HAX Doppler Inclination versus Monopulse Inclination.....	125
Figure 124. HAX Eccentricity Histogram.....	126
Figure 125. HAX Eccentricity Histogram for Catalogued Objects.....	127
Figure 126. HAX Eccentricity Histogram for RORSAT NaK Debris.....	128
Figure 127. HAX Eccentricity Histogram excluding RORSAT NaK Debris.....	129
Figure 128. HAX Principal Polarization SNR versus Eccentricity.....	130
Figure 129. HAX Orthogonal Polarization SNR versus Eccentricity.....	131
Figure 130. Histogram of the Daily Time of HAX Detections.....	132
Figure 131. Histogram of the Daily Time of Catalogued HAX Detections.....	133
Figure 132. Histogram of the Daily Time of RORSAT NaK Detections.....	134
Figure 133. Histogram of the Daily Time of Detections excluding RORSAT NaK Debris.....	135
Figure 134. HAX Doppler Inclination versus the Daily Time of Detections.....	136
Figure 135. HAX Time of Detection versus Observation Schedule throughout the Year.....	137
Figure 136. HAX Monopulse Inclination Histogram.....	138
Figure 137. HAX Monopulse Histogram for Catalogued Objects.....	139
Figure 138. Haystack Monopulse Histogram for RORSAT NaK Debris.....	140
Figure 139. Haystack Monopulse Histogram excluding RORSAT NaK Debris.....	141
Figure 140. HAX Polarization versus Altitude.....	142
Figure 141. HAX Principal Polarization SNR Histogram.....	143
Figure 142. HAX Orthogonal Polarization SNR Histogram.....	144
Figure 143. HAX Principal Polarization SNR versus Doppler Inclination.....	145
Figure 144. HAX Principal Polarization SNR versus Monopulse Inclination.....	146
Figure 145. HAX Principal Polarization SNR versus Range Rate.....	147
Figure 146. HAX Orthogonal Polarization versus Doppler Inclination.....	148
Figure 147. HAX Orthogonal Polarization versus Range Rate.....	149
Figure 148. HAX Principal Polarization SNR versus Radar Return Signal Polarization.....	150
Figure 149. HAX Orthogonal Polarization SNR versus Radar Return Signal Polarization.....	151
Figure 150. HAX Histogram of Observation Schedule throughout the Year.....	152
Figure 151. HAX Histogram of Observation Schedule of Catalogued Objects throughout the Year.....	153
Figure 152. HAX Histogram of Observation Schedule of RORSAT NaK throughout the Year.....	154
Figure 153. HAX Histogram of Observation Schedule excluding RORSAT NaK Debris throughout the Year.....	155
Figure 154. HAX Principal Polarization versus Hour of Day of Detections.....	156
Figure 155. HAX Orthogonal Polarization versus Hour of Day of Detections.....	157
Figure 156. HAX Altitude versus Hour of Day of Detections.....	158
Figure 157. HAX Altitude versus Observation Schedule throughout the Year.....	159
Figure 158. HAX Diameter versus Observation Schedule throughout the Year.....	160
Figure 159. HAX Doppler Inclination versus Observation Schedule throughout the Year.....	161
Figure 160. HAX Principal Polarization SNR versus Observation Schedule throughout the Year.....	162
Figure 161. HAX Orthogonal Polarization SNR versus Observation Schedule throughout the Year.....	163
Figure 162. HAX Range versus Observation Schedule throughout the Year.....	164

Figure 163. HAX Radar Return Signal Polarization versus Observation Schedule throughout the Year.....	165
Figure 164. HAX Range versus Observation Schedule throughout the Year.....	166
Figure 165. HAX Monopulse Inclination versus Observation Schedule throughout the Year..	167

For the collection year FY2003, all data were collected at 75° elevation, 90° azimuth (East looking). Table 11 and Table 2 show the number of hours data collected for each radar.

Table 1. Haystack FY2003 Data Summary

Altitude Window (km)	Range Window (km)	Usable Altitude Window (km)	Usable Range Window (km)	Hours	Det>5.5 dB INTSNR*	FA < 0.1/hr Detections (INTSNR*> 5.521dB)	Valid Detections (within range window)
302.77	312.33	351	352	633.3	6830	6209	4611
1837.05	1885.29	1787	1835				

* 16 pulse non-coherent average

** sidelobe, noise and arcing removed

Table 2. HAX FY2003 Data Summary

Altitude Window (km)	Range Window (km)	Usable Altitude Window (km)	Usable Range Window (km)	Hours	Det>5.5 dB INTSNR*	FA < 0.01/hr Detections (INTSNR*> 5.749dB)	Valid Detections (within range window)
302.77	312.33	351	352	541.8	1926	1550	543
1837.05	1885.29	1787	1835				

* 16 pulse non-coherent average

** sidelobe, noise and arcing removed

Table 3. Debris Mode Operating Parameters

	Operating Parameter	HAX	Hay
Peak power (kW)	50	250	
Transmitter Frequency (GHz)	16.7	10.0	
Transmitter Wavelength (cm)	1.8	3.0	
Antenna Diameter (m)	12.2	36.6	
Antenna Beam Width (deg)	0.10	0.058	
Antenna Gain (dB)	63.64	67.23	
System temperature (K)	161	186	
Total System losses (dB)	4.5	3.9	
Waveform Code	4	4	
Range Gates	16	16	
Intermediate Frequency Bandwidth (KHz)	1000	1000	
Independent Range/Doppler Samples	12126	12126	
FFT Size	2048	2048	
Number of non-coherent integrated pulses used for detection	16	16	
Pulse width (msec)	1.6384	1.6384	
Pulse repetition frequency (Hz)	60	60	
Receiver window (msec)	12.126	12.126	
Single Pulse SNR on 0 dBm ² target at 10 ³ km (dB)	40.56	59.2	
Average Power (kW)	4.89	24.5	
Doppler Extent (km/second)	± 4.5	± 7.5	

FY 2003 Haystack and HAX, 75° East
Detection Rate vs. Signal-to-Noise Ratio

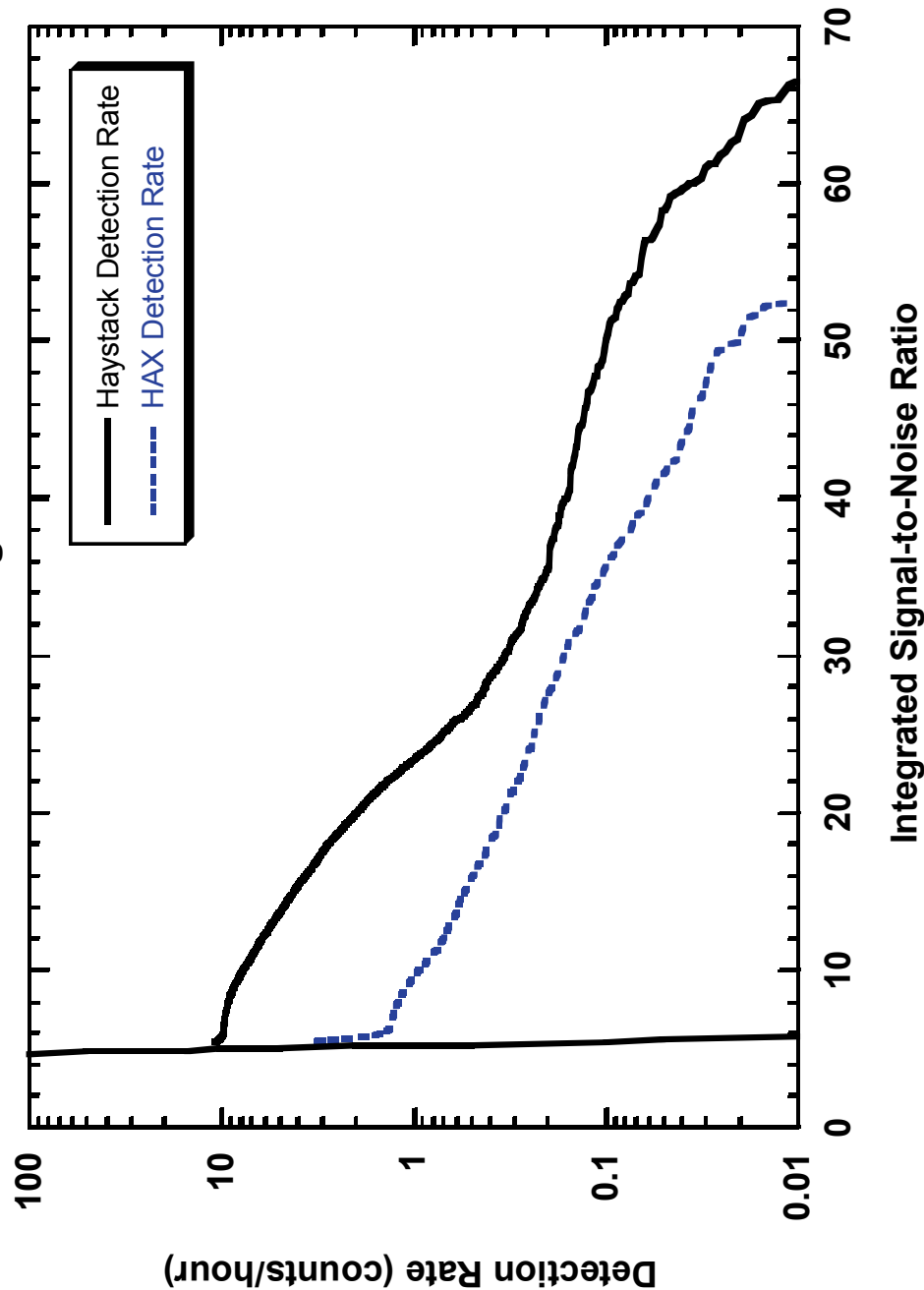


Figure 1. Detection Rate versus Integrated SNR for Haystack and HAX.

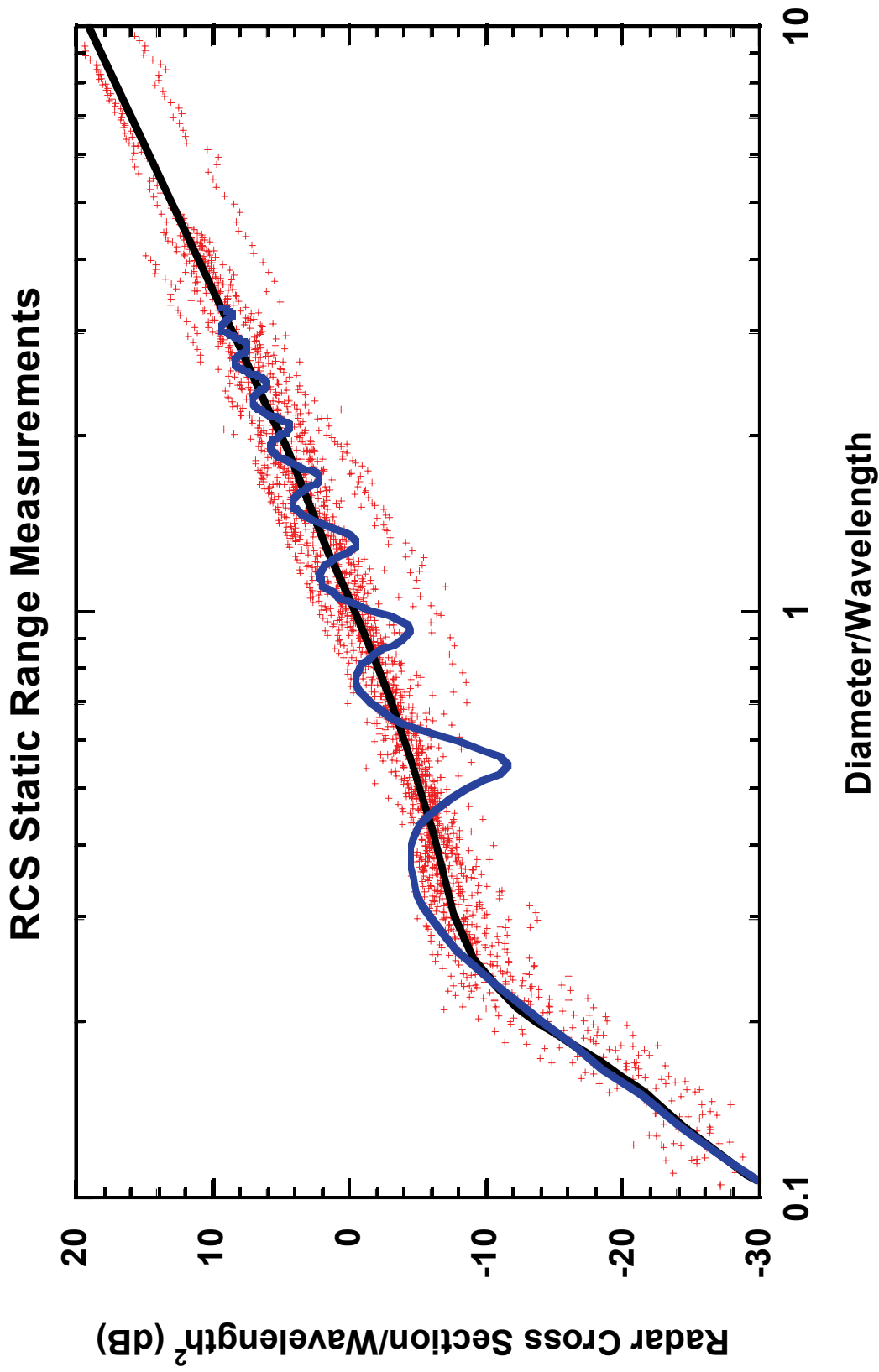


Figure 2. RCS parameter versus Size Parameter used in the NASA SEM.

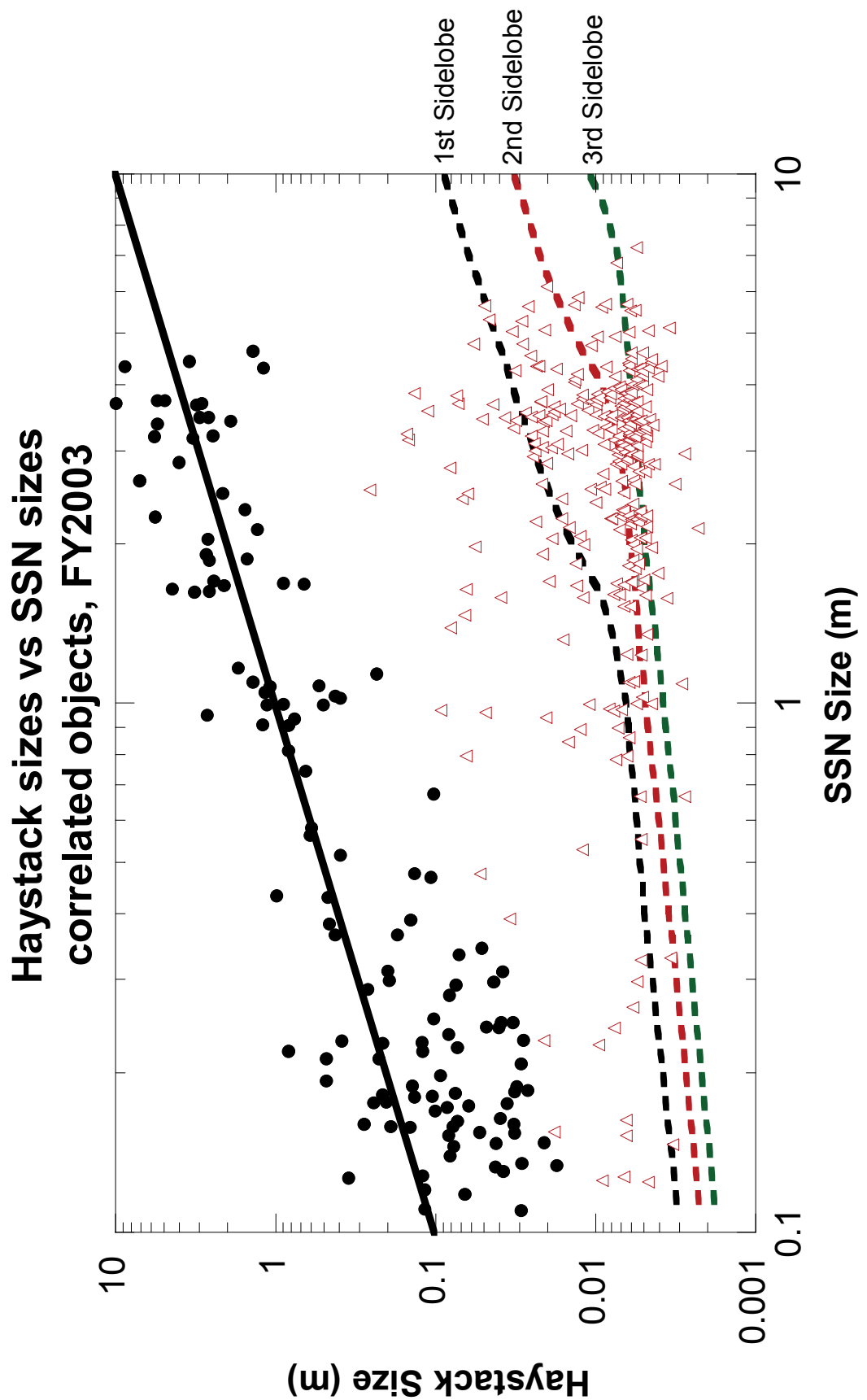


Figure 3. Haystack Size versus SSN Size with Mainlobe and Sidelobes illustrated.

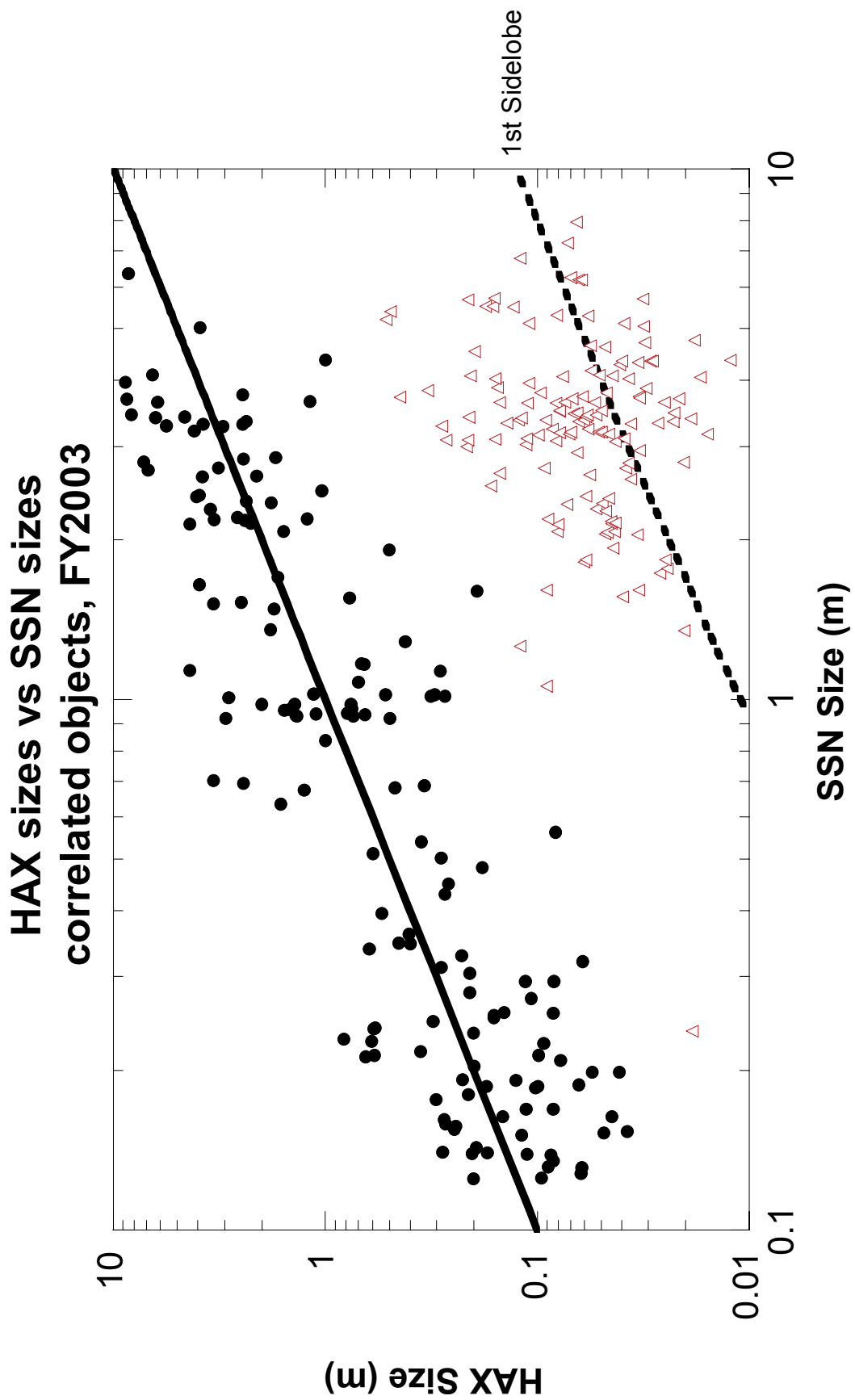


Figure 4. Haystack Size versus SSN Size with Mainlobe and Sidelobes Illustrated.

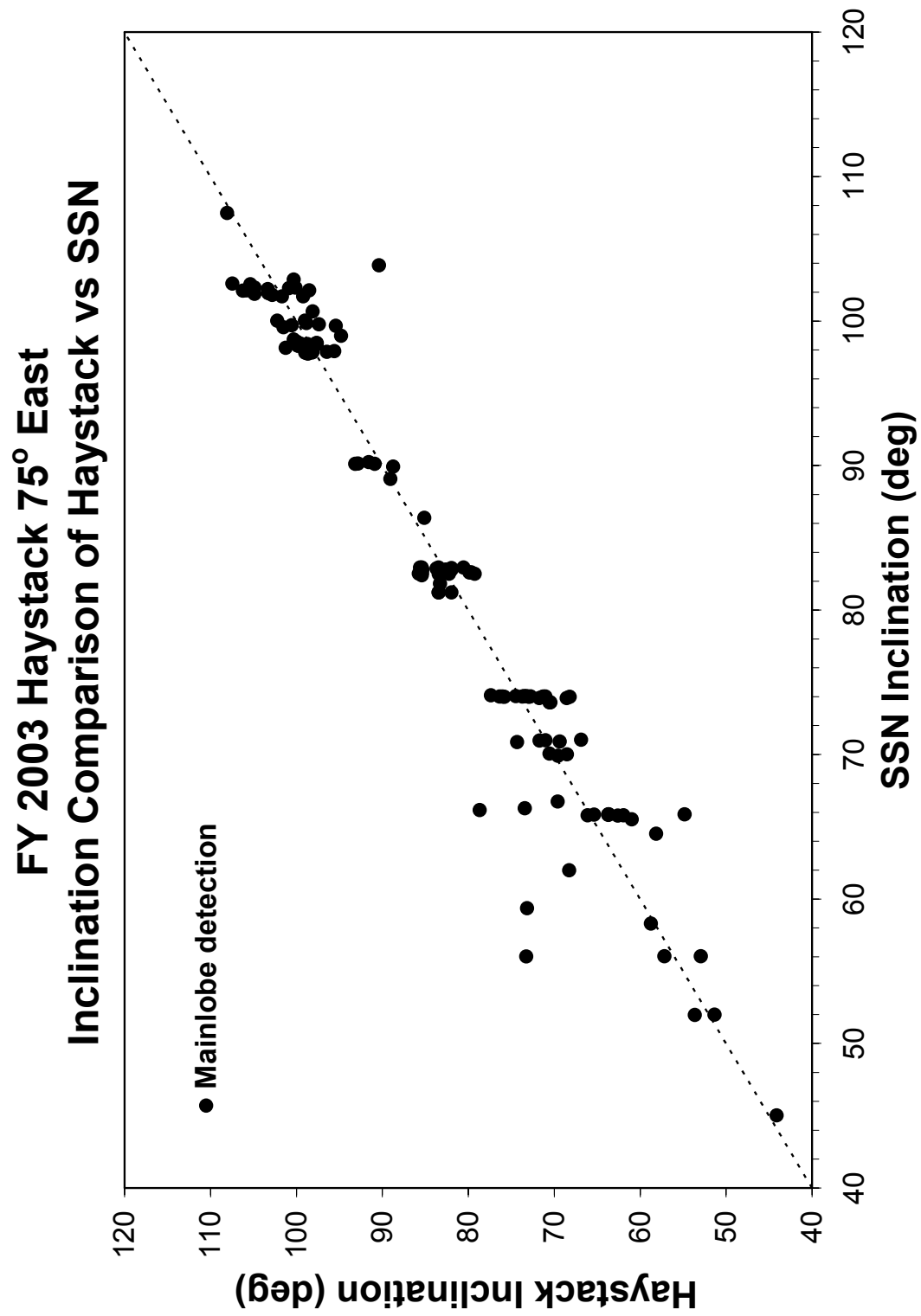


Figure 5. Haystack Inclination versus SSN Inclination.

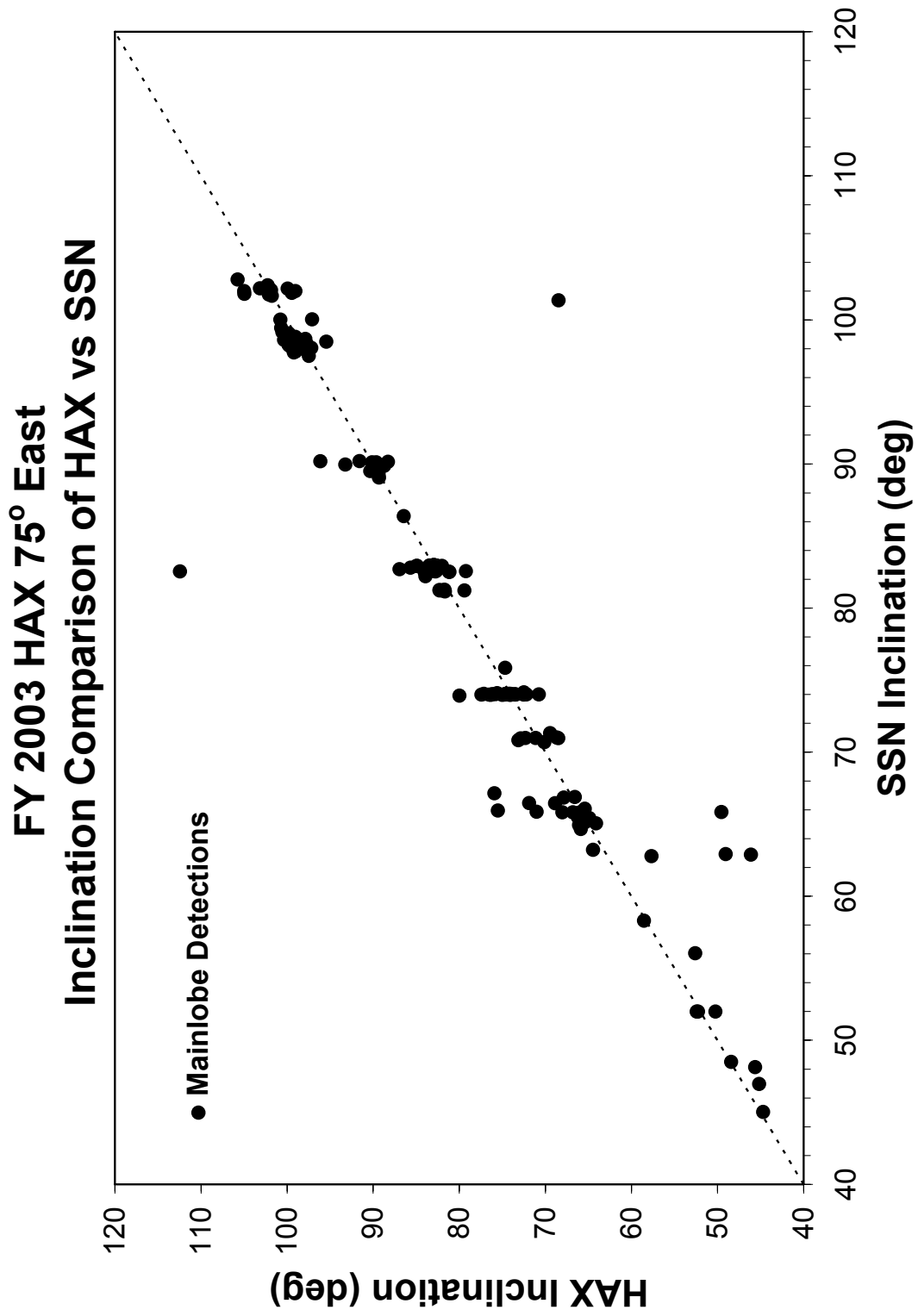


Figure 6. HAX Inclination versus SSN Inclination.

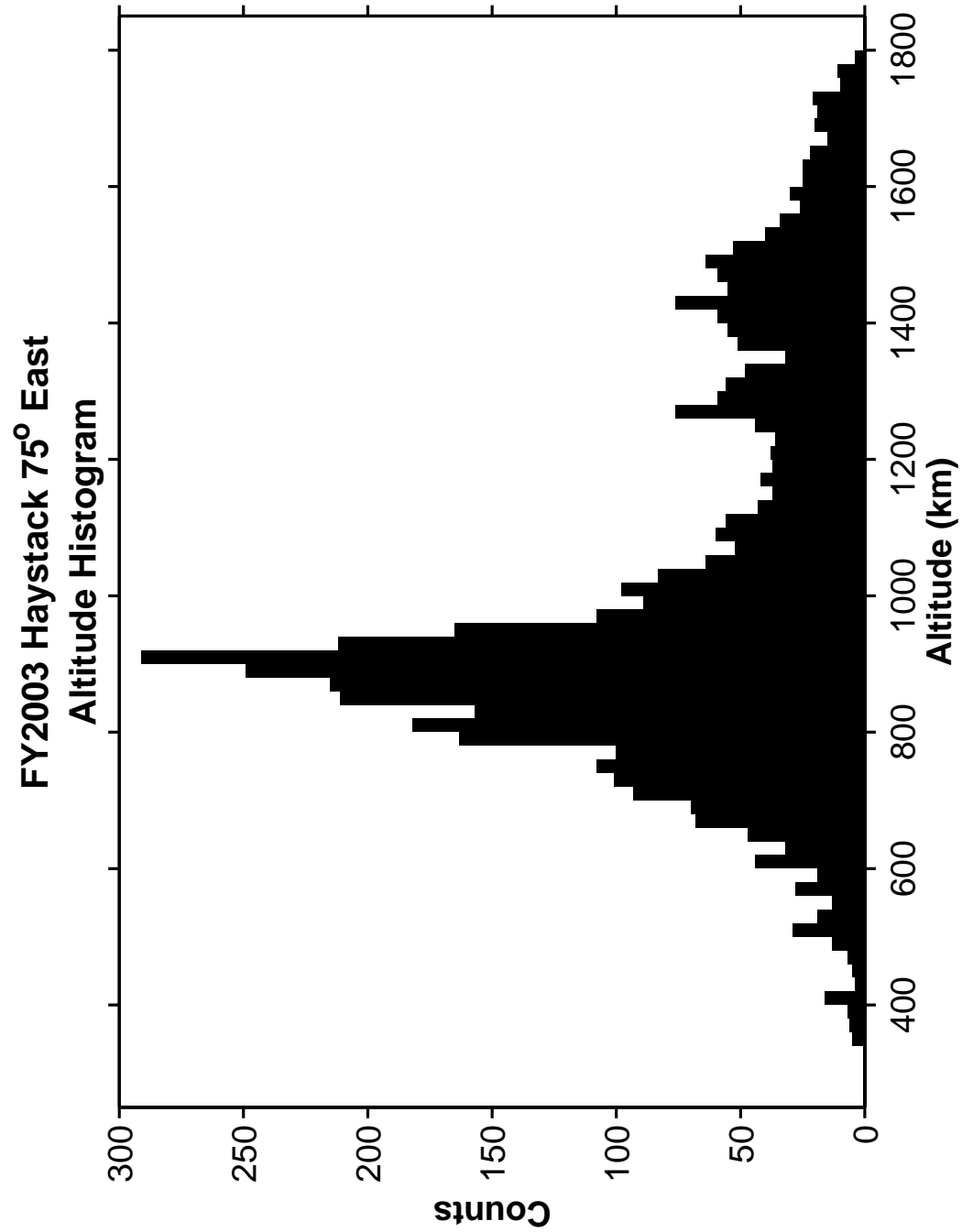


Figure 7. Haystack Altitude Histogram.

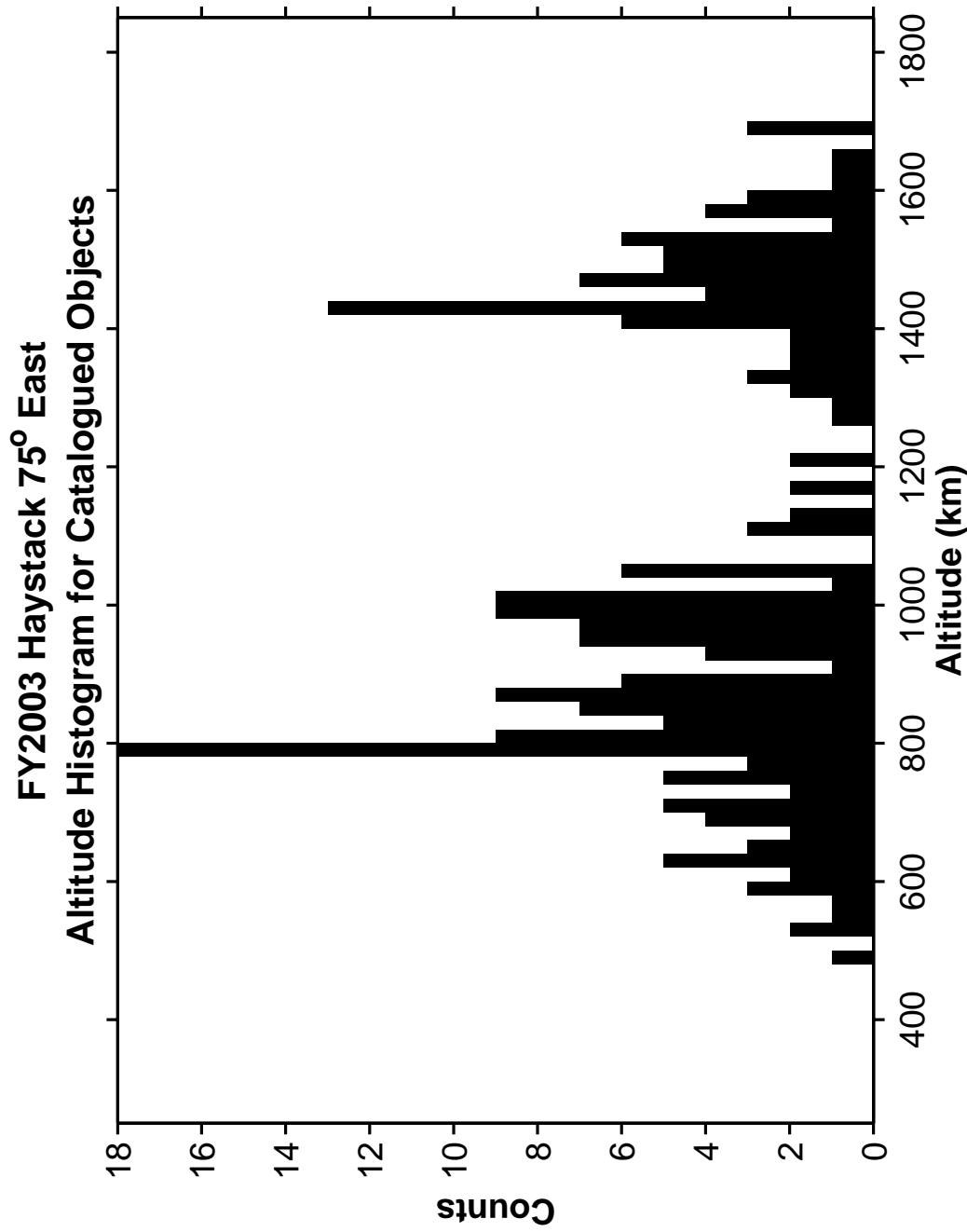


Figure 8. Haystack Altitude Histogram for Catalogued Objects.

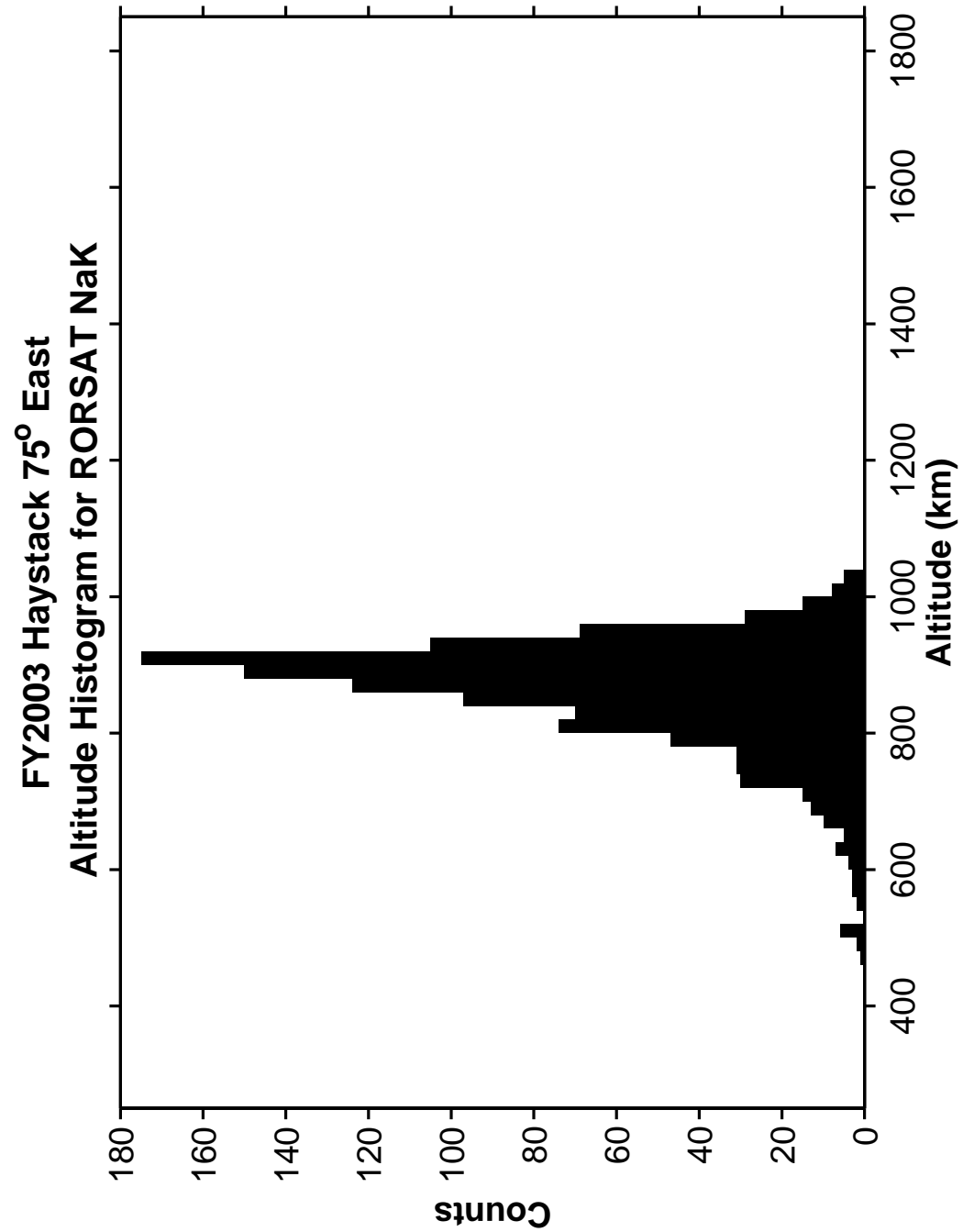


Figure 9. Haystack Altitude Histogram for RORSAT Nak Debris.

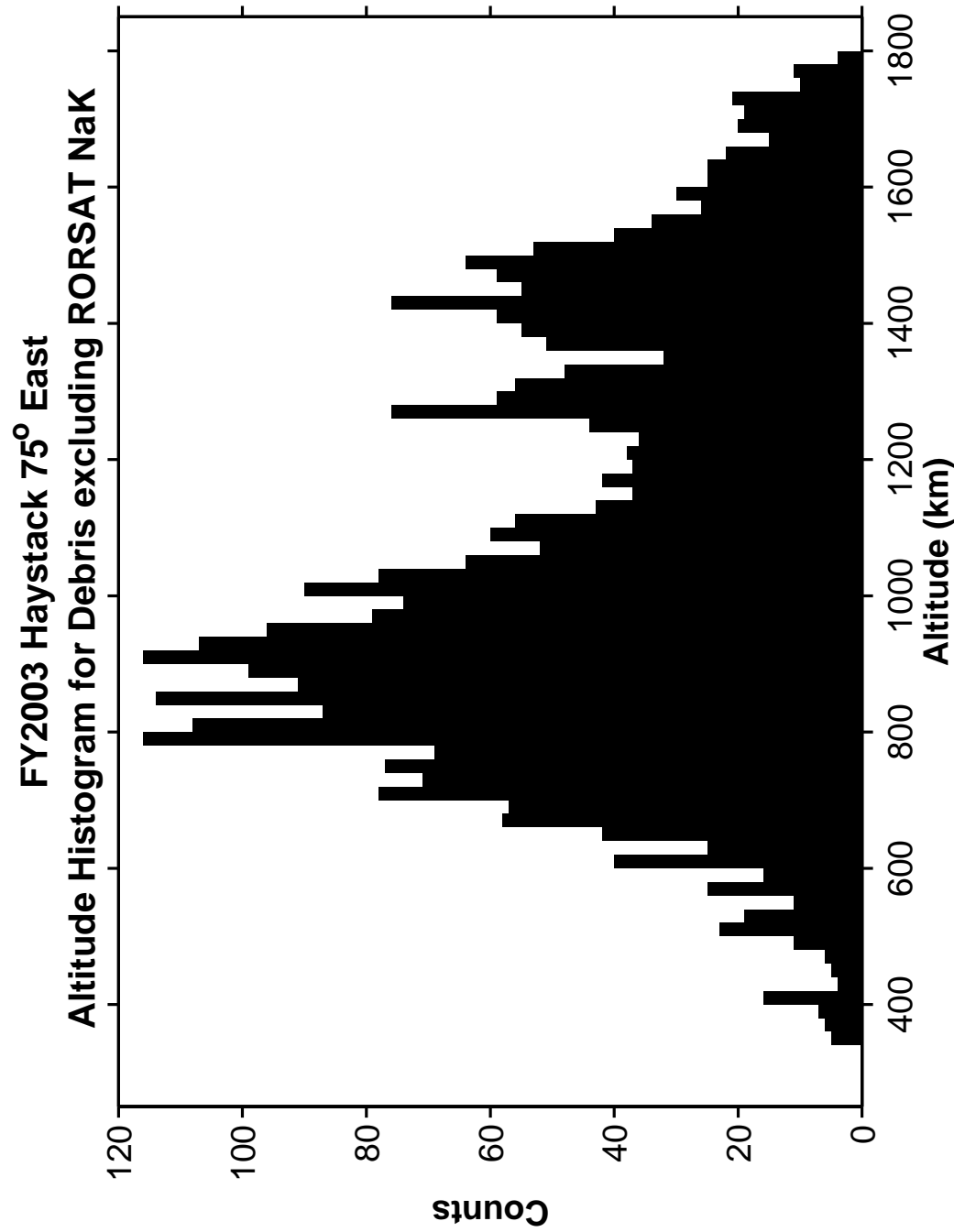


Figure 10. Haystack Altitude Histogram for Debris excluding RORSAT NaK Debris.

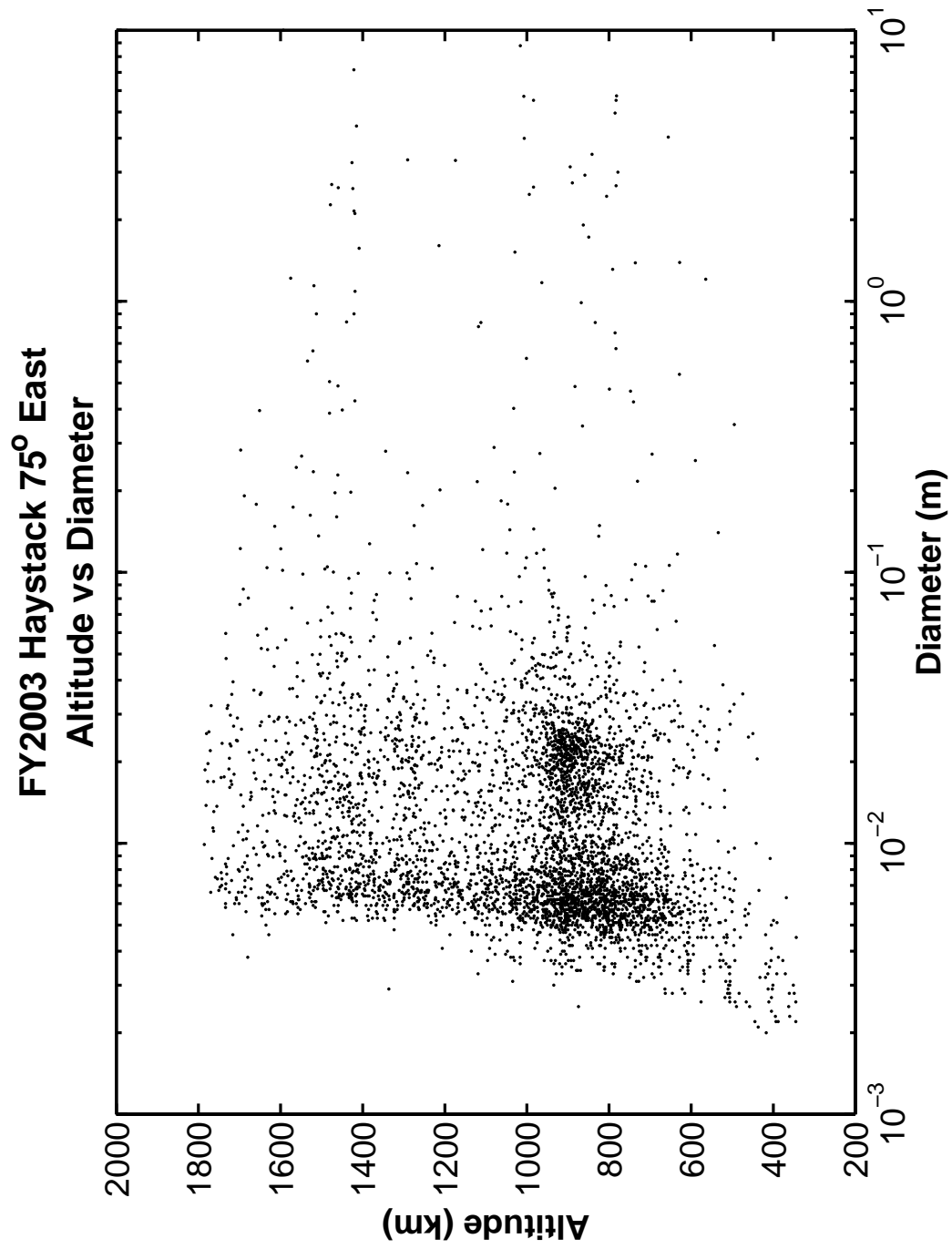


Figure 11. Haystack Altitude versus Diameter.

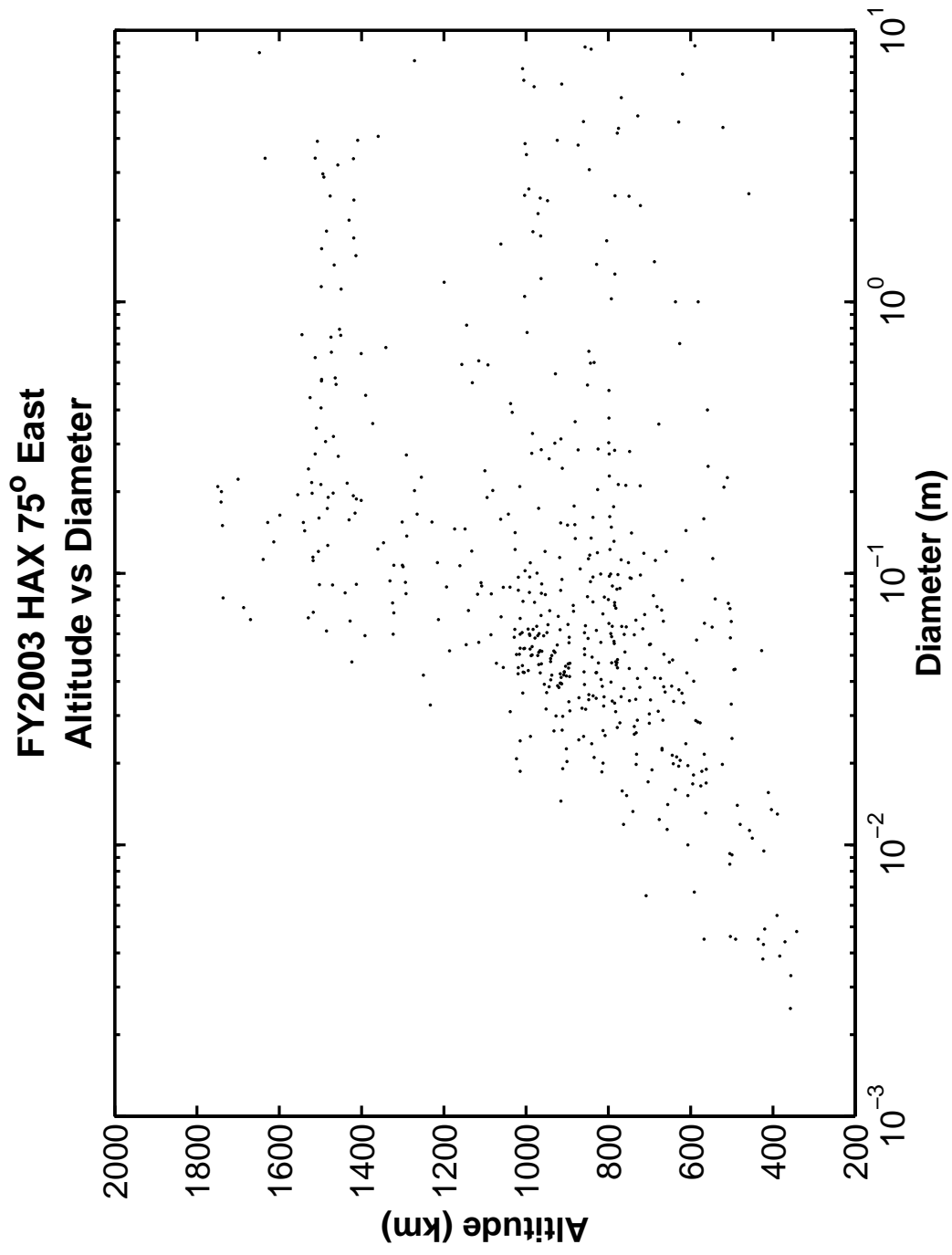


Figure 12. HAX Altitude versus Diameter.

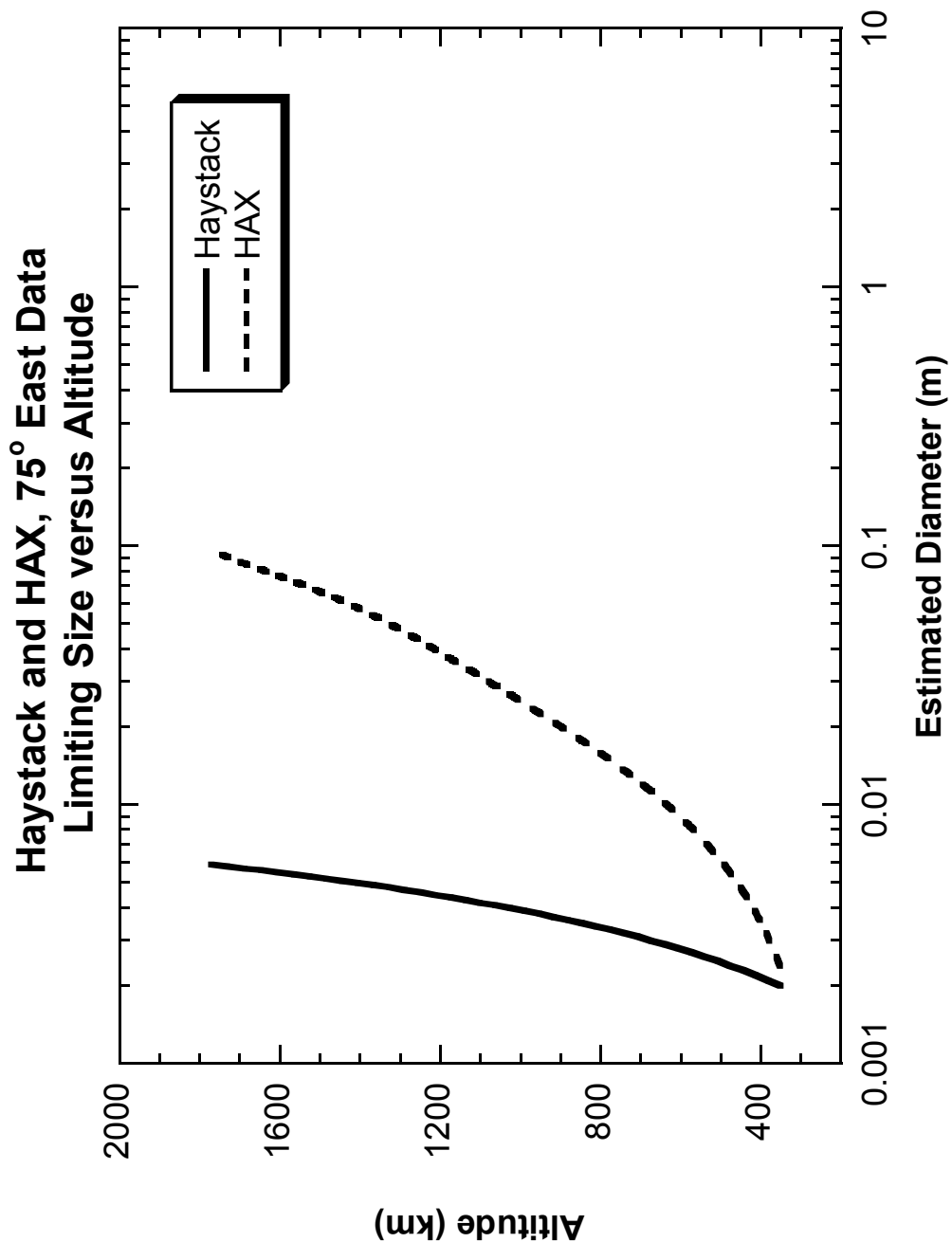


Figure 13. Haystack and HAX Minimum Detectable Diameter versus Altitude.

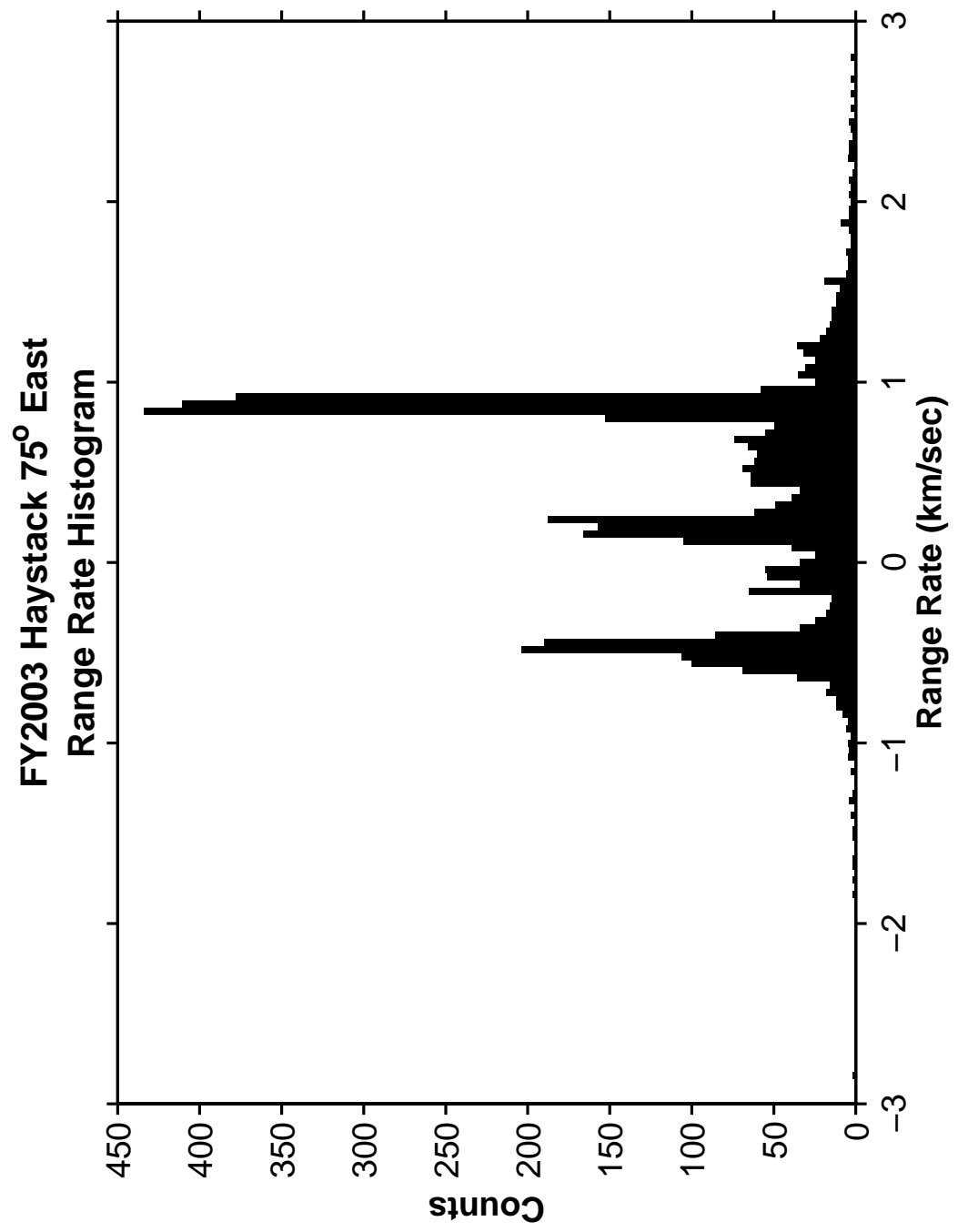


Figure 14. Haystack Range Rate Histogram.

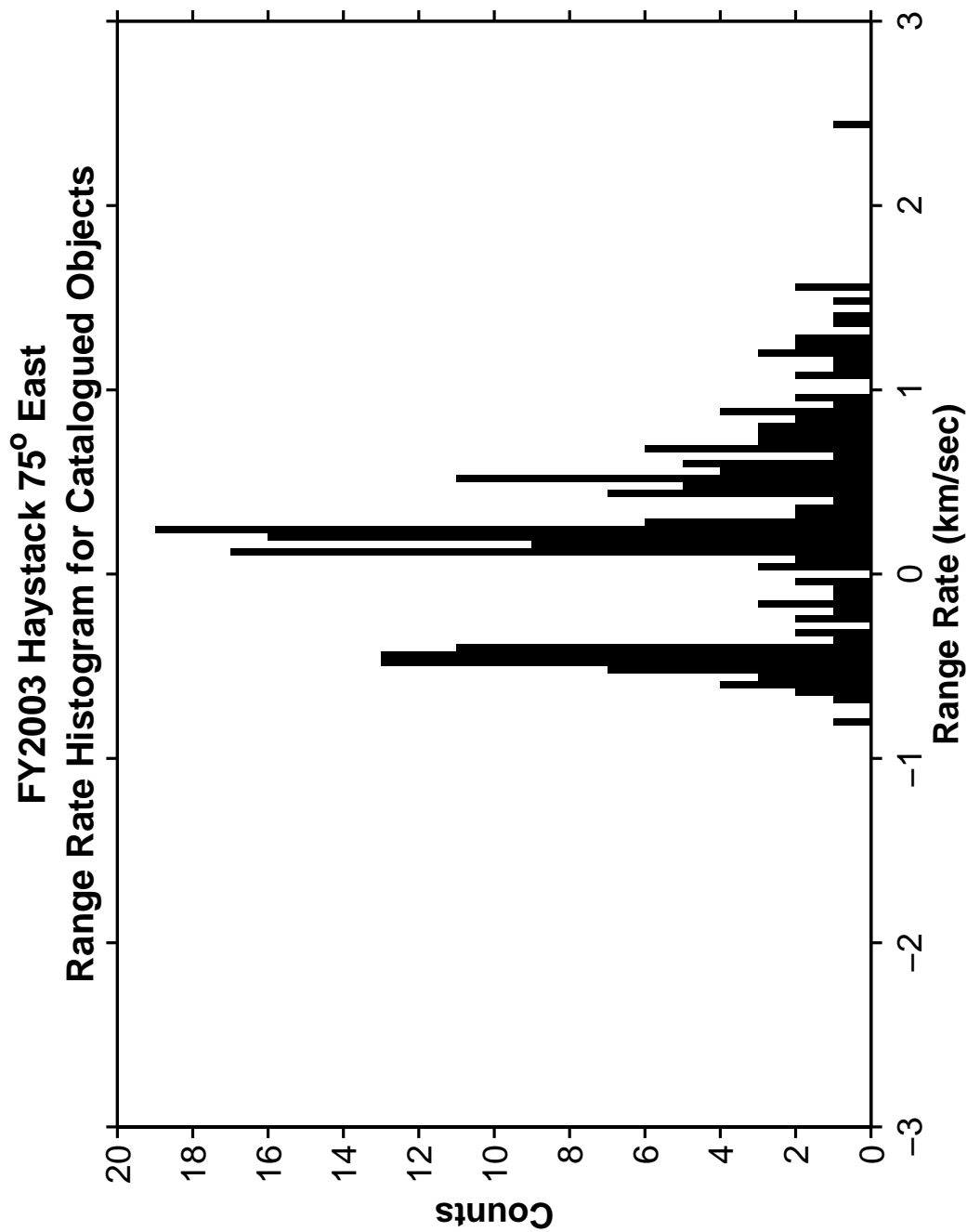


Figure 15. Haystack Range Rate Histogram for Catalogued Objects.

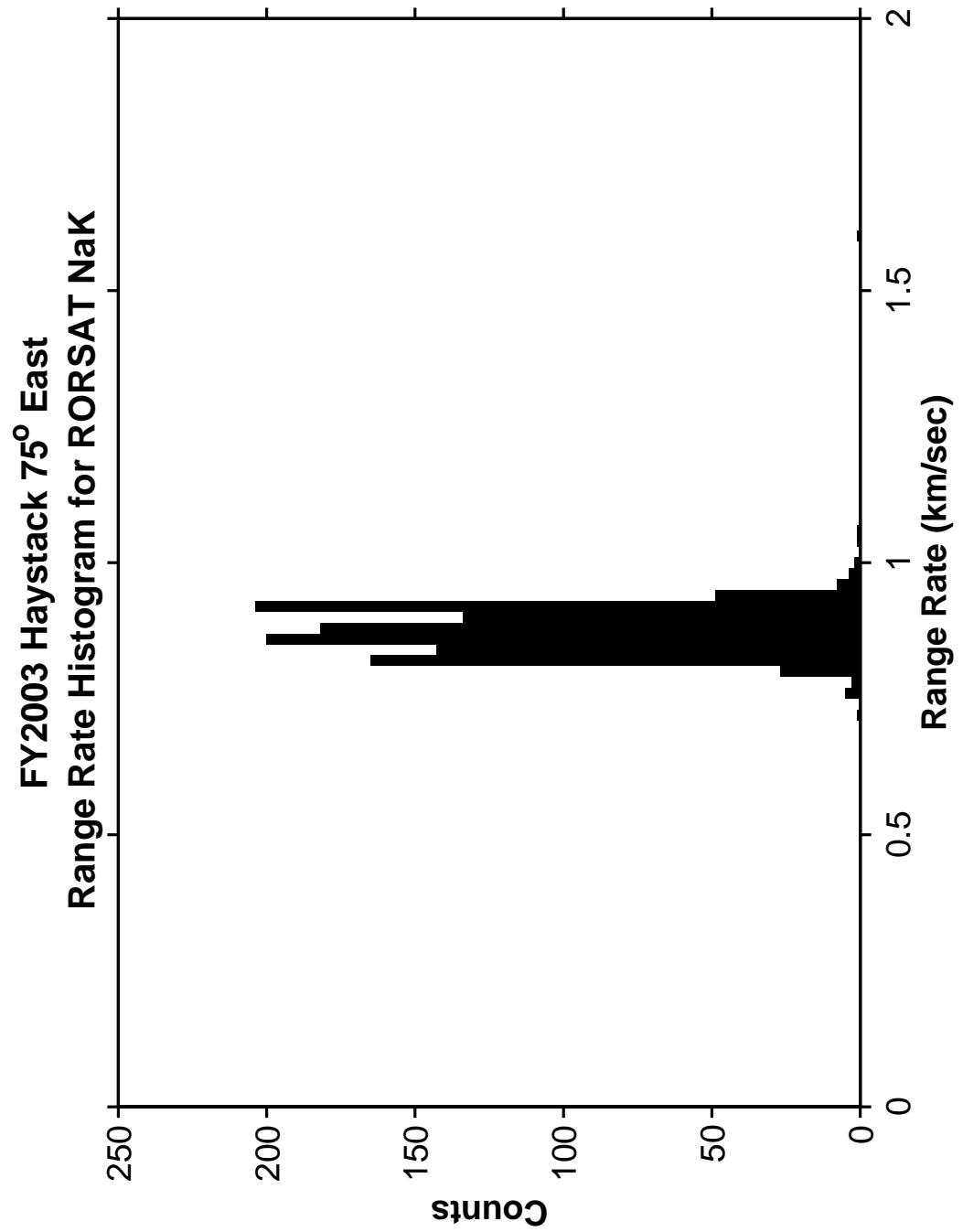


Figure 16. Haystack Range Rate Histogram for RORSAT NaK Debris.

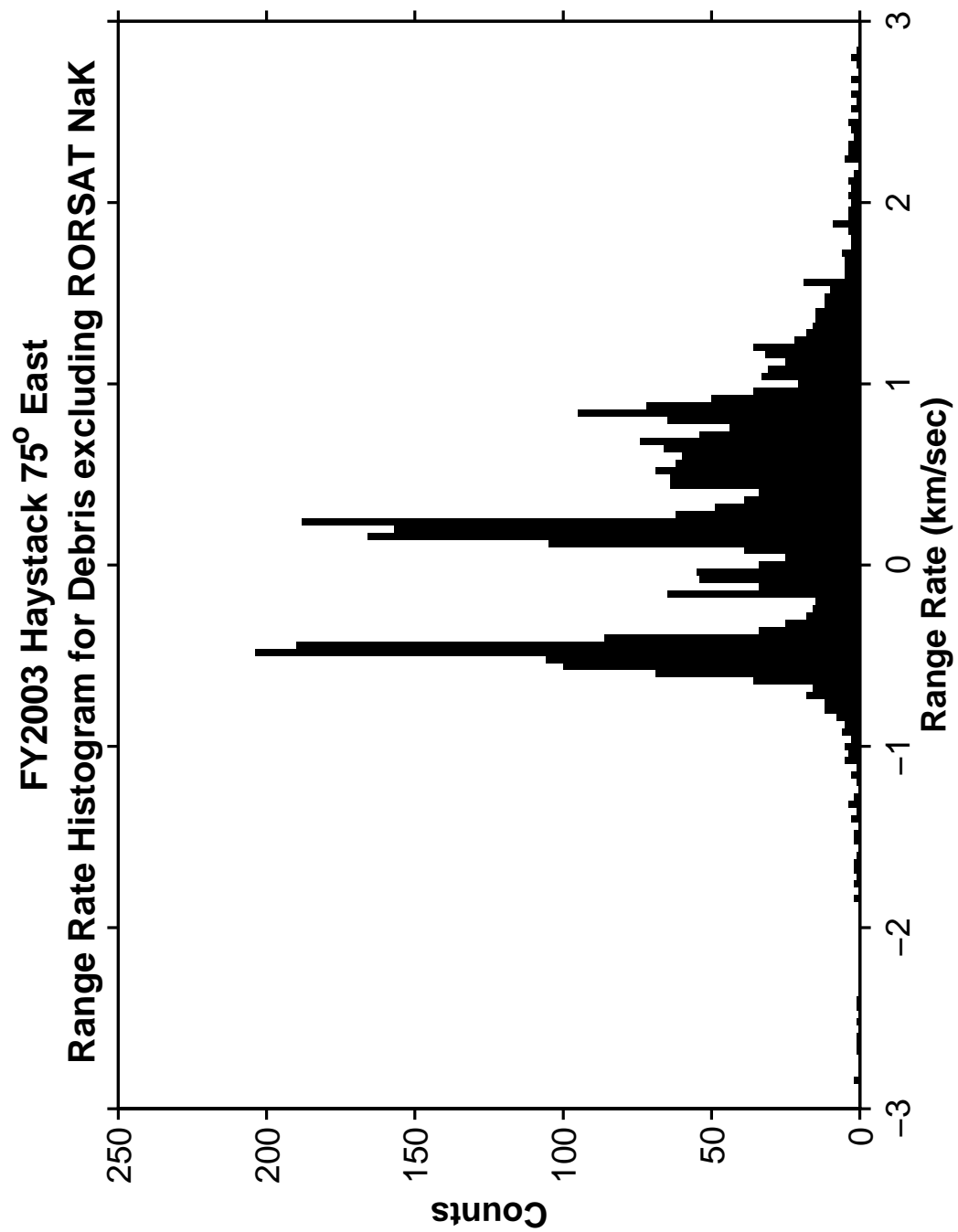


Figure 17. Haystack Range Rate Histogram excluding RORSAT Nak Debris.

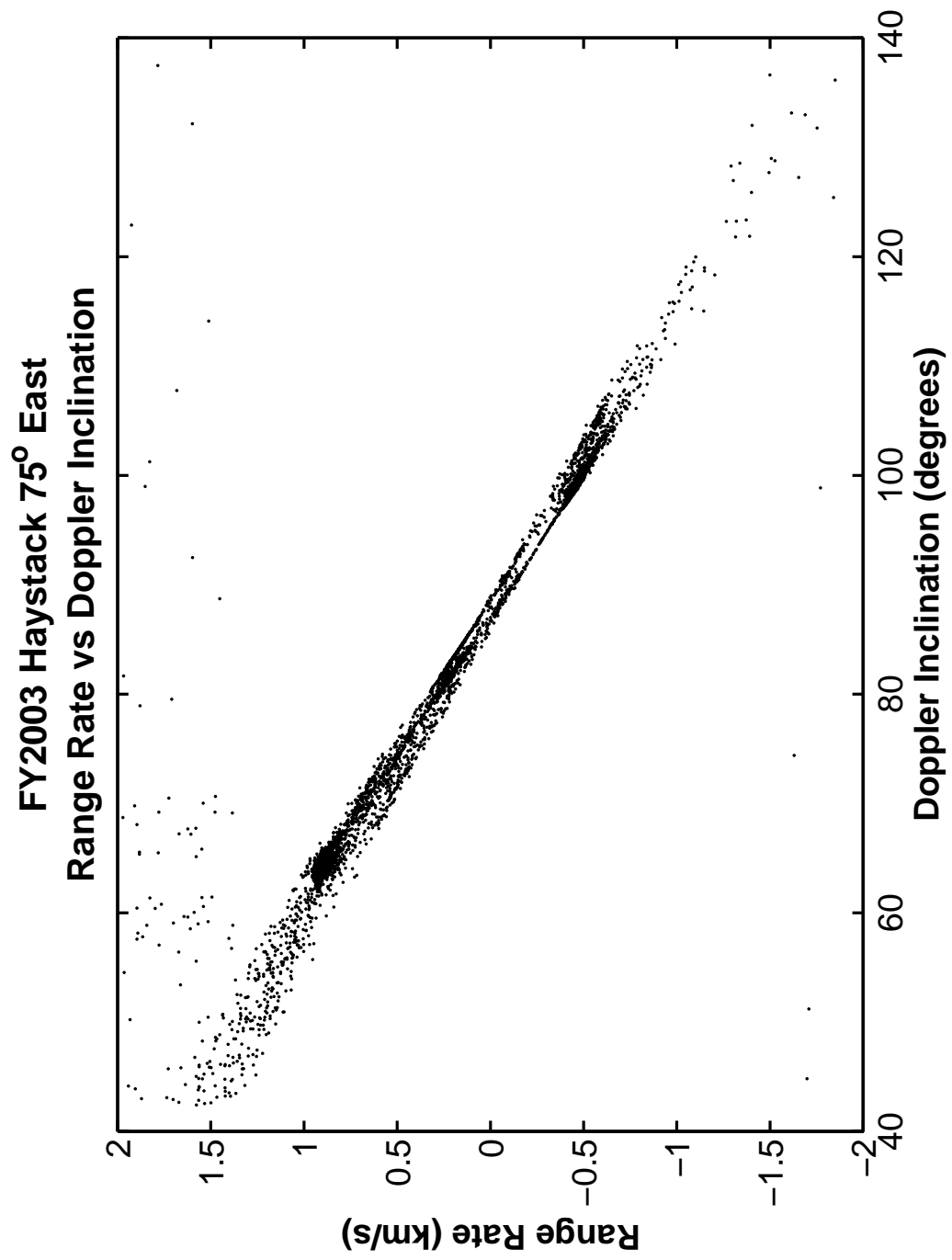


Figure 18. Haystack Range Rate versus Doppler Inclination.

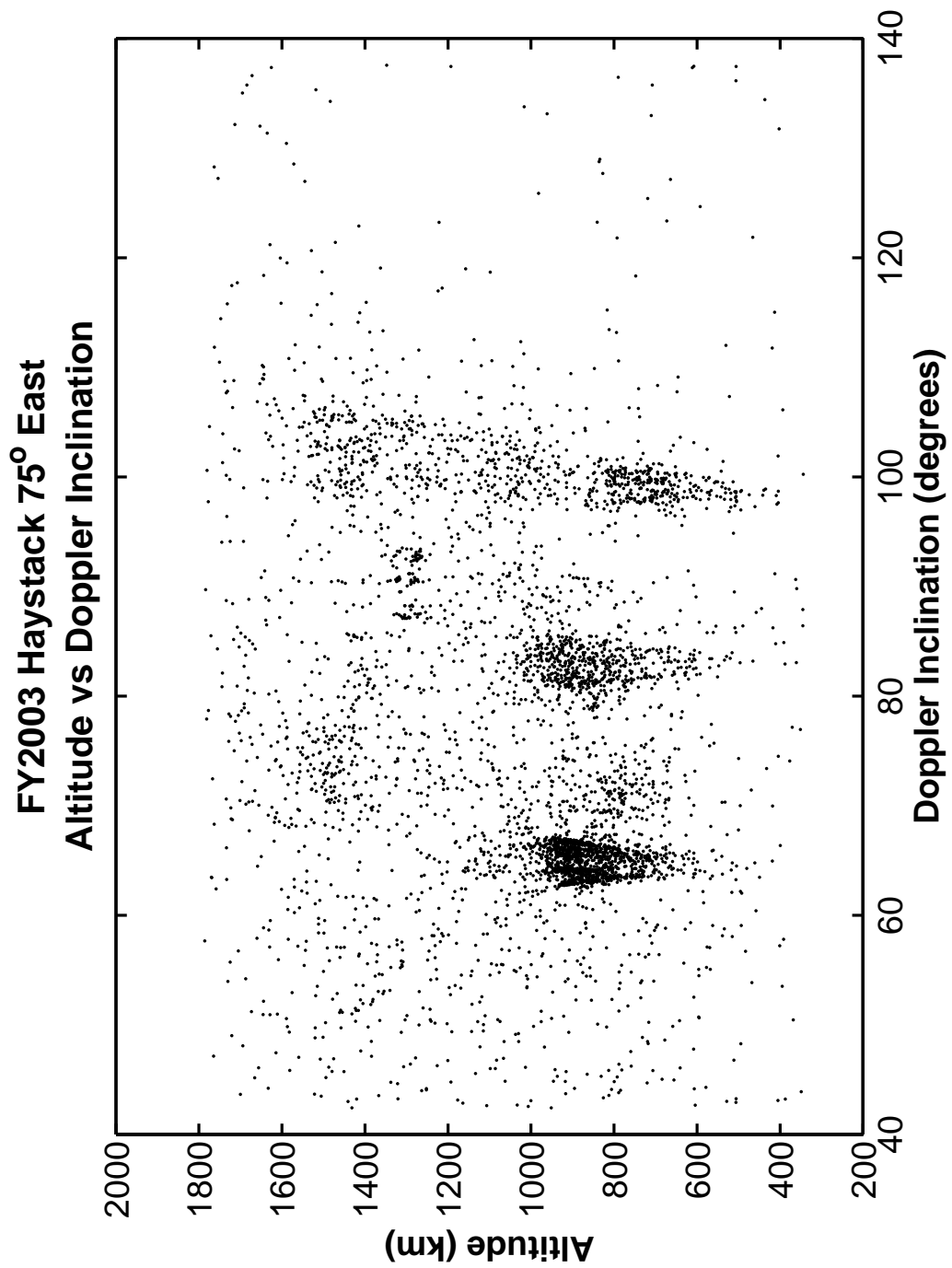


Figure 19. Haystack Altitude versus Doppler Inclination.

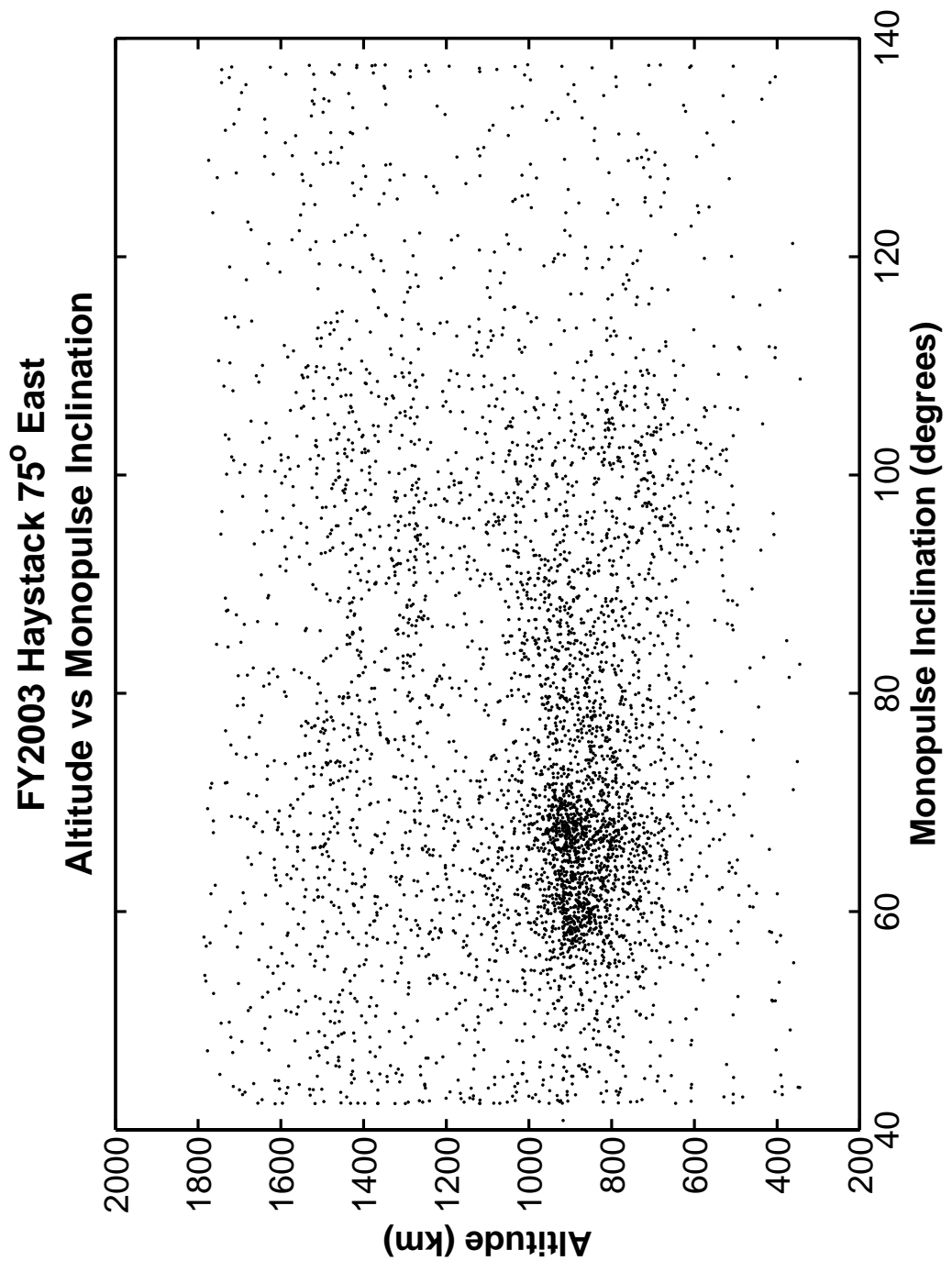


Figure 20. Haystack Altitude versus Monopulse Inclination.

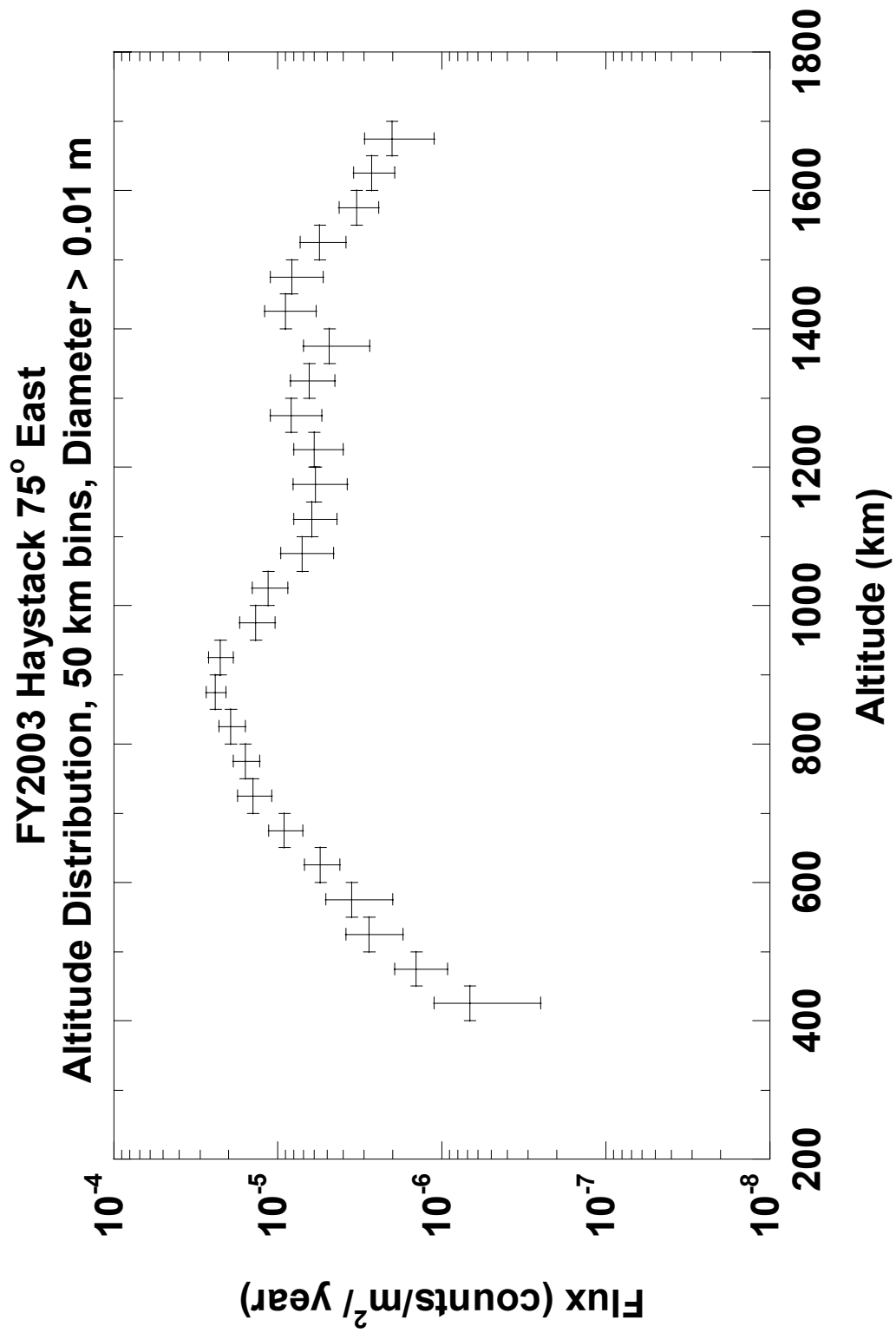


Figure 21. Haystack Flux versus Altitude in 50 km bins for debris with diameter > 0.01 m.

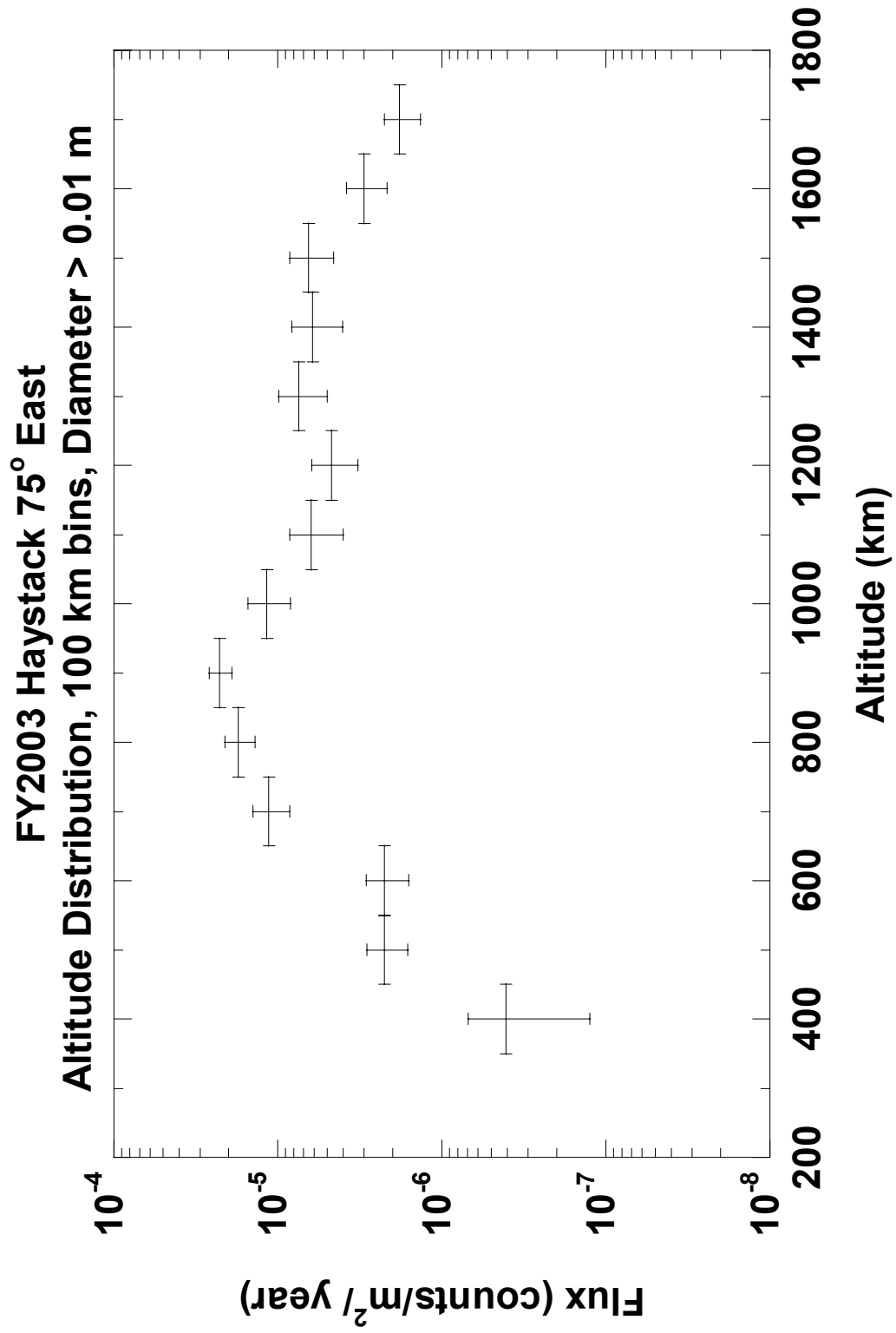


Figure 22. Haystack Flux versus Altitude in 100 km bins for debris with diameter > 0.01 m.

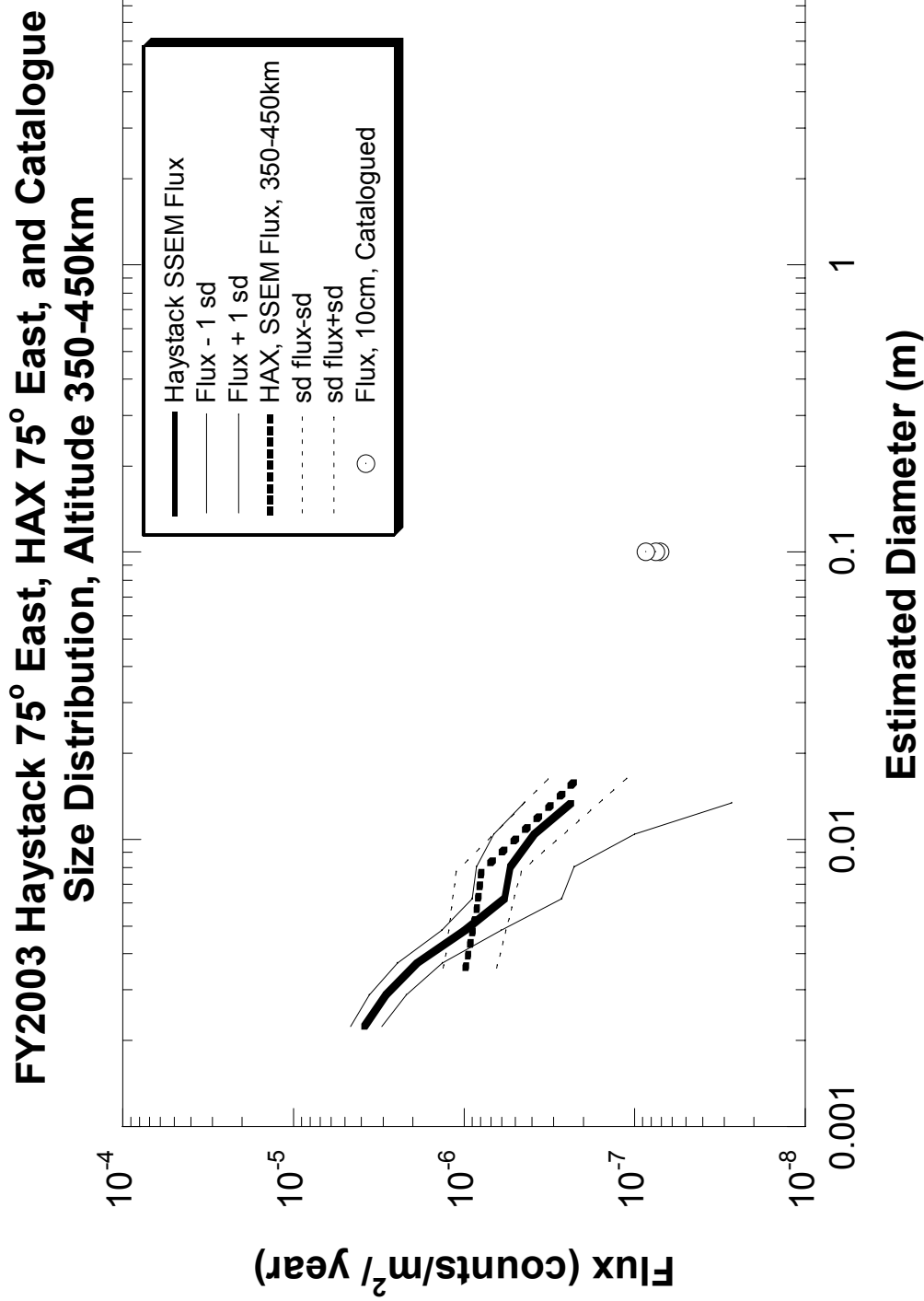


Figure 23. Haystack, HAX, and the 10 cm Catalogue Flux versus Diameter for 350-450 km Altitude.

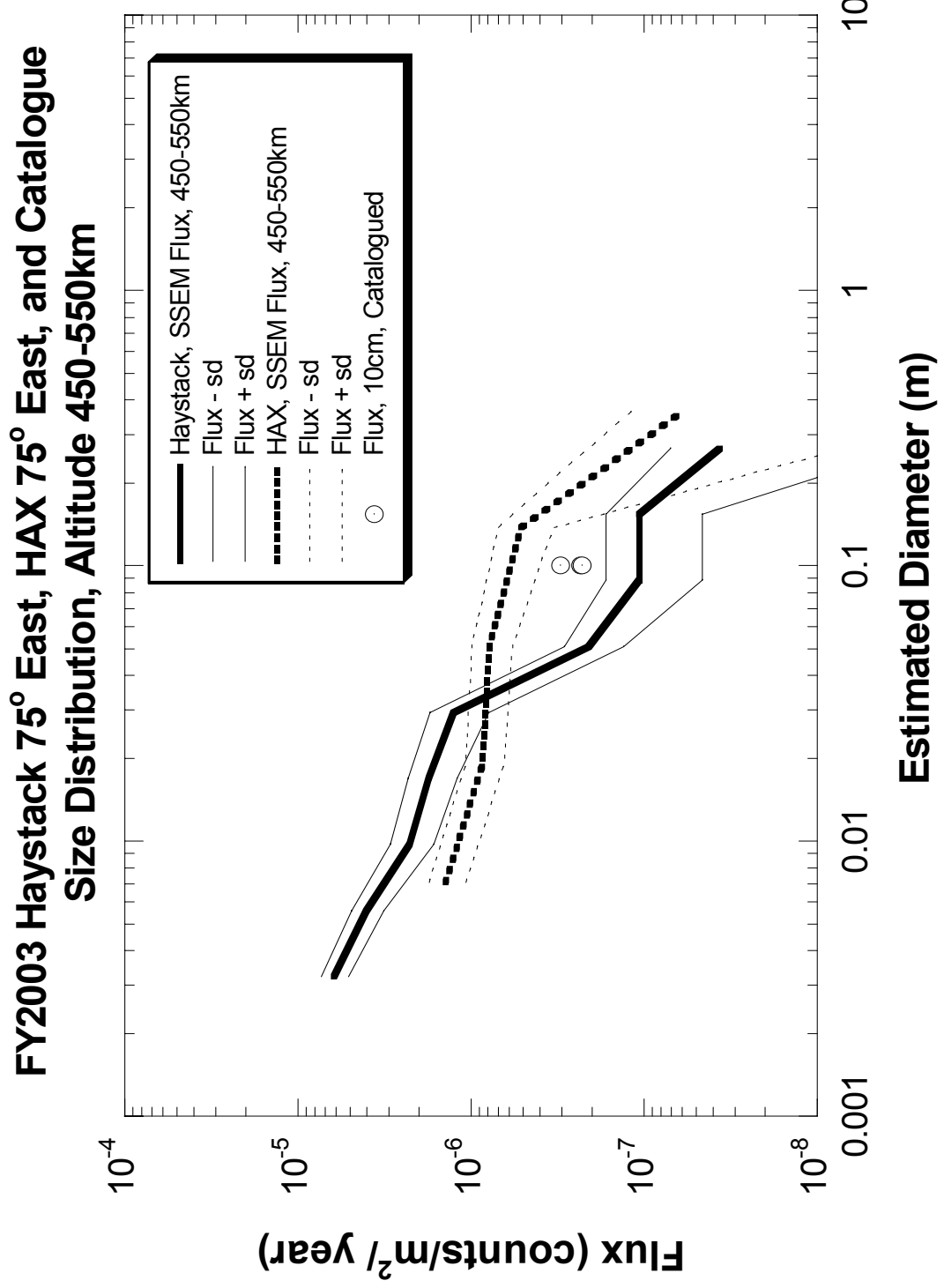


Figure 24. Haystack, HAX, and the 10 cm Catalogue Flux versus Diameter for 450-550 km Altitude.

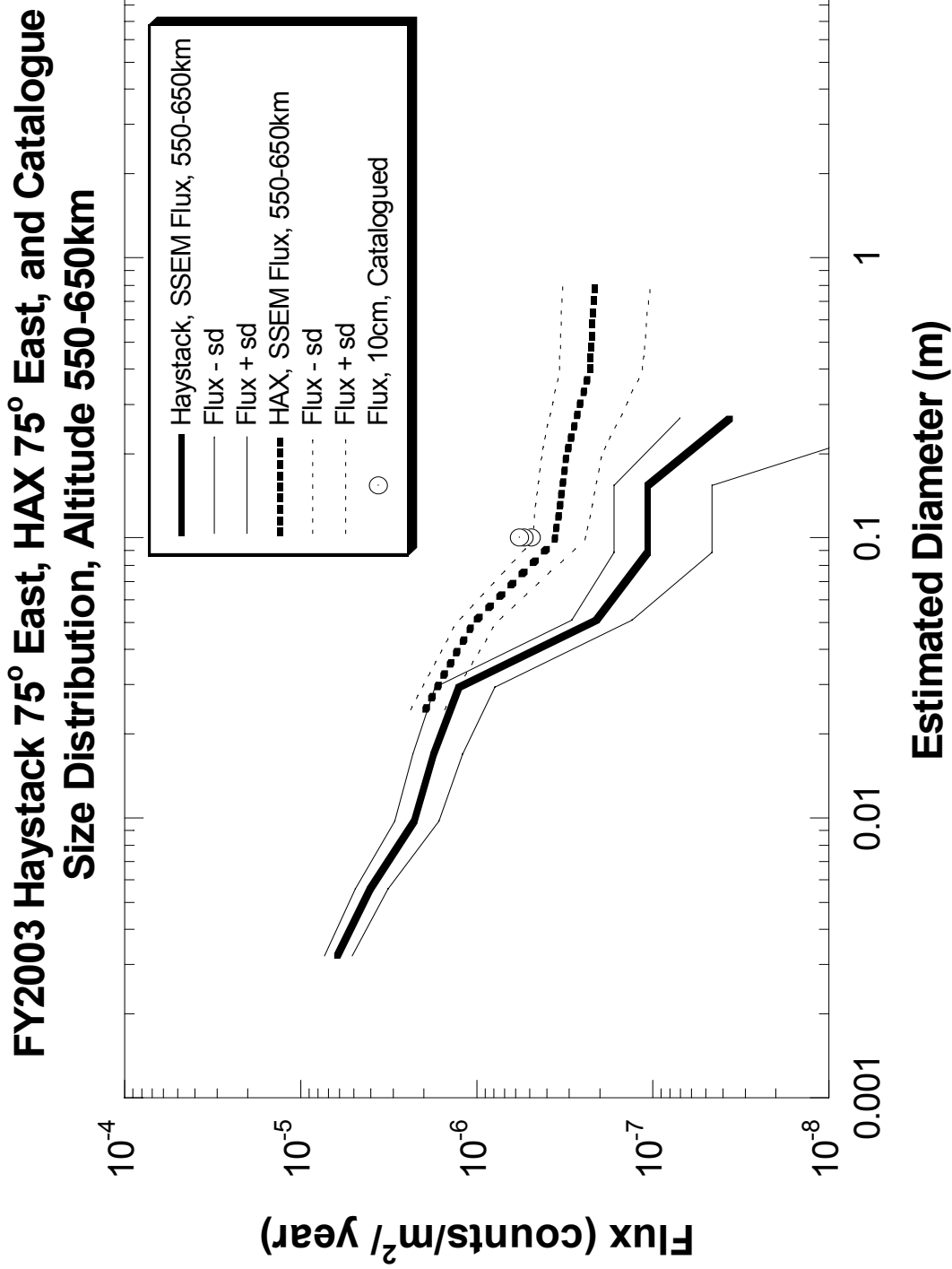


Figure 25. Haystack, HAX, and the 10 cm Catalogue Flux versus Diameter for 550-650 km Altitude.

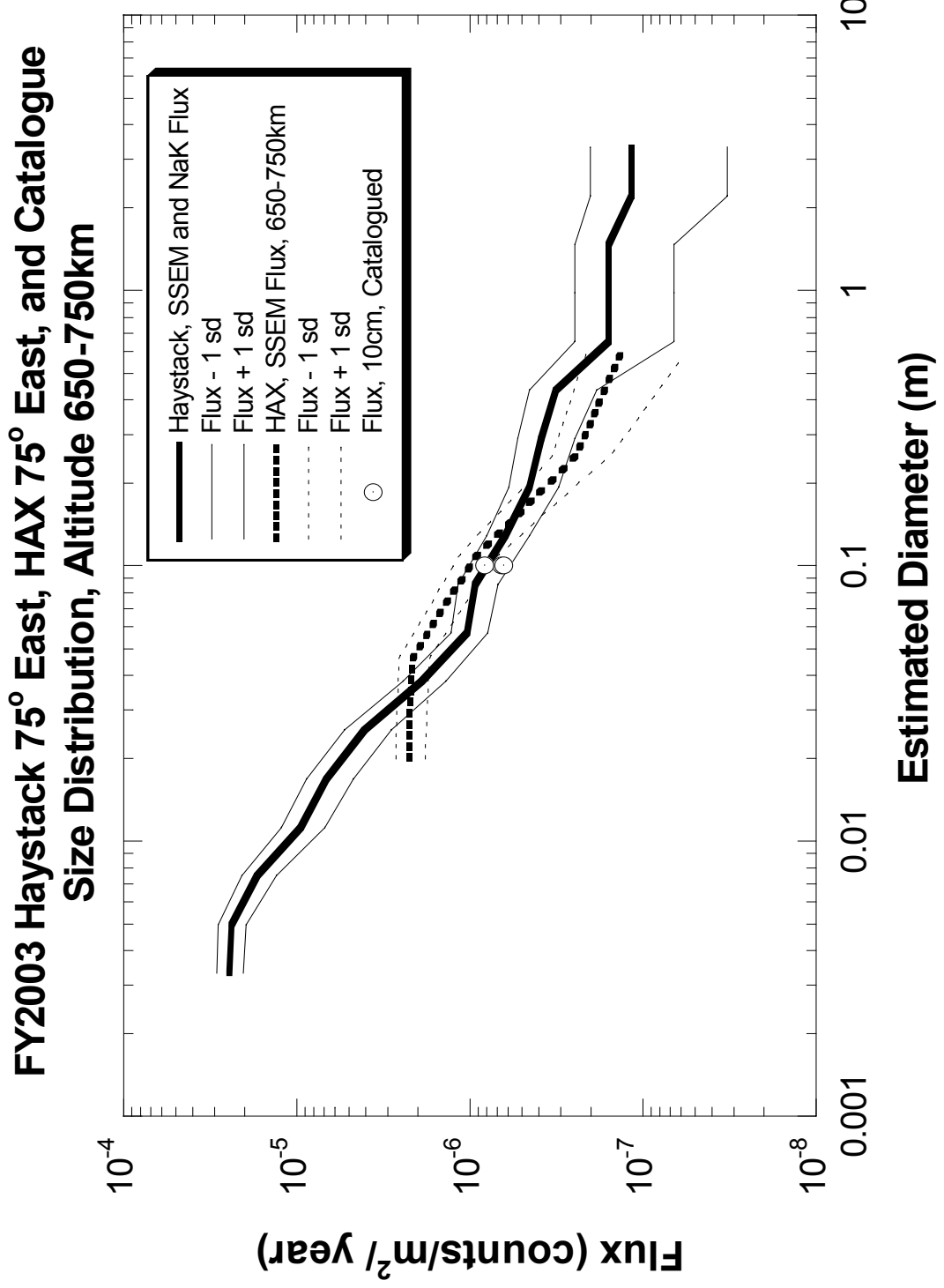


Figure 26. Haystack, HAX, and the 10 cm Catalogue Flux versus Diameter for 650-750 km Altitude.

FY2003 Haystack 75° East, HAX 75° East, and Catalogue Size Distribution, Altitude 750-850km

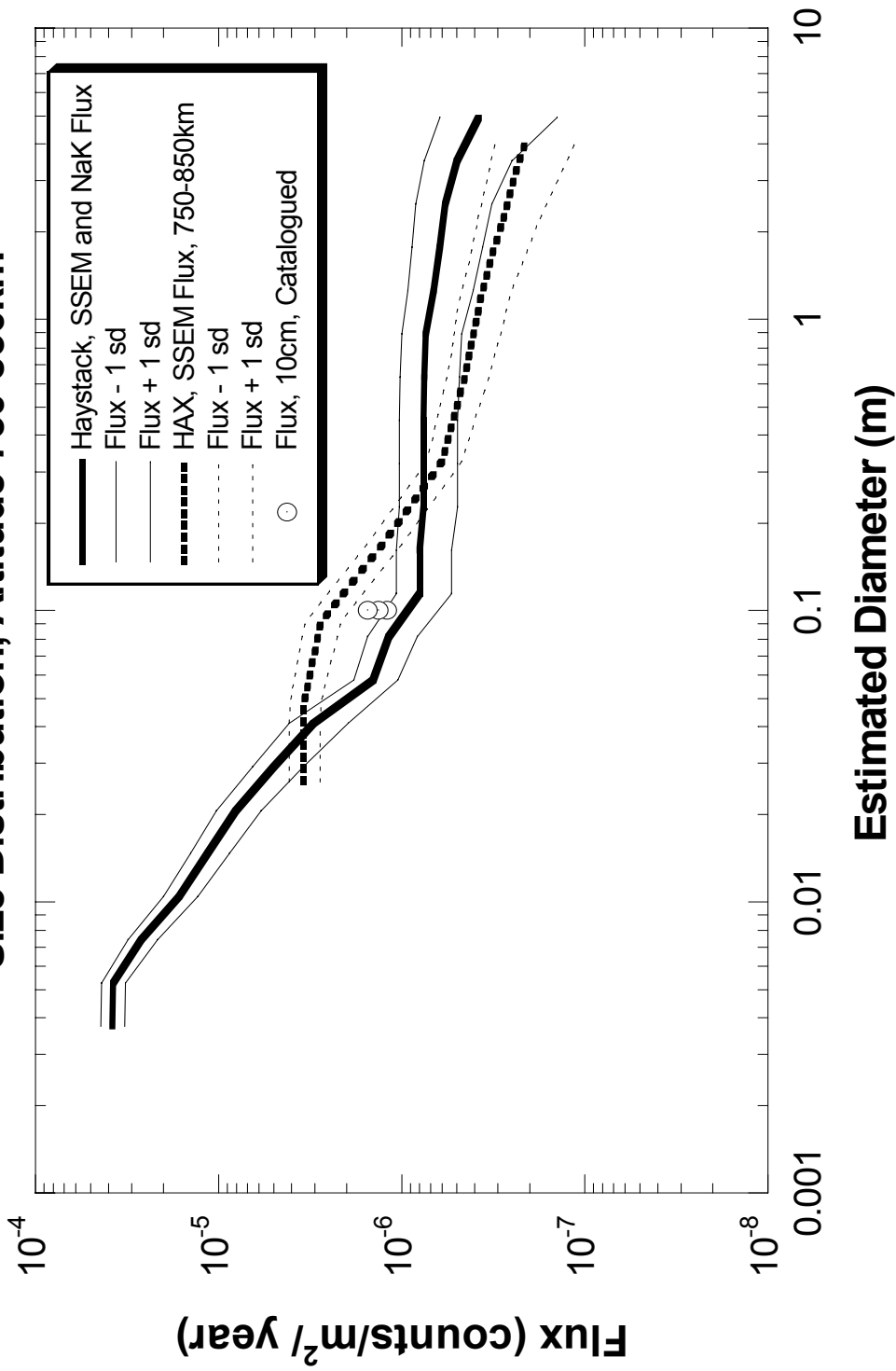


Figure 27. Haystack, HAX, and the 10 cm Catalogue Flux versus Diameter for 750-850 km Altitude.

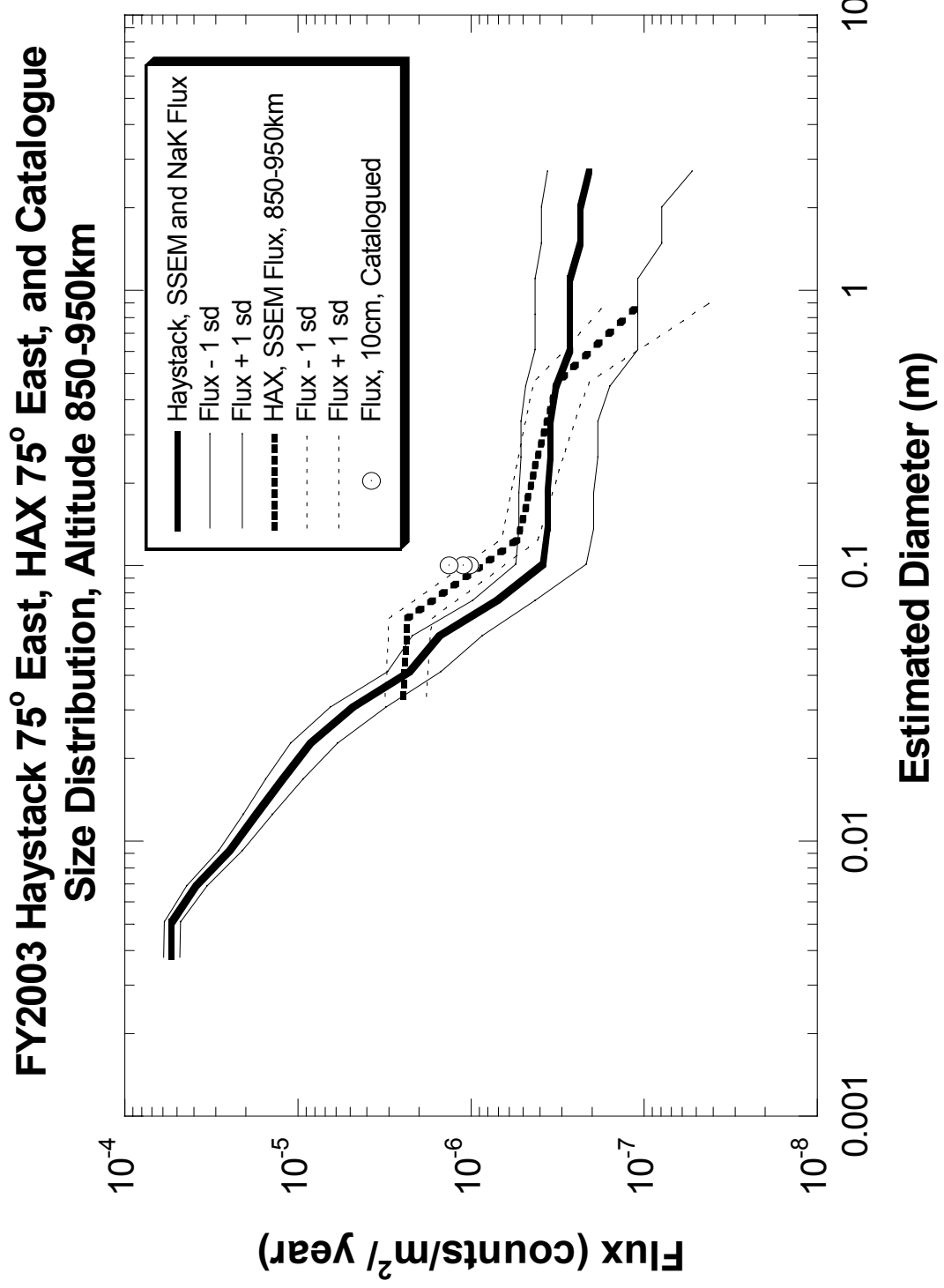


Figure 28. Haystack, HAX, and the 10 cm Catalogue Flux versus Diameter for 850-950 km Altitude.

FY2003 Haystack 75° East, HAX 75° East, and Catalogue Size Distribution, Altitude 950-1050km

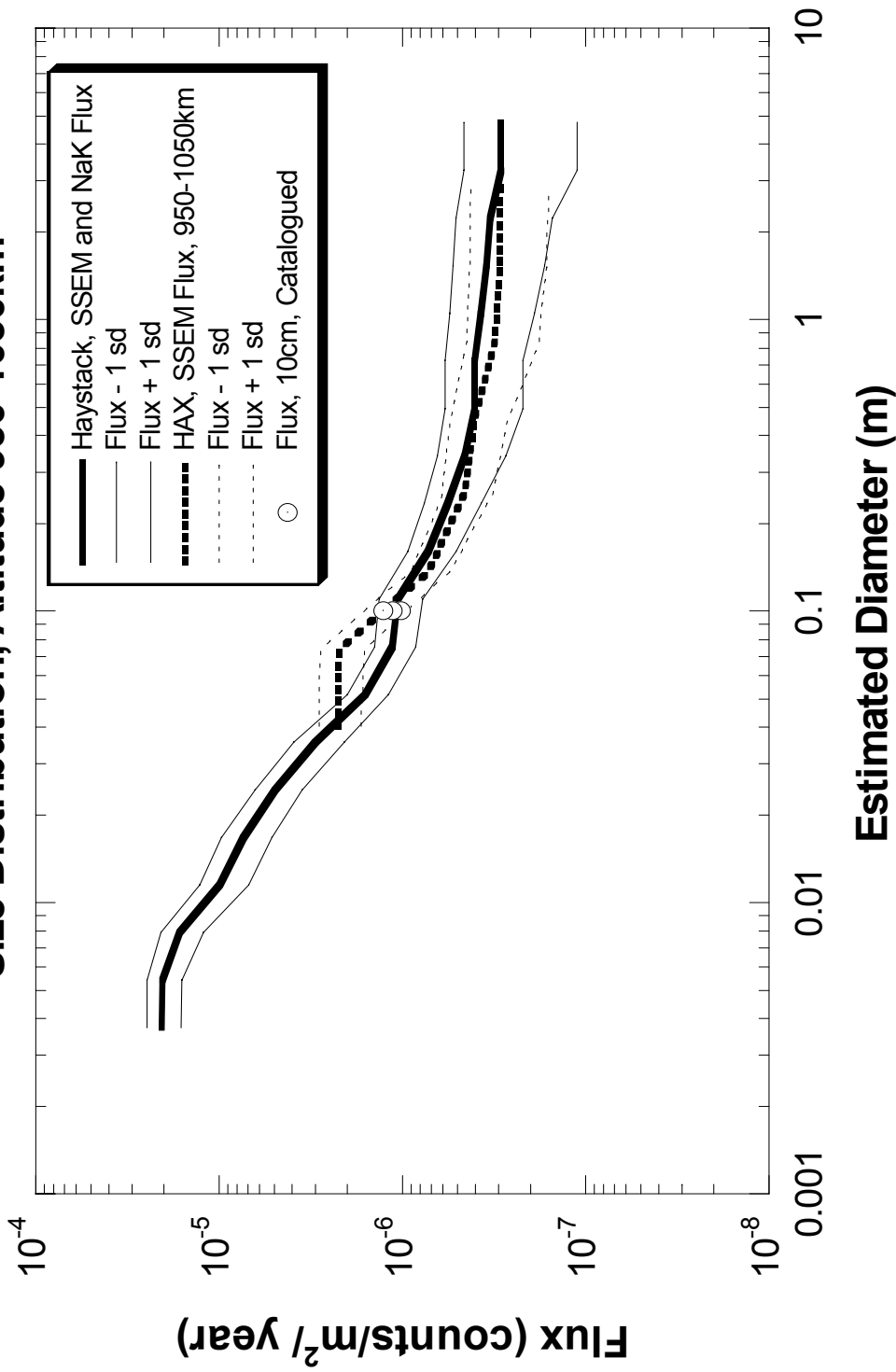


Figure 29. Haystack, HAX, and the 10 cm Catalogue Flux versus Diameter for 950-1050 km Altitude.

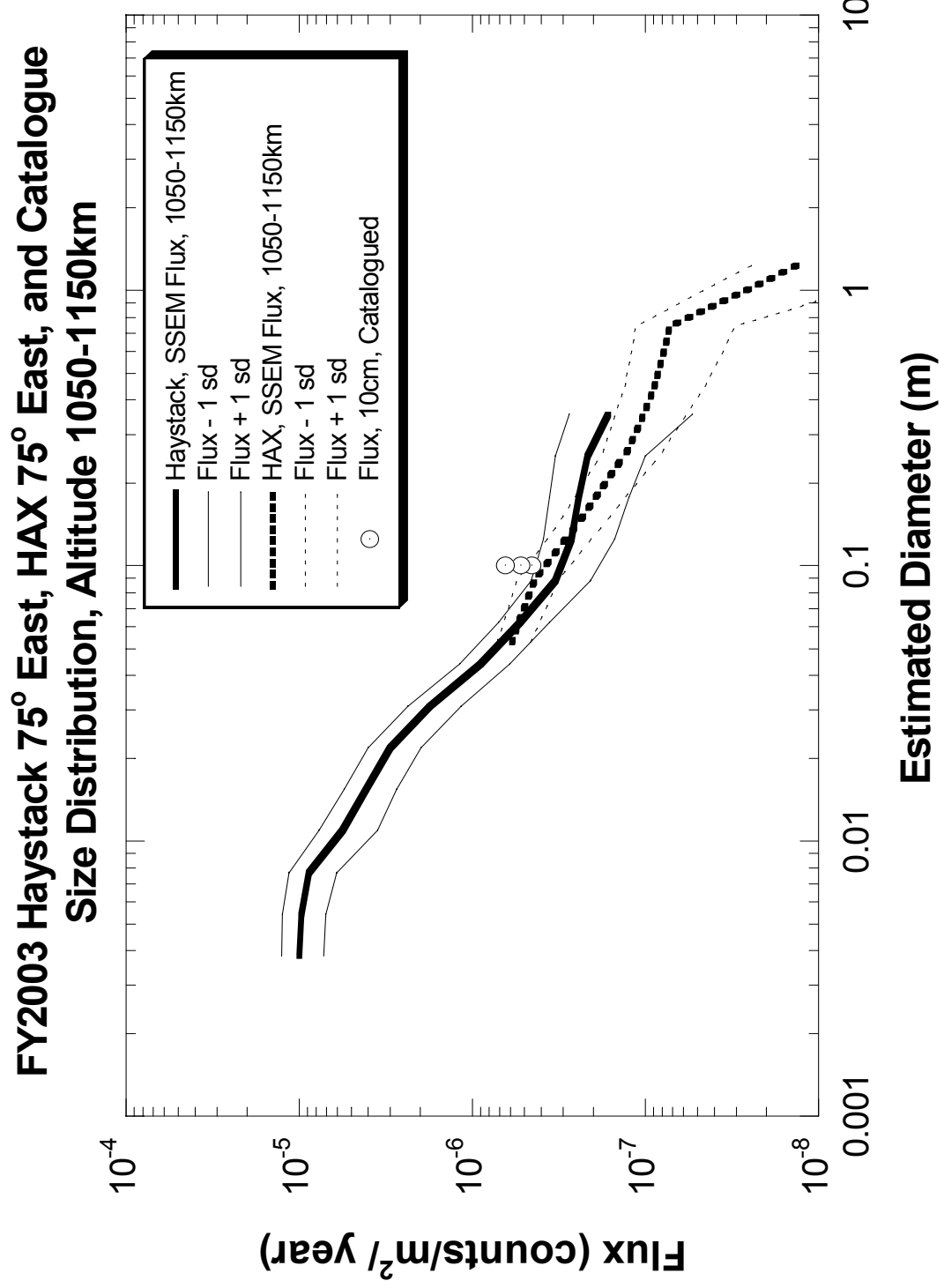


Figure 30. Haystack, HAX, and the 10 cm Catalogue Flux versus Diameter for 1050-1150 km Altitude.

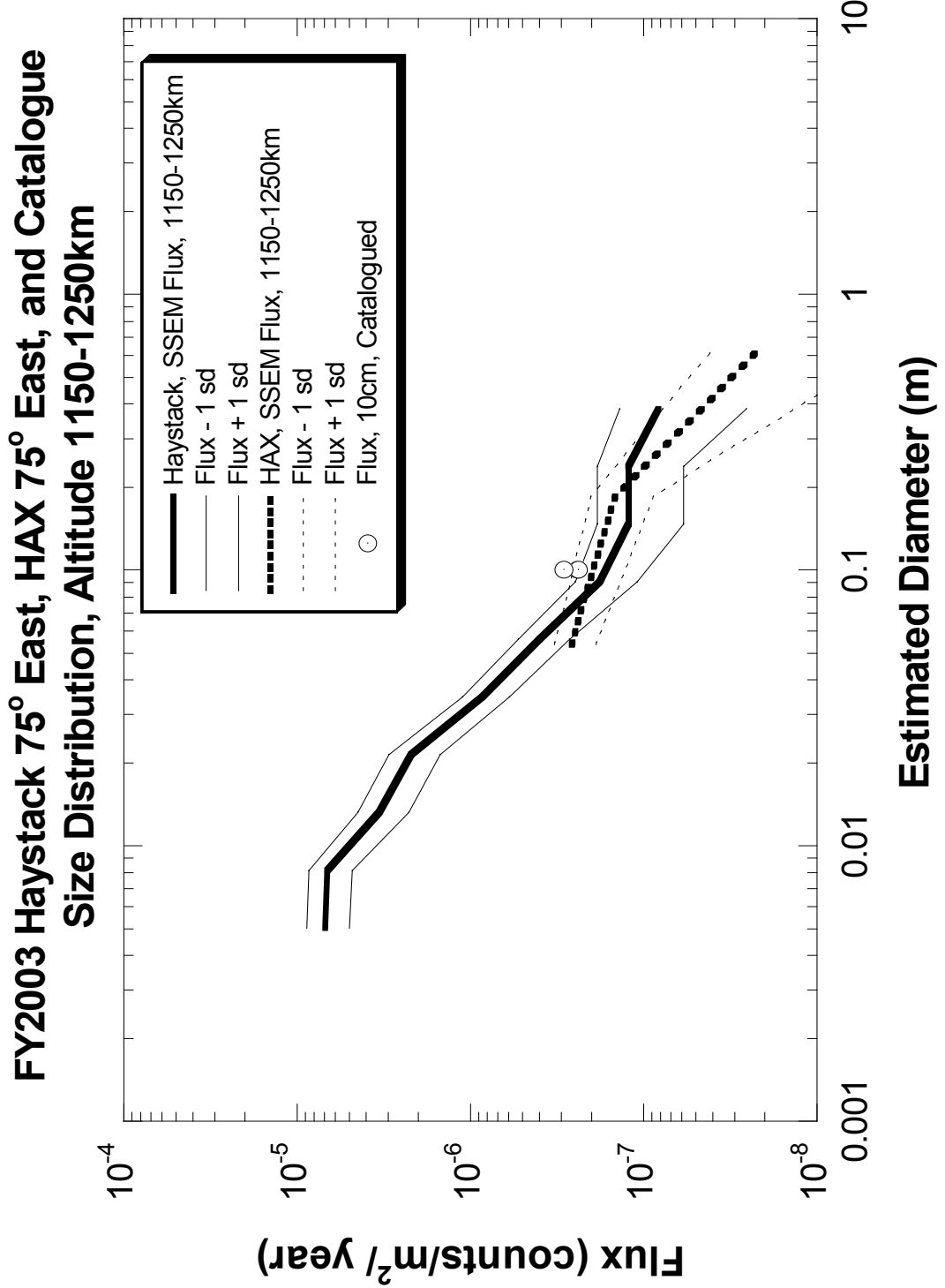


Figure 31. Haystack, HAX, and the 10 cm Catalogue Flux versus Diameter for 1150-1250 km Altitude.

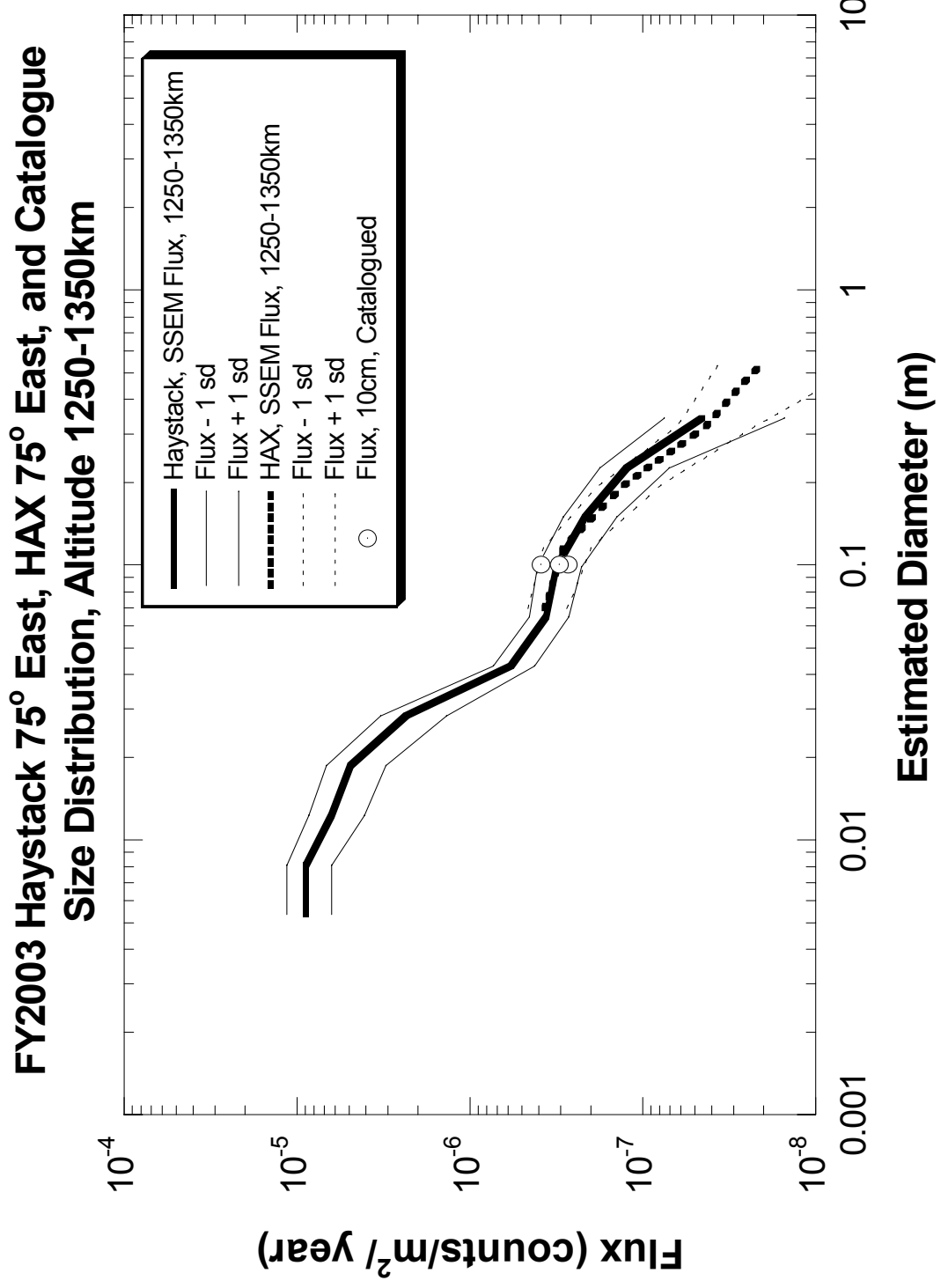


Figure 32. Haystack, HAX, and the 10 cm Catalogue Flux versus Diameter for 1250-1350 km Altitude.

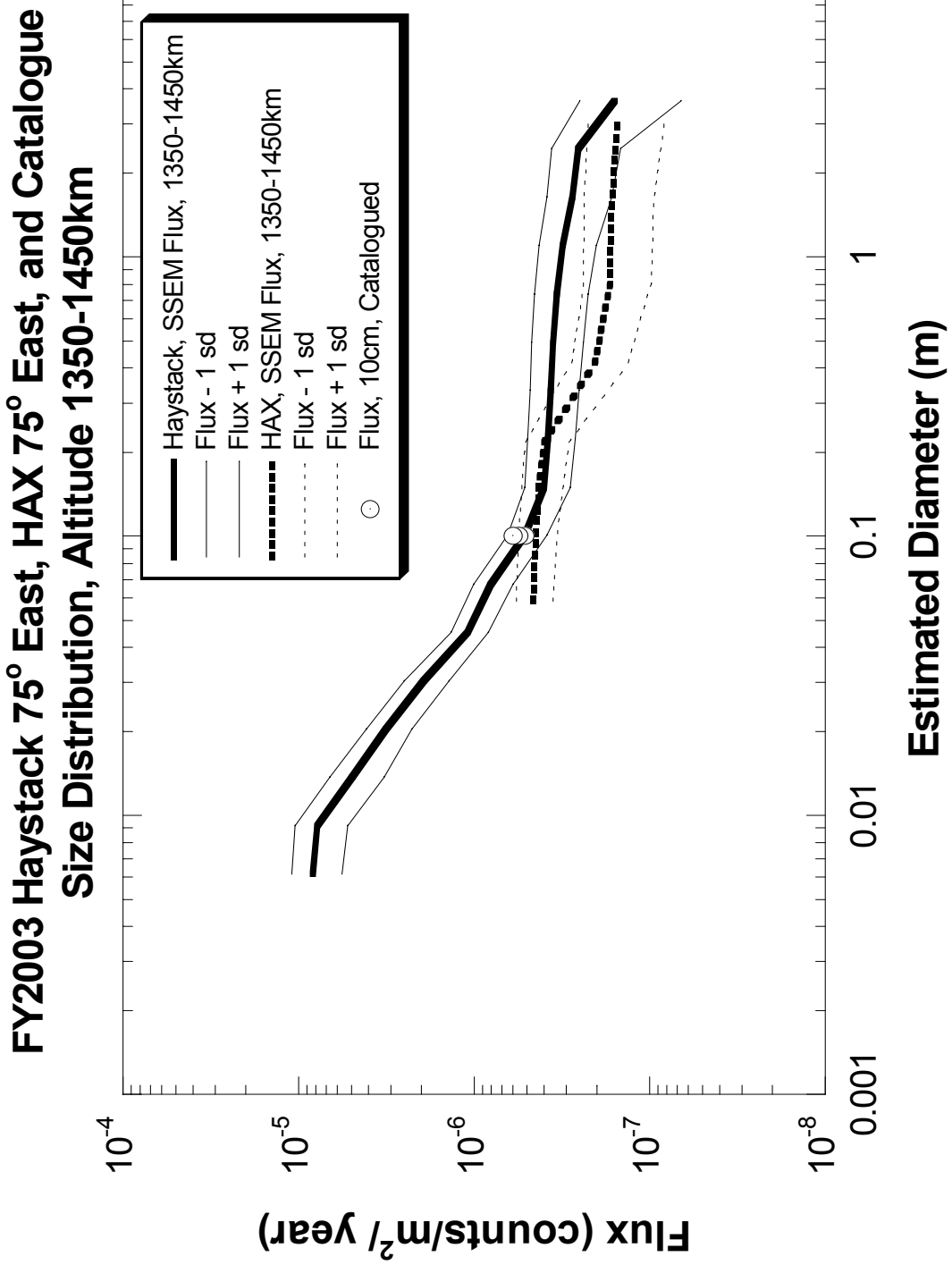


Figure 33. Haystack, HAX, and the 10 cm Catalogue Flux versus Diameter for 1350-1450 km Altitude.

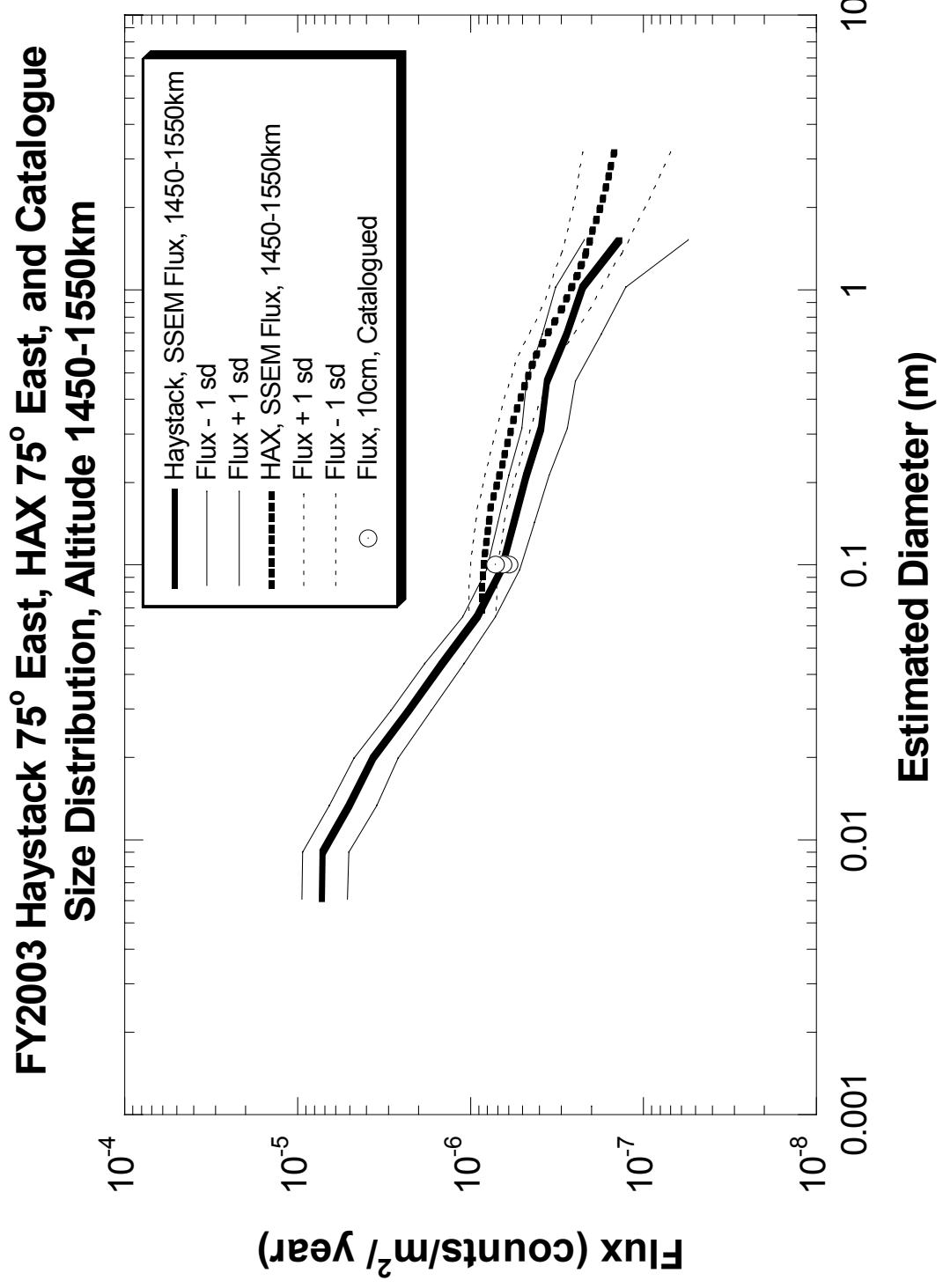


Figure 34. Haystack, HAX, and the 10 cm Catalogue Flux versus Diameter for 1450-1550 km Altitude.

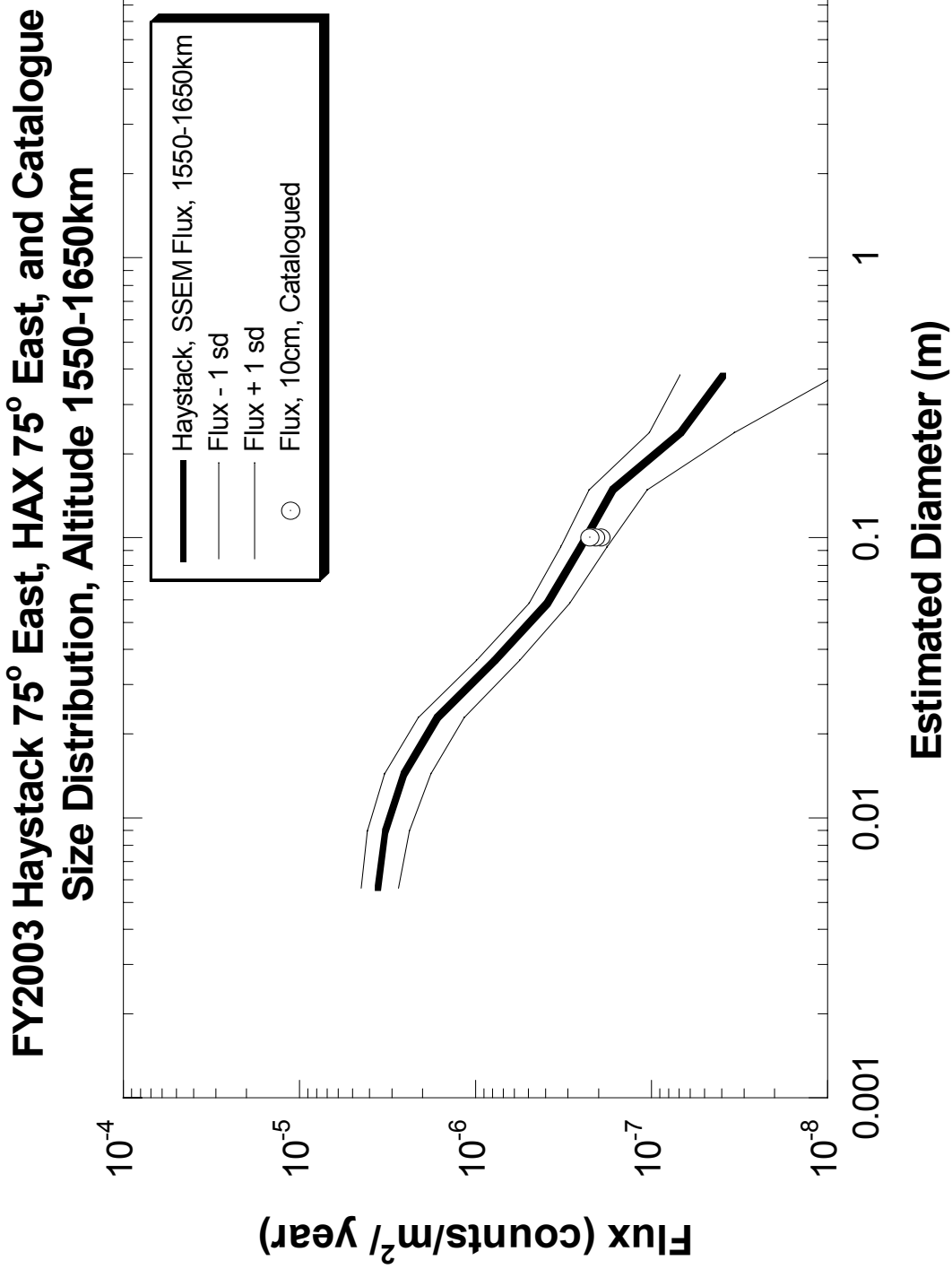


Figure 35. Haystack, HAX, and the 10 cm Catalogue Flux versus Diameter for 1550-1650 km Altitude.

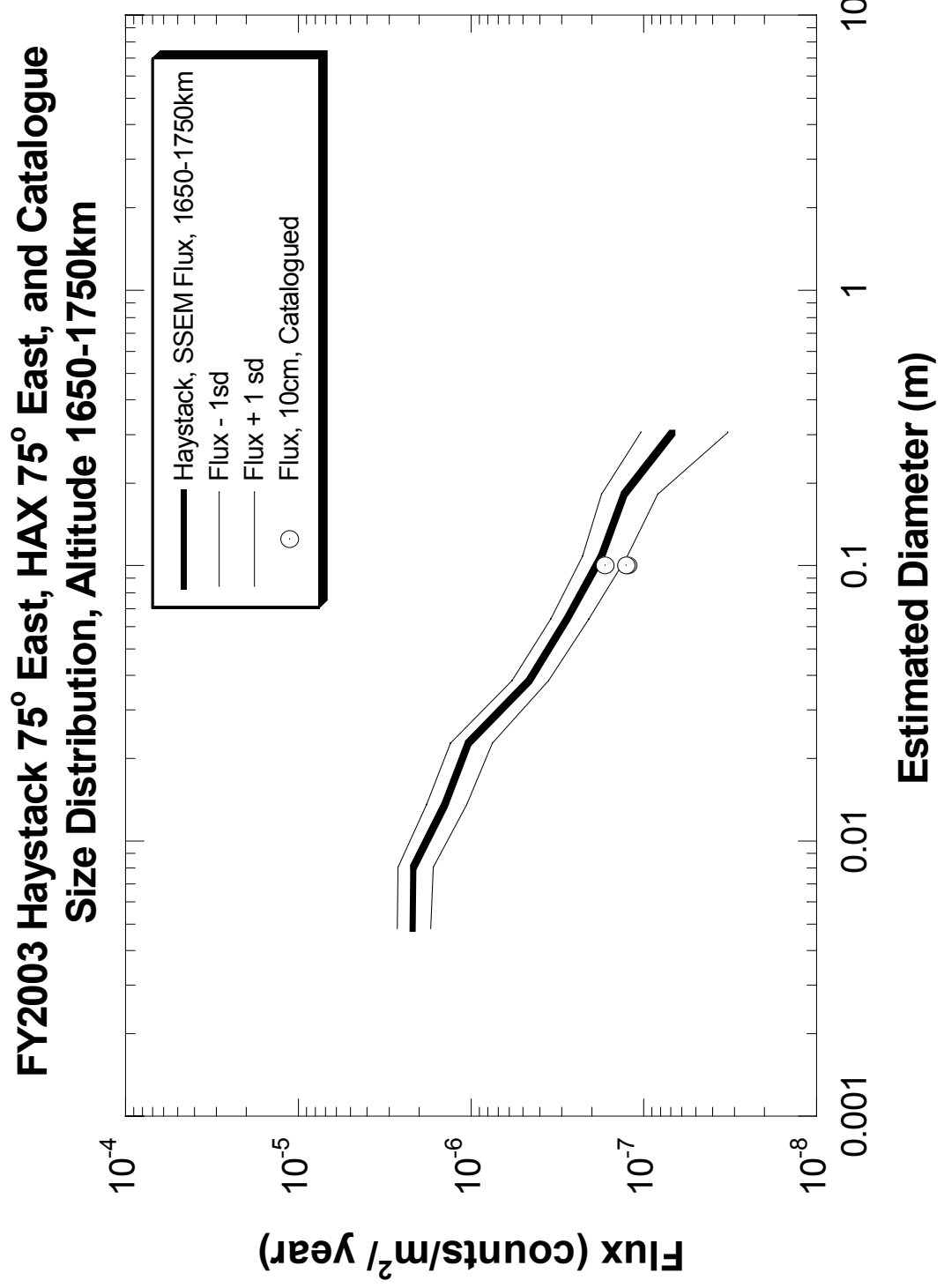


Figure 36. Haystack, HAX, and the 10 cm Catalogue Flux versus Diameter for 1650-1750 km Altitude.

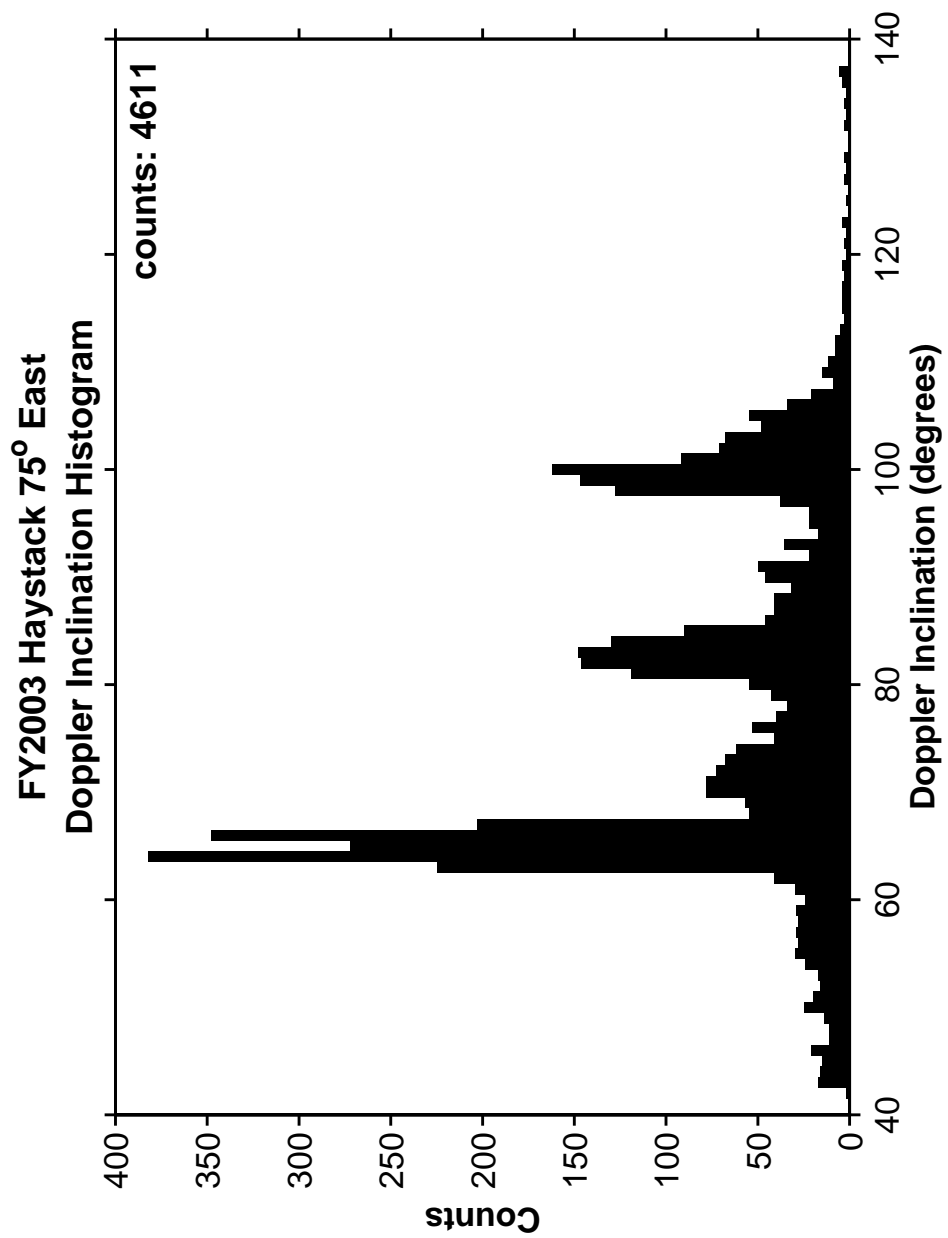


Figure 37. Haystack Doppler Inclination Histogram.

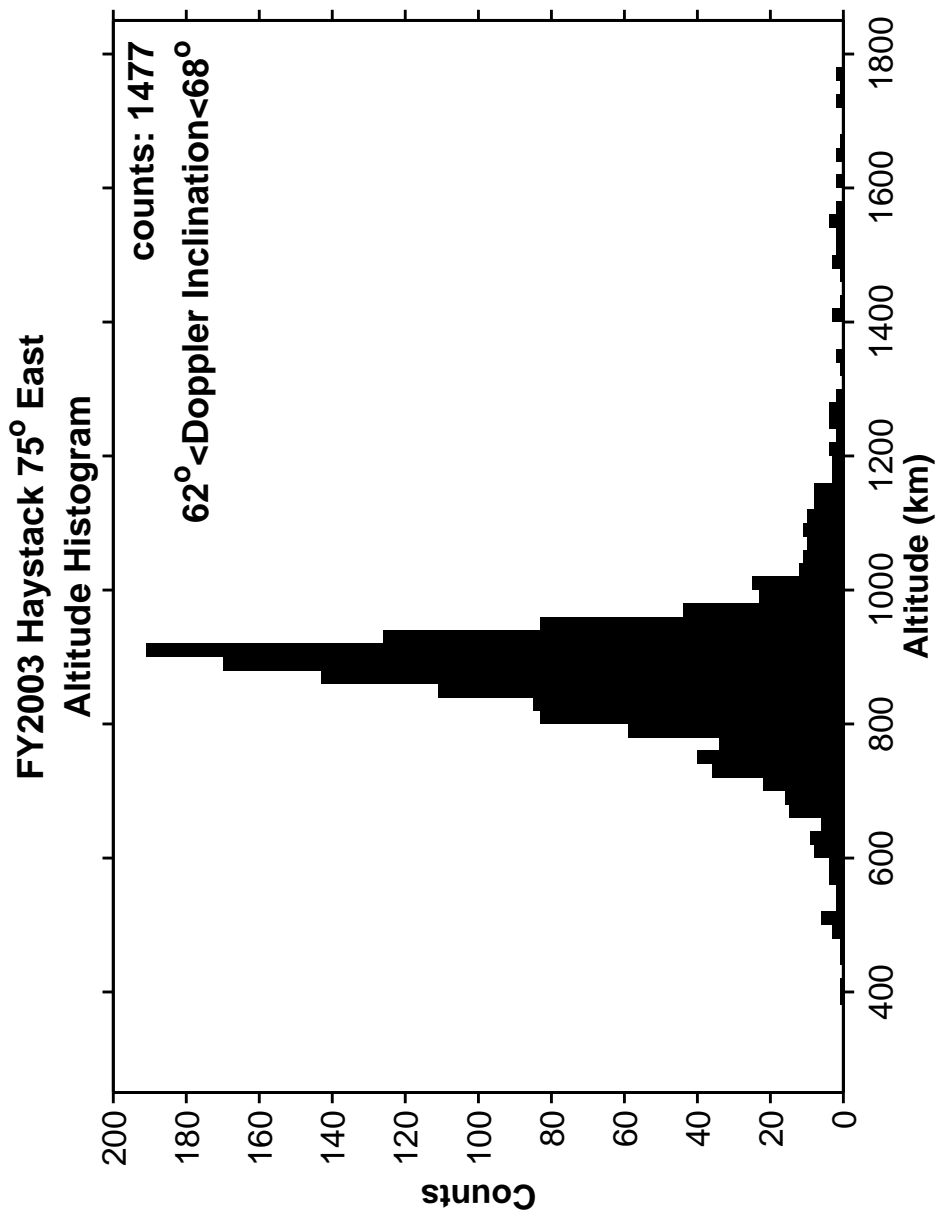


Figure 38. Haystack Altitude Histogram for Debris with Doppler Inclination between 62° and 68° .

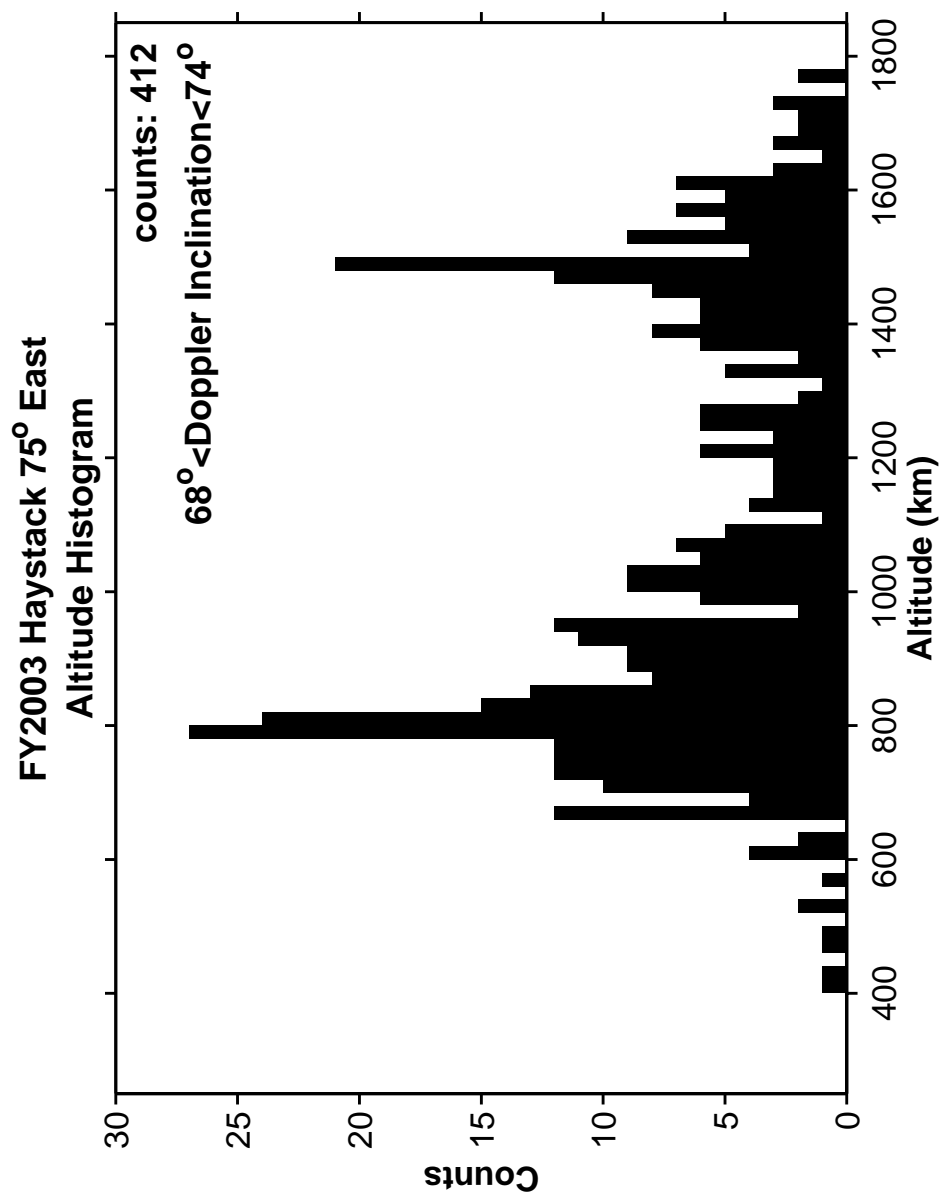


Figure 39. Haystack Altitude Histogram for Debris with Doppler Inclination between 68° and 74° .

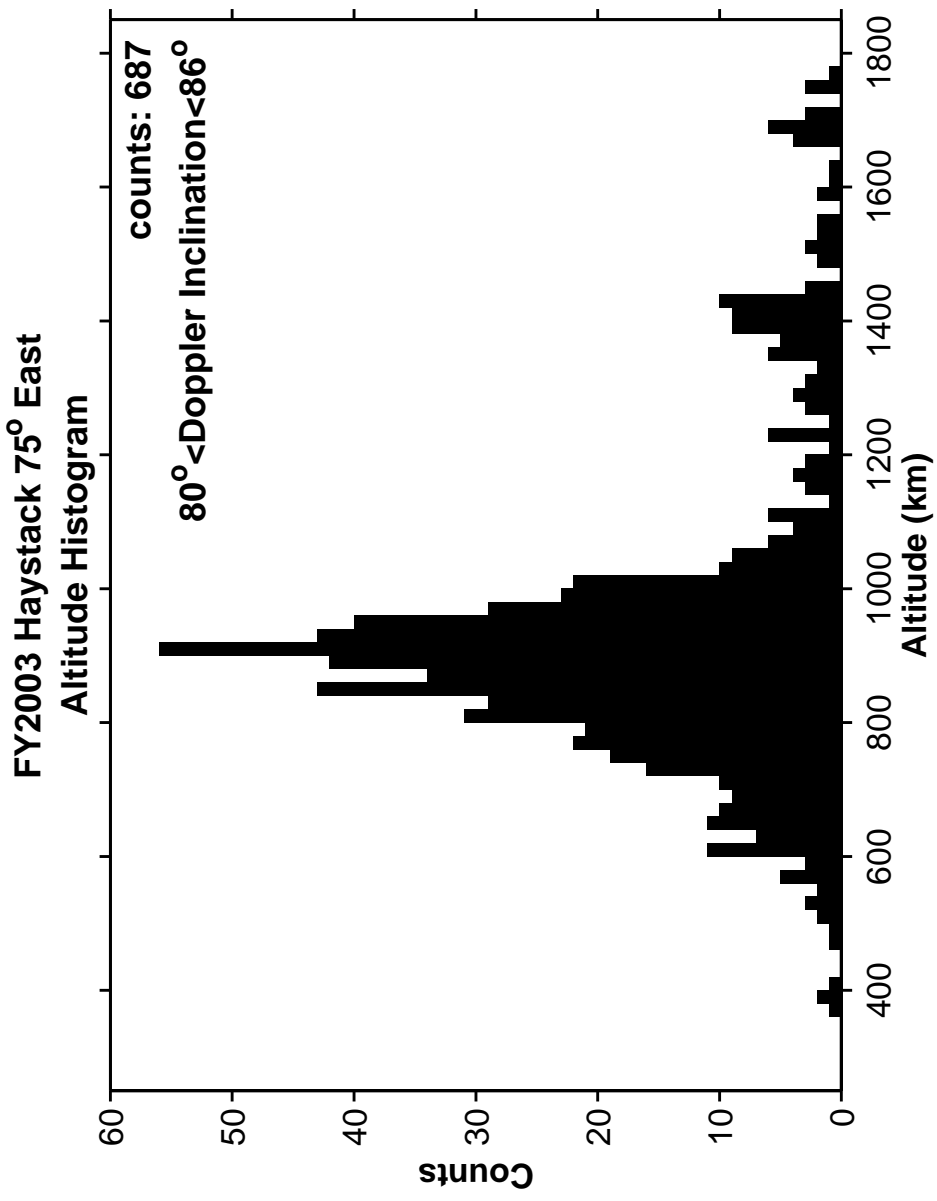
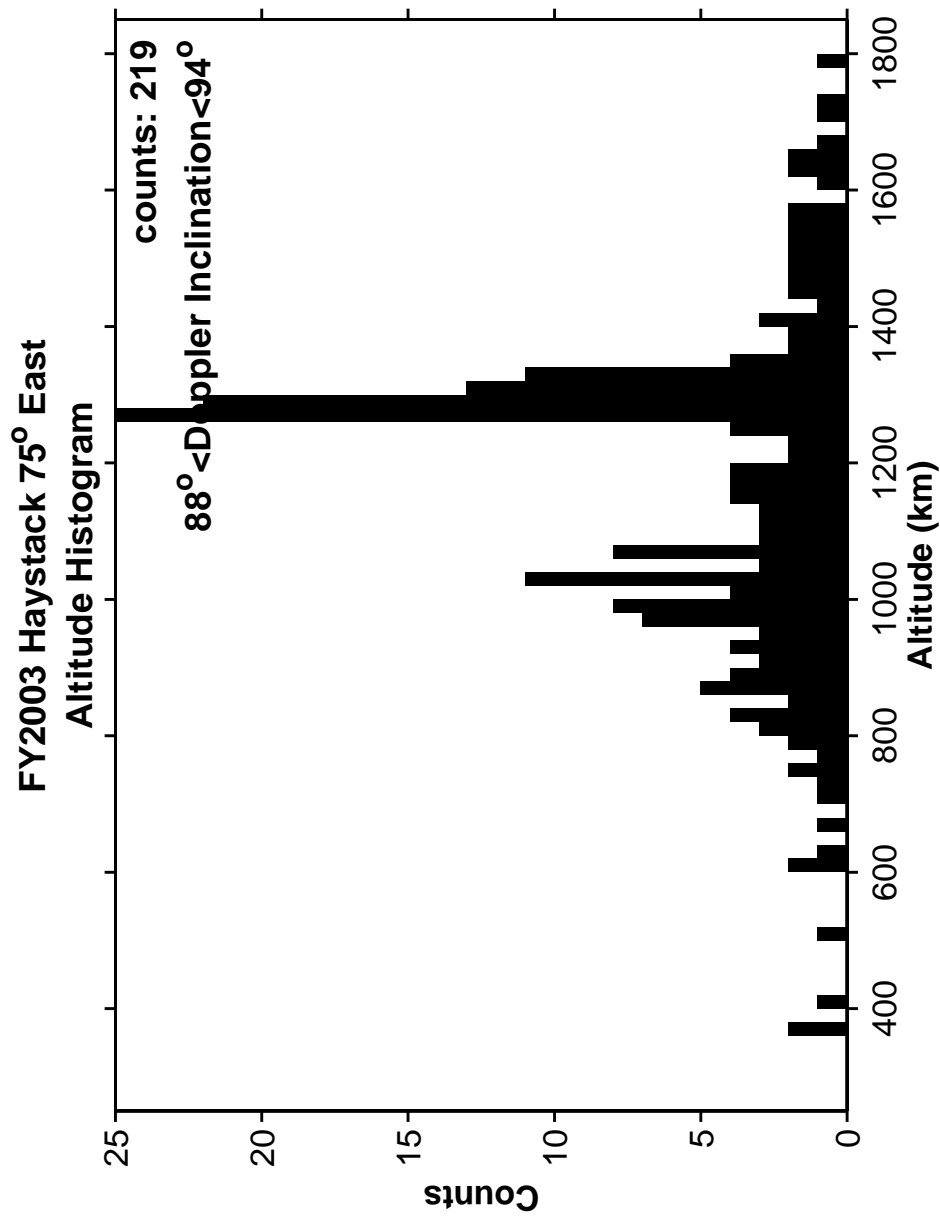


Figure 40. Haystack Altitude Histogram for Debris with Doppler Inclination between 80° and 86°.



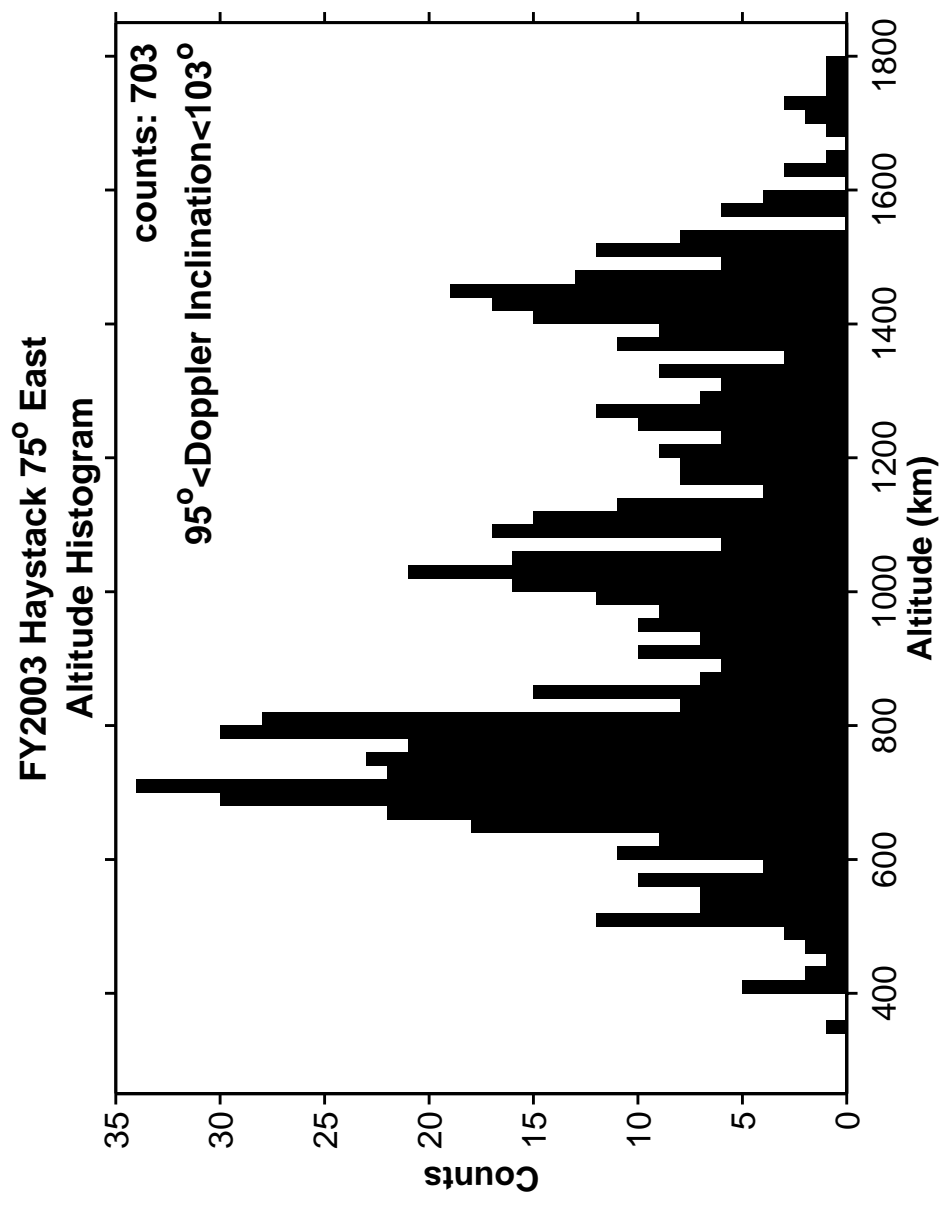


Figure 42. Haystack Altitude Histogram for Debris with Doppler Inclination between 95° and 103° .

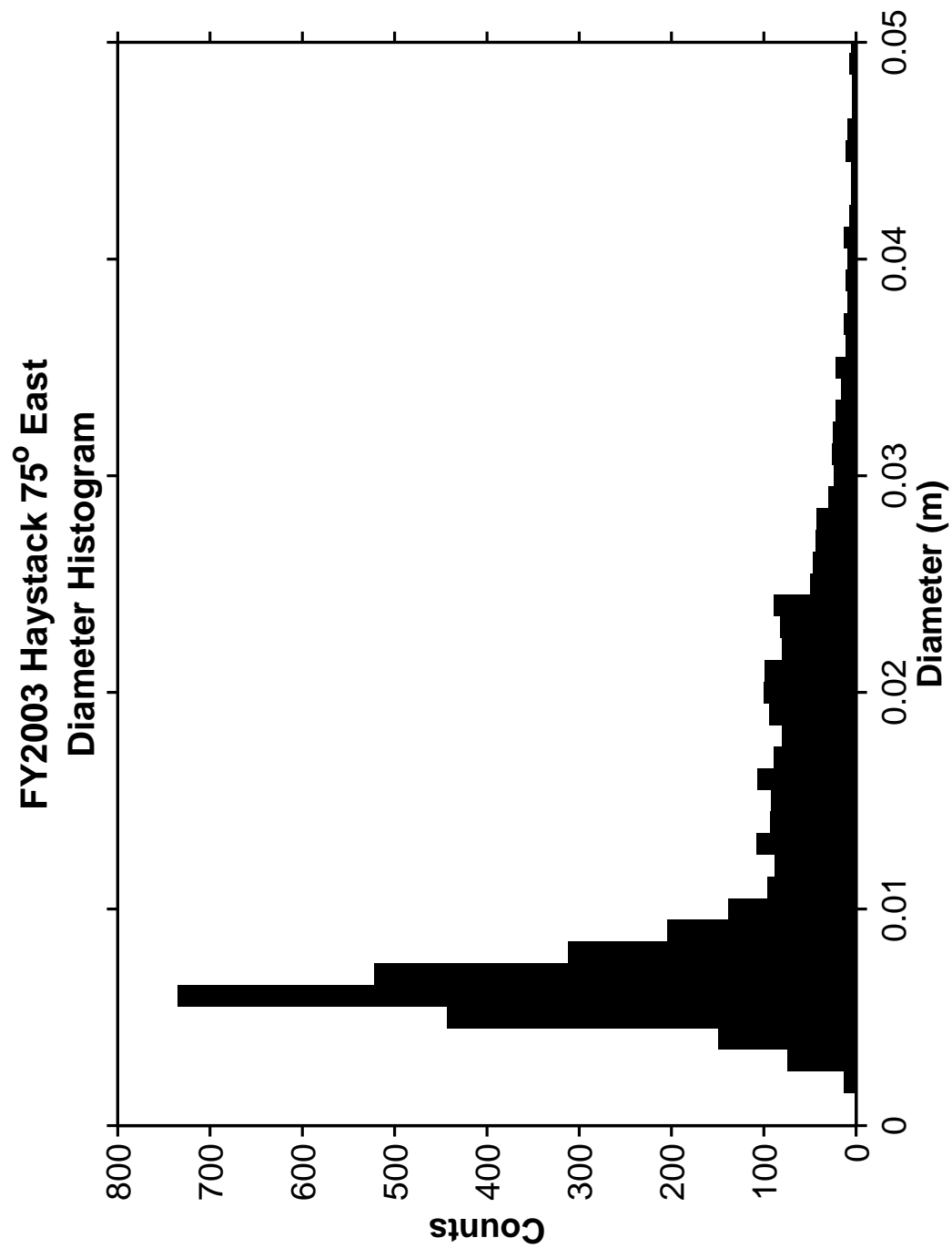


Figure 43. Haystack Diameter Histogram.

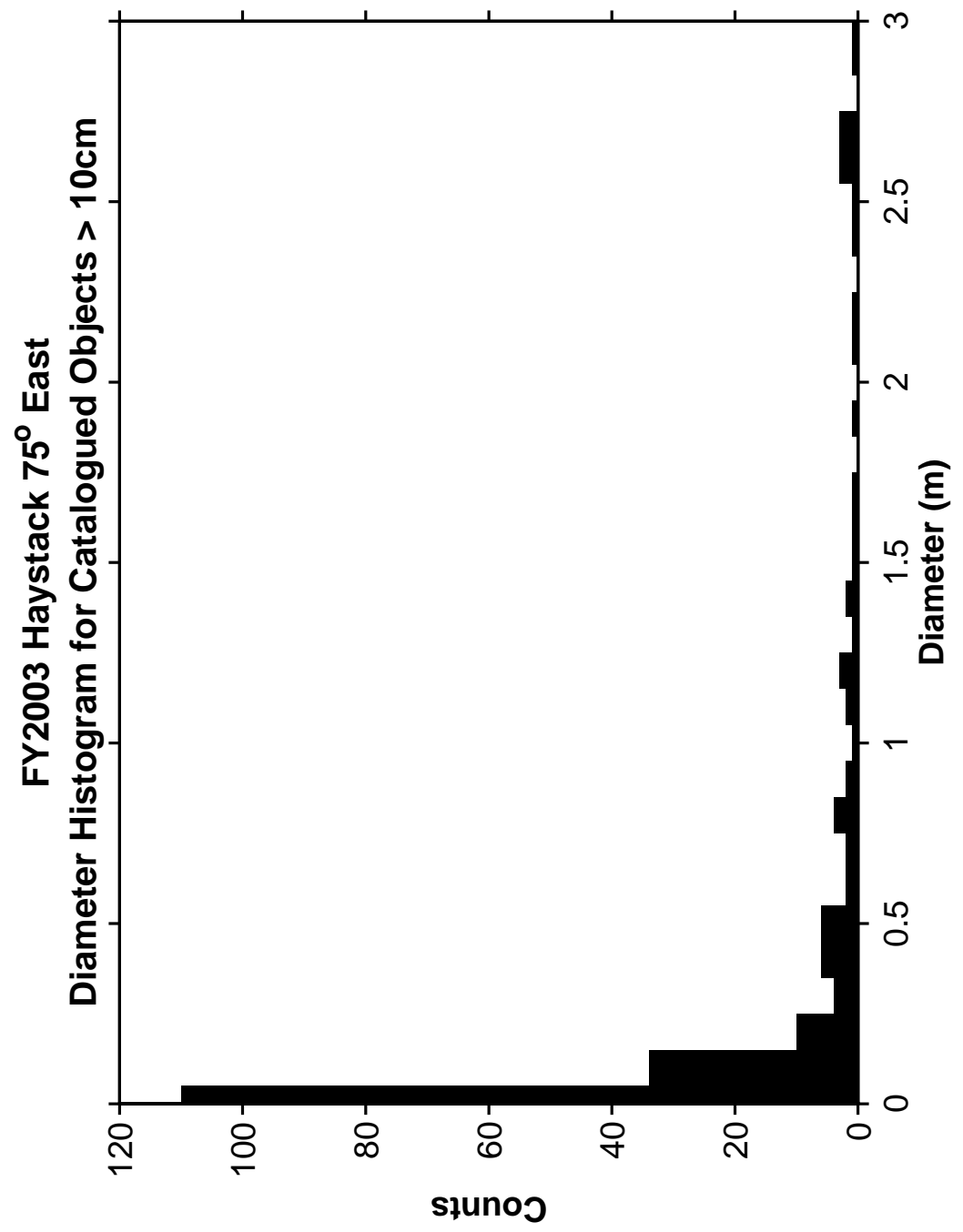


Figure 44. Haystack Diameter Histogram for Catalogued Objects.

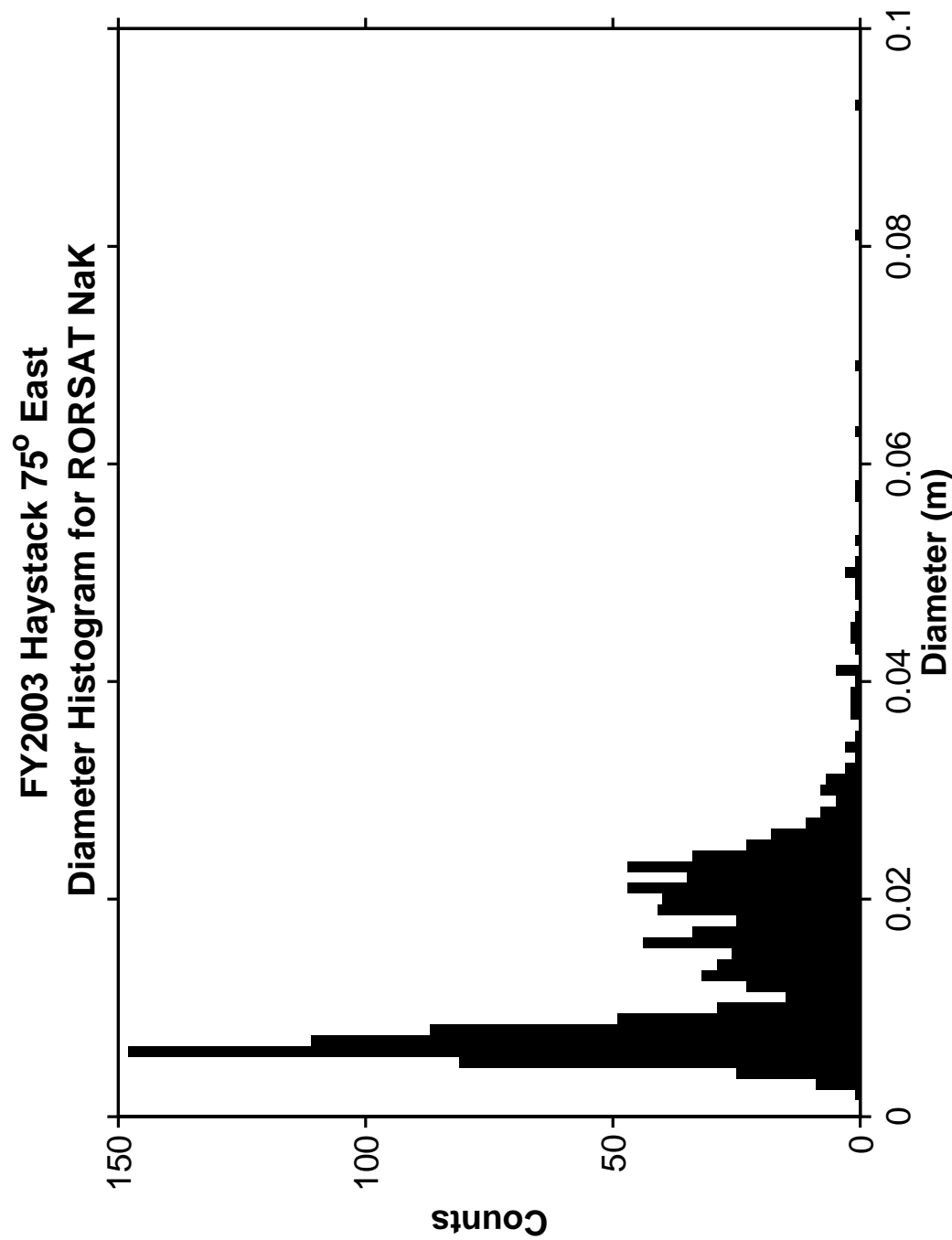


Figure 45. Haystack Diameter Histogram for RORSAT NaK Debris.

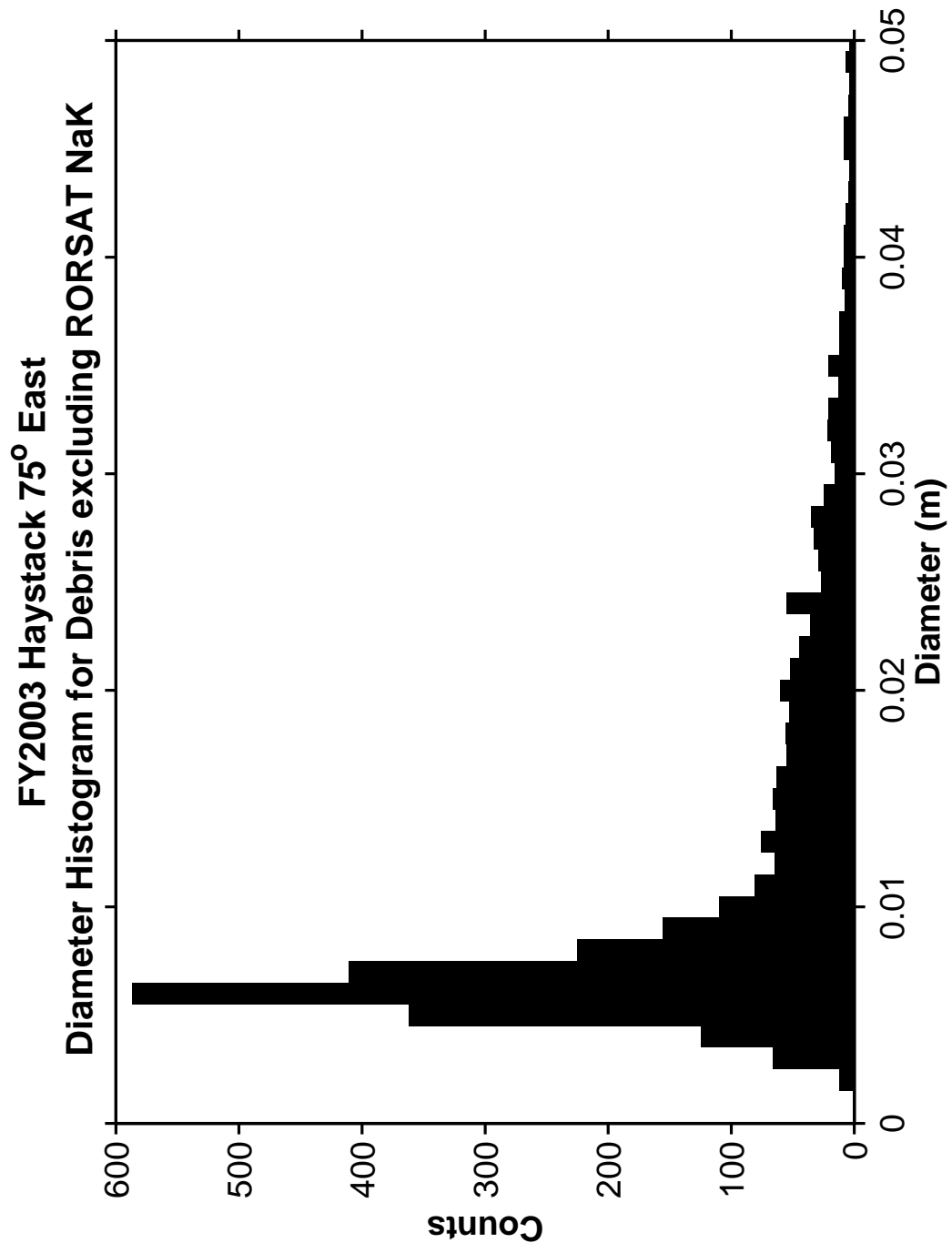


Figure 46. Haystack Diameter Histogram for Debris excluding RORSAT NaK Debris.

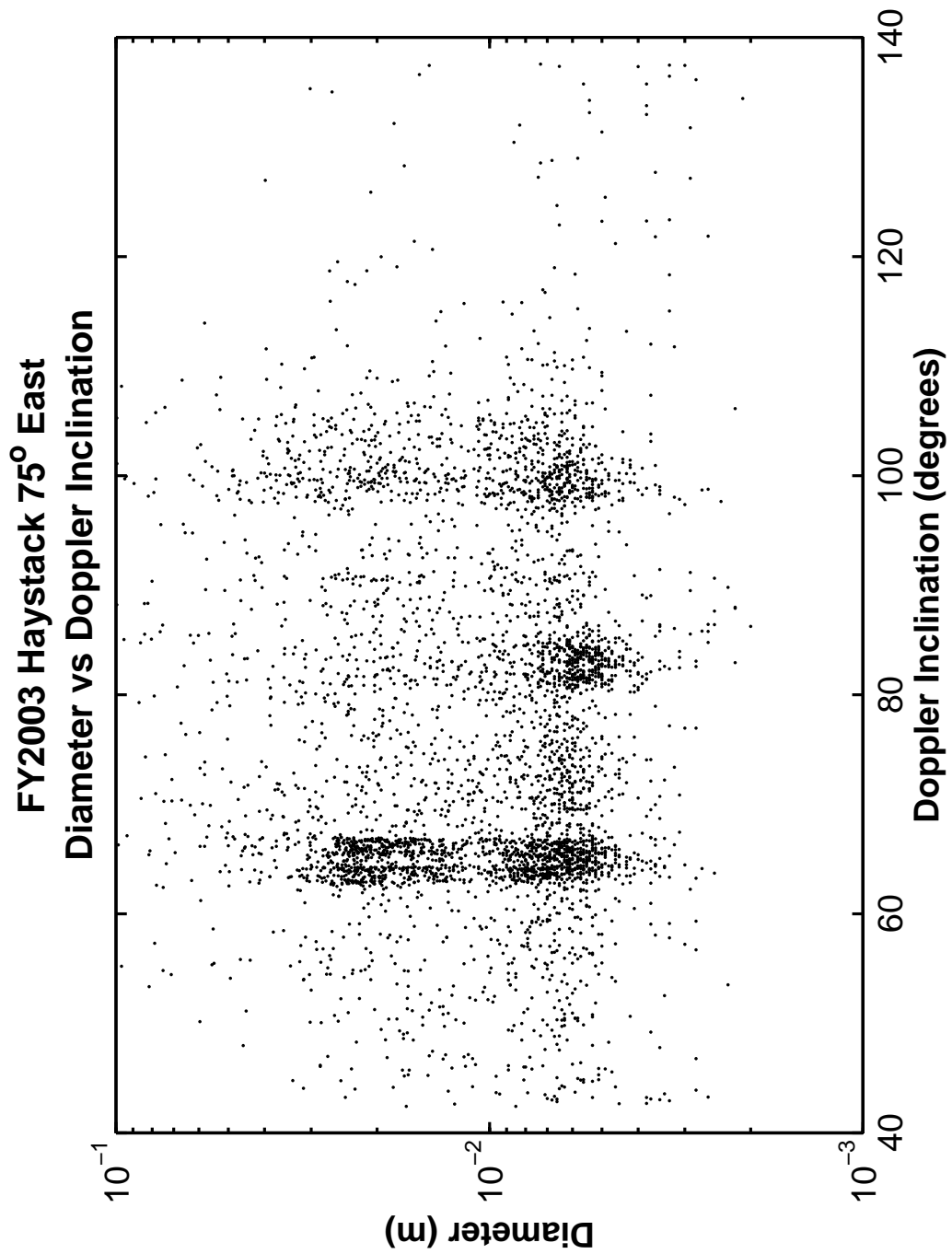


Figure 47. Haystack Diameter versus Doppler Inclination.

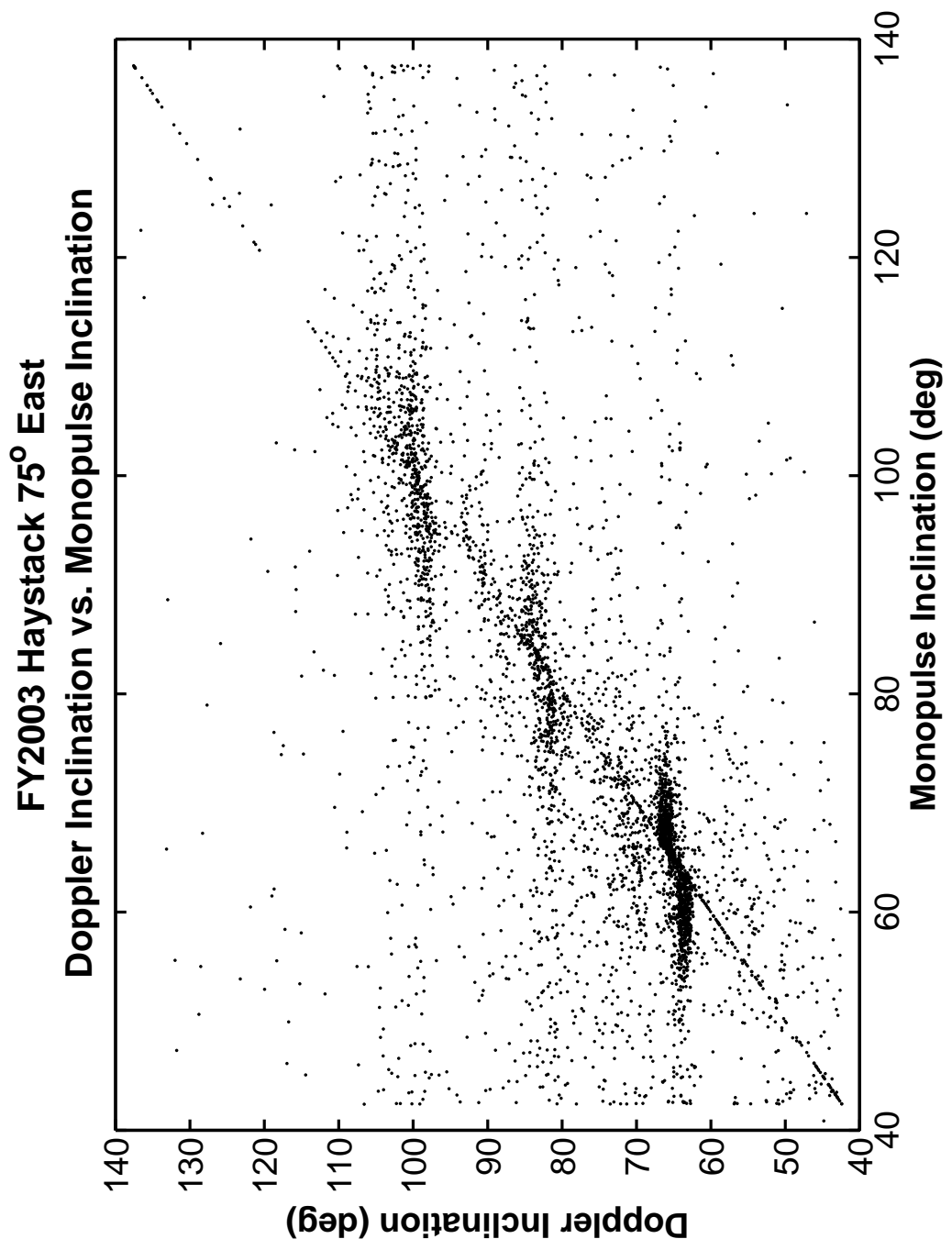


Figure 48. Haystack Doppler Inclination versus Monopulse Inclination.

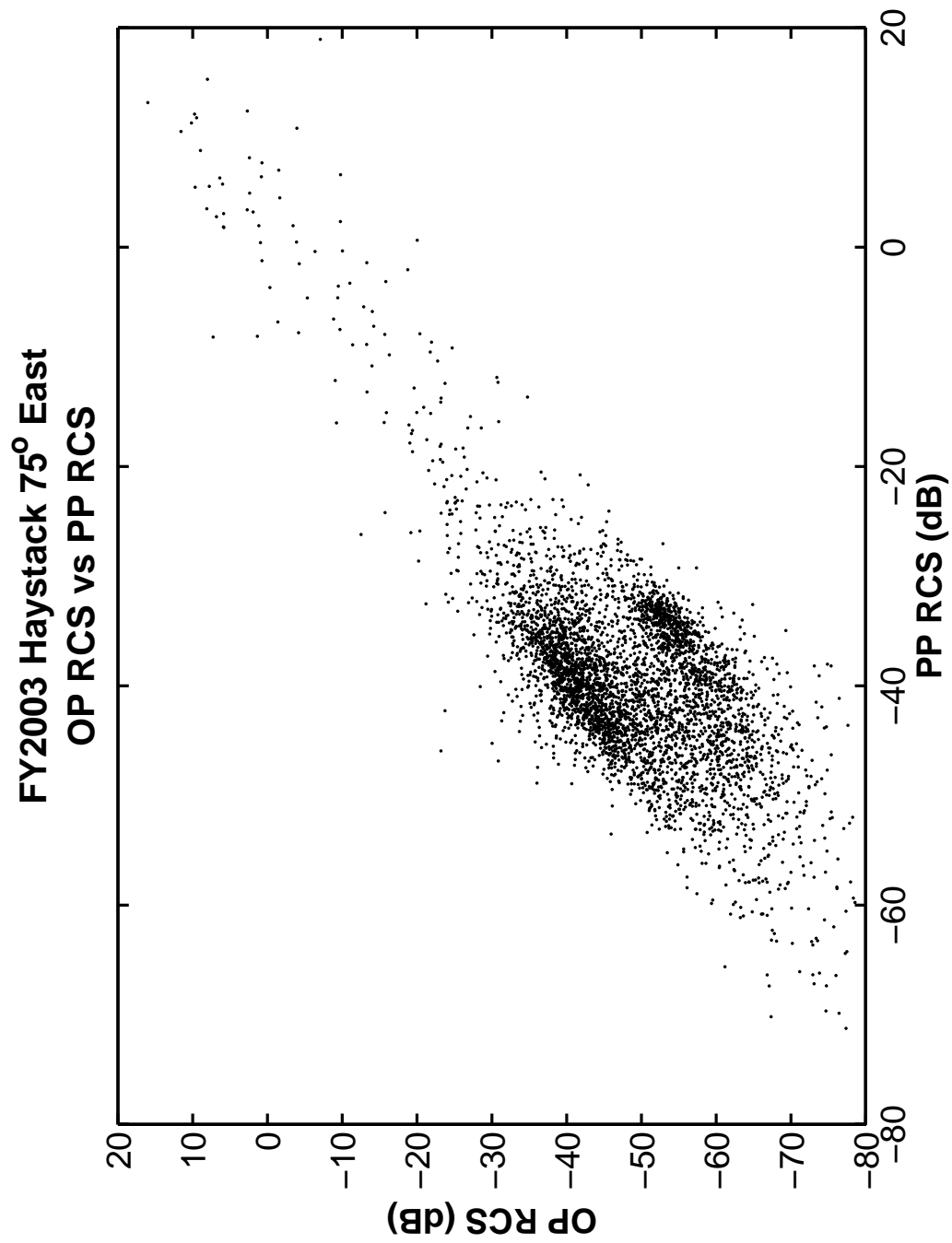


Figure 49. Haystack Orthogonal Polarization RCS versus Principal Polarization RCS.

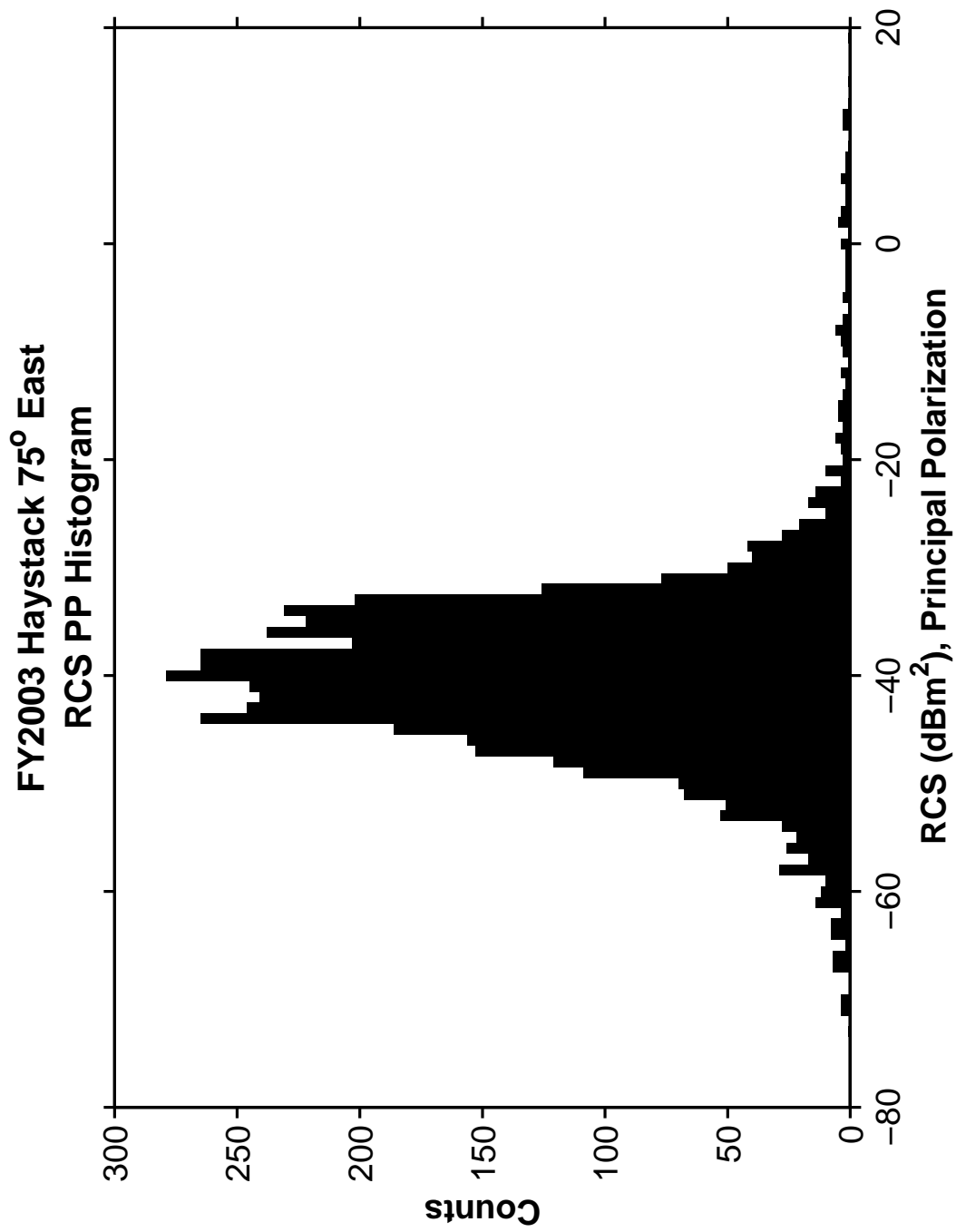


Figure 50. Haystack Principal Polarization RCS Histogram.

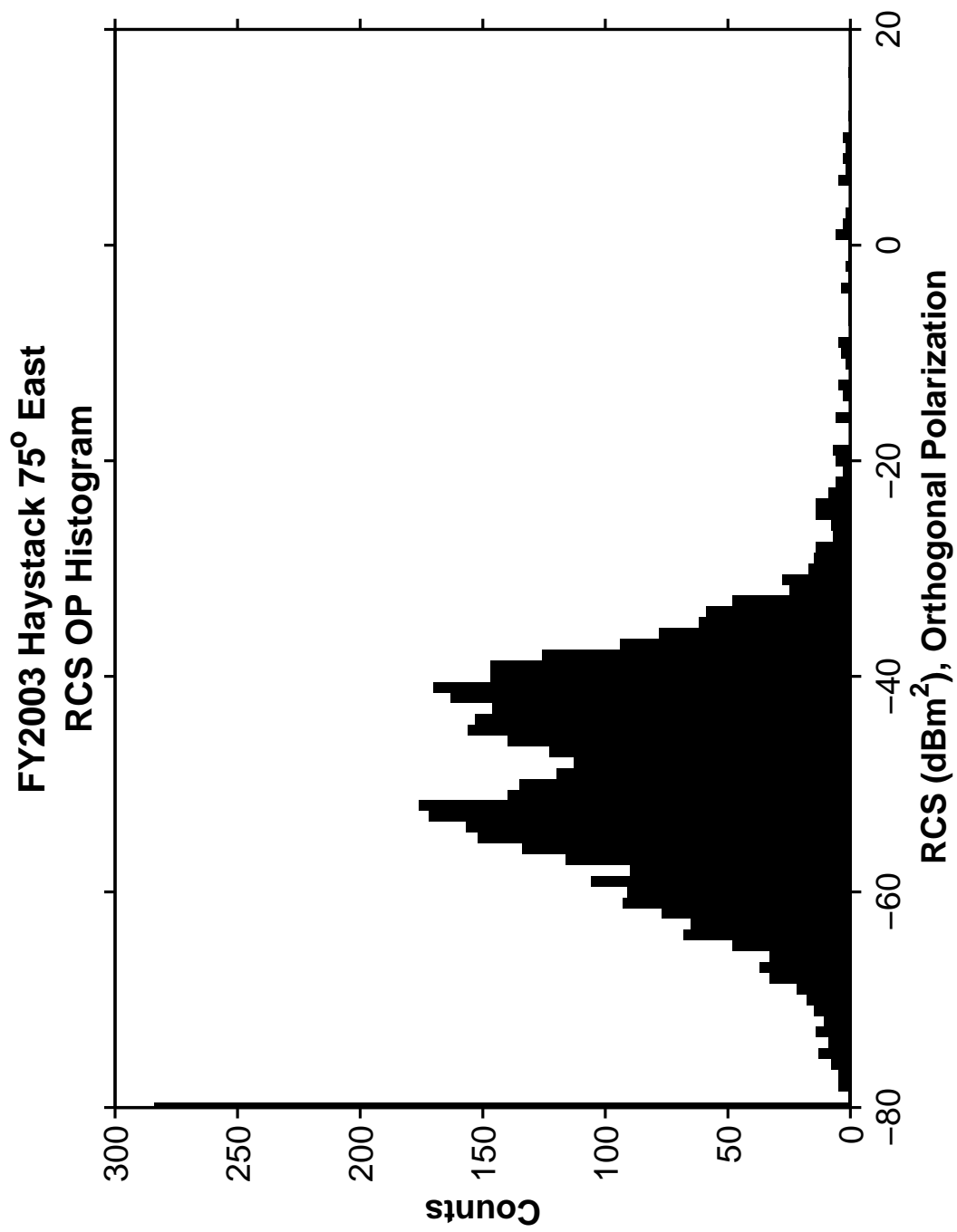


Figure 51. Haystack Orthogonal Polarization Histogram.

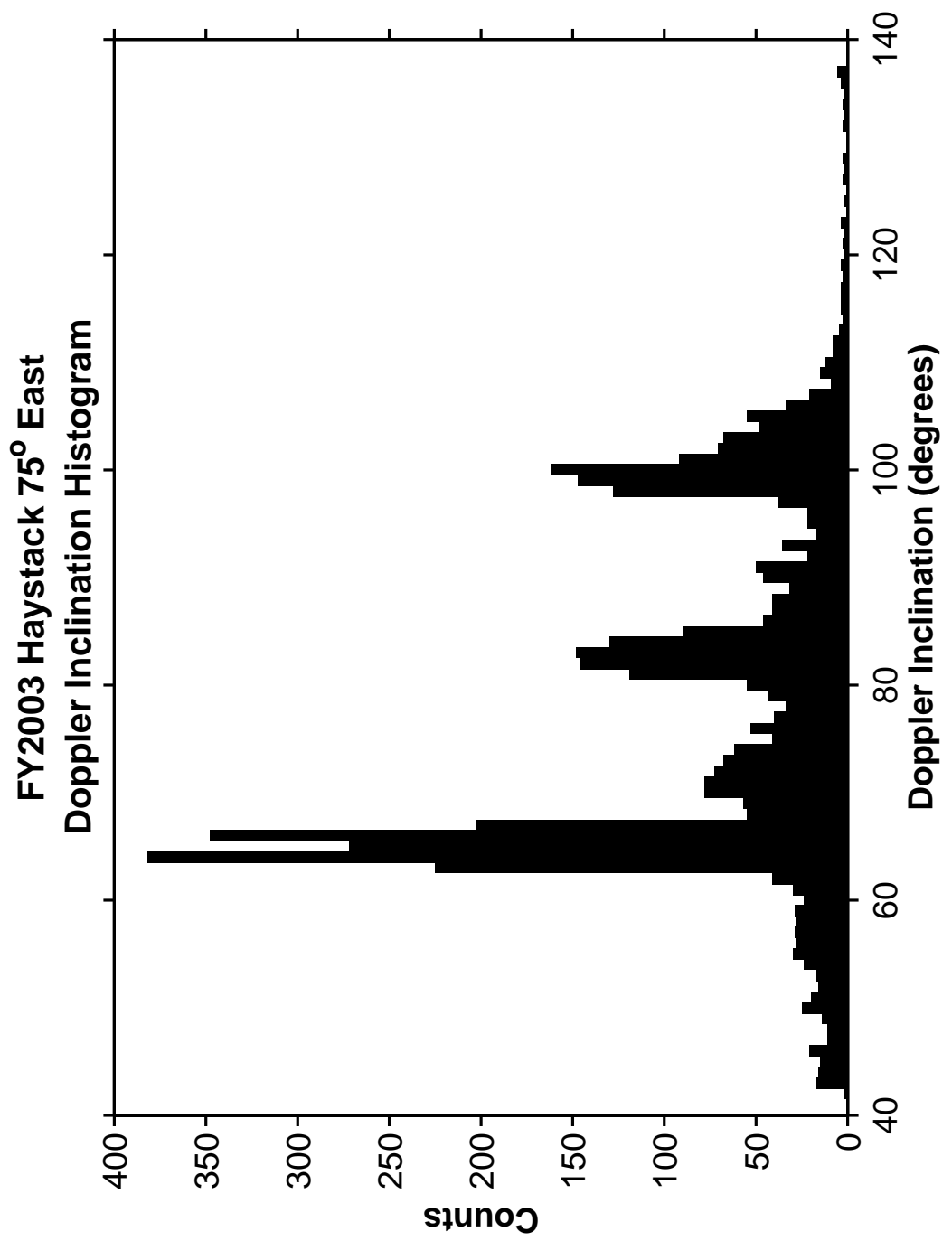


Figure 52. Haystack Doppler Inclination Histogram.

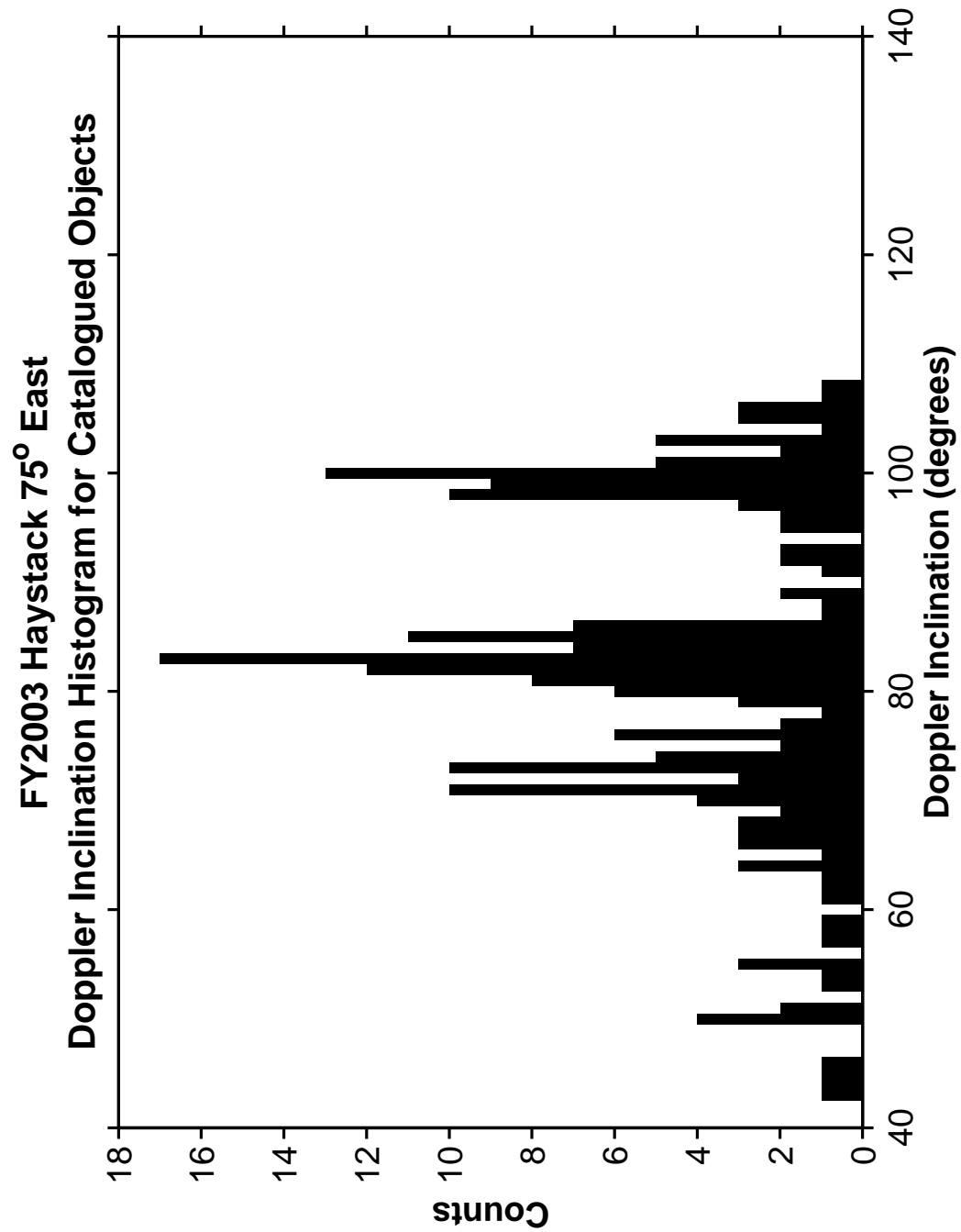


Figure 53. Haystack Doppler Inclination Histogram for Catalogued Objects.

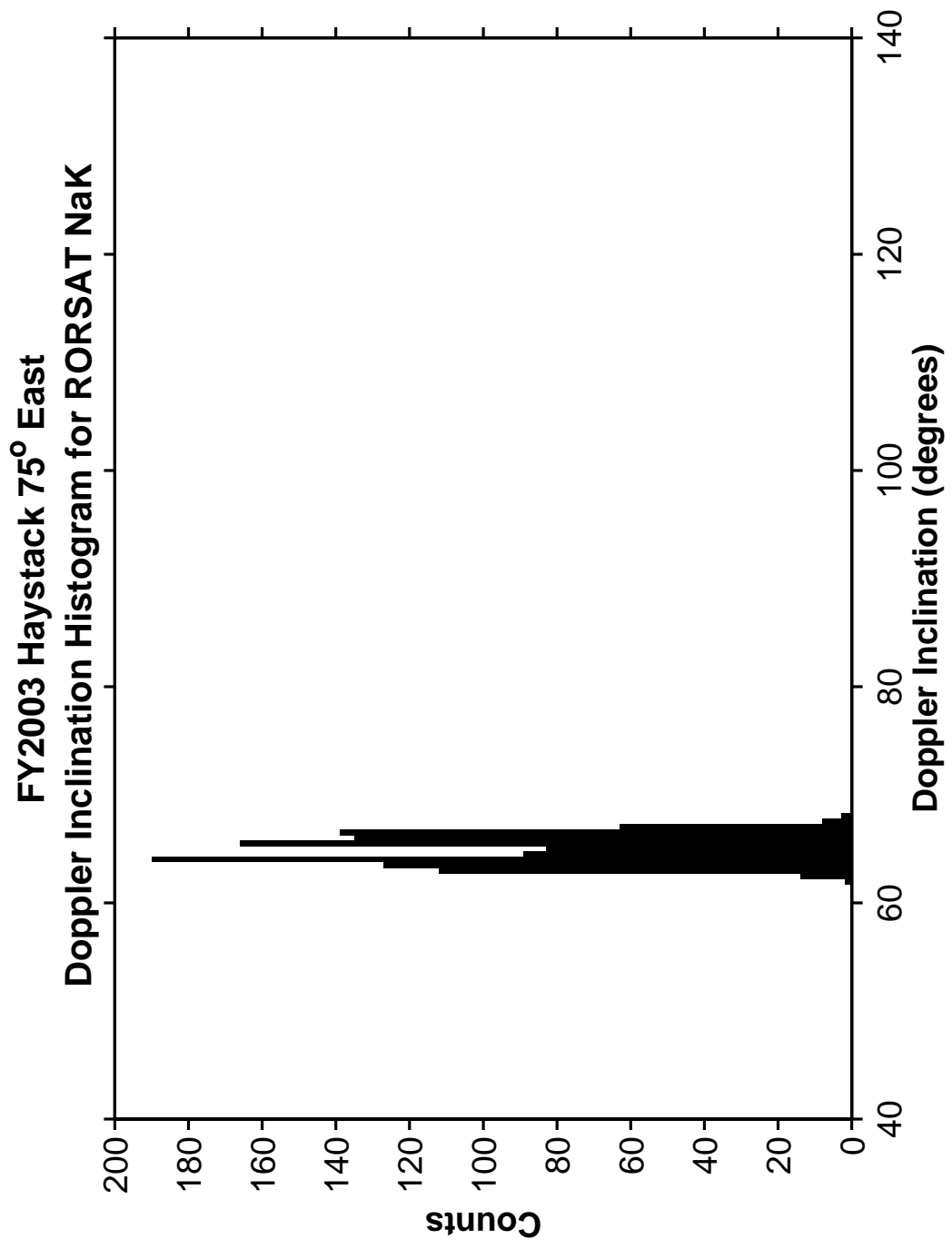


Figure 54. Haystack Doppler Inclination Histogram for RORSAT Nak.

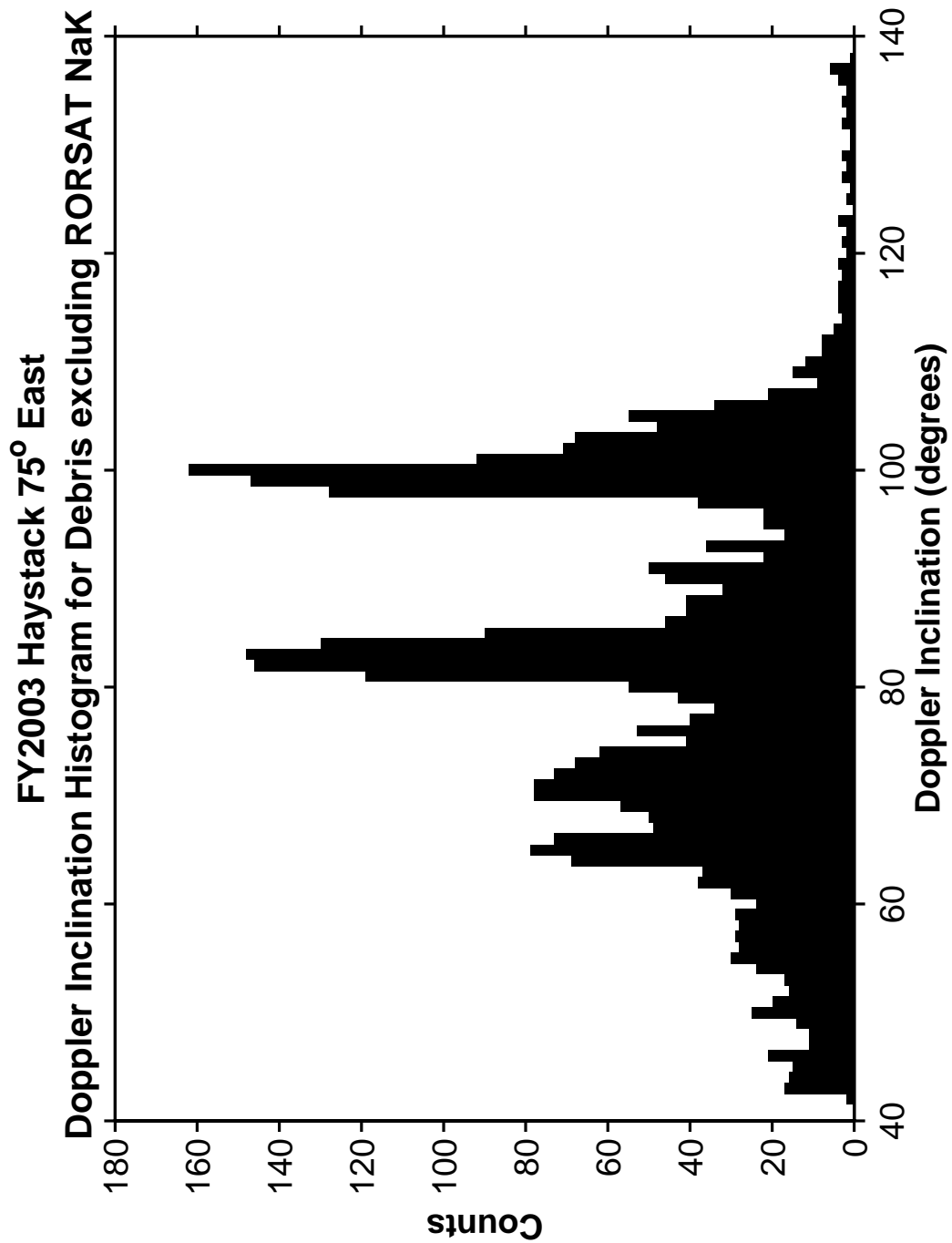


Figure 55. Haystack Doppler Inclination Histogram excluding RORSAT Nak Debris.

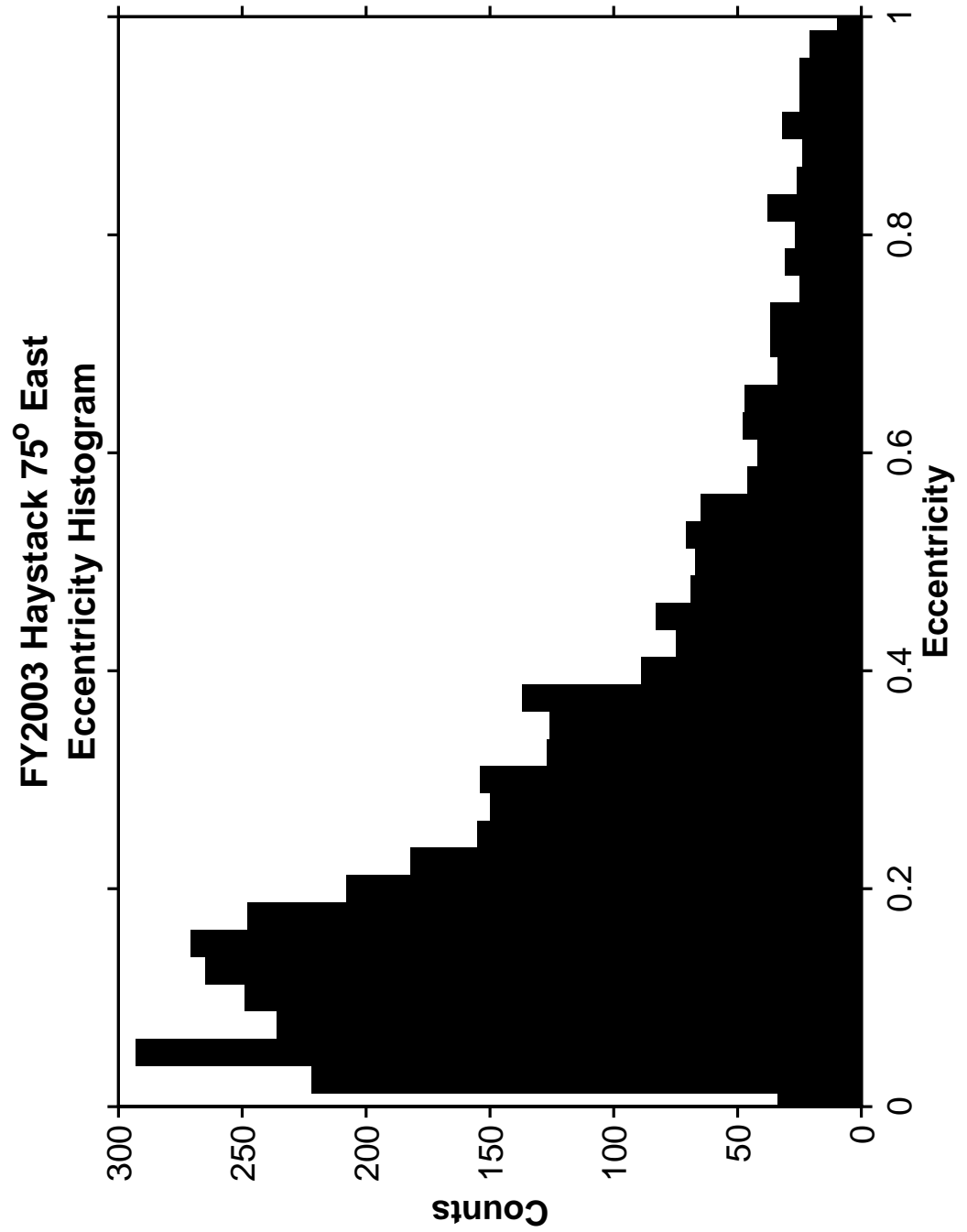


Figure 56. Haystack Eccentricity Histogram.

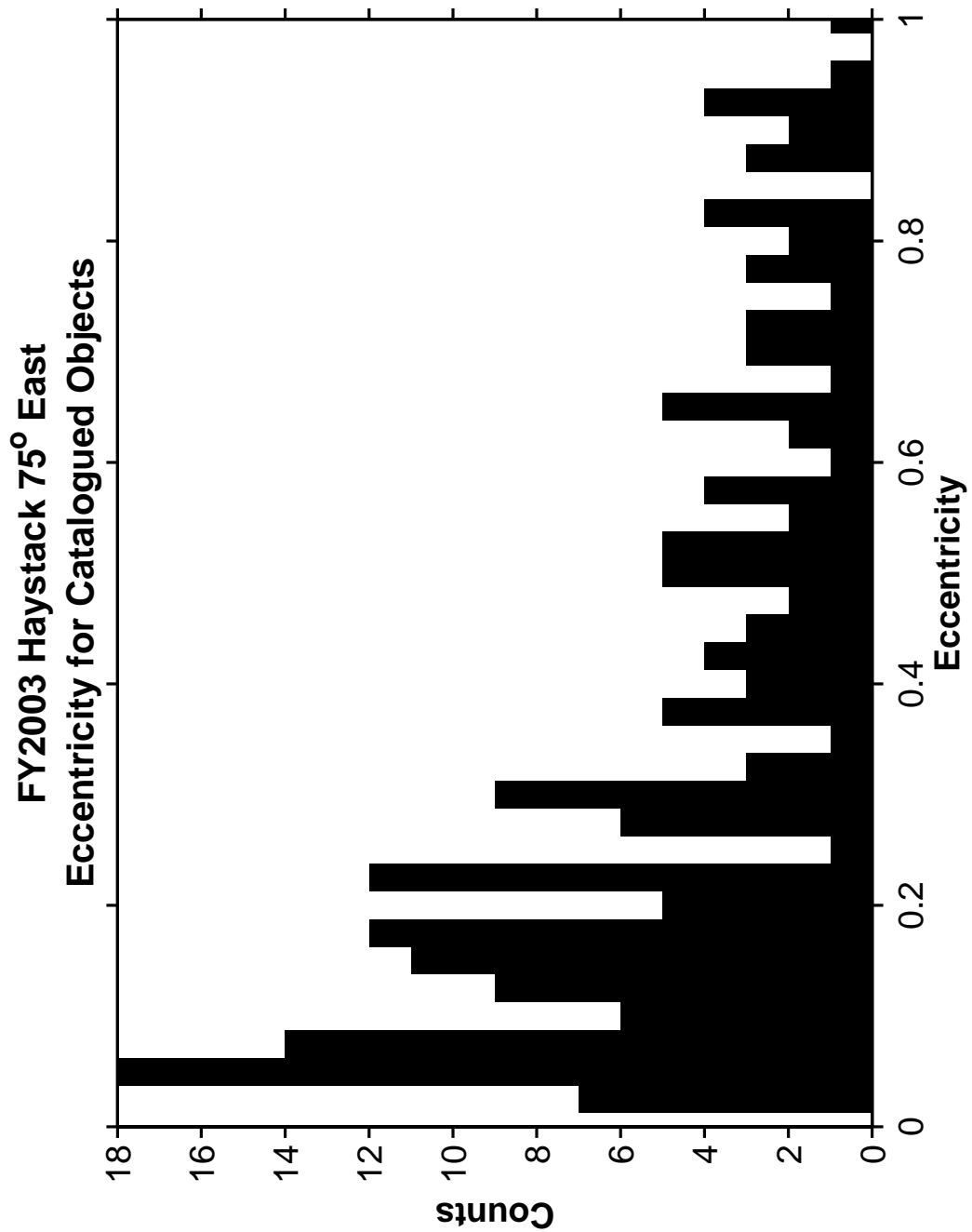


Figure 57. Haystack Eccentricity Histogram for Catalogued Objects.

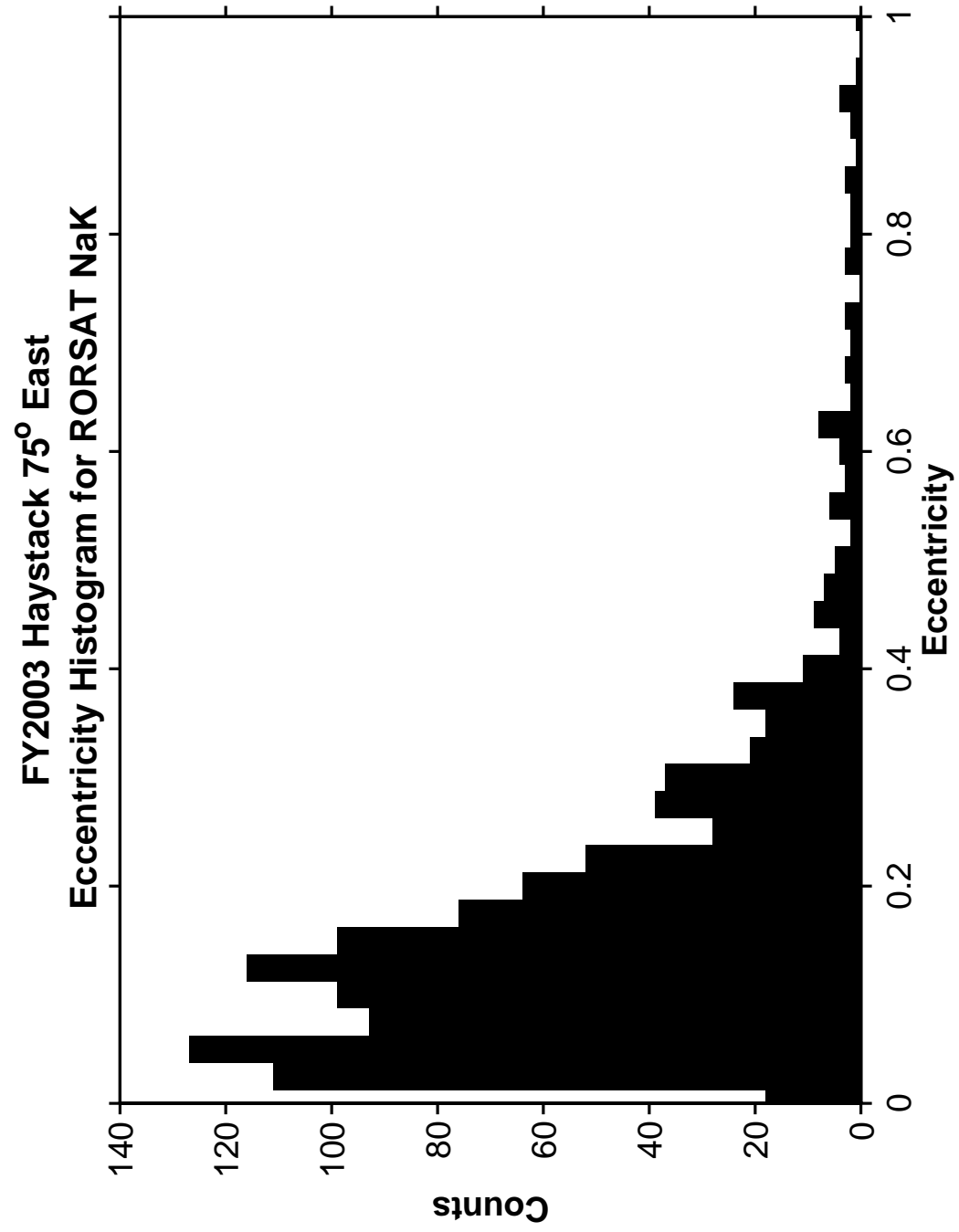


Figure 58. Haystack Eccentricity Histogram for RORSAT Nak.

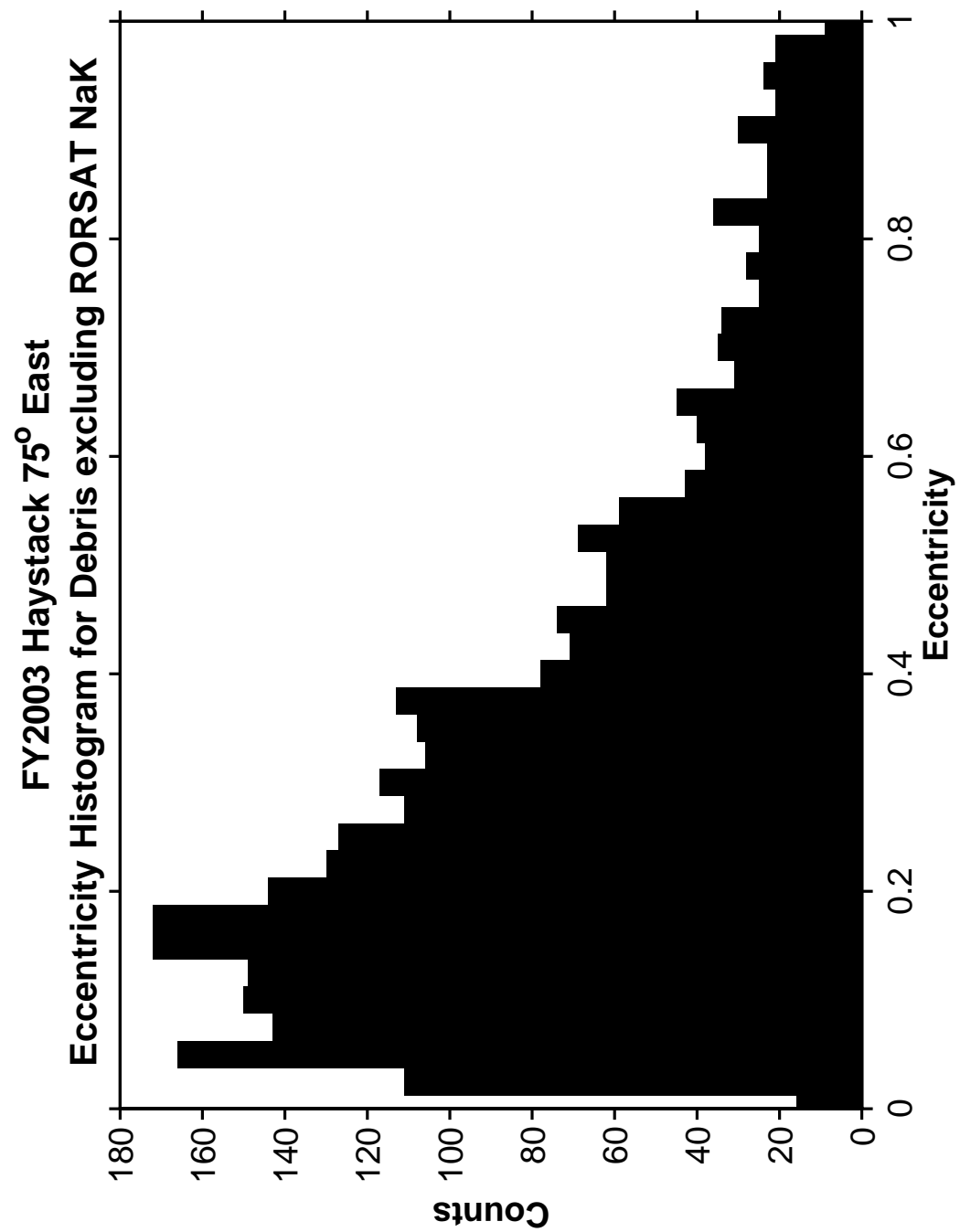


Figure 59. Haystack Eccentricity Histogram excluding RORSAT Nak Debris.

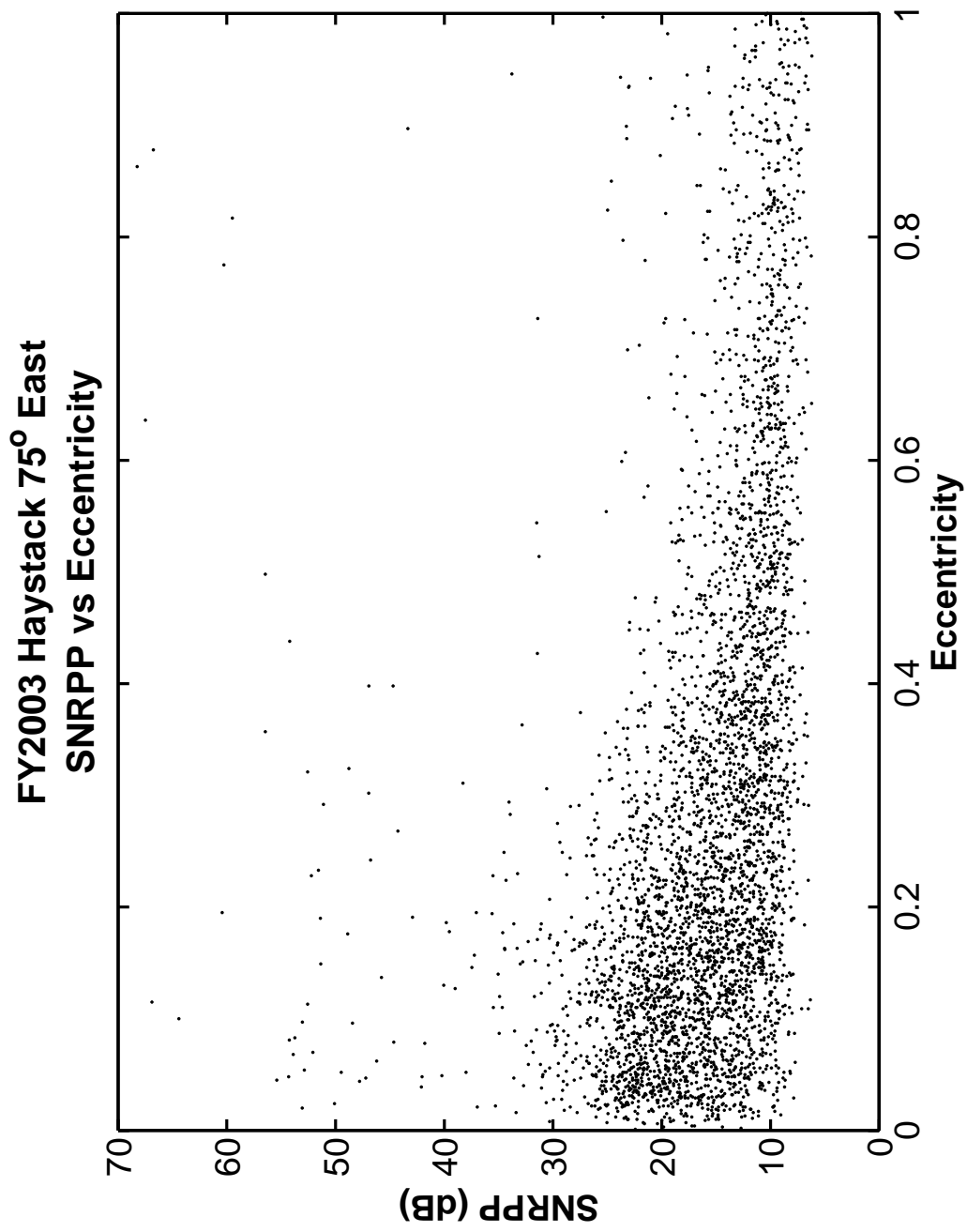


Figure 60. Haystack Principal Polarization SNR versus Eccentricity.

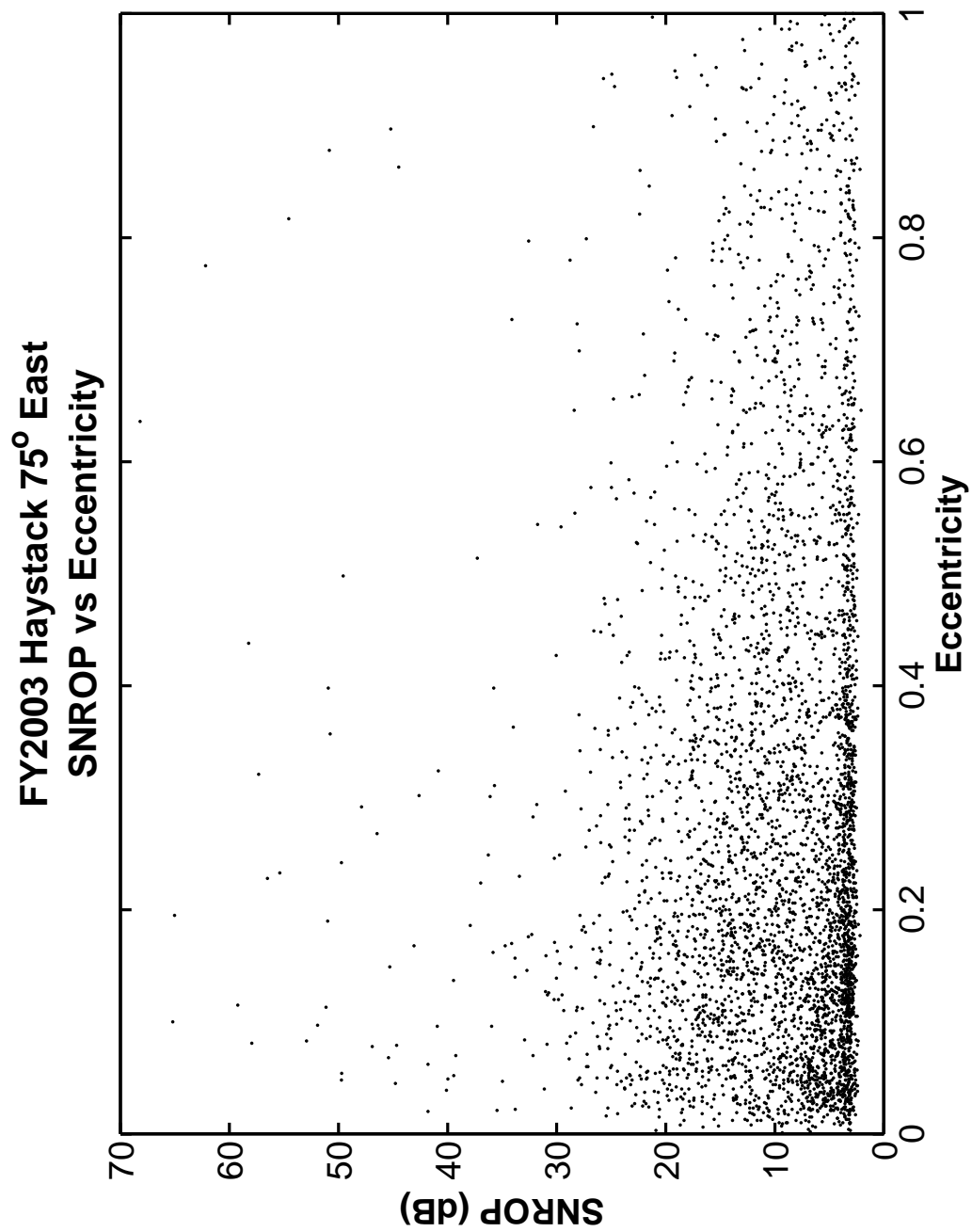


Figure 61. Haystack Orthogonal Polarization SNR versus Eccentricity.

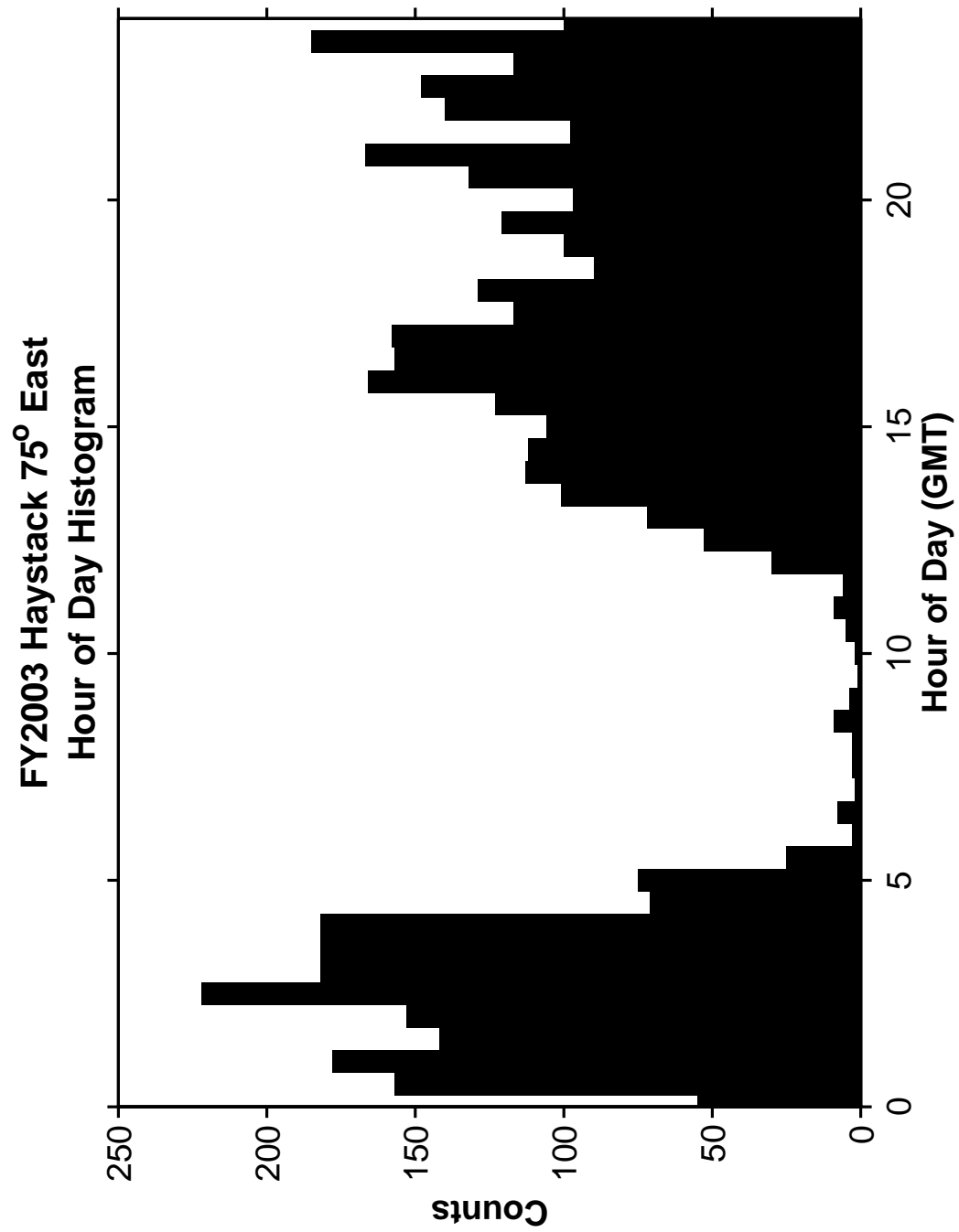


Figure 62. Haystack Hour of Day of Detection Histogram.

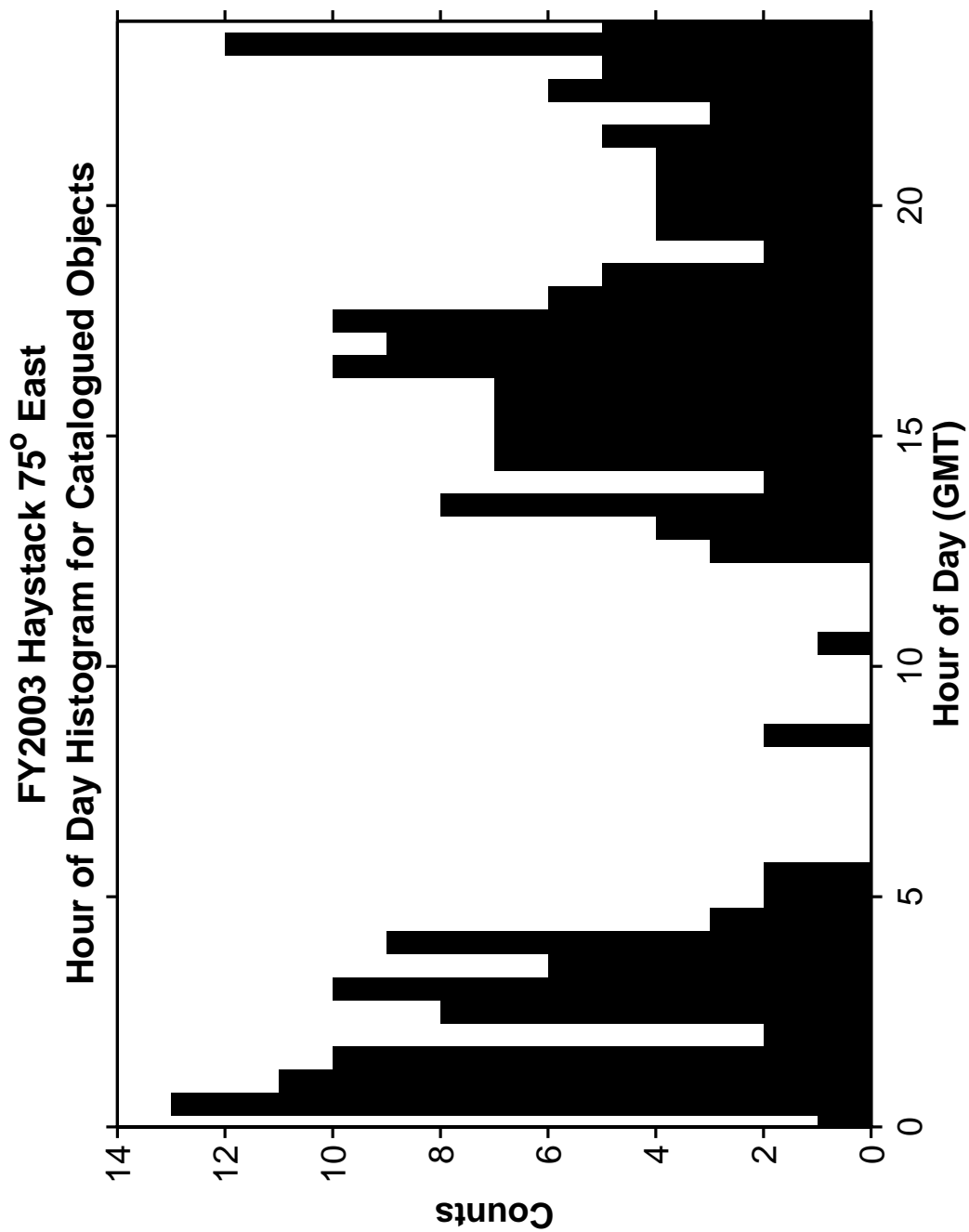


Figure 63. Haystack Hour of Day of Detection Histogram for Catalogued Objects.

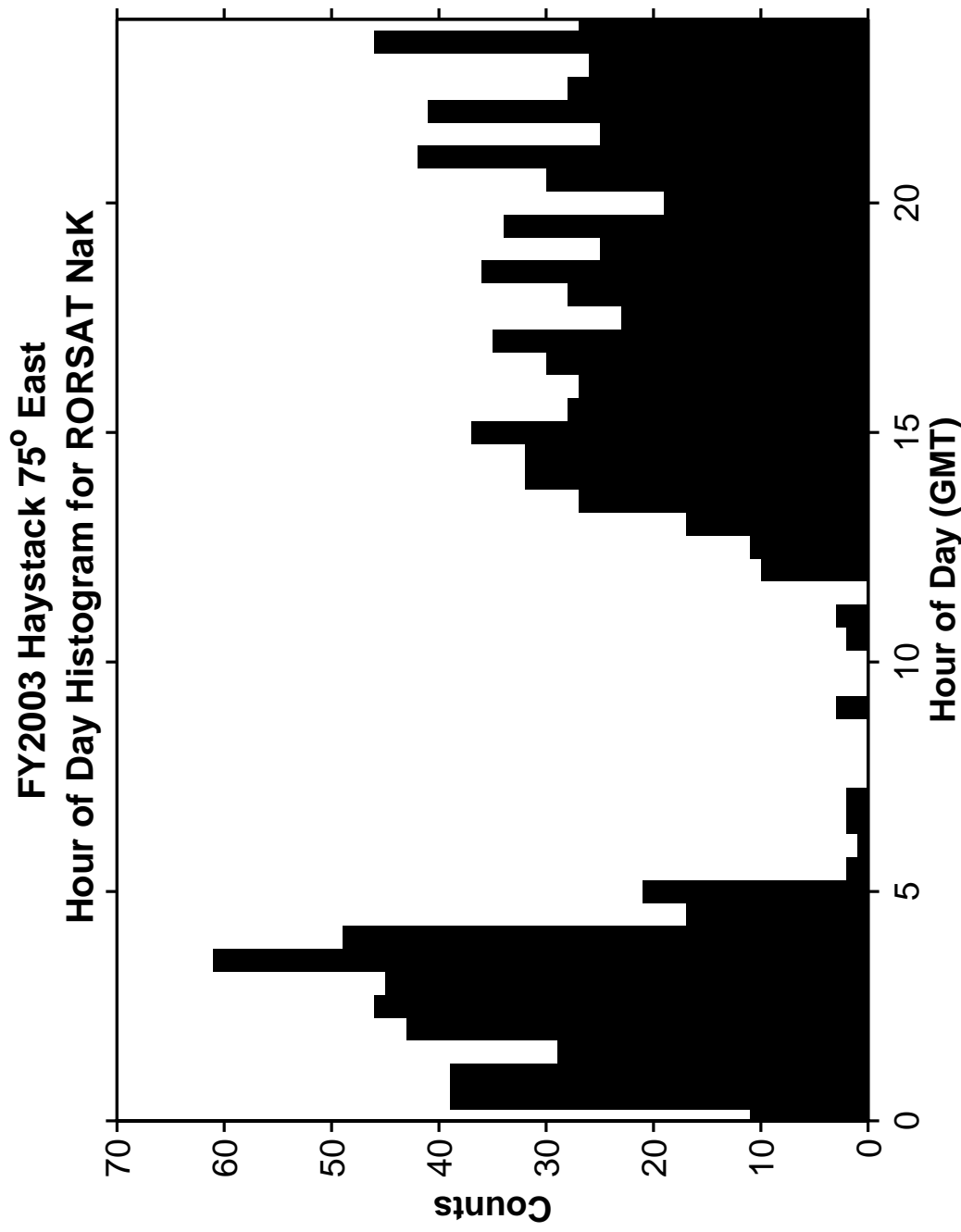


Figure 64. Haystack Hour of Day of Detection Histogram for RORSAT NaK Debris.

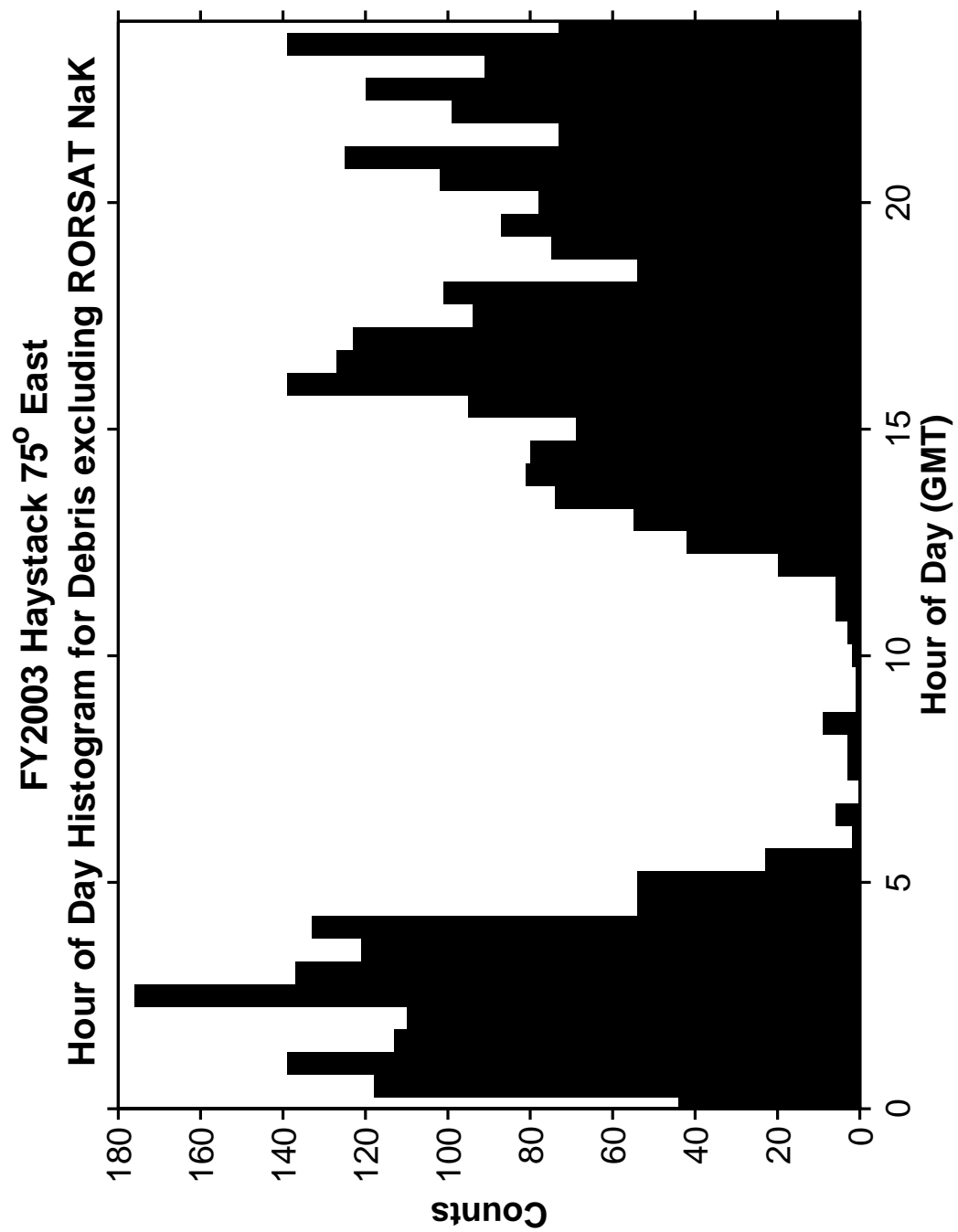


Figure 65. Haystack Hour of Day of Detection Histogram excluding RORSAT Nak Debris.

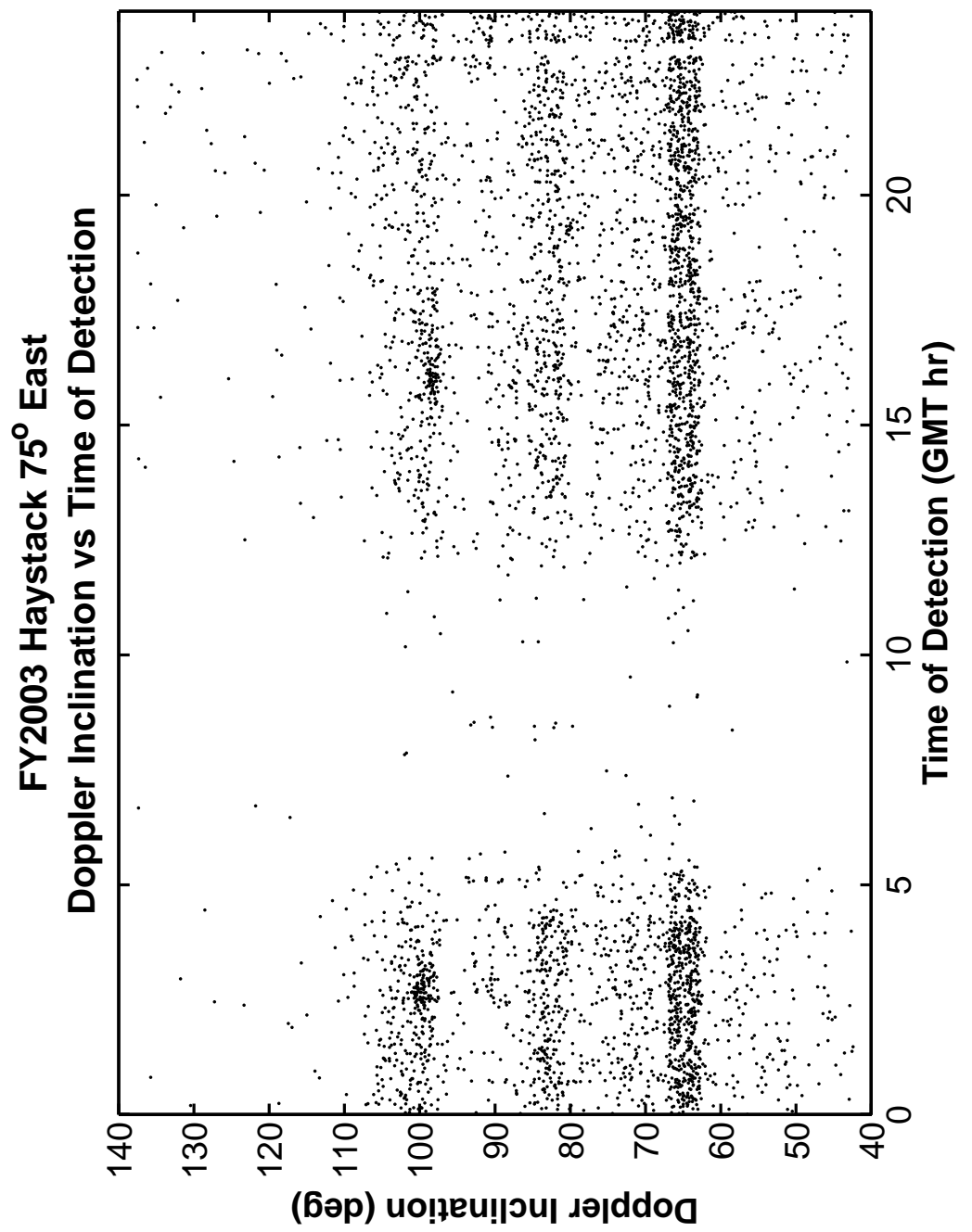


Figure 66. Haystack Doppler Inclination versus Time of Detection.

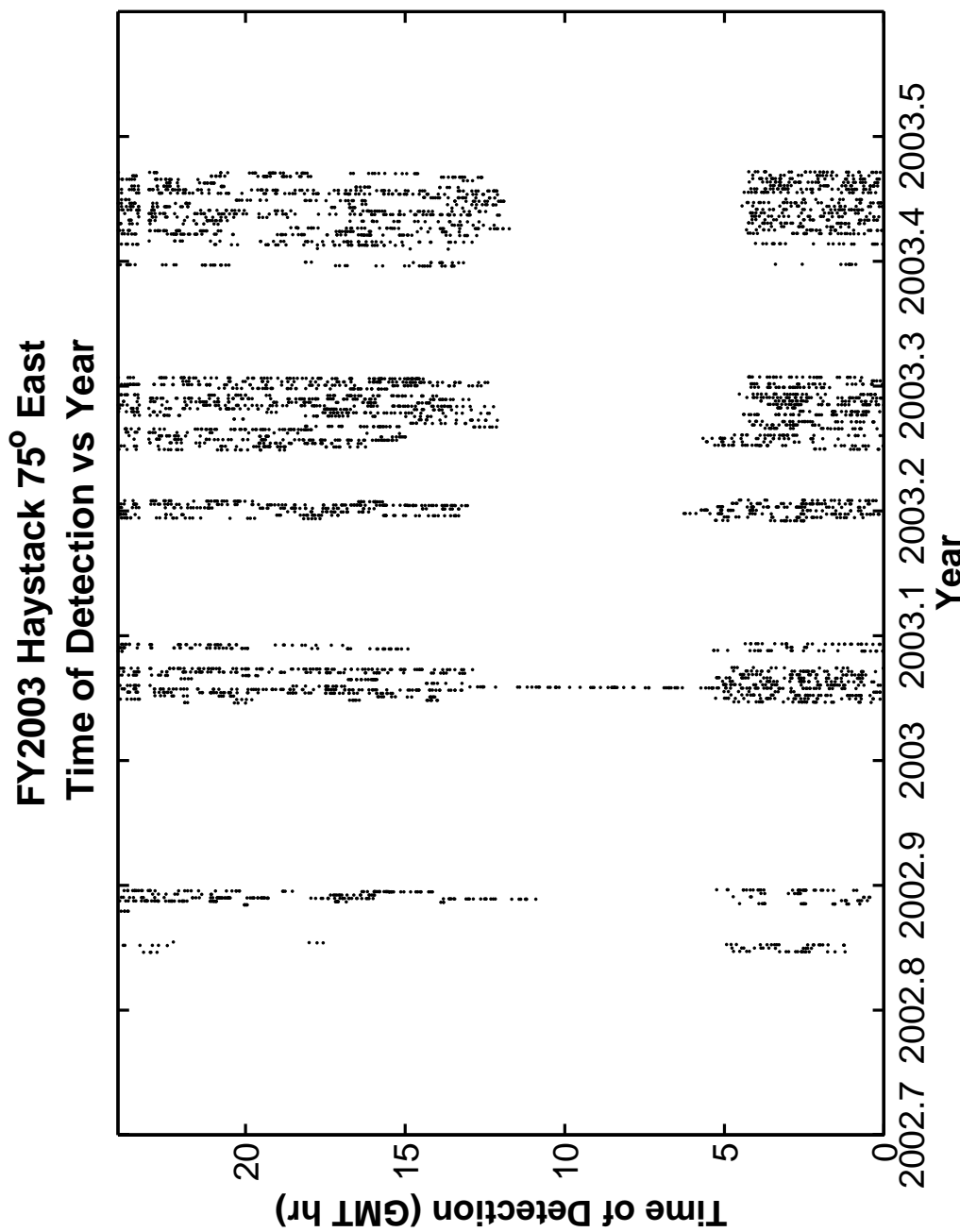


Figure 67. Haystack Daily Time of Detection versus Time of Year of Detection.

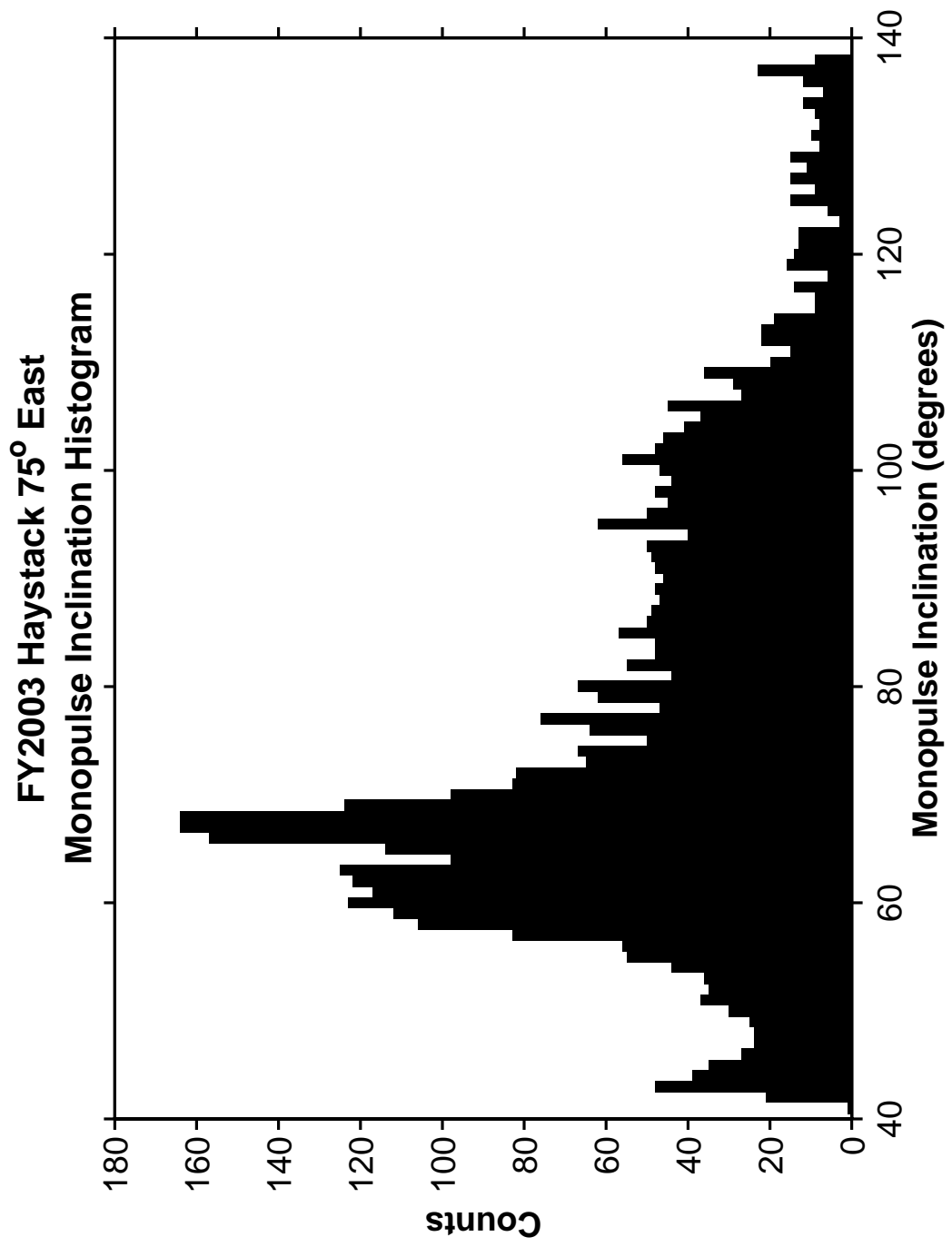


Figure 68. Haystack Monopulse Inclination Histogram.

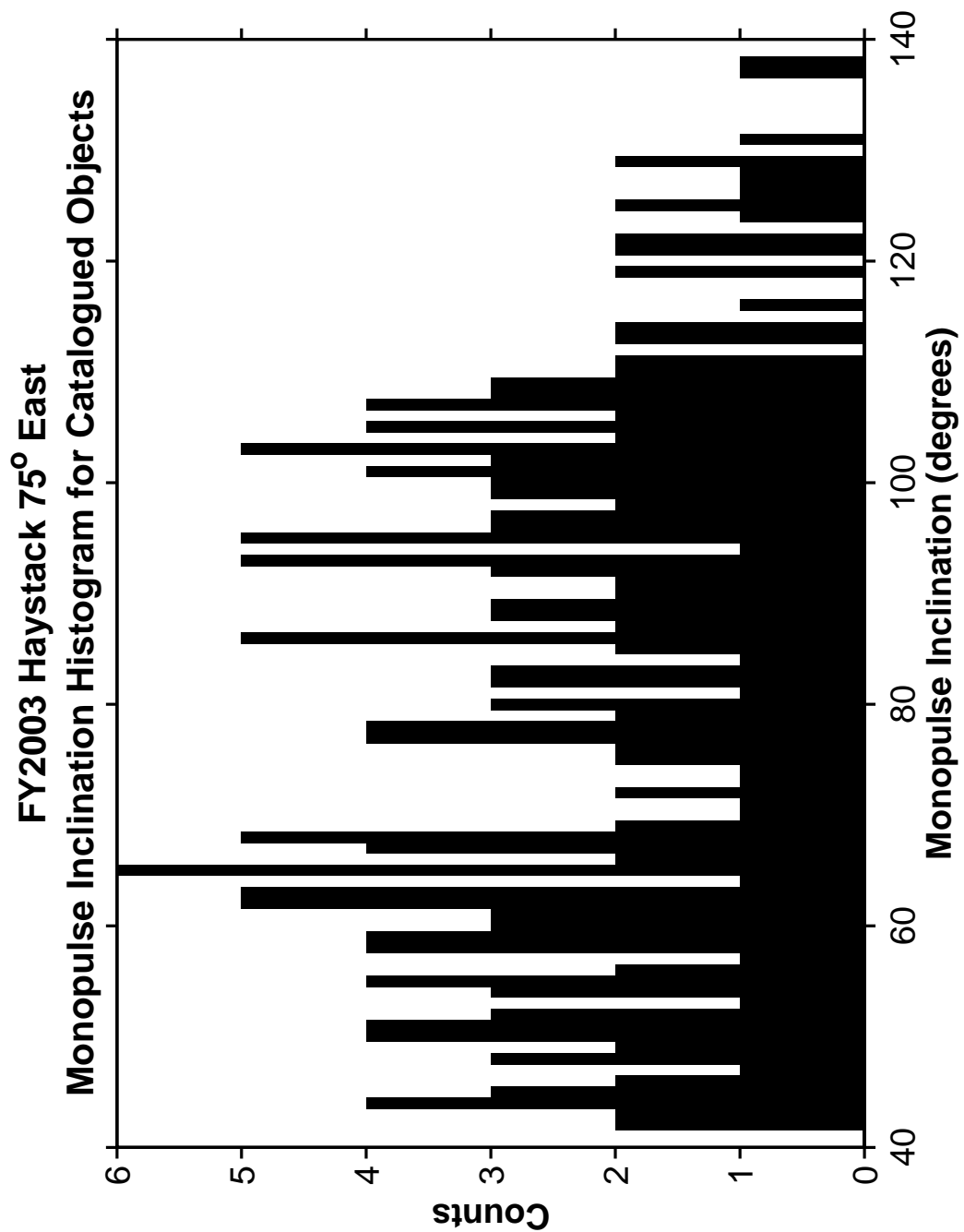


Figure 69. Haystack Monopulse Inclination Histogram for Catalogued Objects.

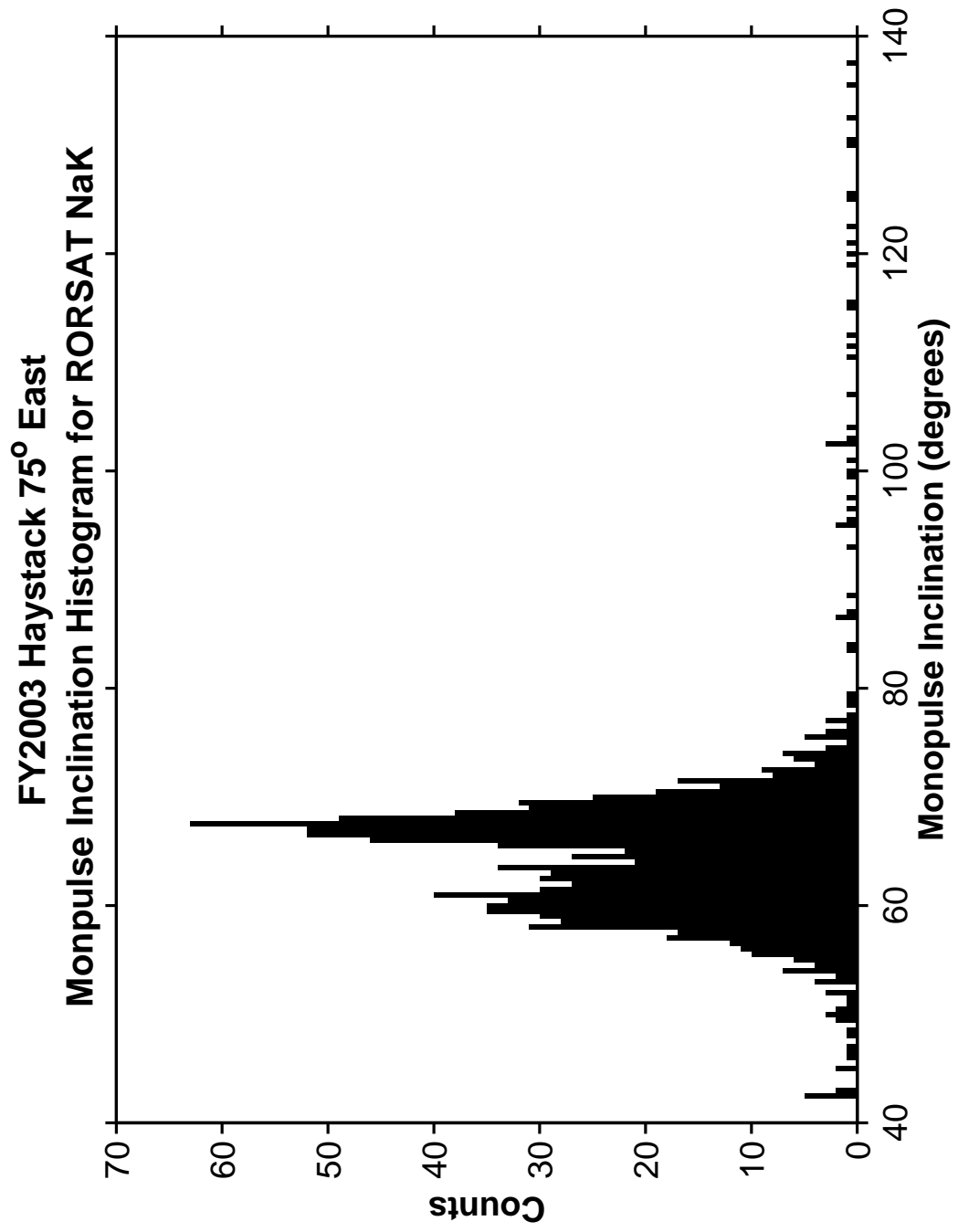


Figure 70. Haystack Monopulse Inclination Histogram for RORSAT NaK.

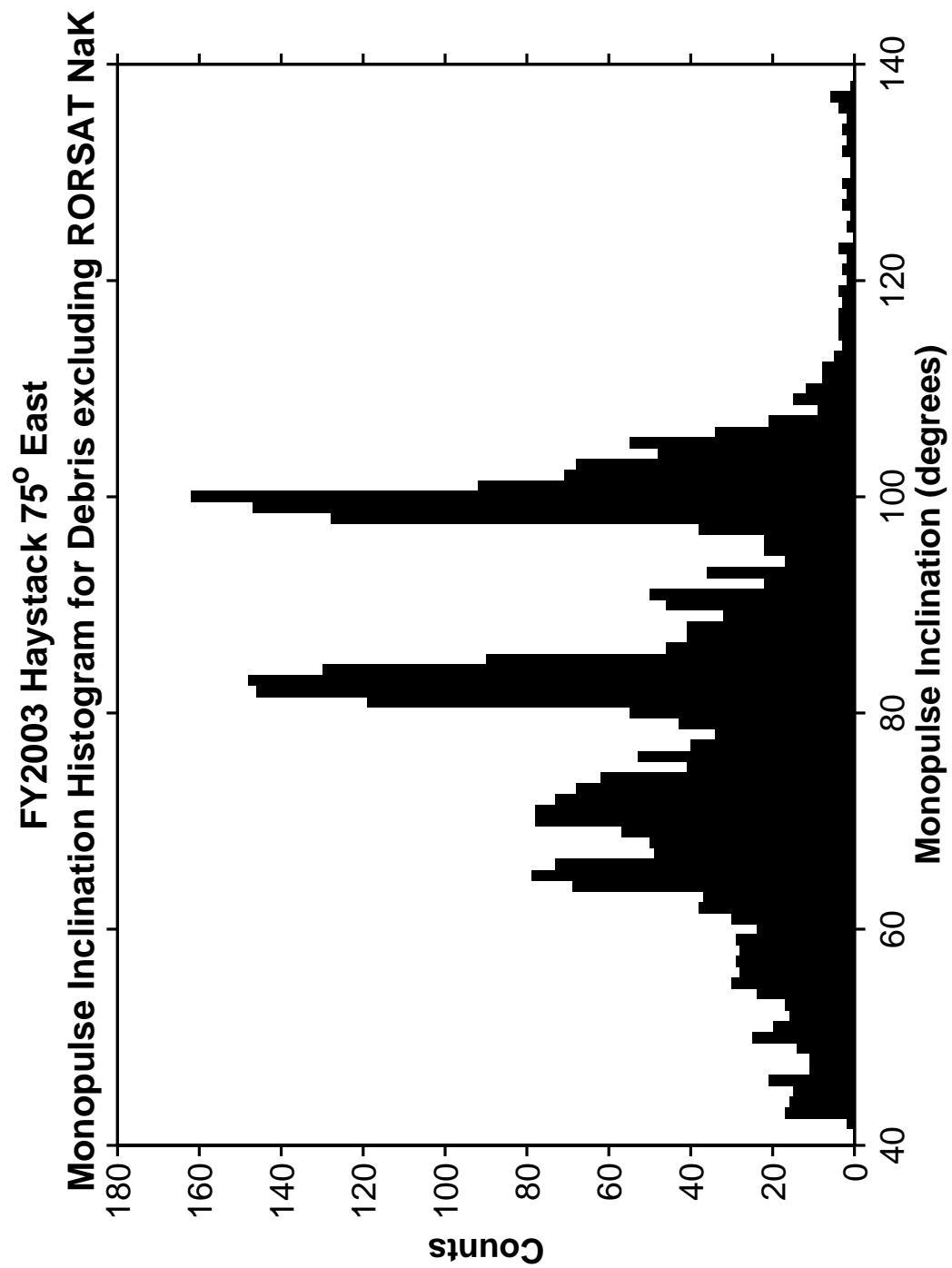


Figure 71. Haystack Monopulse Inclination Histogram excluding RORSAT NaK Debris.

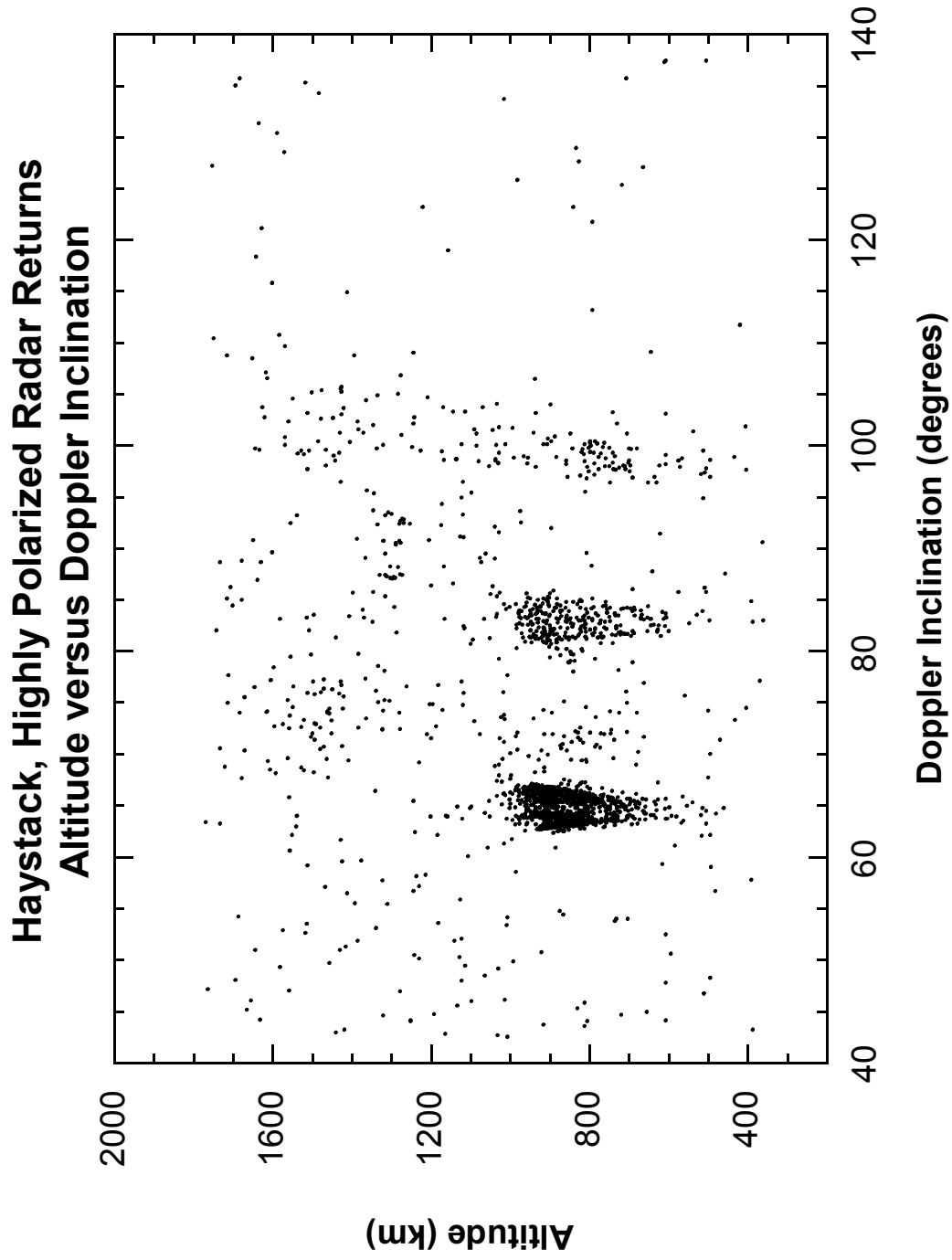


Figure 72. Haystack Altitude versus Doppler Inclination for Highly Polarized Radar Returns.

FY2003 Haystack 75° East
Polarization vs Altitude

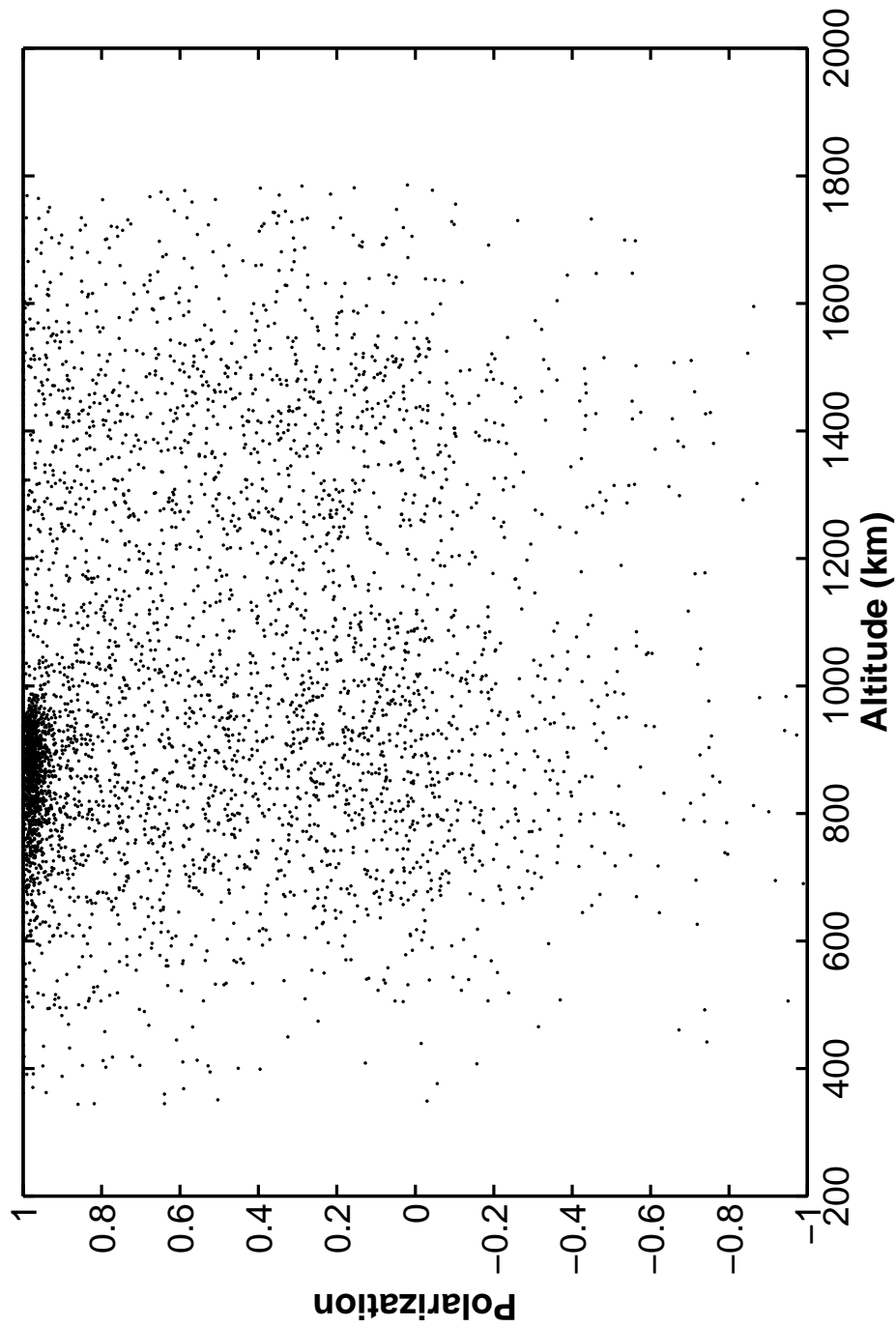


Figure 73. Haystack Radar Return Signal Polarization versus Altitude.

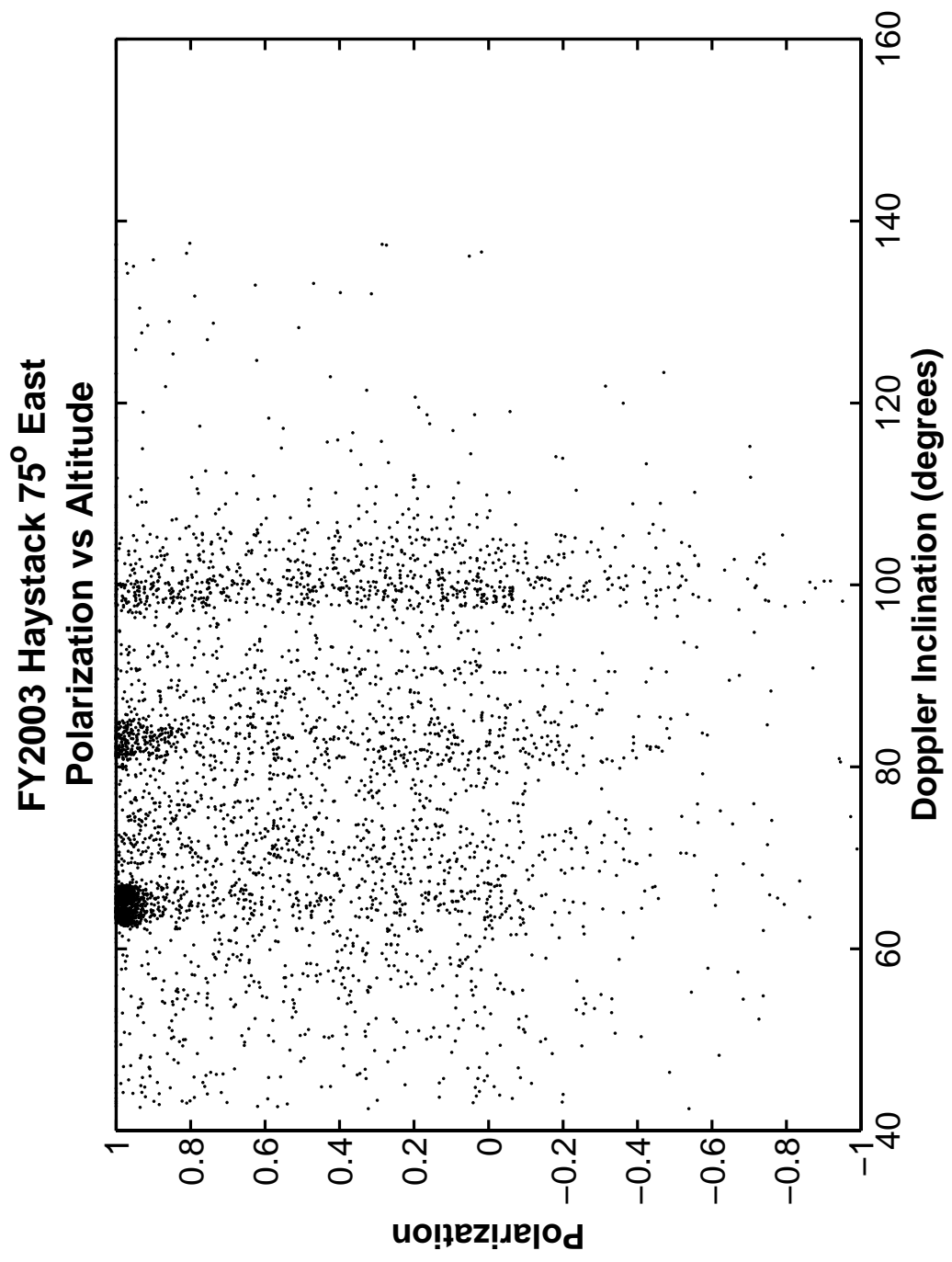


Figure 74. Haystack Radar Return Signal Polarization versus Doppler Inclination.

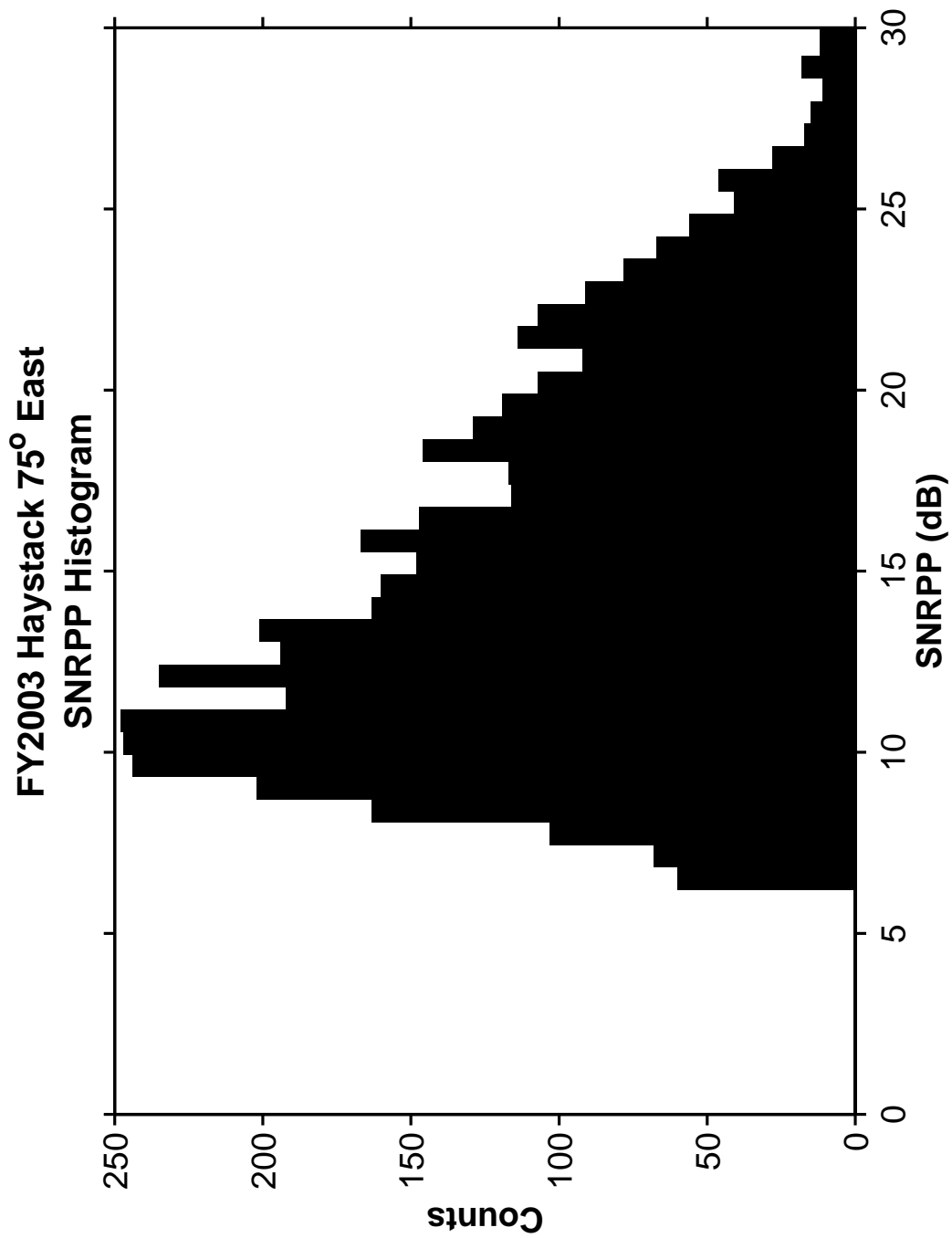


Figure 75. Haystack Principal Polarization SNR Histogram. Minimum SNR threshold is higher than shown in the radar report

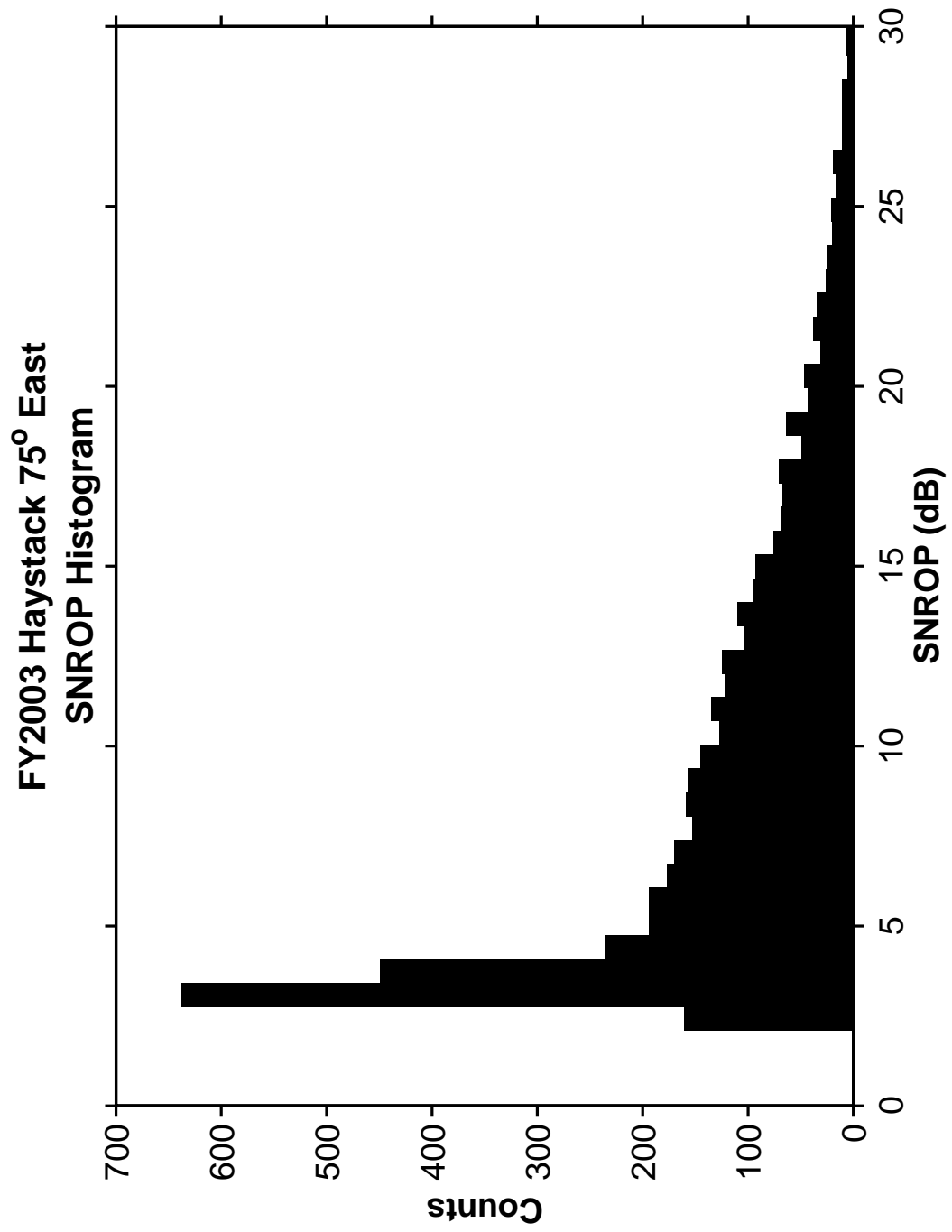


Figure 76. Haystack Orthogonal Polarization SNR Histogram.

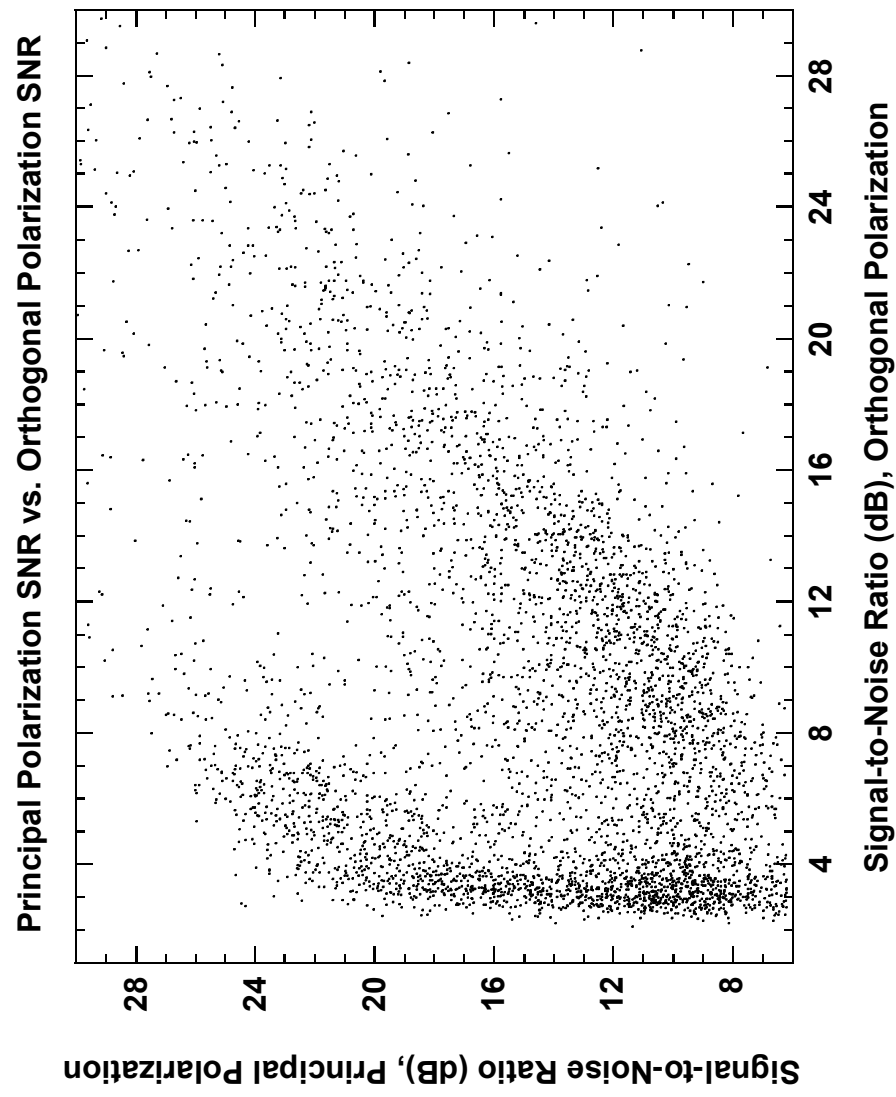


Figure 77. Haystack Principal Polarization SNR versus Orthogonal Polarization SNR.

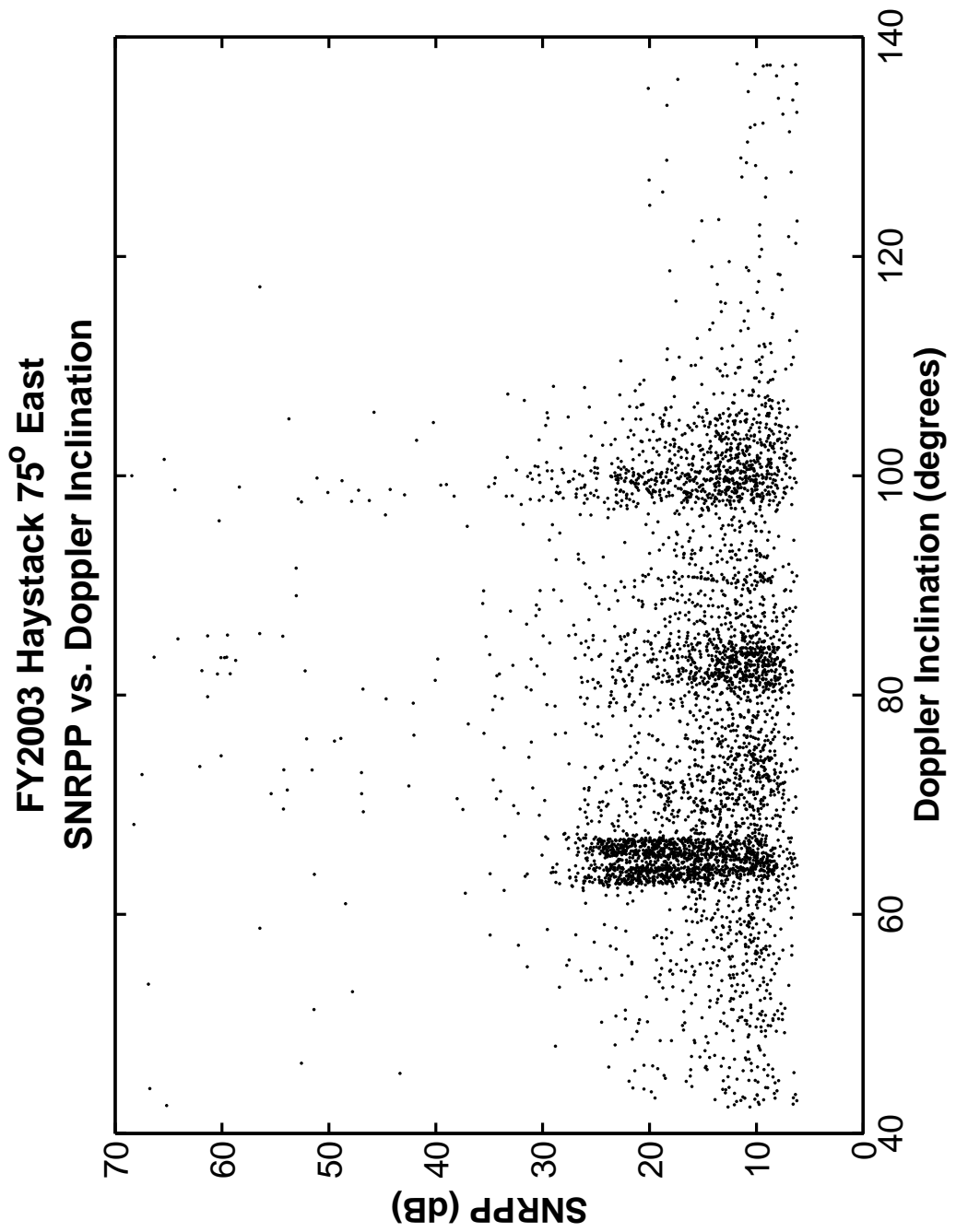


Figure 78. Haystack Principal Polarization SNR versus Doppler Inclination.

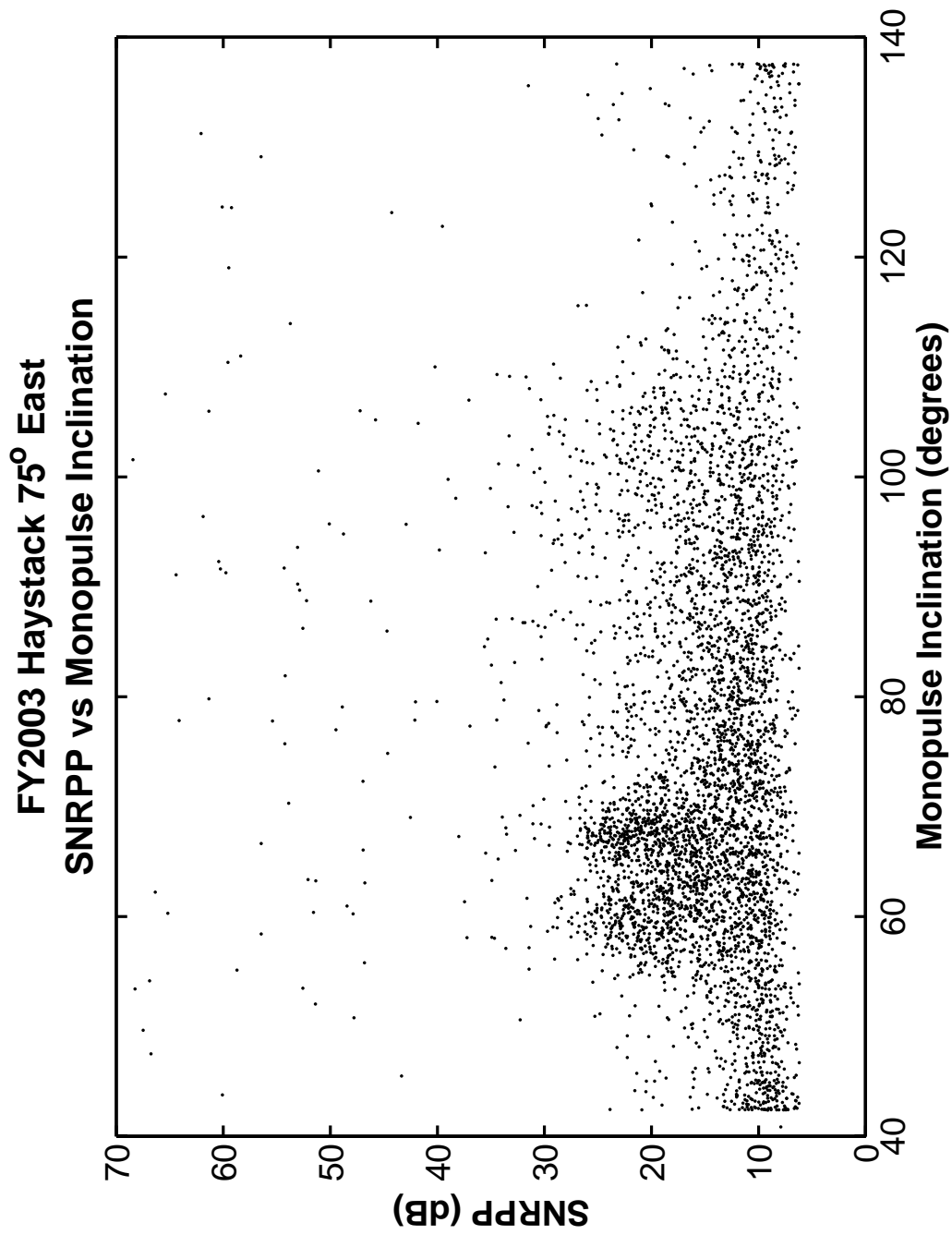


Figure 79. Haystack Principal Polarization SNR versus Monopulse Inclination.

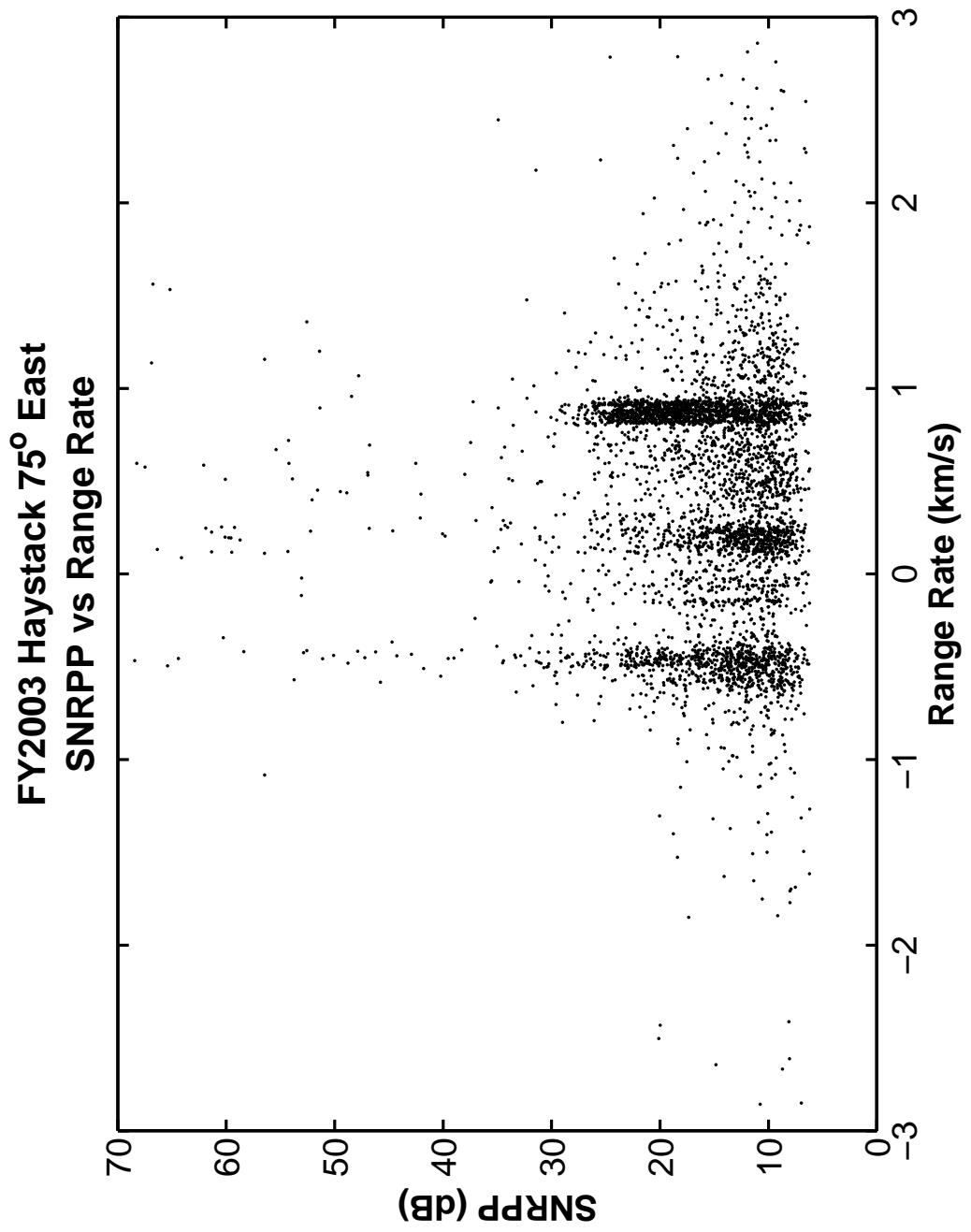


Figure 80. Haystack Principal Polarization SNR versus Range Rate.

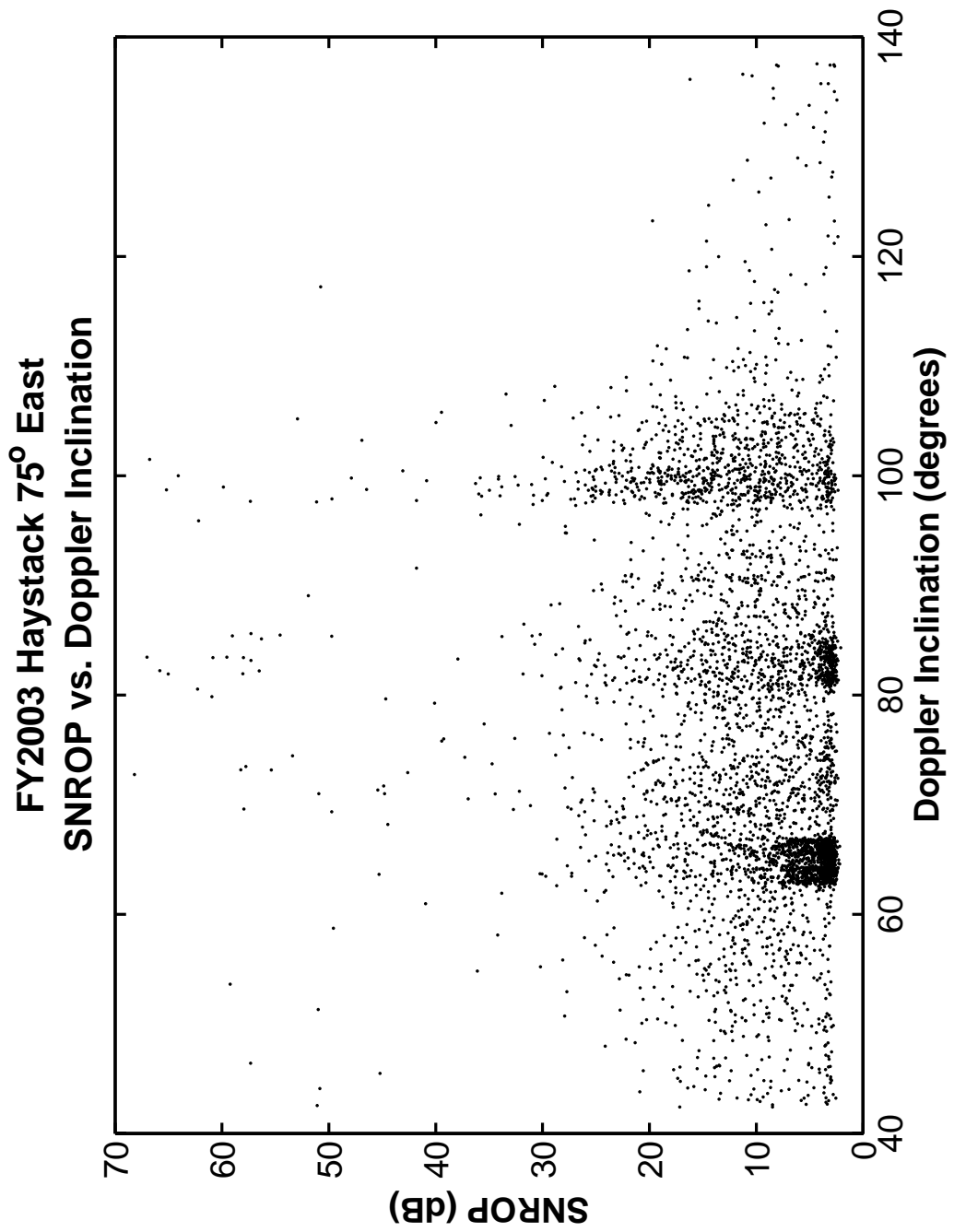


Figure 81. Haystack Orthogonal Polarization SNR versus Doppler Inclination.

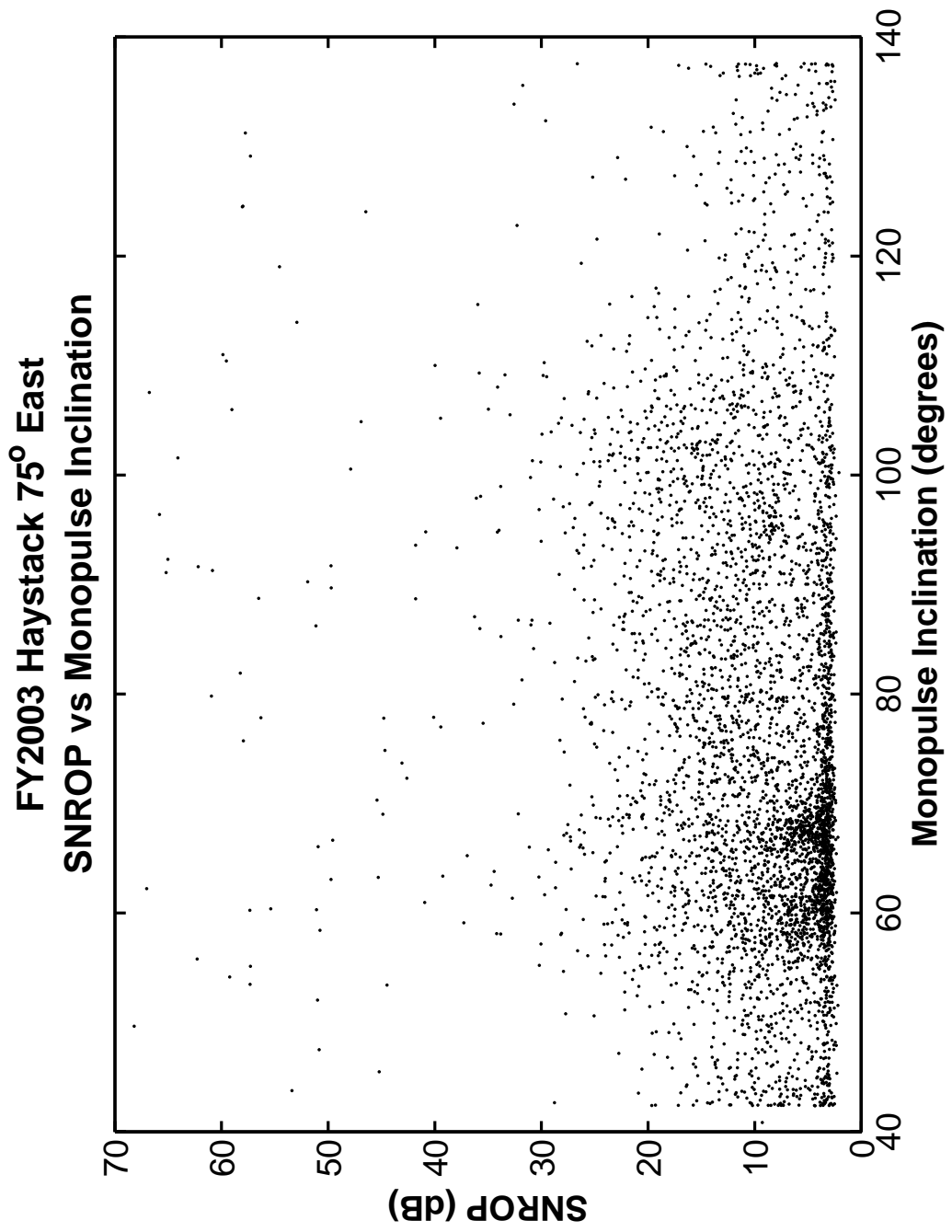


Figure 82. Haystack Orthogonal Polarization SNR versus Monopulse Inclination.

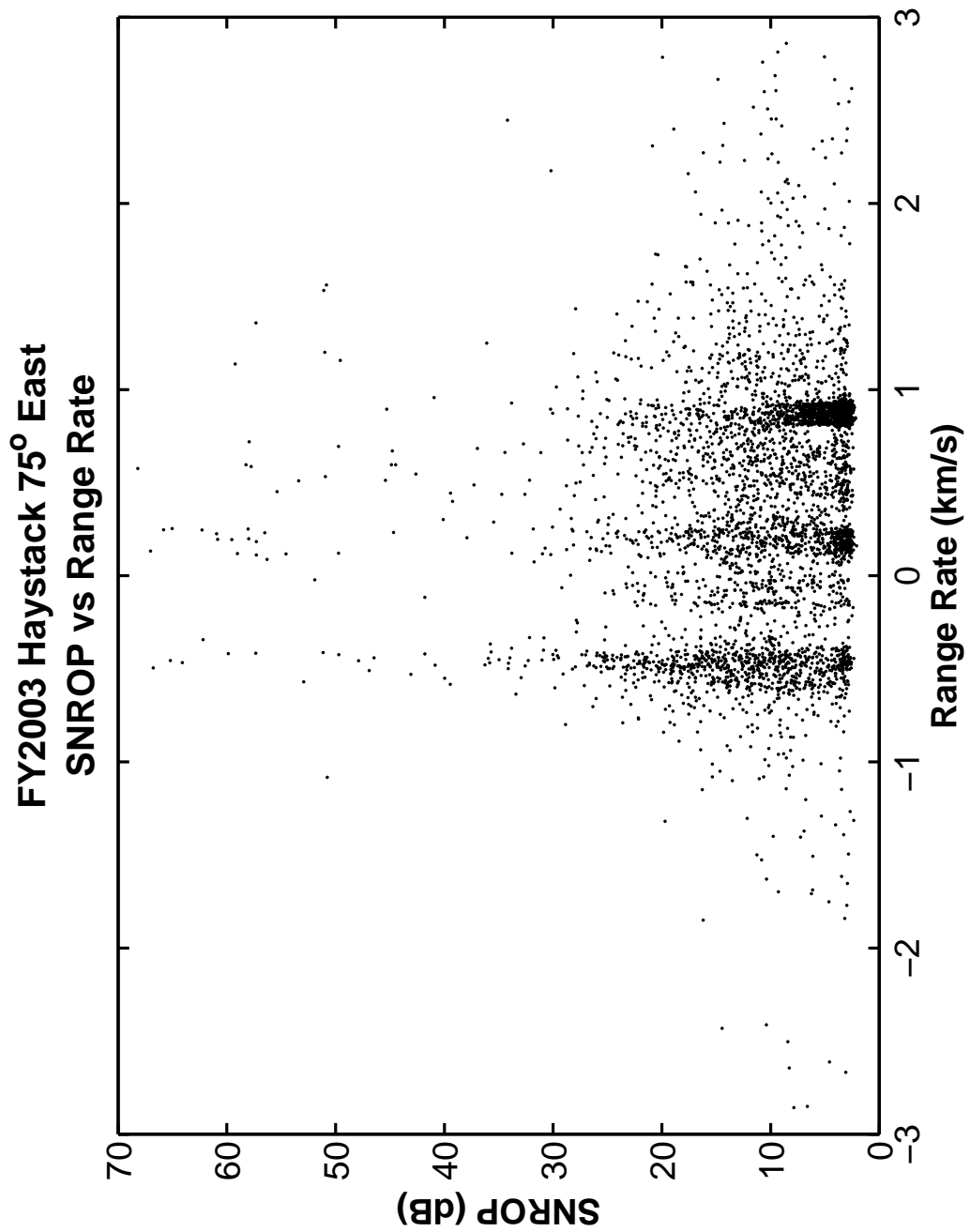


Figure 83. Haystack Orthogonal Polarization SNR versus Range Rate.

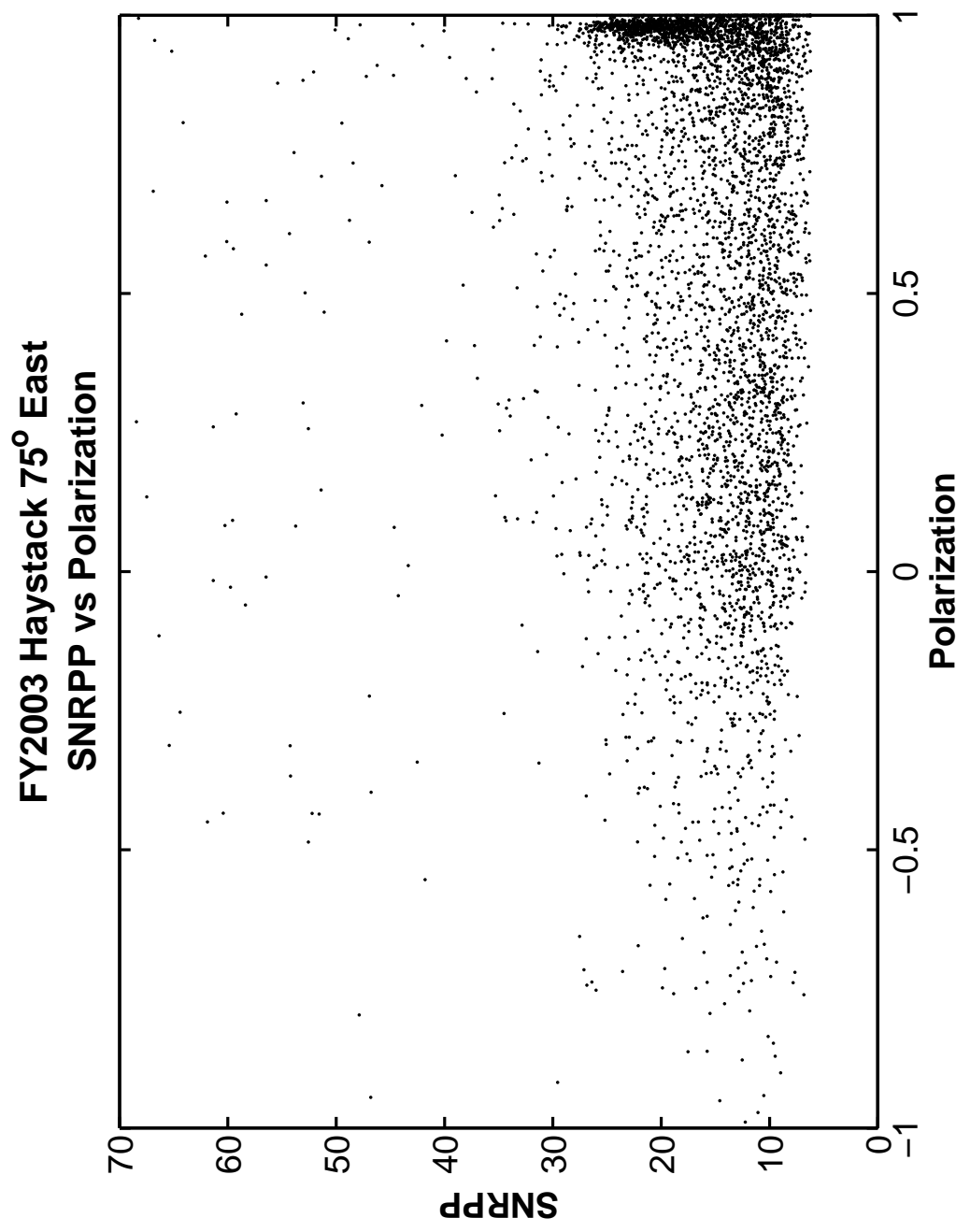


Figure 84. Haystack Principal Polarization SNR versus Polarization.

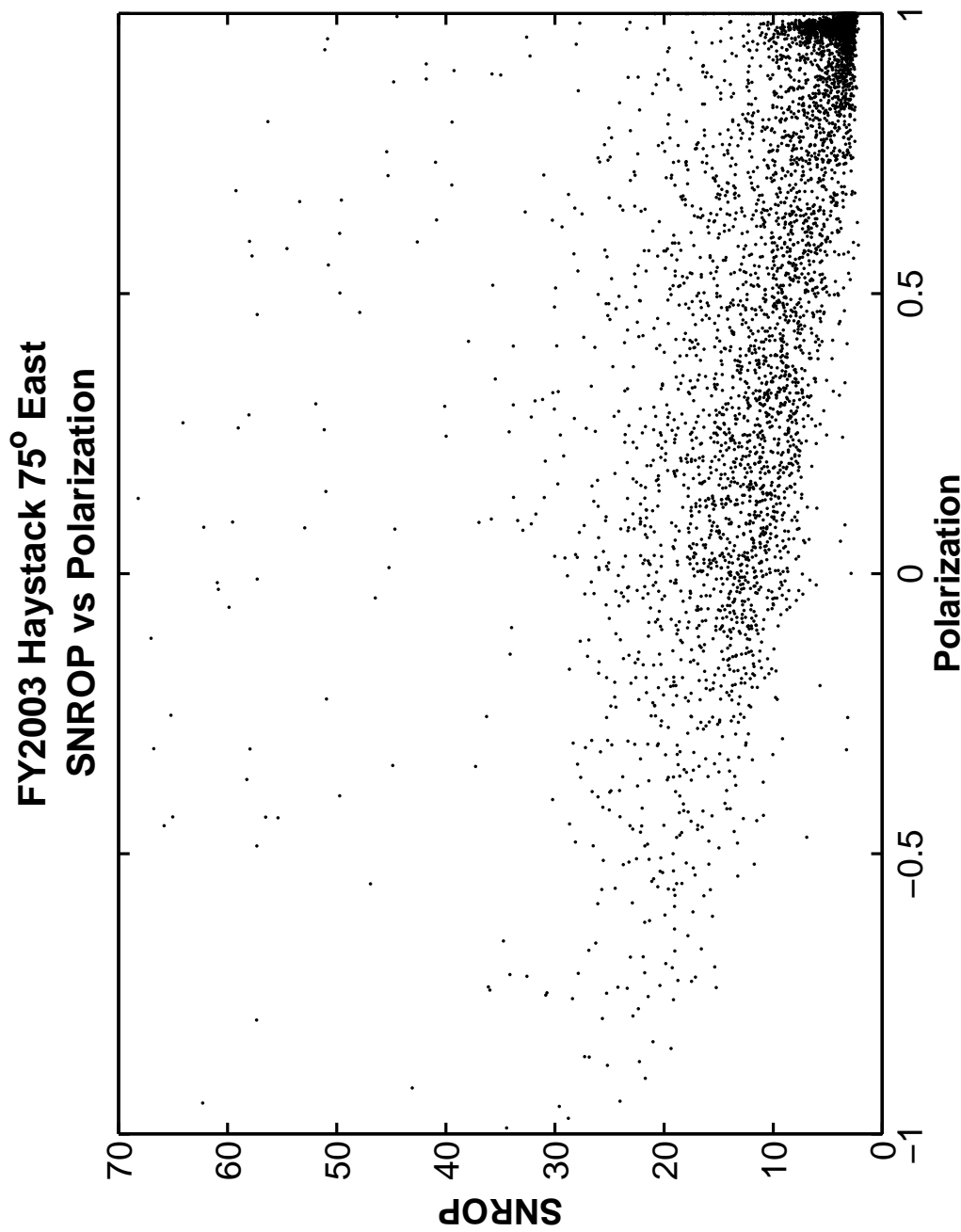


Figure 85. Haystack Orthogonal Polarization SNR versus Polarization.

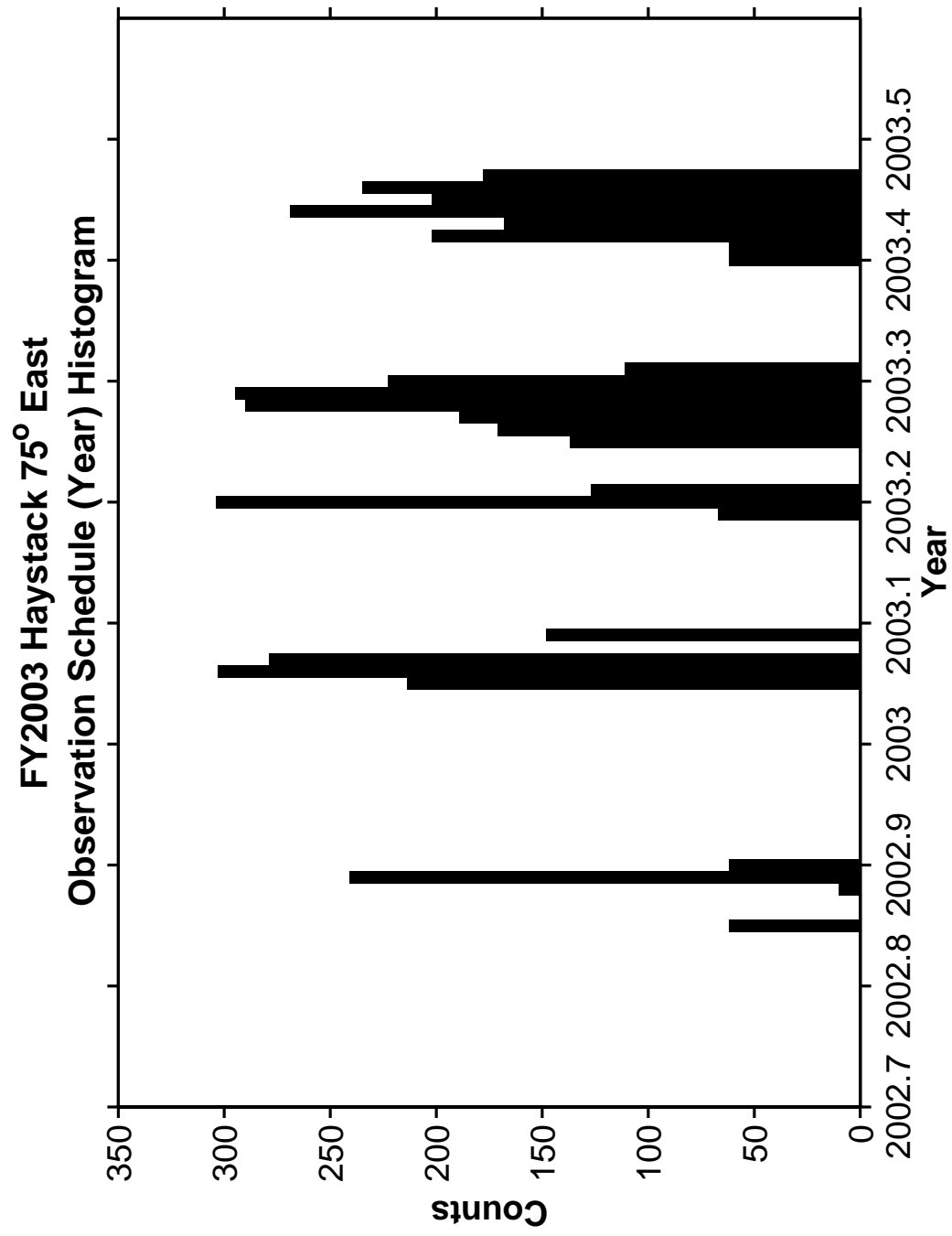


Figure 86. Histogram of Haystack Observation Schedule throughout the Year.

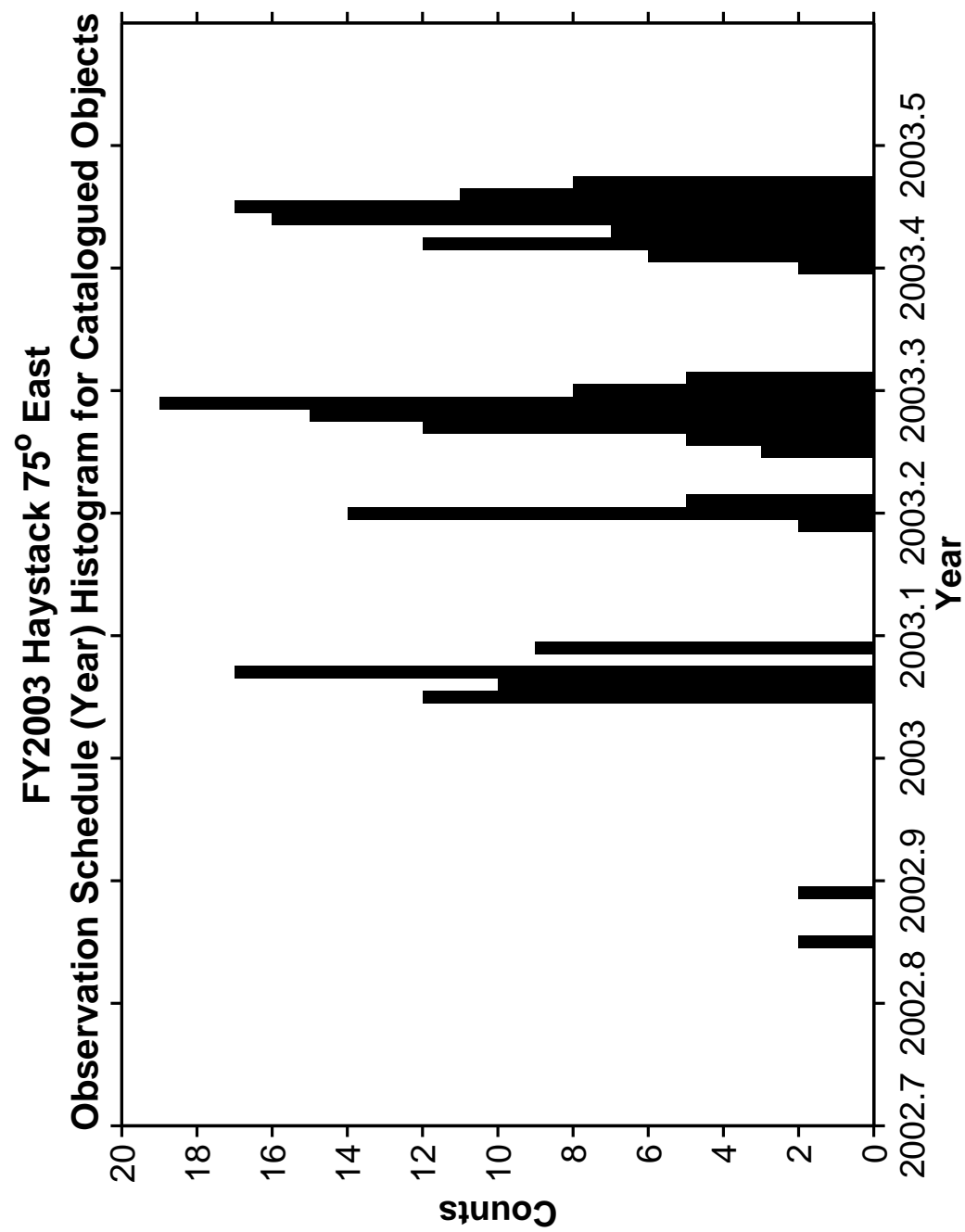


Figure 87. Histogram of Haystack Observation Schedule throughout the Year of Catalogued Objects.

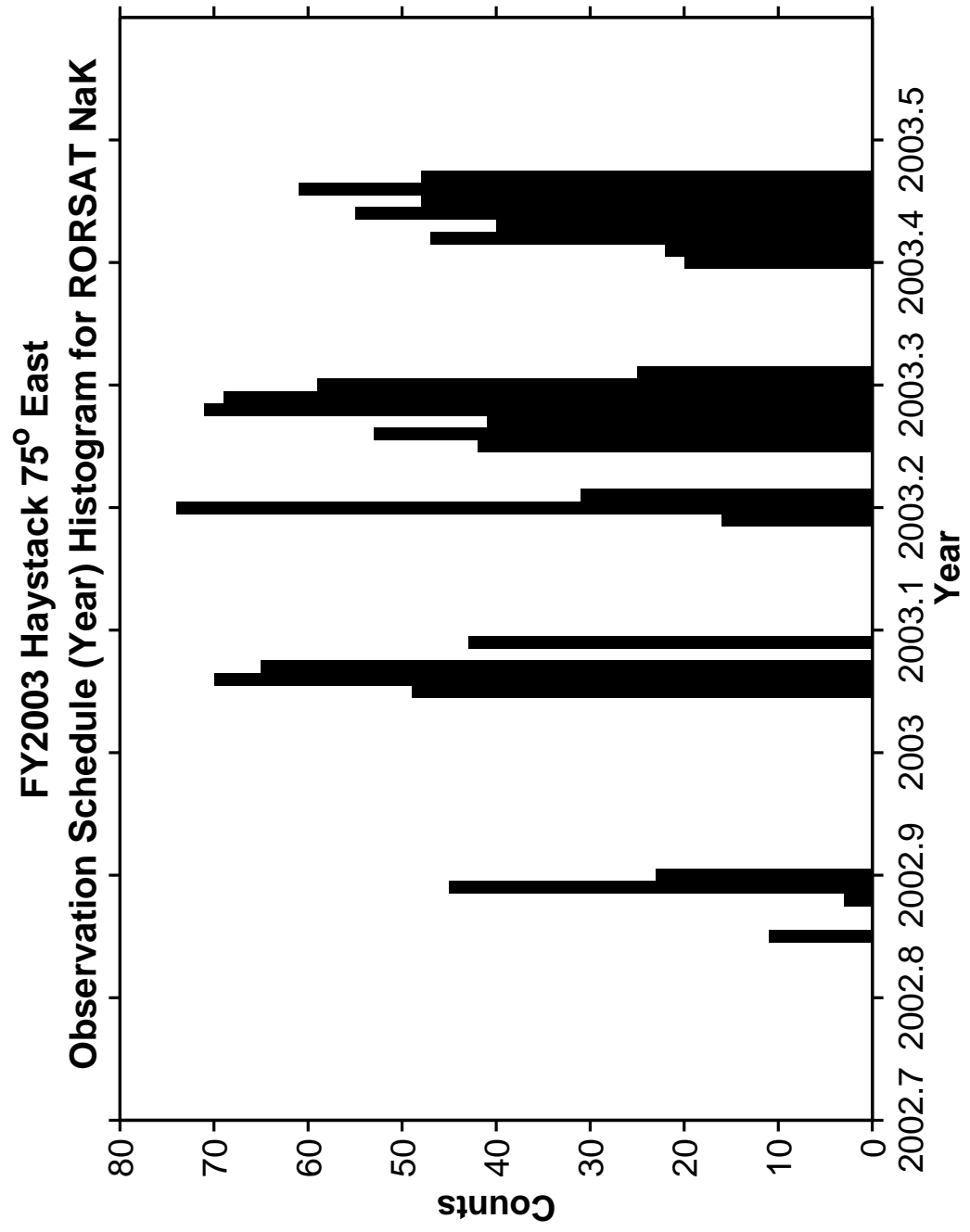


Figure 88. Histogram of Haystack Observation Schedule throughout the Year of RORSAT NaK Debris.

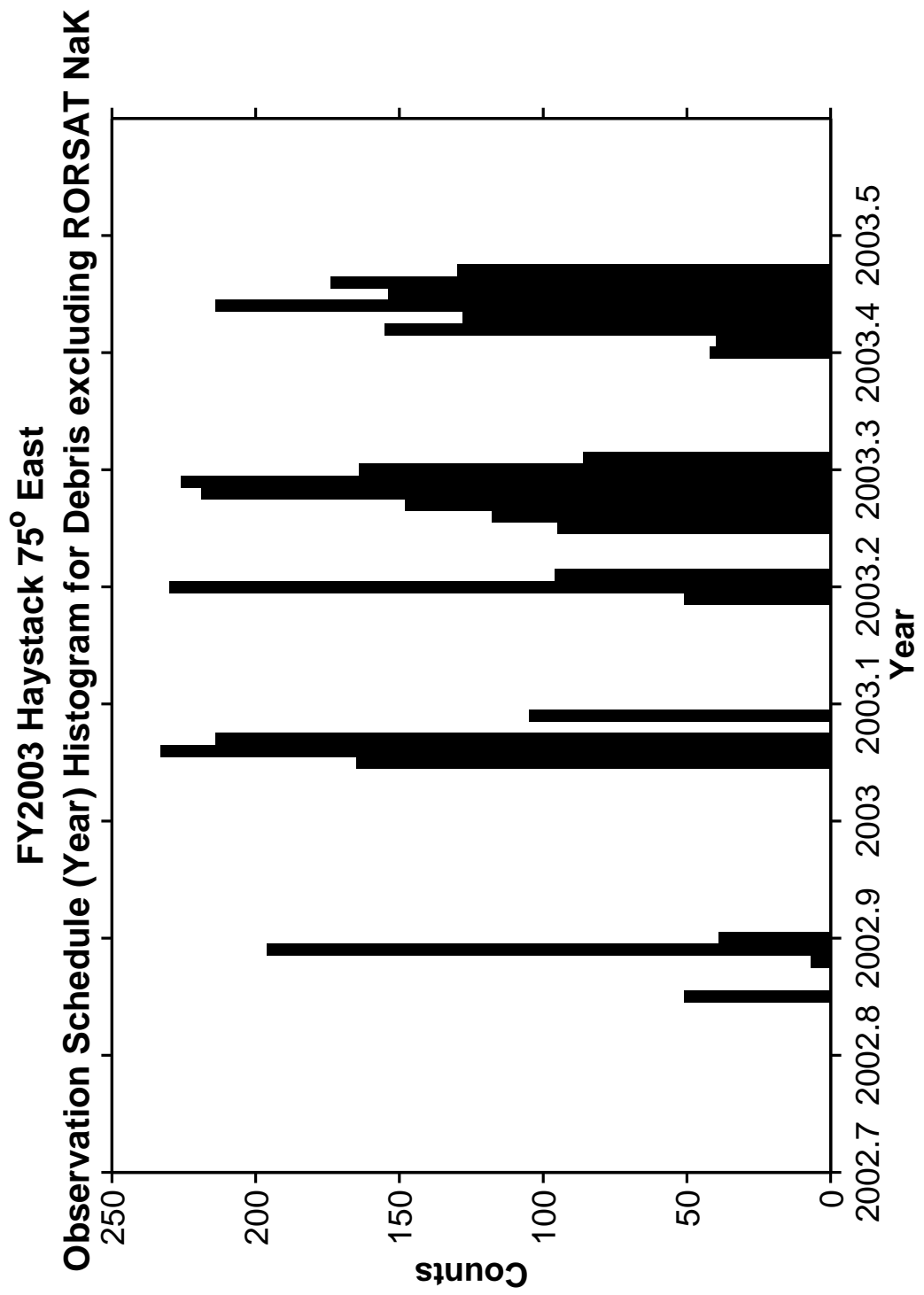


Figure 89. Histogram of Haystack Observation Schedule throughout the Year of Debris excluding RORSAT NaK Debris.

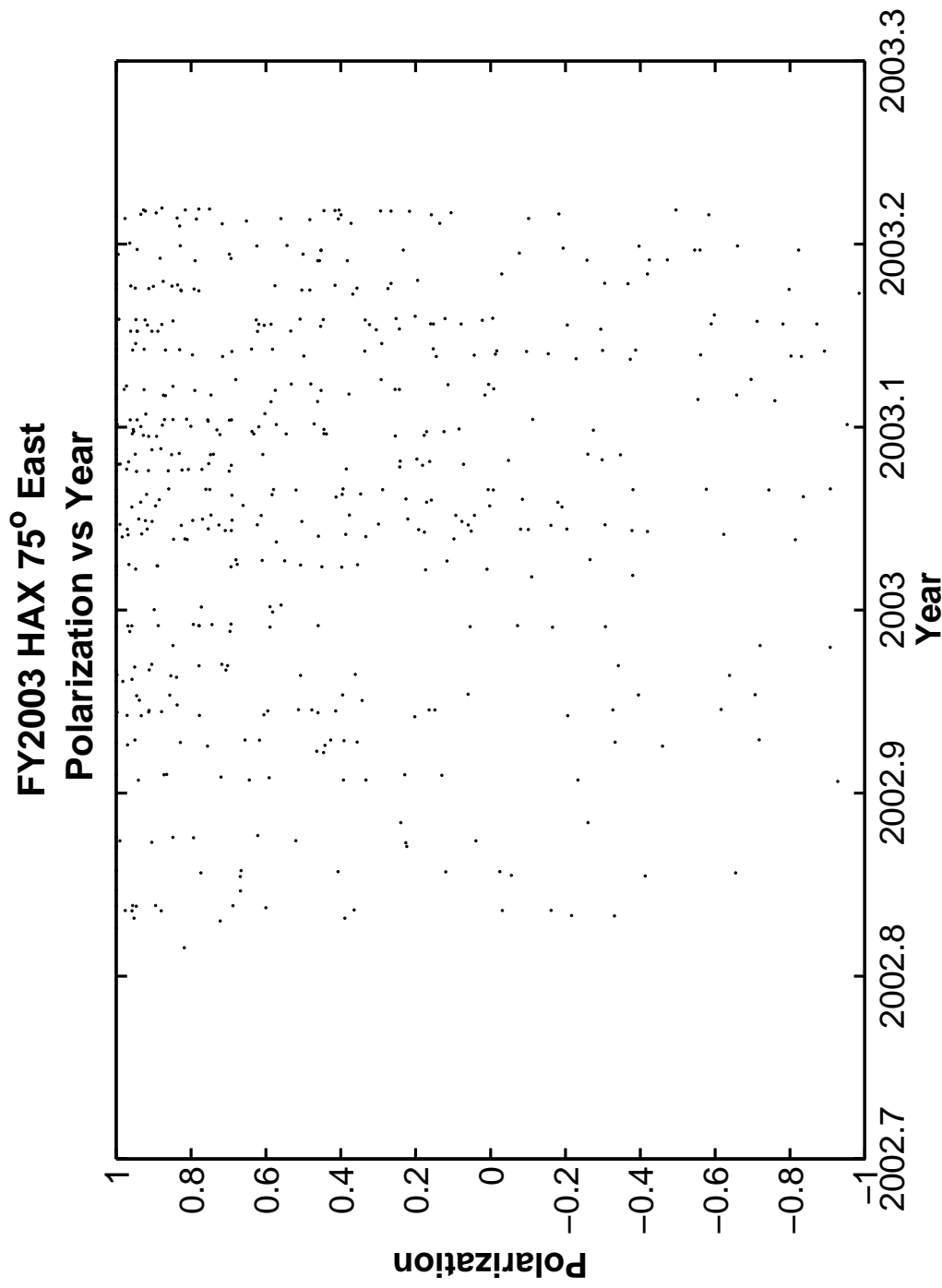


Figure 90. Haystack Polarization versus Observation throughout the Year.

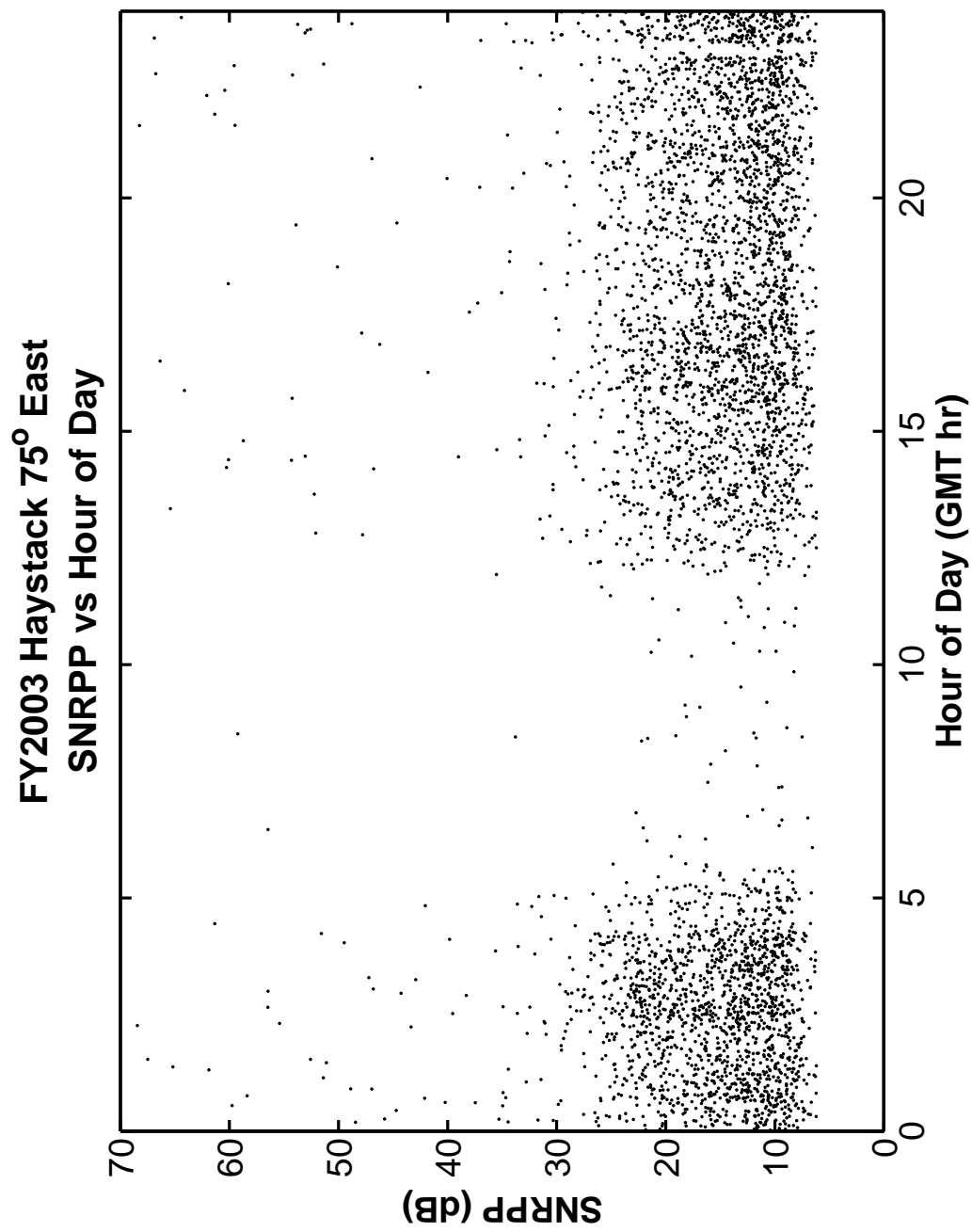


Figure 91. Haystack Principal Polarization SNR versus Hour of Day of Detection.

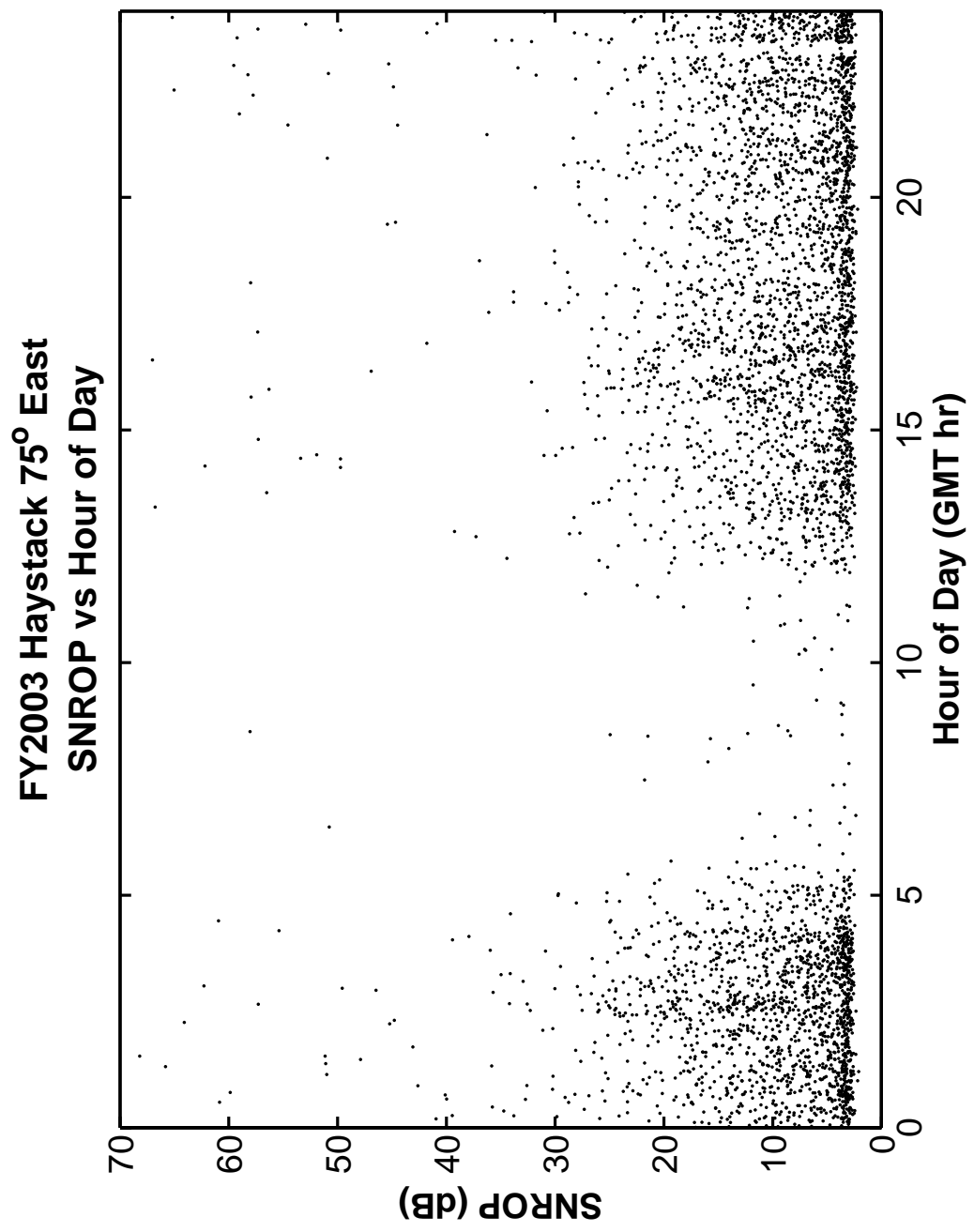


Figure 92. Haystack Orthogonal Polarization SNR versus Hour of Day of Detection.

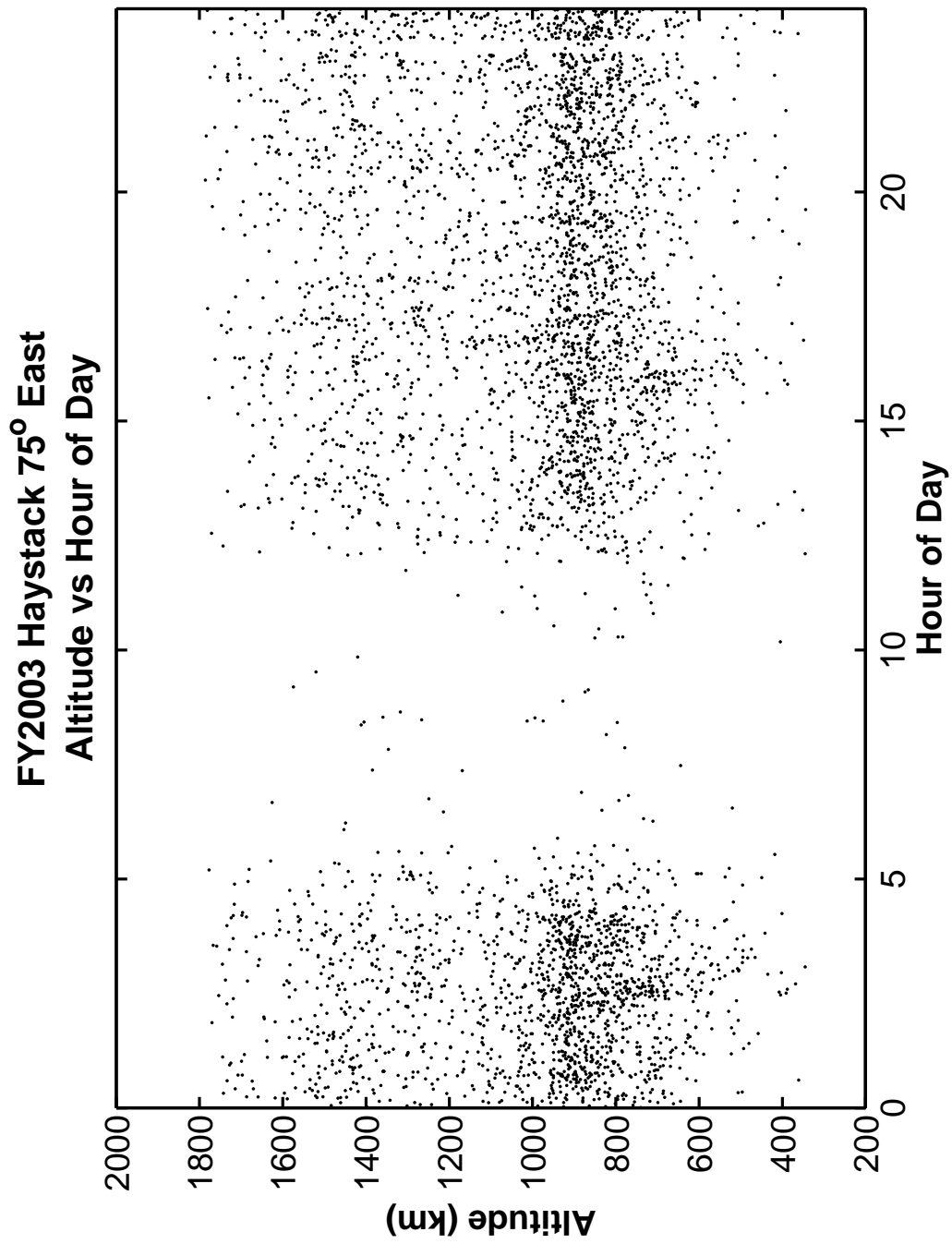


Figure 93. Haystack Altitude versus Hour of Day of Detection.

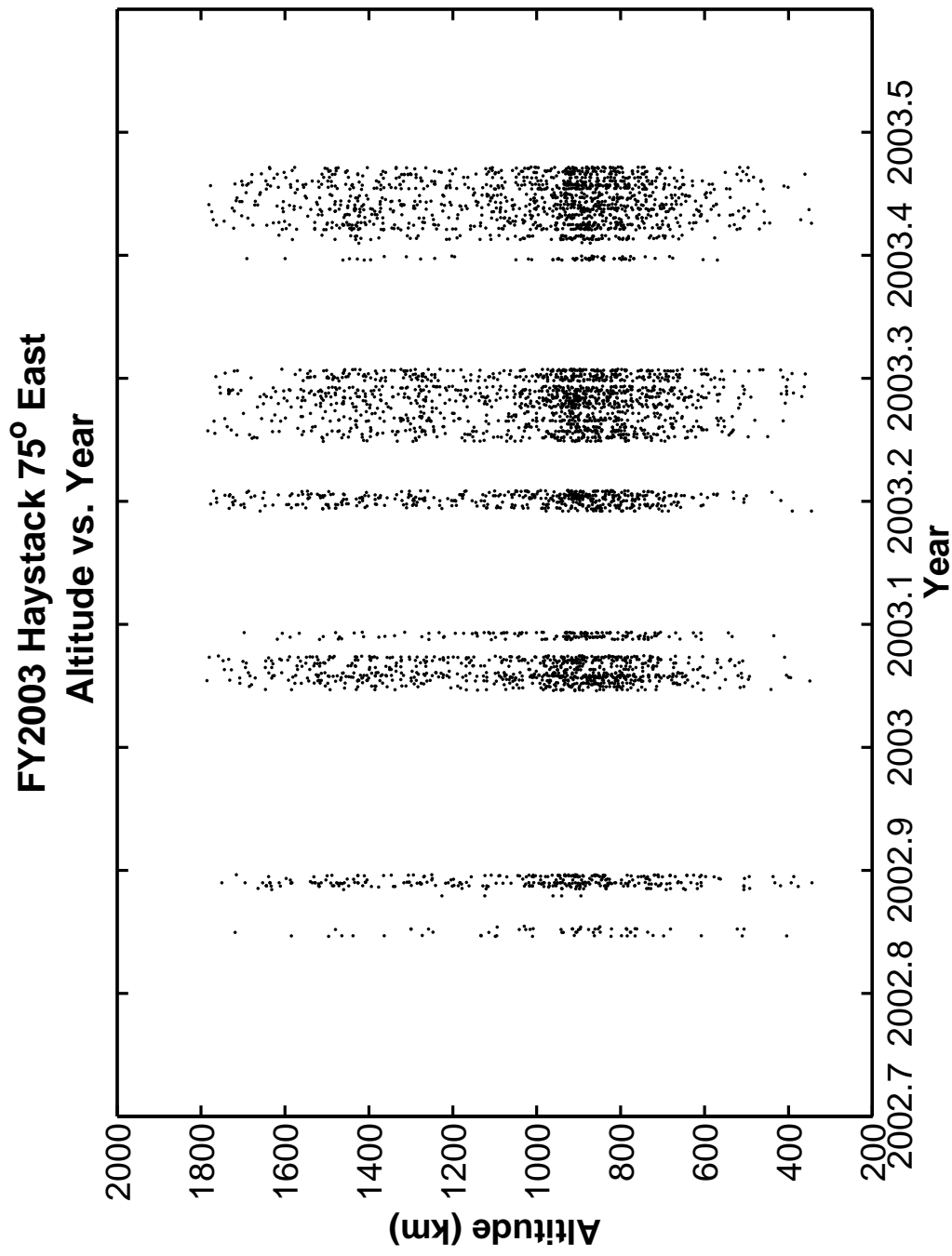


Figure 94. Haystack Altitude versus Observation Schedule throughout the Year.

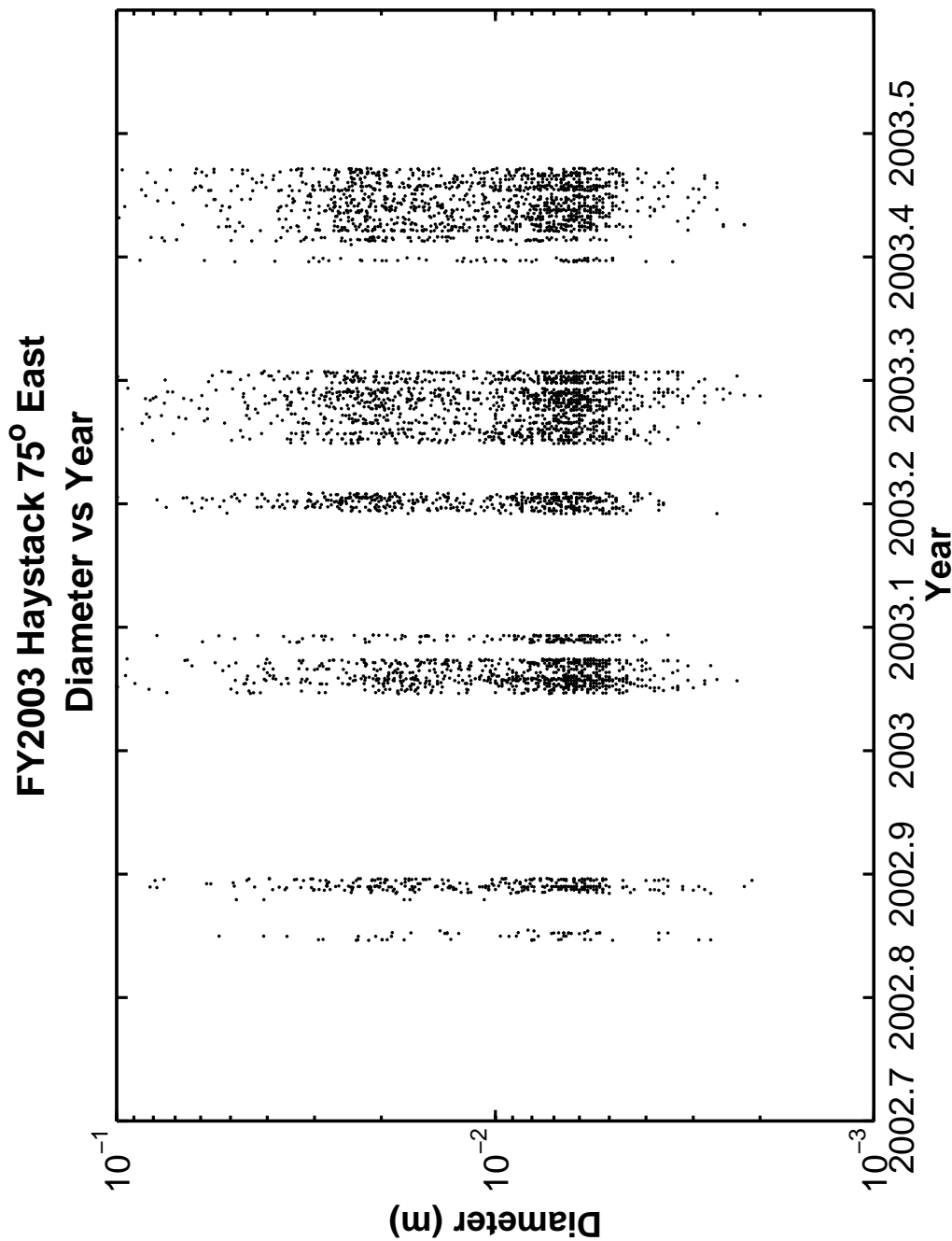


Figure 95. Haystack Diameter versus Observation Schedule throughout the Year.

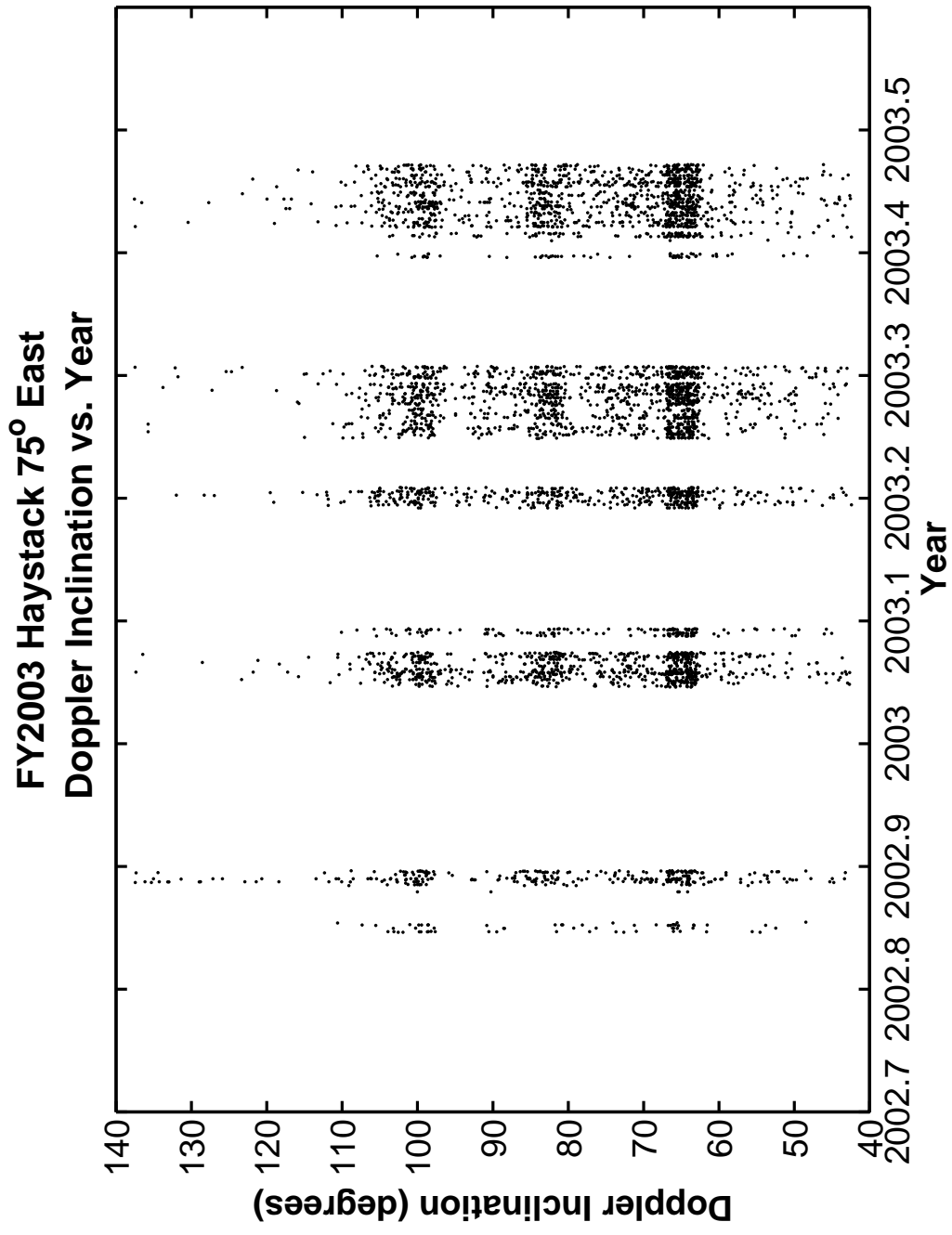


Figure 96. Haystack Doppler Inclination versus Observation Schedule throughout the Year.

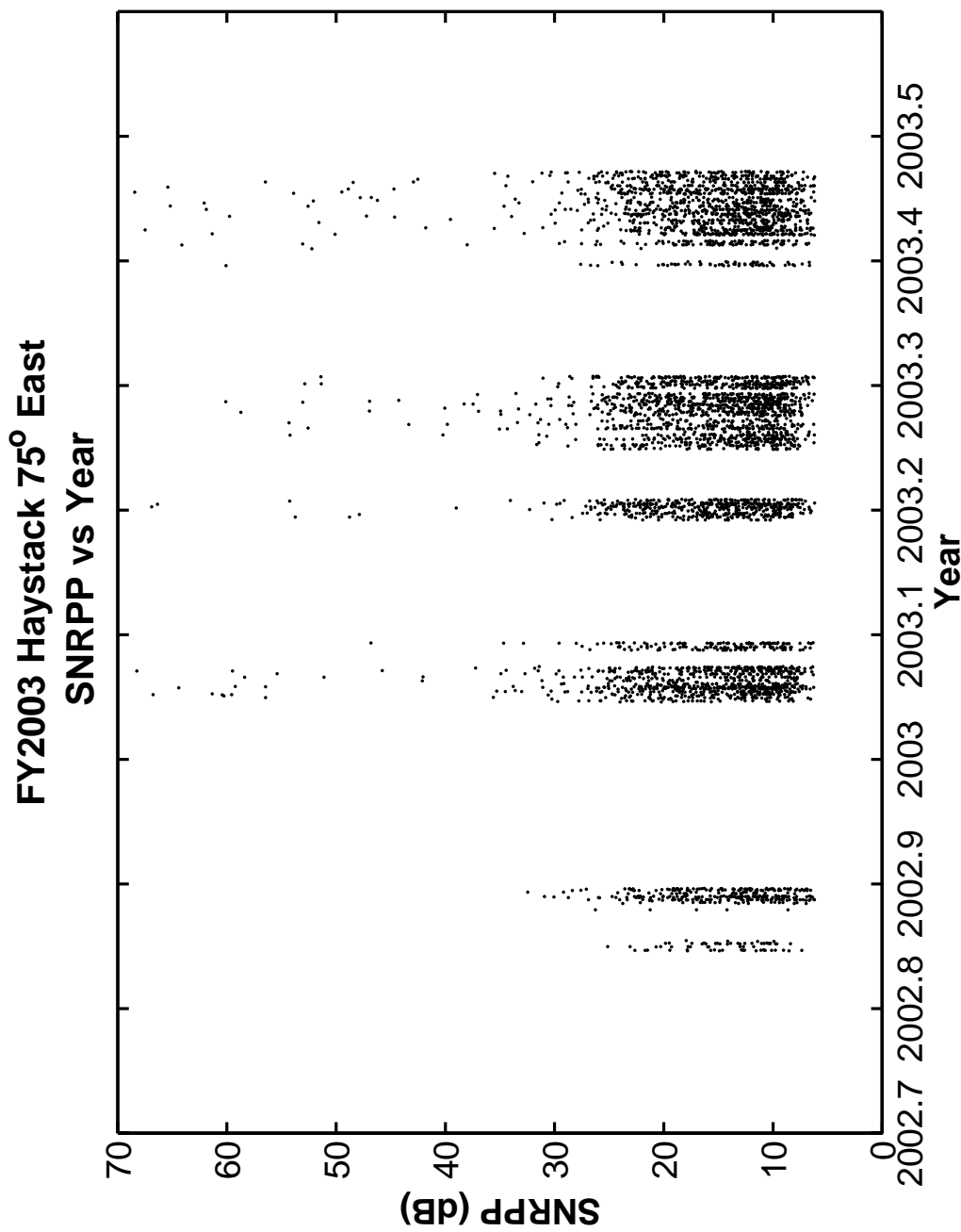


Figure 97. Haystack Principal Polarization SNR versus Observation Schedule throughout the Year.

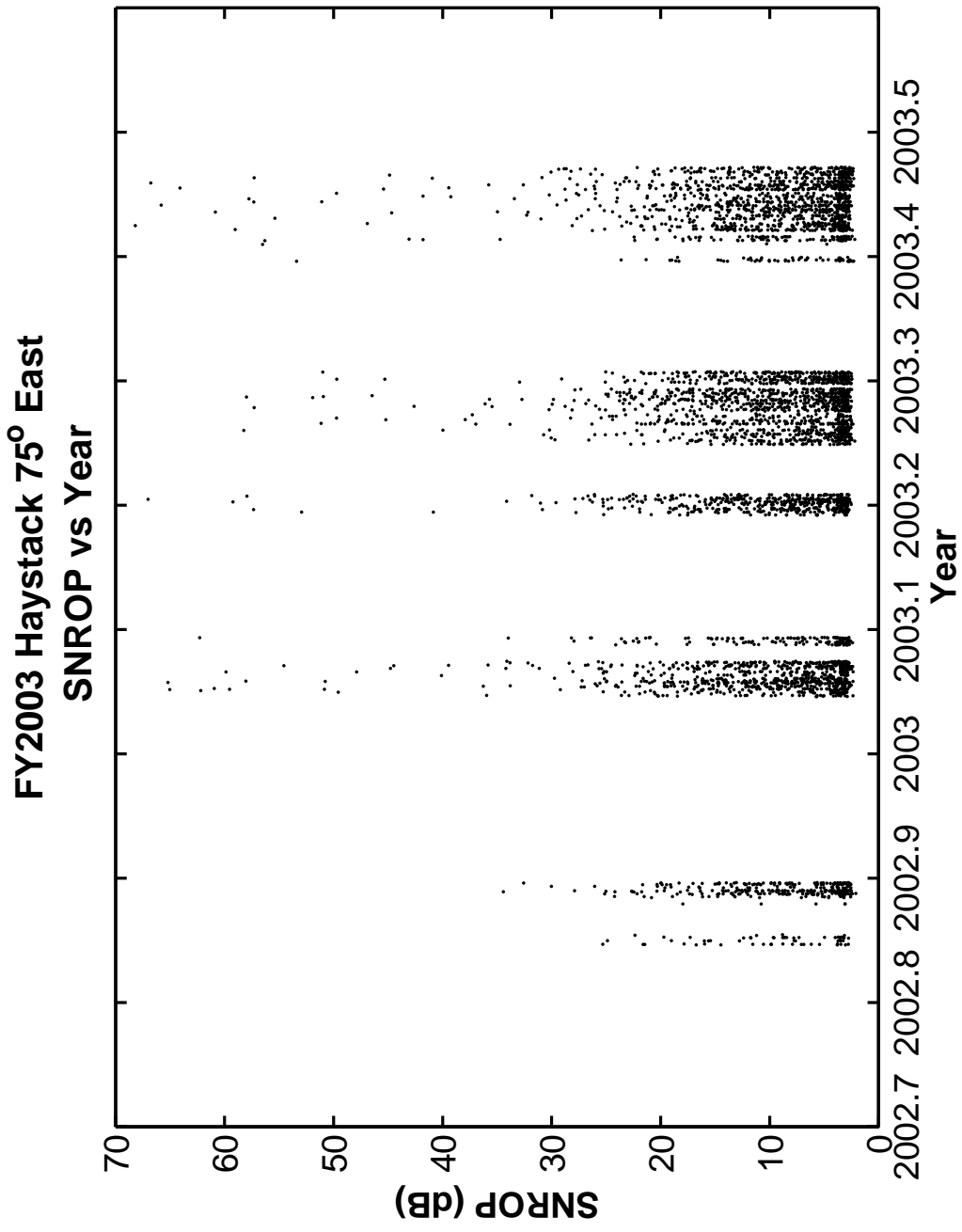


Figure 98. Haystack Orthogonal Polarization versus Observation Schedule throughout the Year.

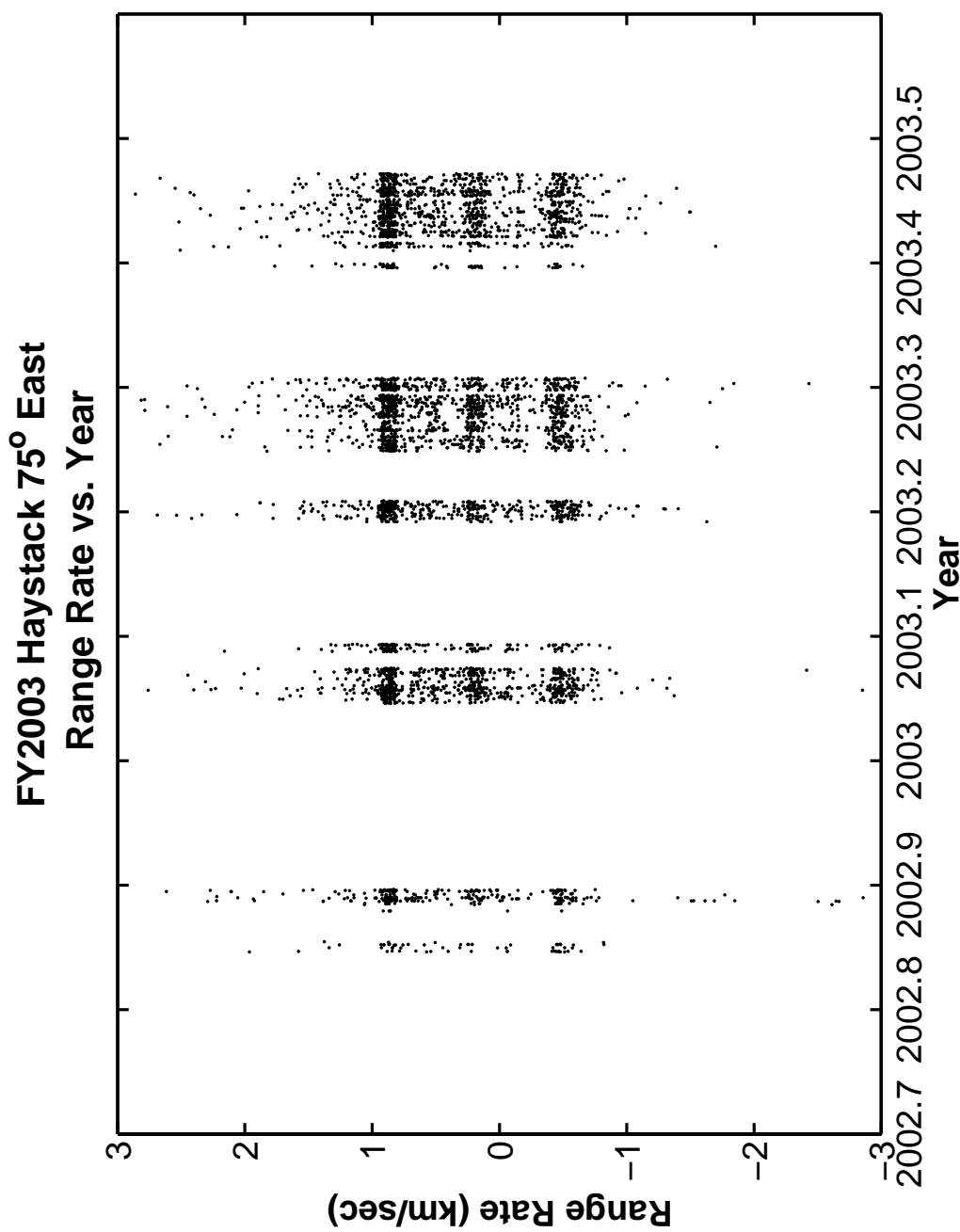


Figure 99. Haystack Range Rate versus Observation Schedule throughout the Year.

FY2003 Haystack 75° East
Polarization vs Year

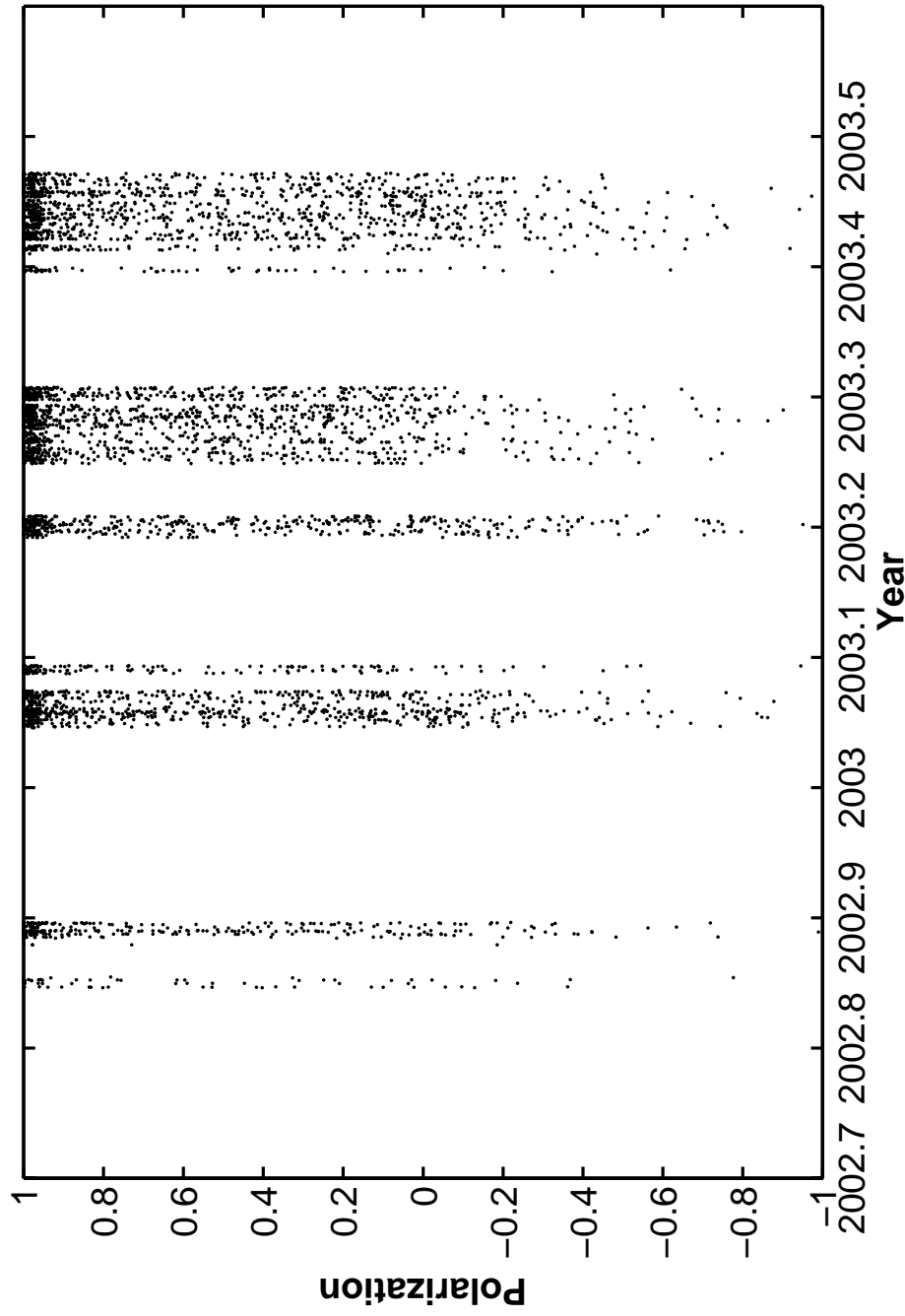


Figure 100. Haystack Radar Return Signal Polarization versus Observation Schedule throughout the Year.

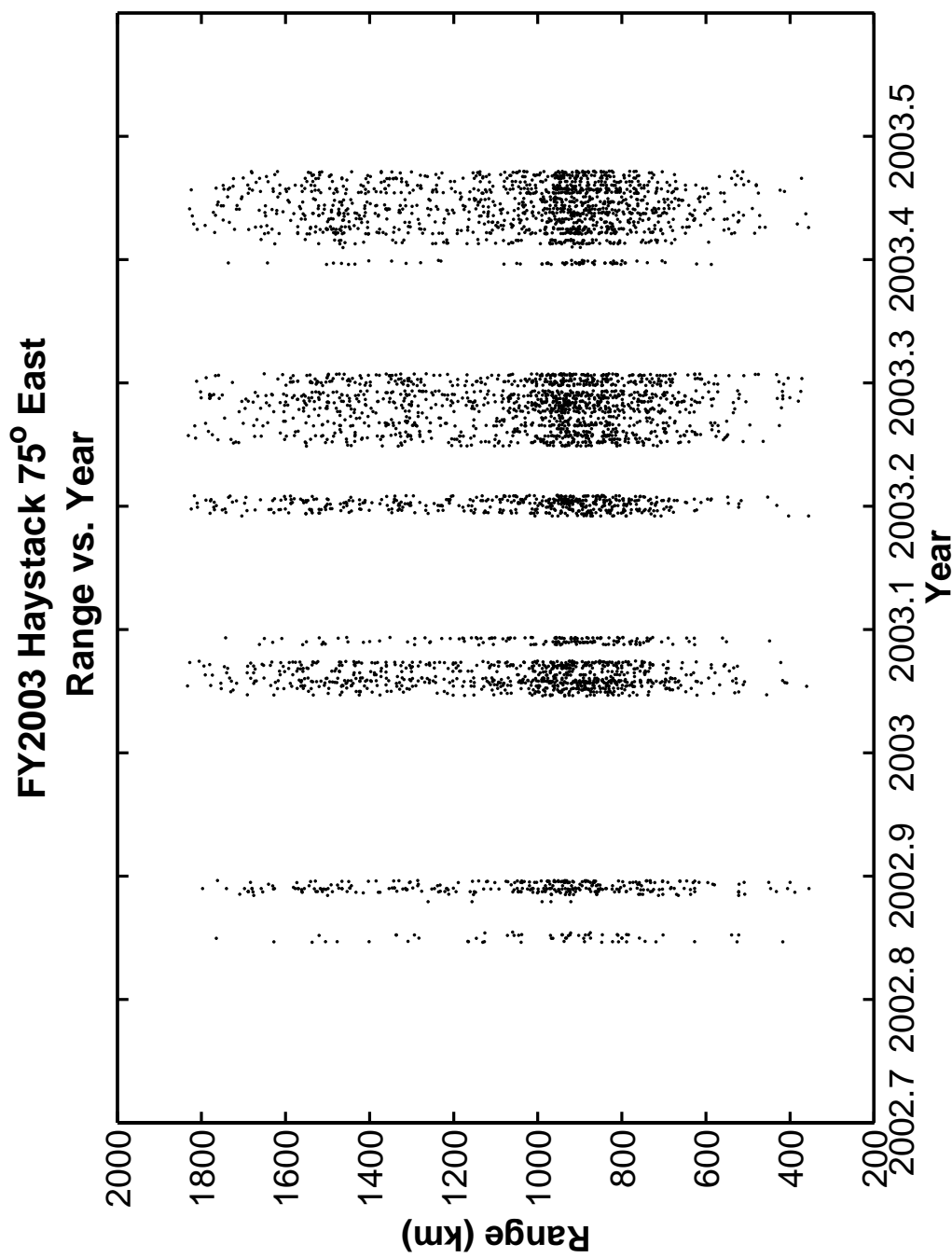


Figure 101. Haystack Range versus Observation Schedule throughout the Year.

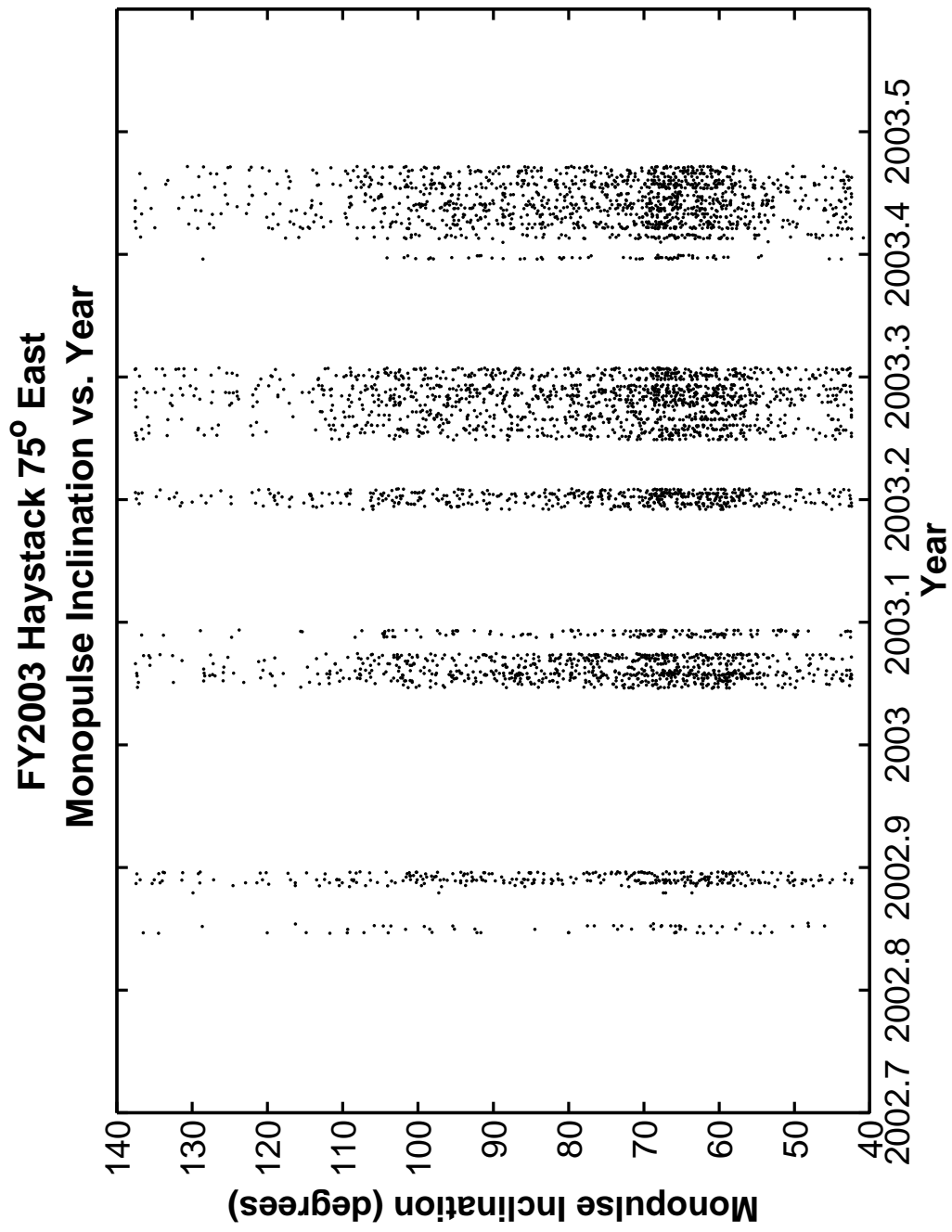


Figure 102. Haystack Monopulse Inclination versus Observation Schedule throughout the Year.

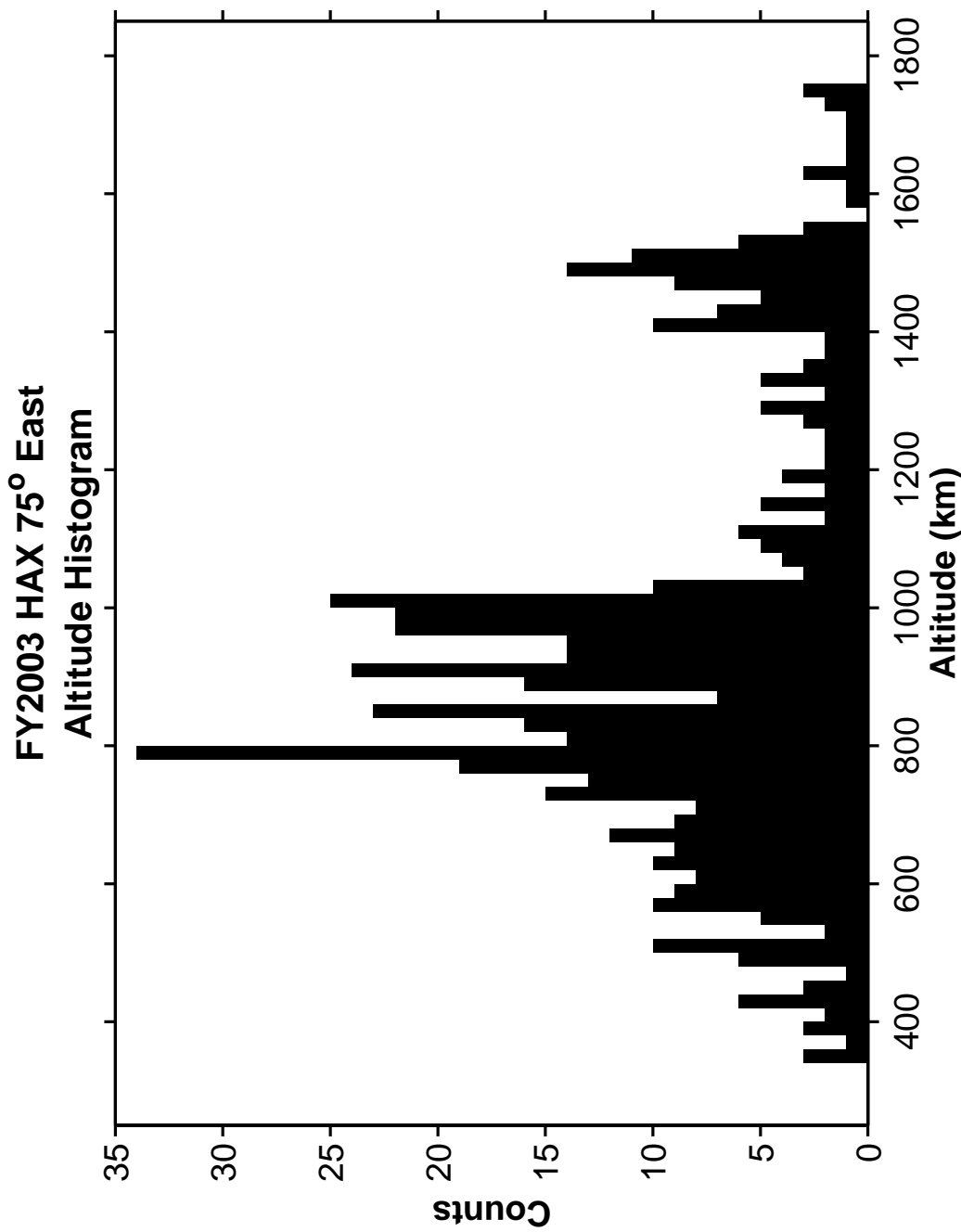


Figure 103. HAX Altitude Histogram.

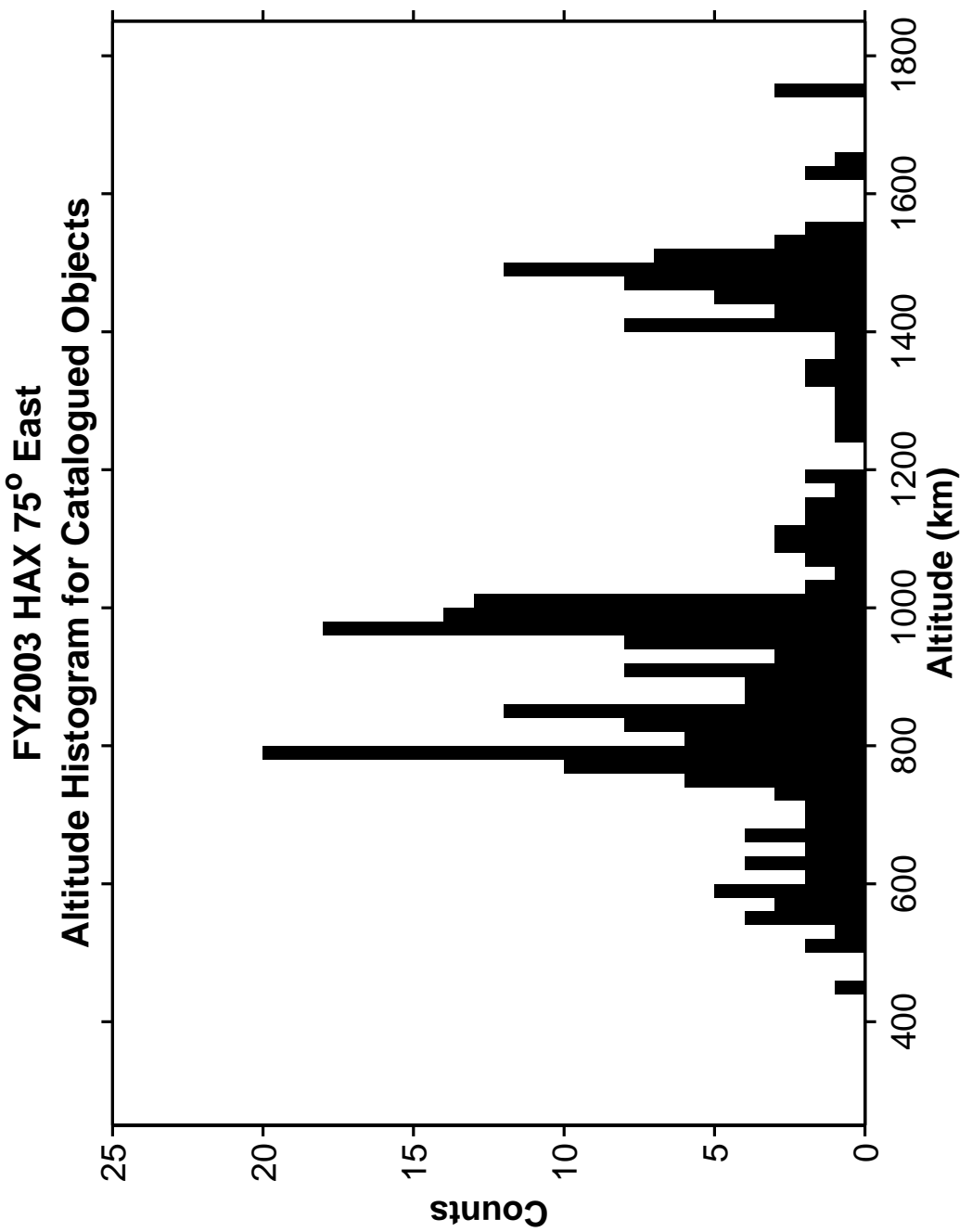


Figure 104. HAX Altitude Histogram of Catalogued Objects.

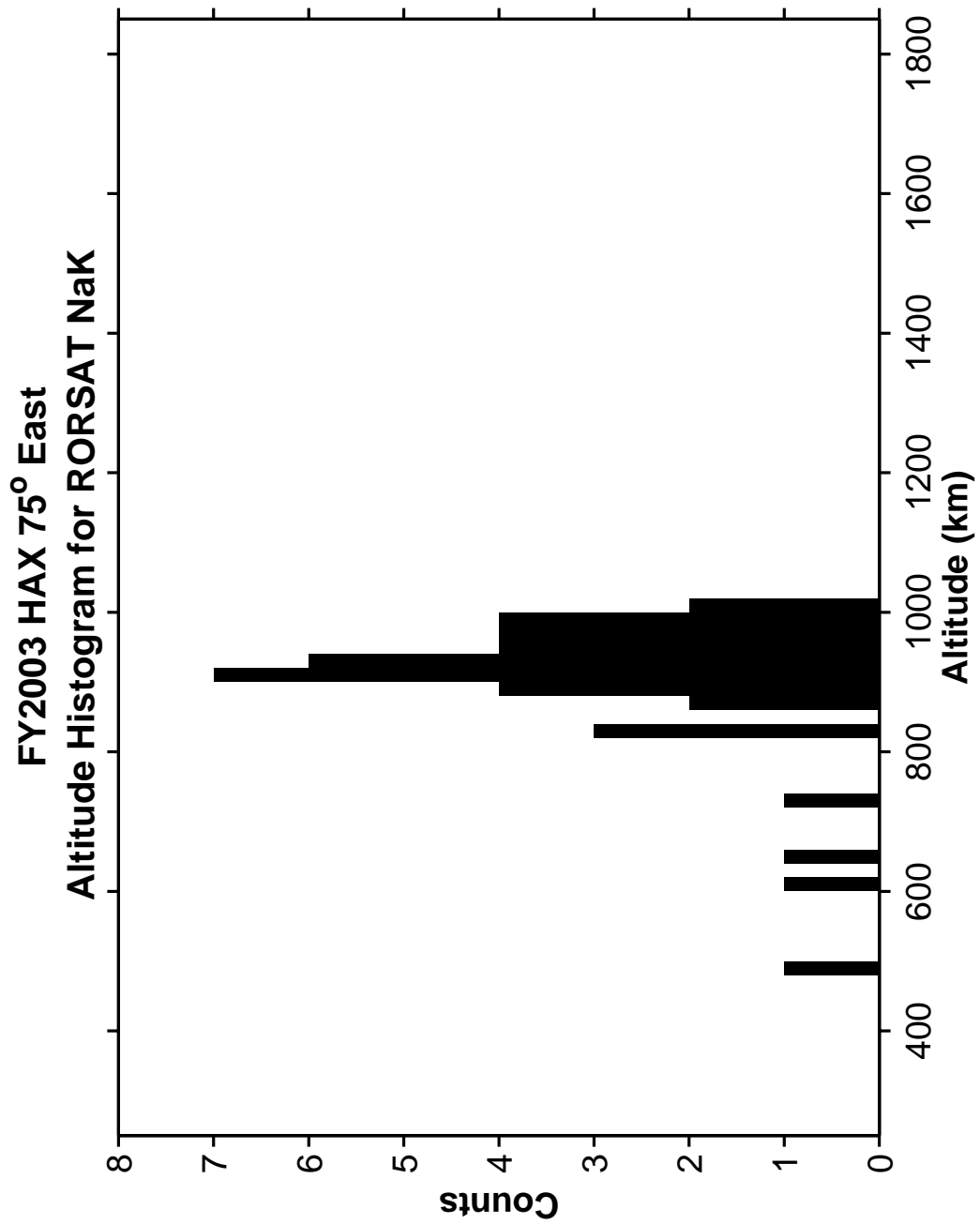


Figure 105. HAX Altitude Histogram of RORSAT NaK Debris.

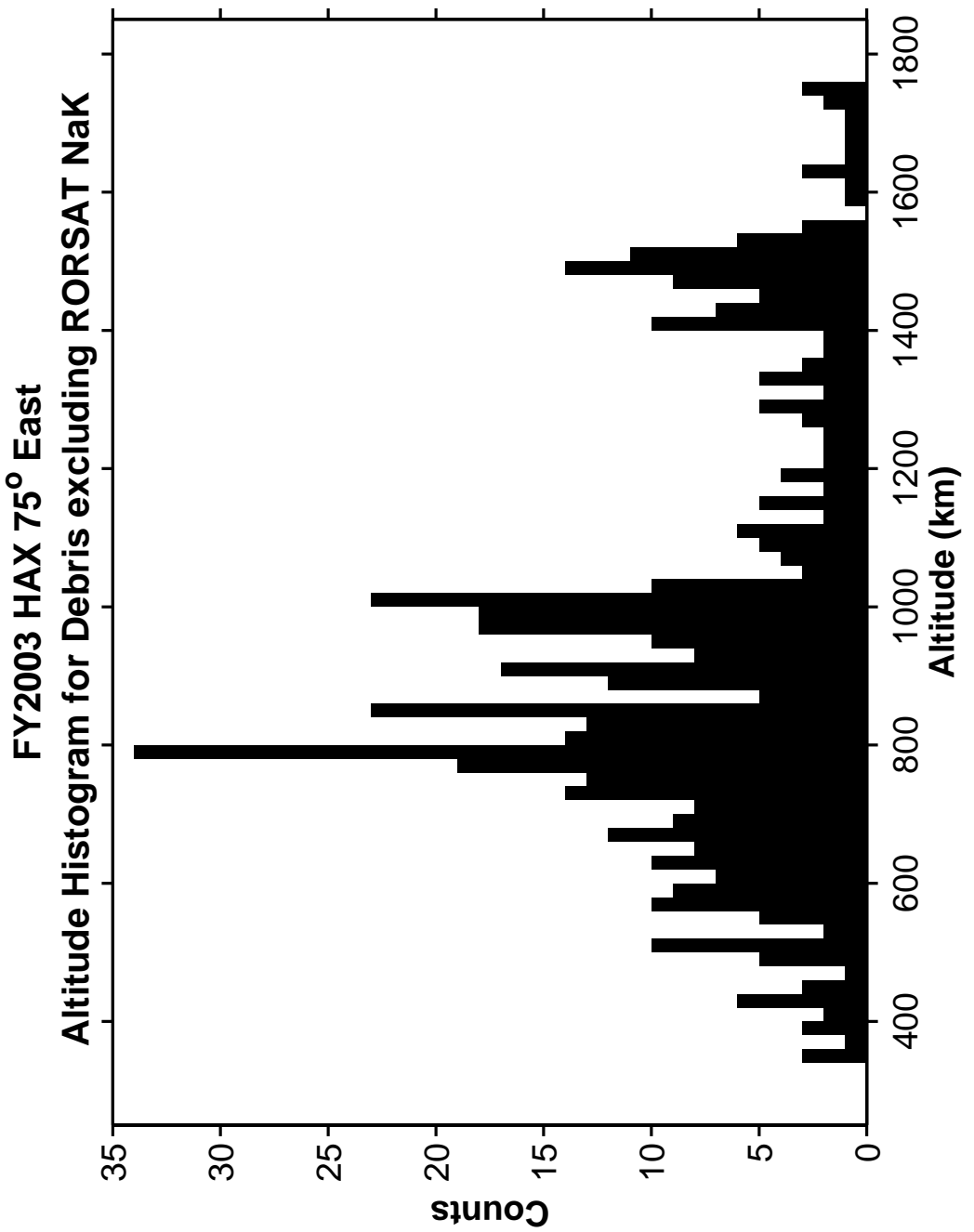


Figure 106. HAX Altitude Histogram excluding RORSAT NaK Debris.

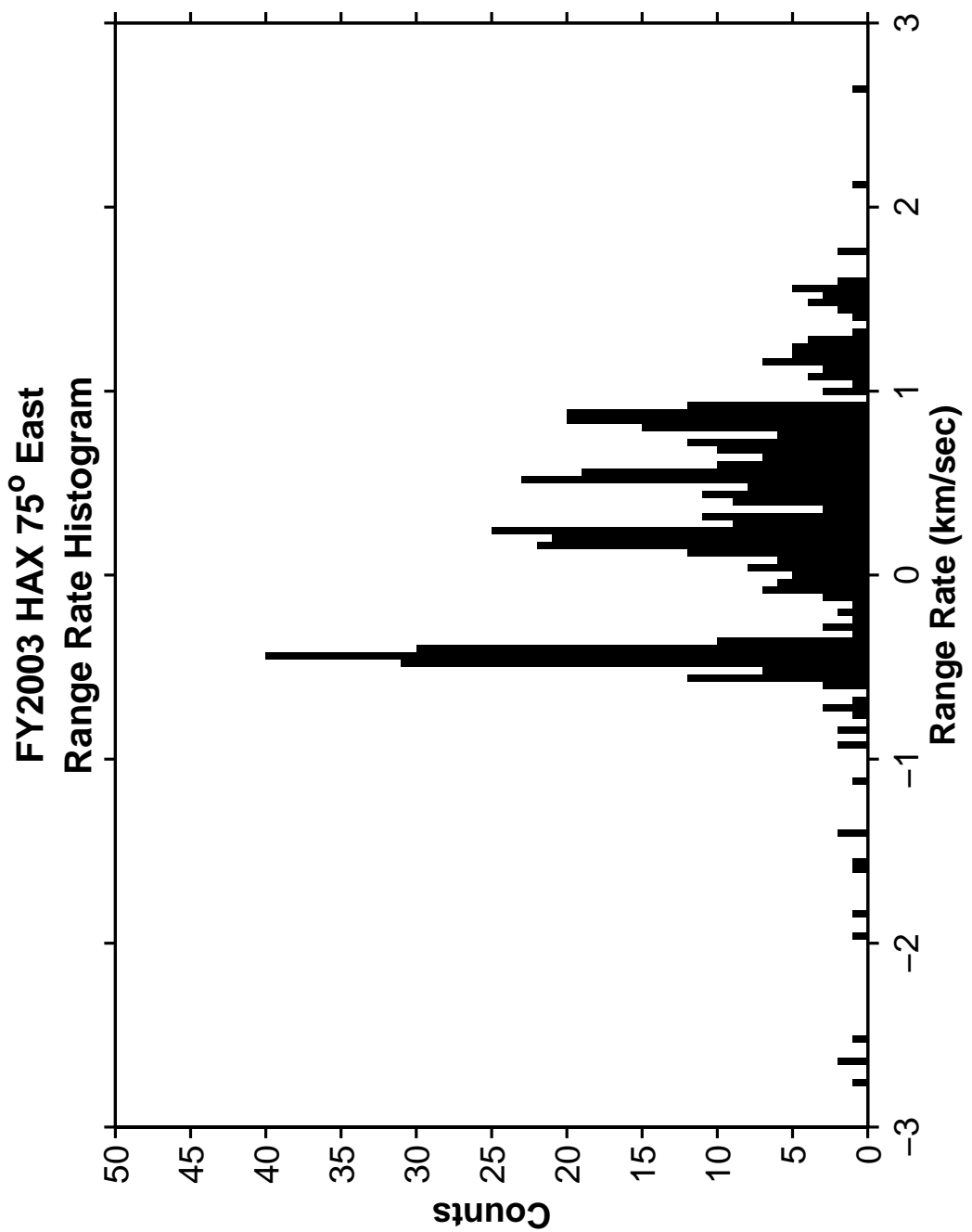


Figure 107. HAX Range Rate Histogram.

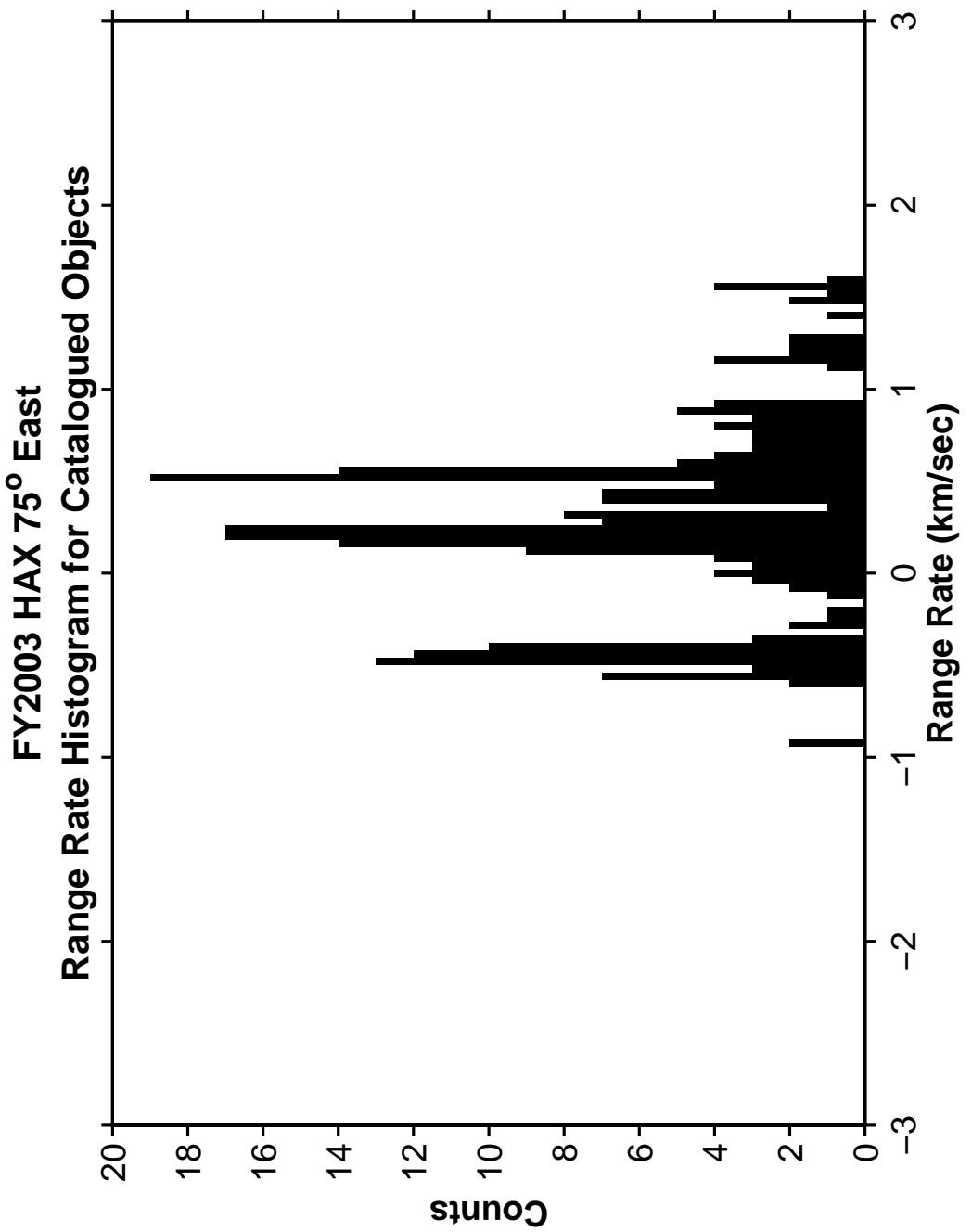


Figure 108. HAX Range Rate Histogram for Catalogued Objects.

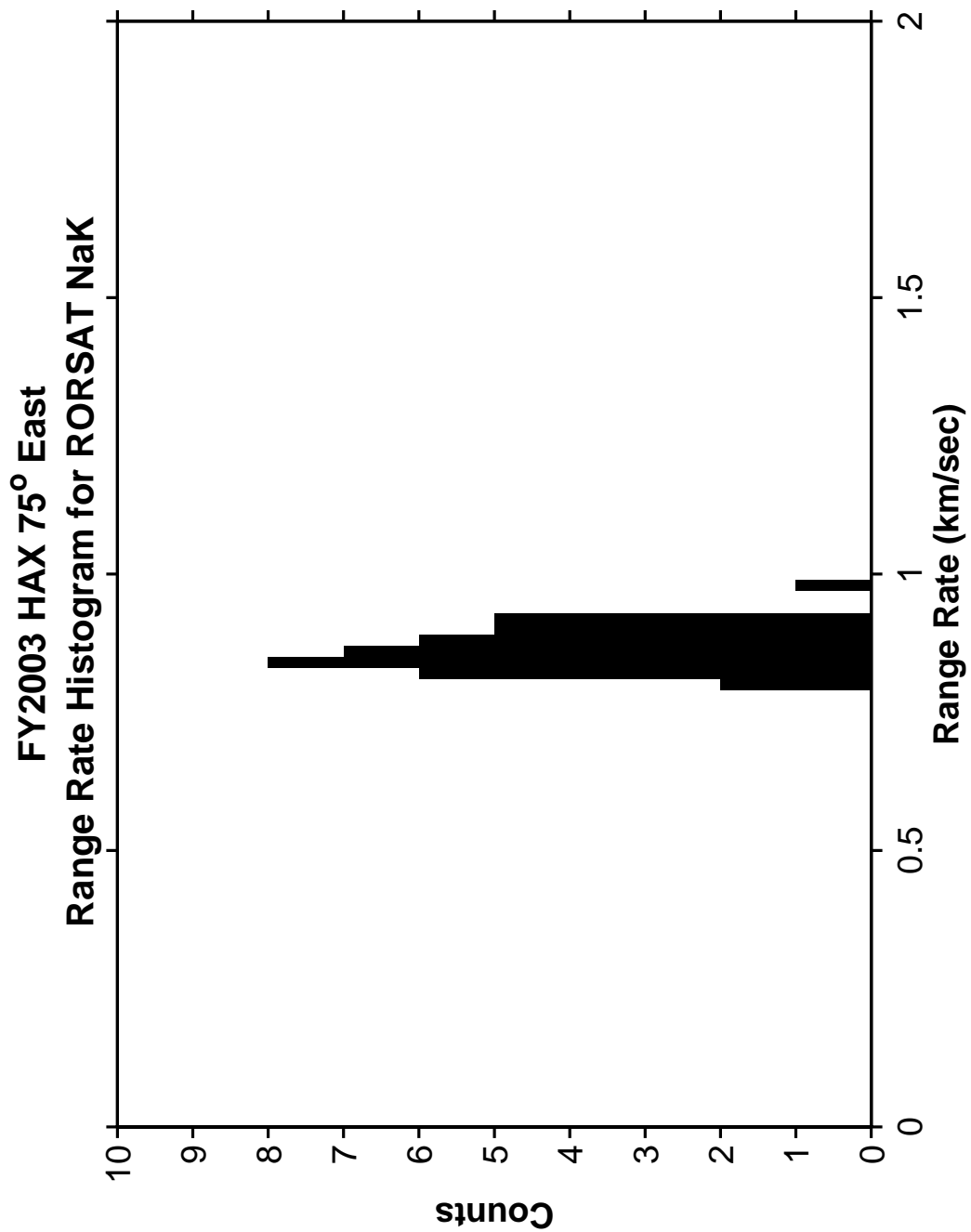


Figure 109. HAX Range Rate Histogram for RORSAT NaK Debris.

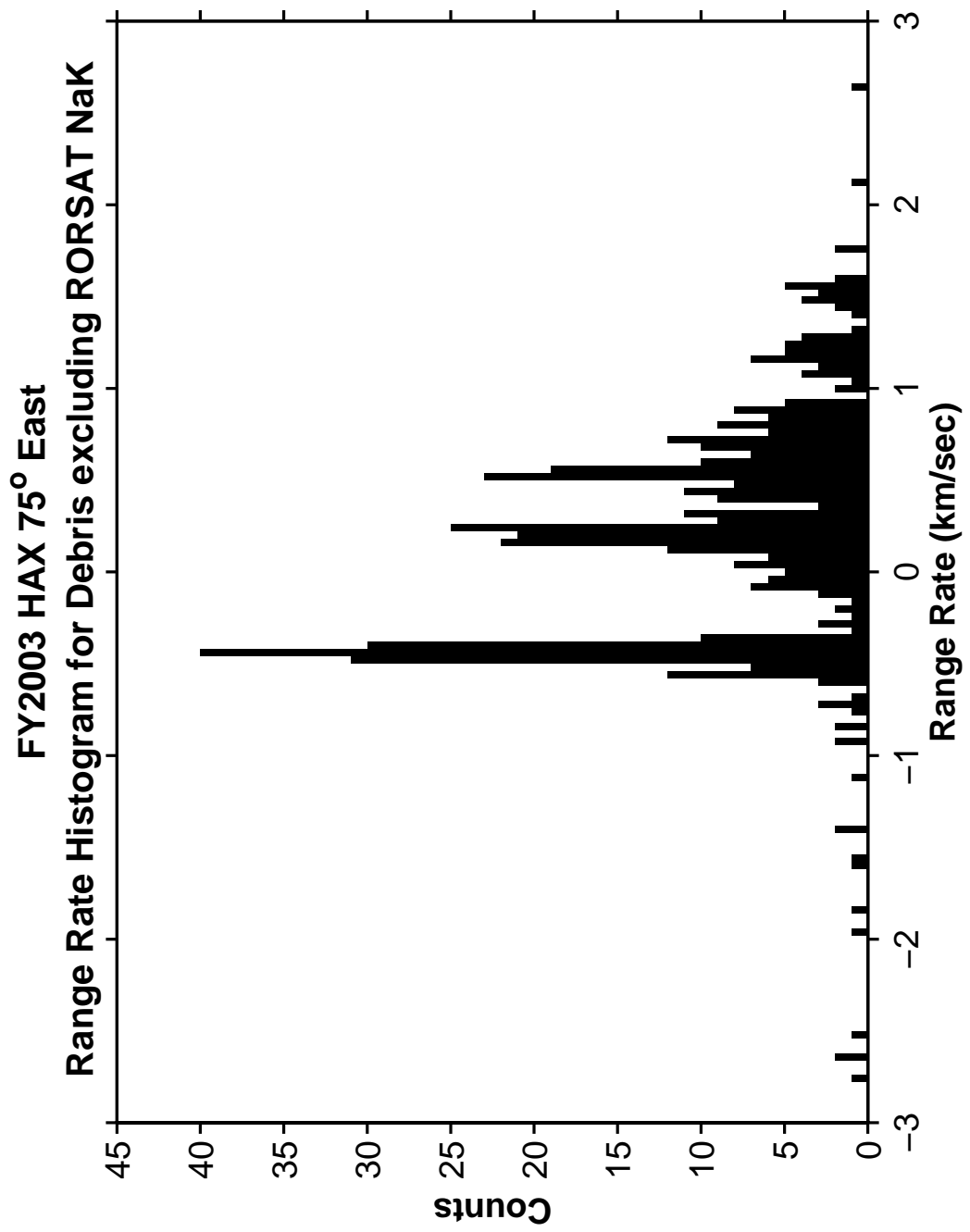


Figure 110. HAX Range Rate Histogram excluding RORSAT NaK Debris.

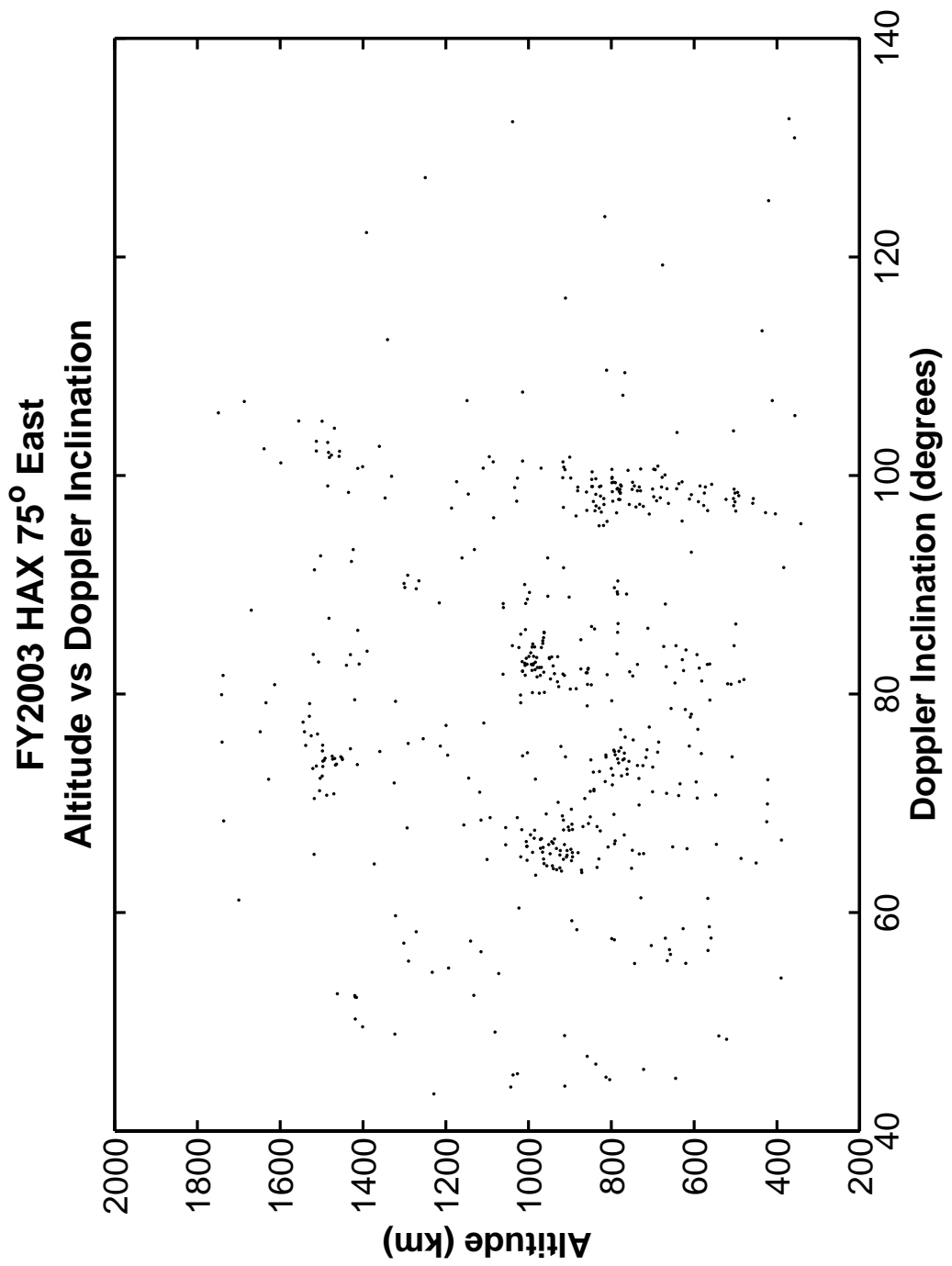


Figure 111. HAX Altitude versus Doppler Inclination.

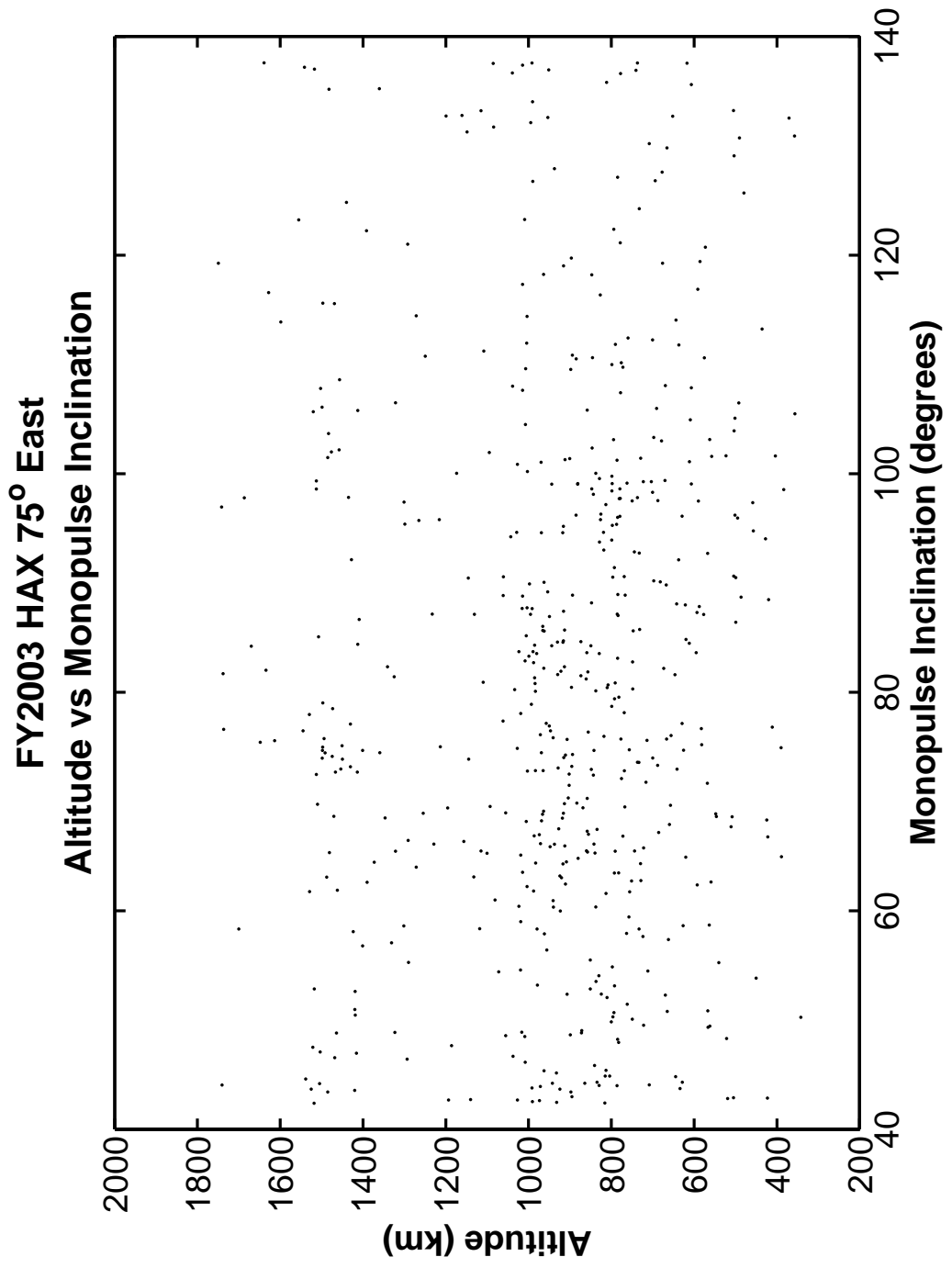


Figure 112. HAX Altitude versus Monopulse Inclination.

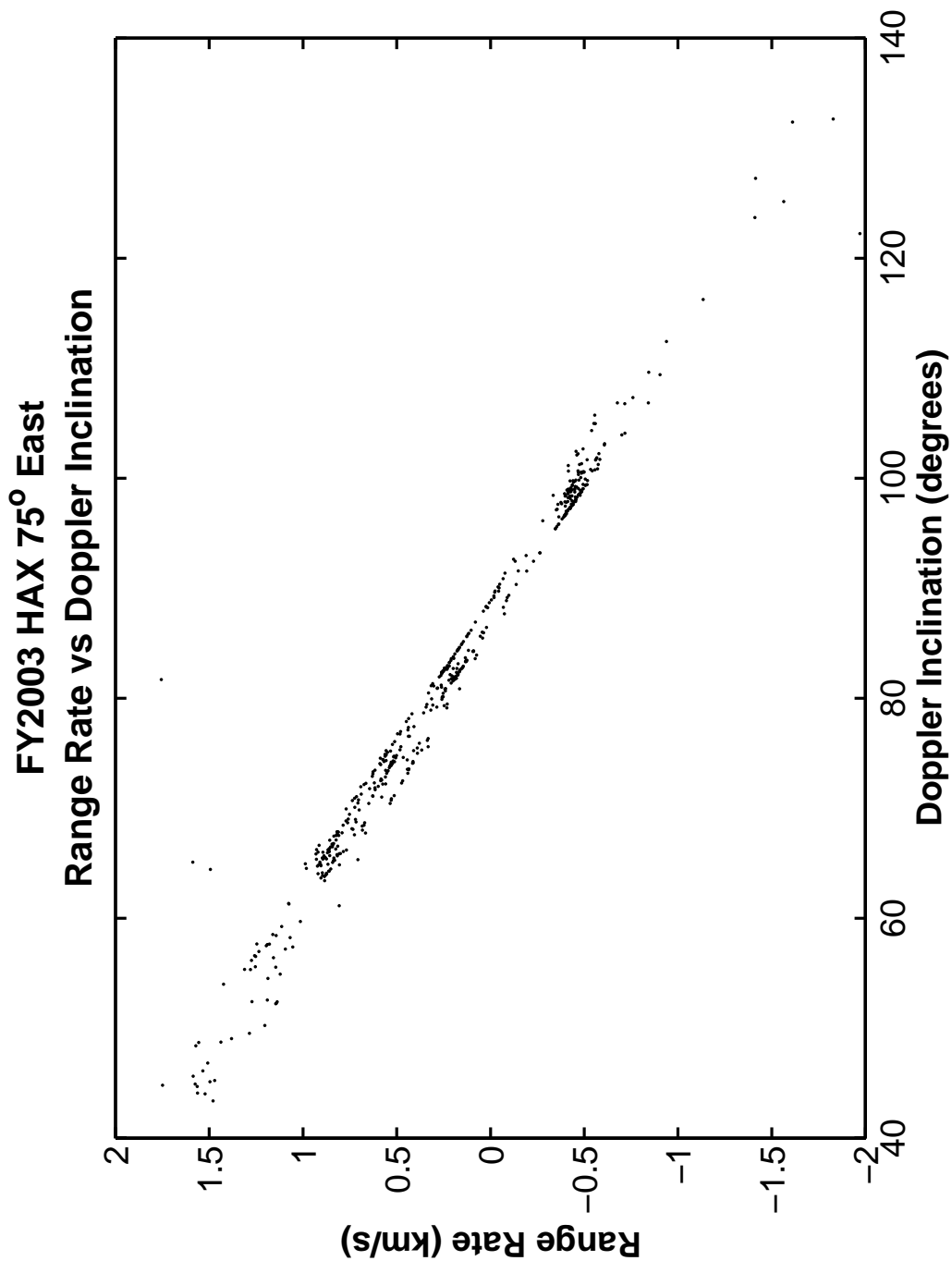


Figure 113. HAX Range Rate versus Doppler Inclination.

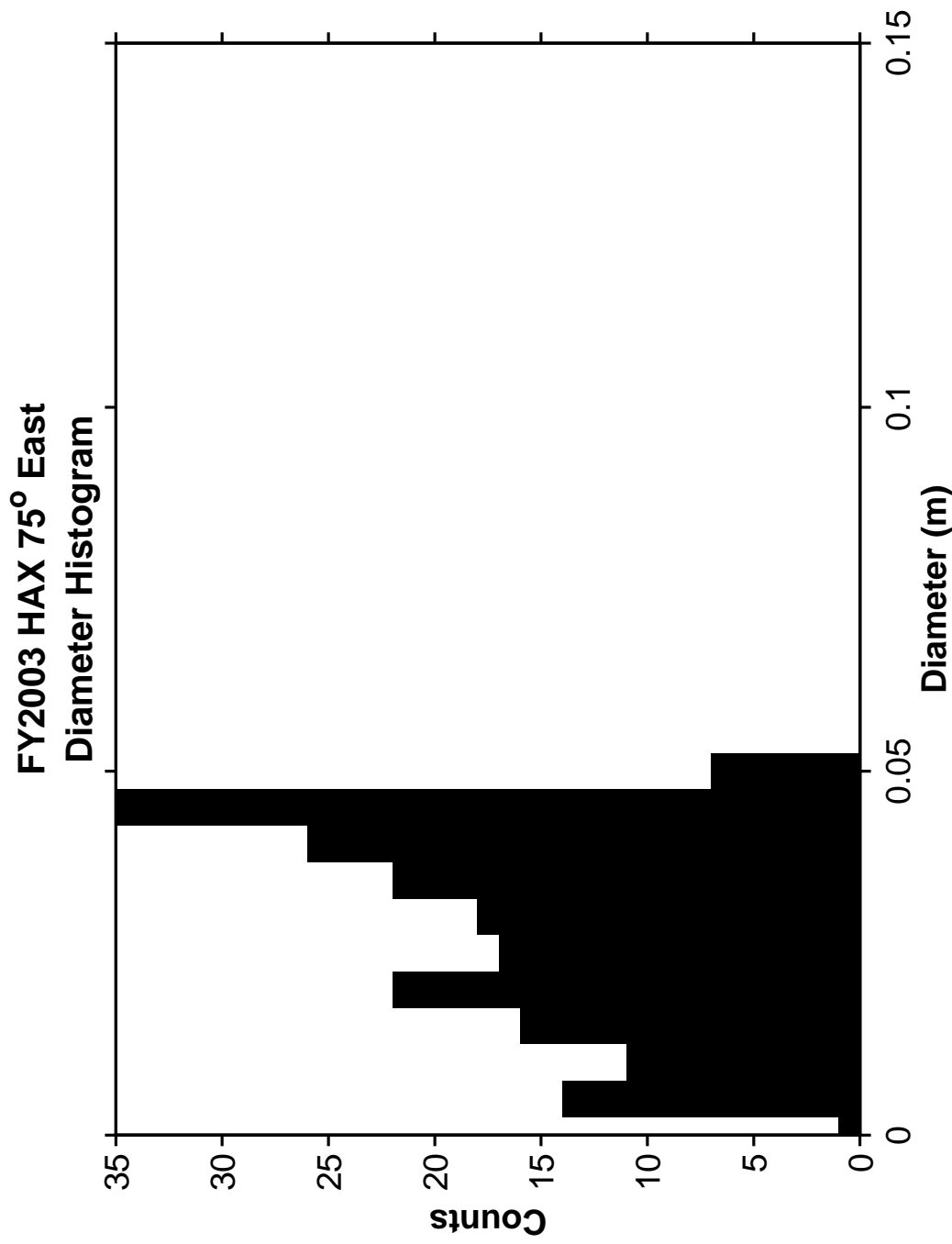


Figure 114. HAX Diameter Histogram.

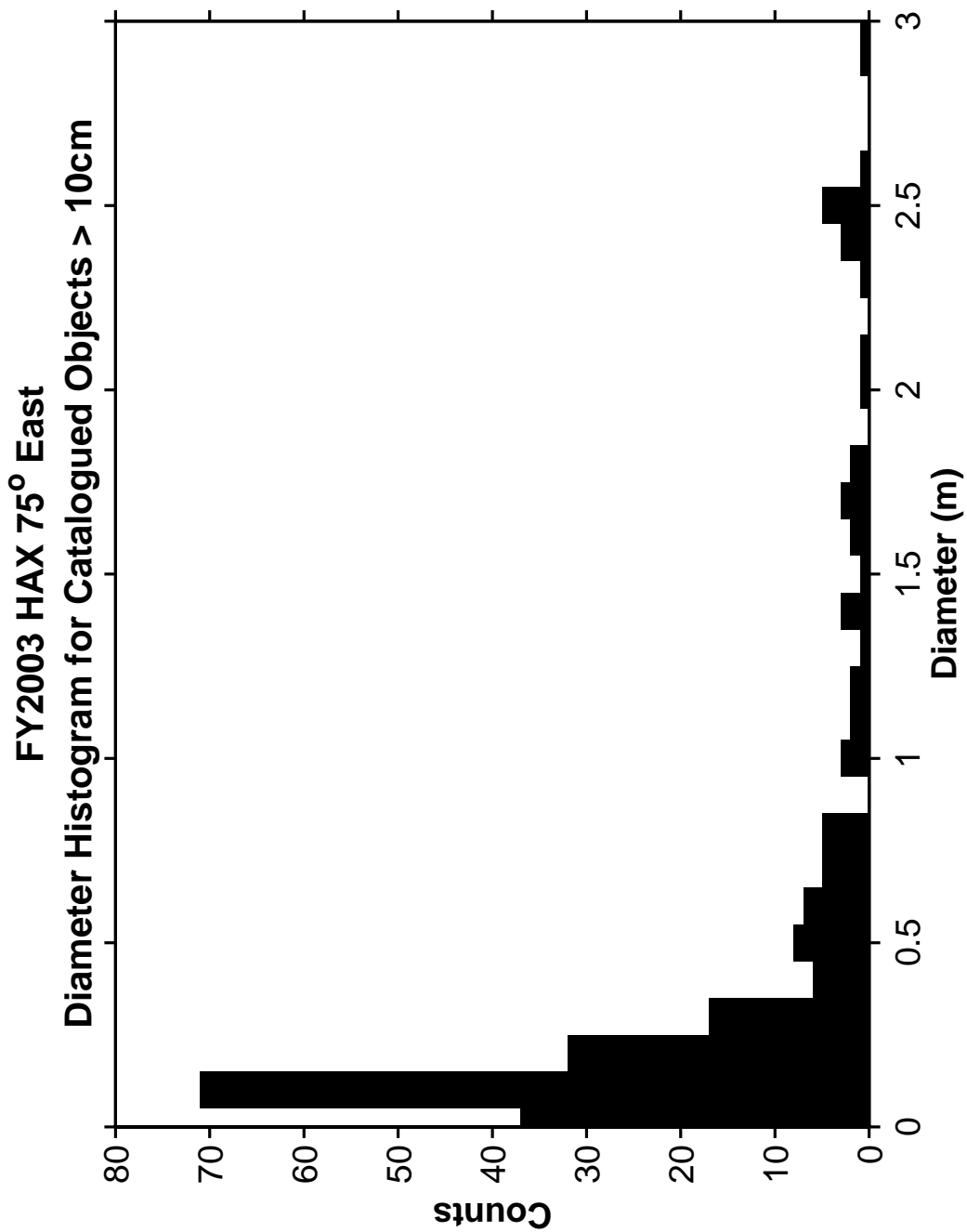


Figure 115. HAX Diameter Histogram for Catalogued Objects > 10 cm.

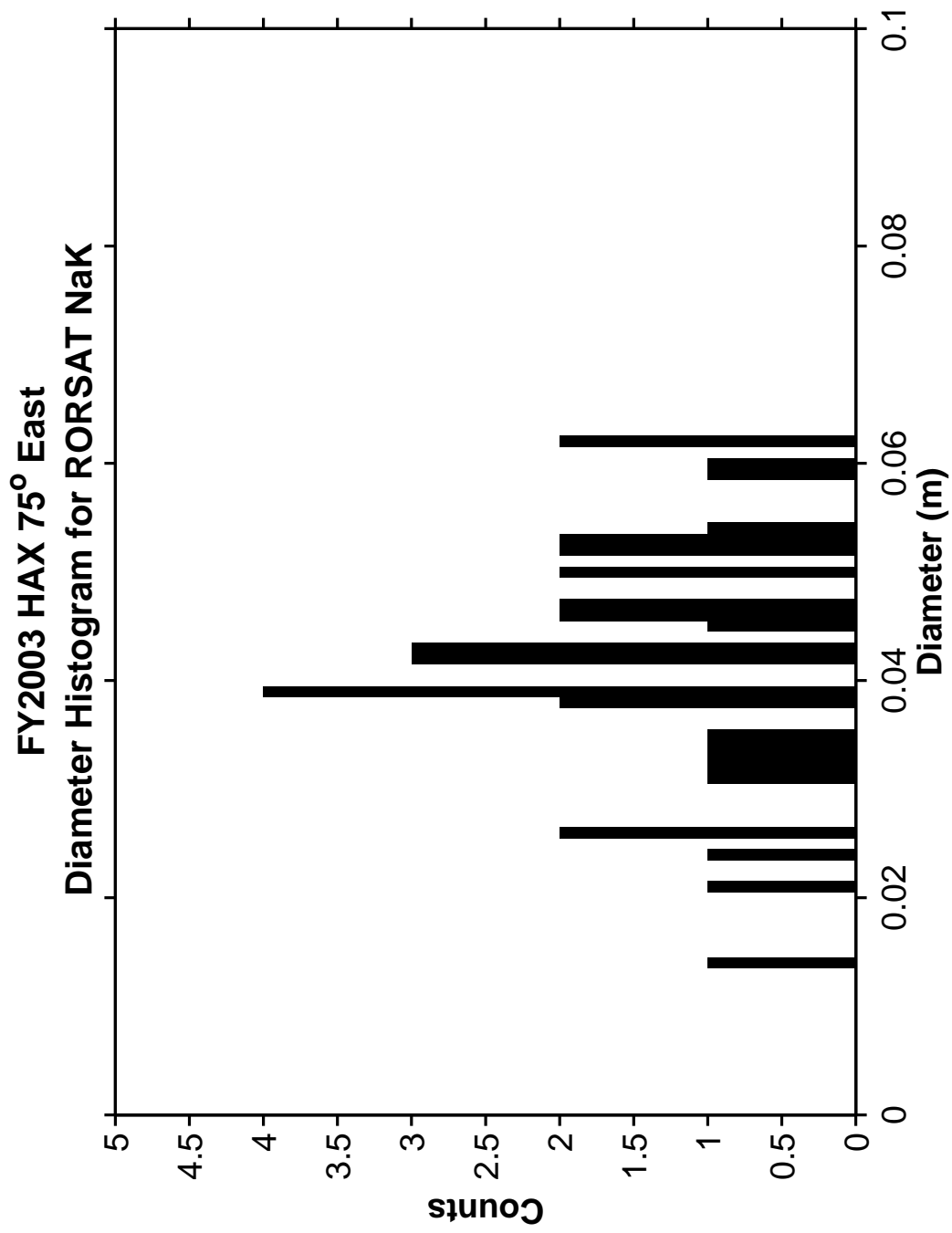


Figure 116. HAX Diameter Histogram for RORSAT NaK Debris.

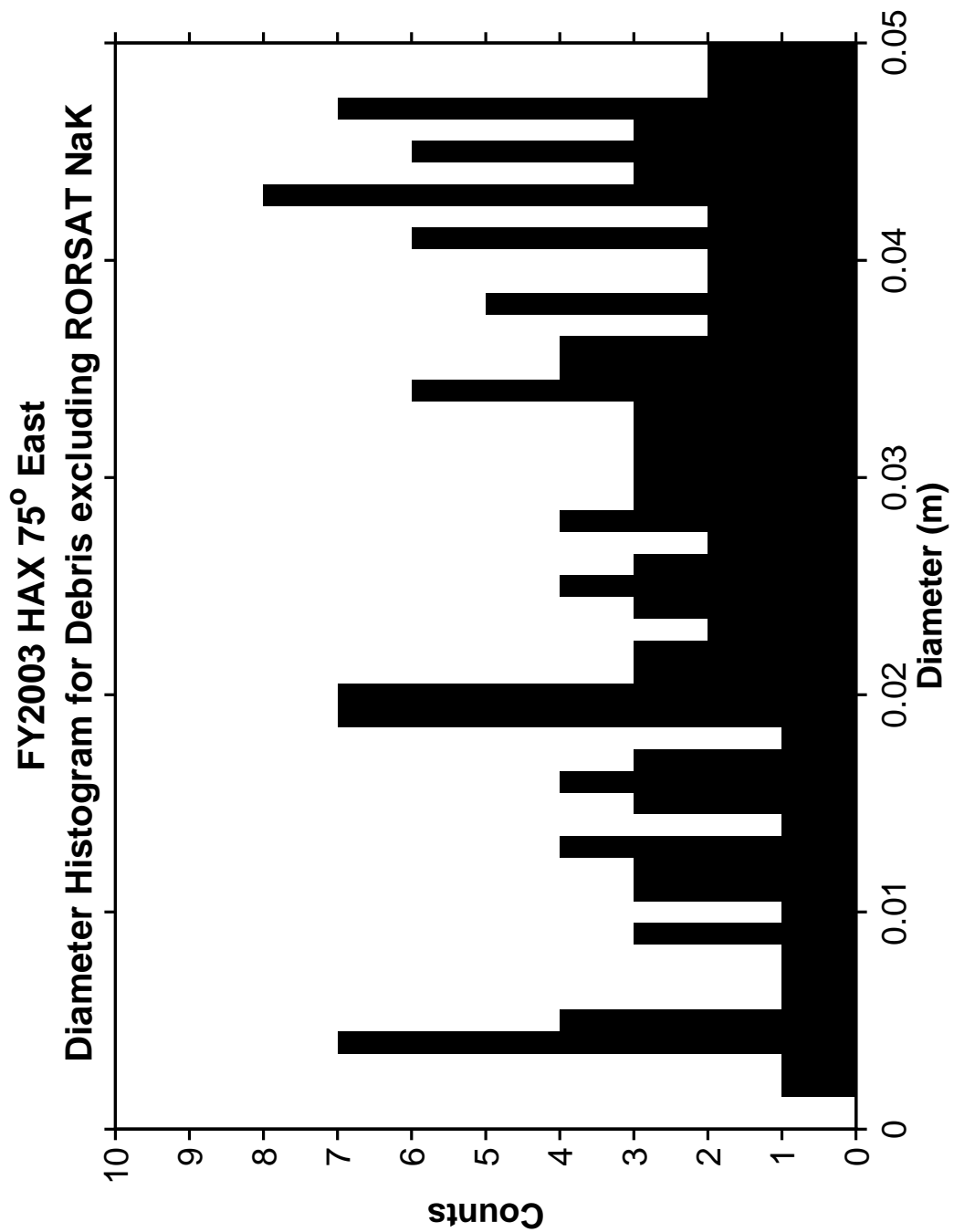


Figure 117. HAX Diameter Histogram excluding RORSAT NaK Debris.

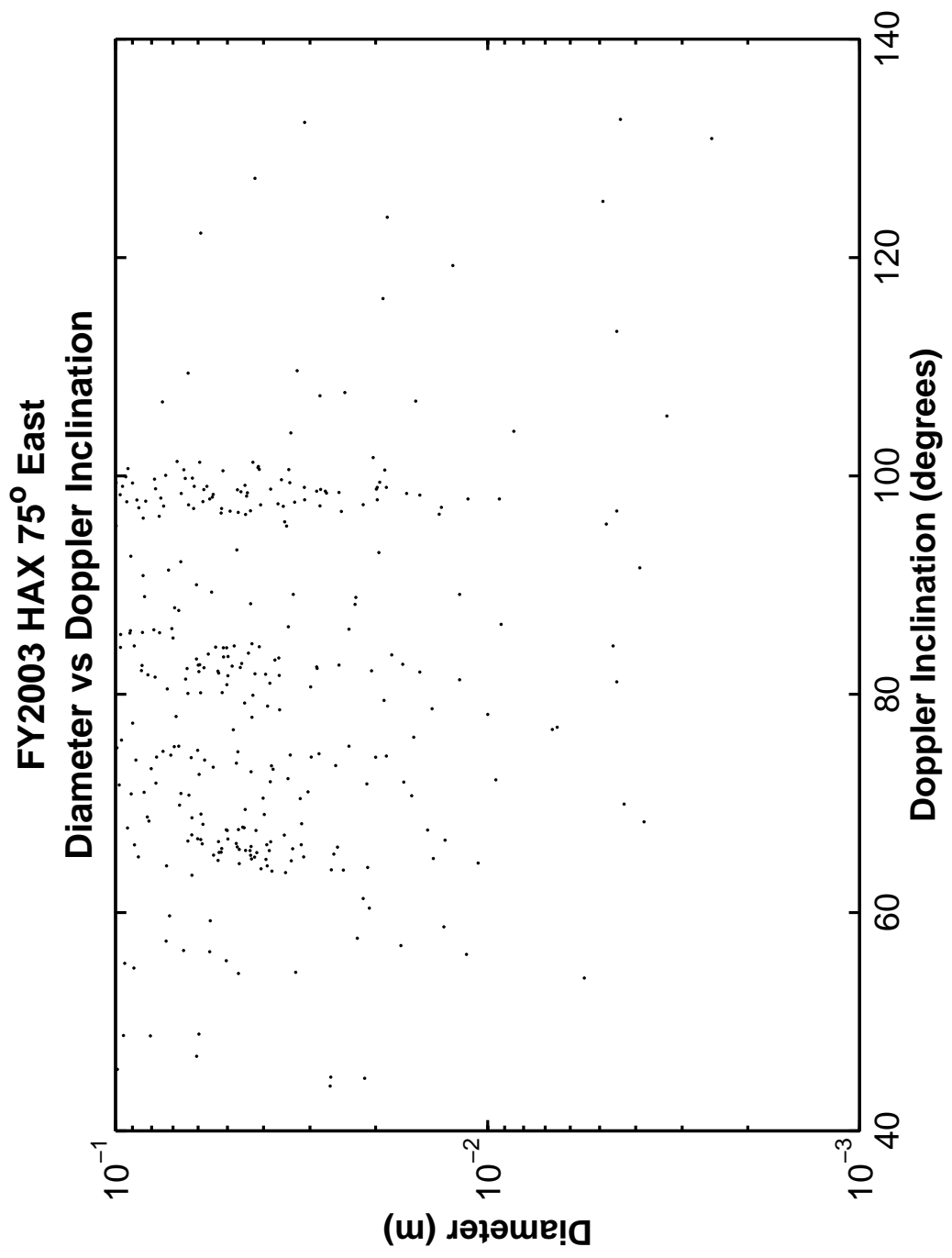


Figure 118. HAX Diameter versus Doppler Inclination.

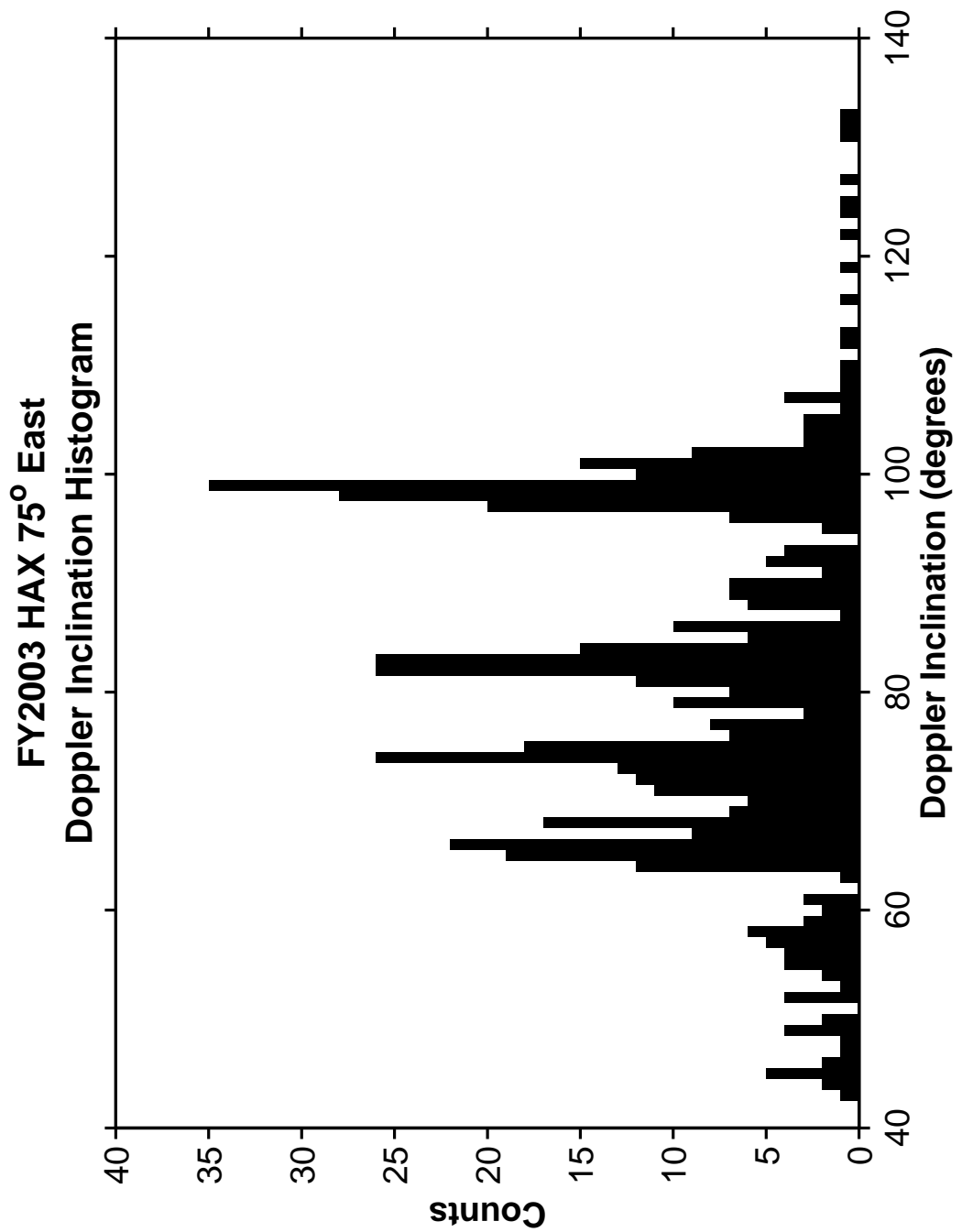


Figure 119. HAX Doppler Inclination Histogram.

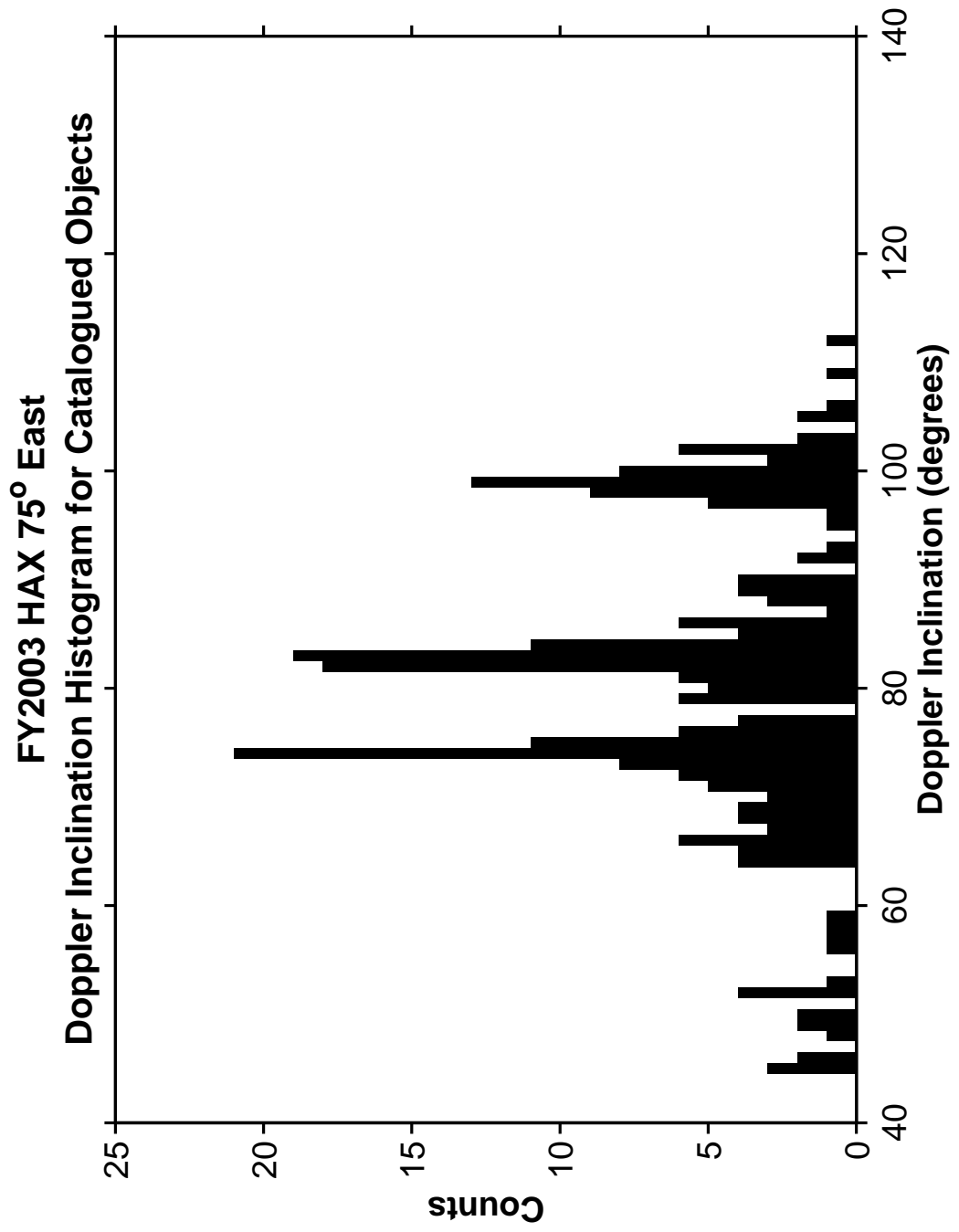


Figure 120. HAX Doppler Inclination Histogram for Catalogued Objects.

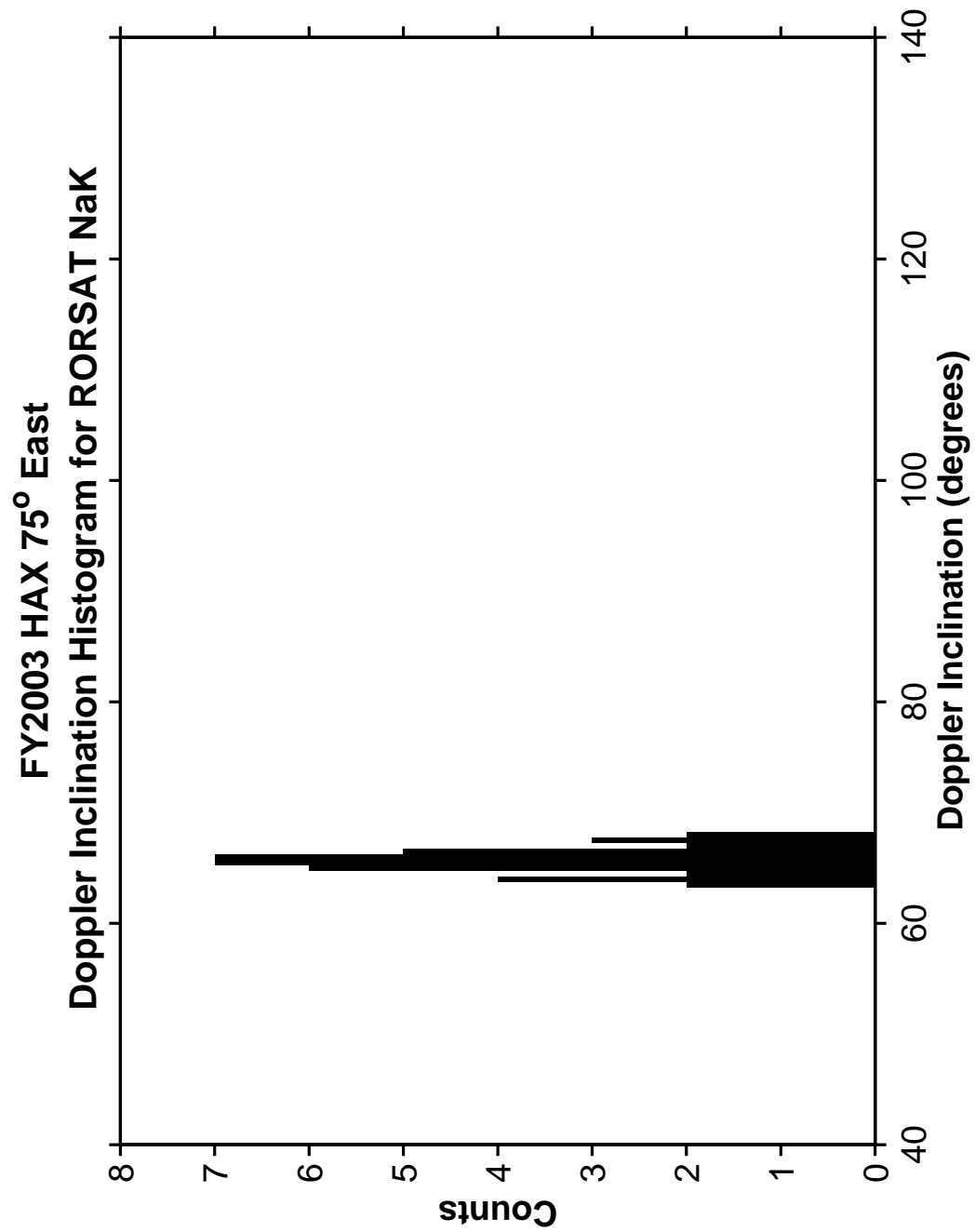


Figure 121. HAX Doppler Inclination Histogram for RORSAT NaK Debris.

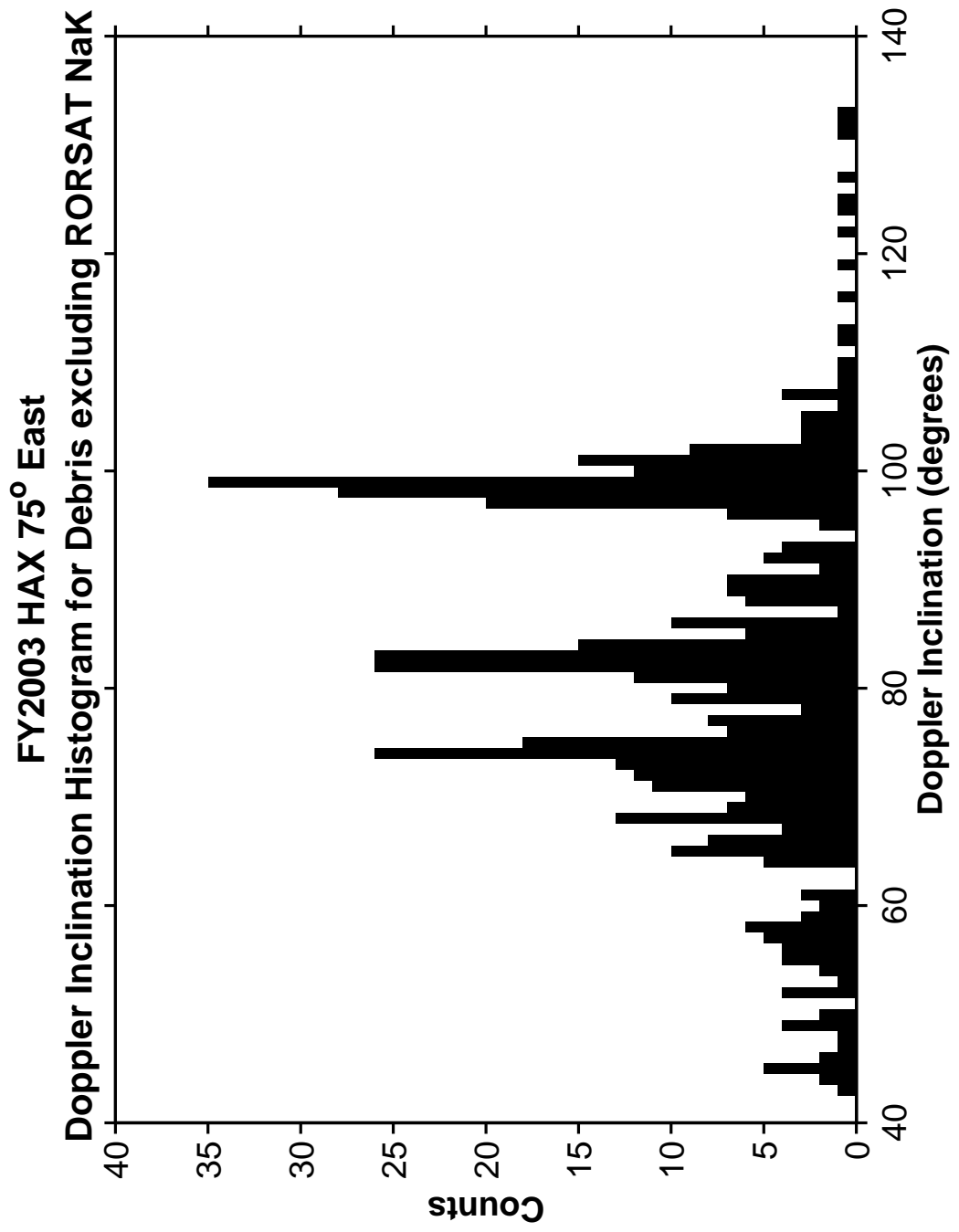


Figure 122. HAX Doppler Inclination Histogram excluding RORSAT NaK Debris.

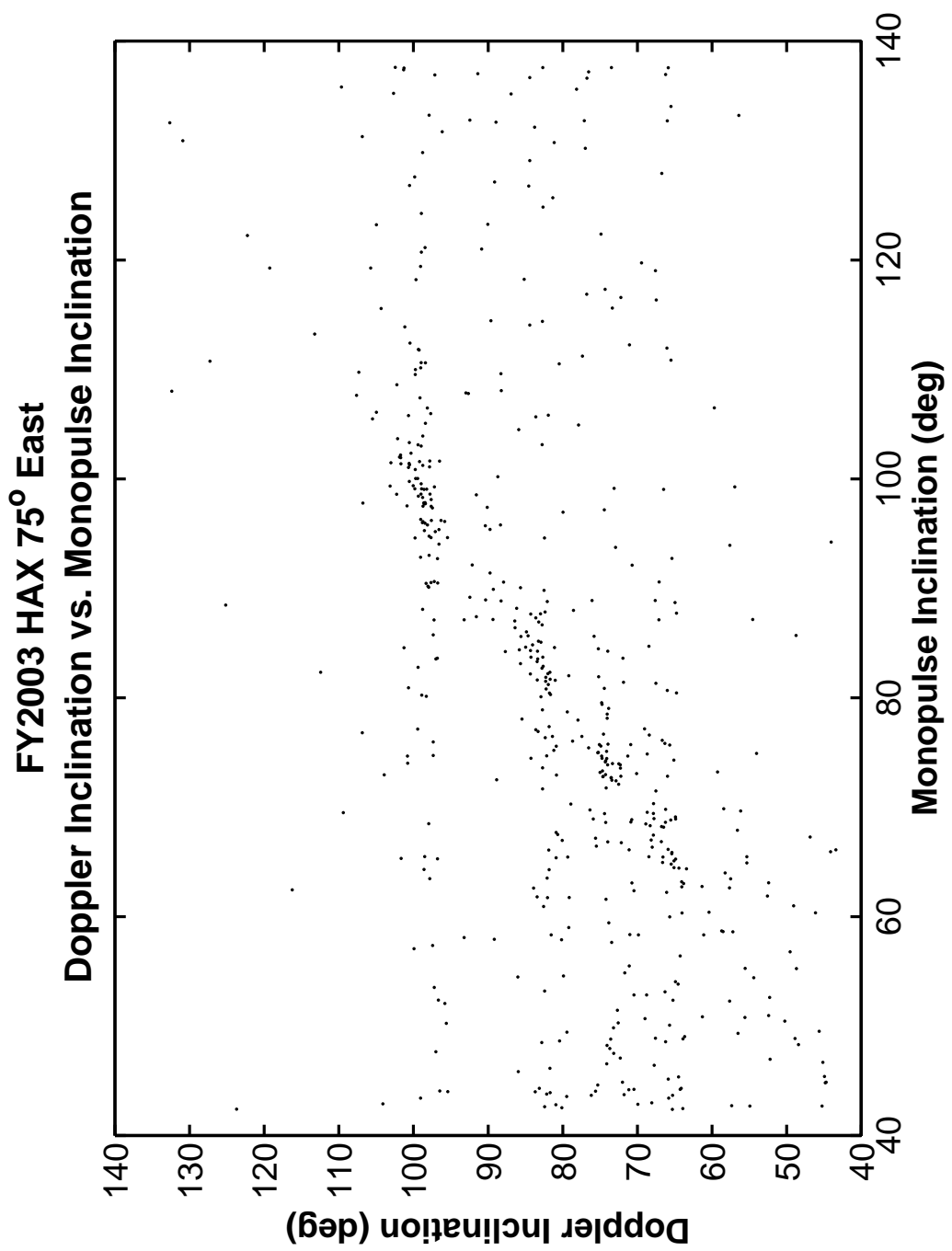


Figure 123. HAX Doppler Inclination versus Monopulse Inclination.

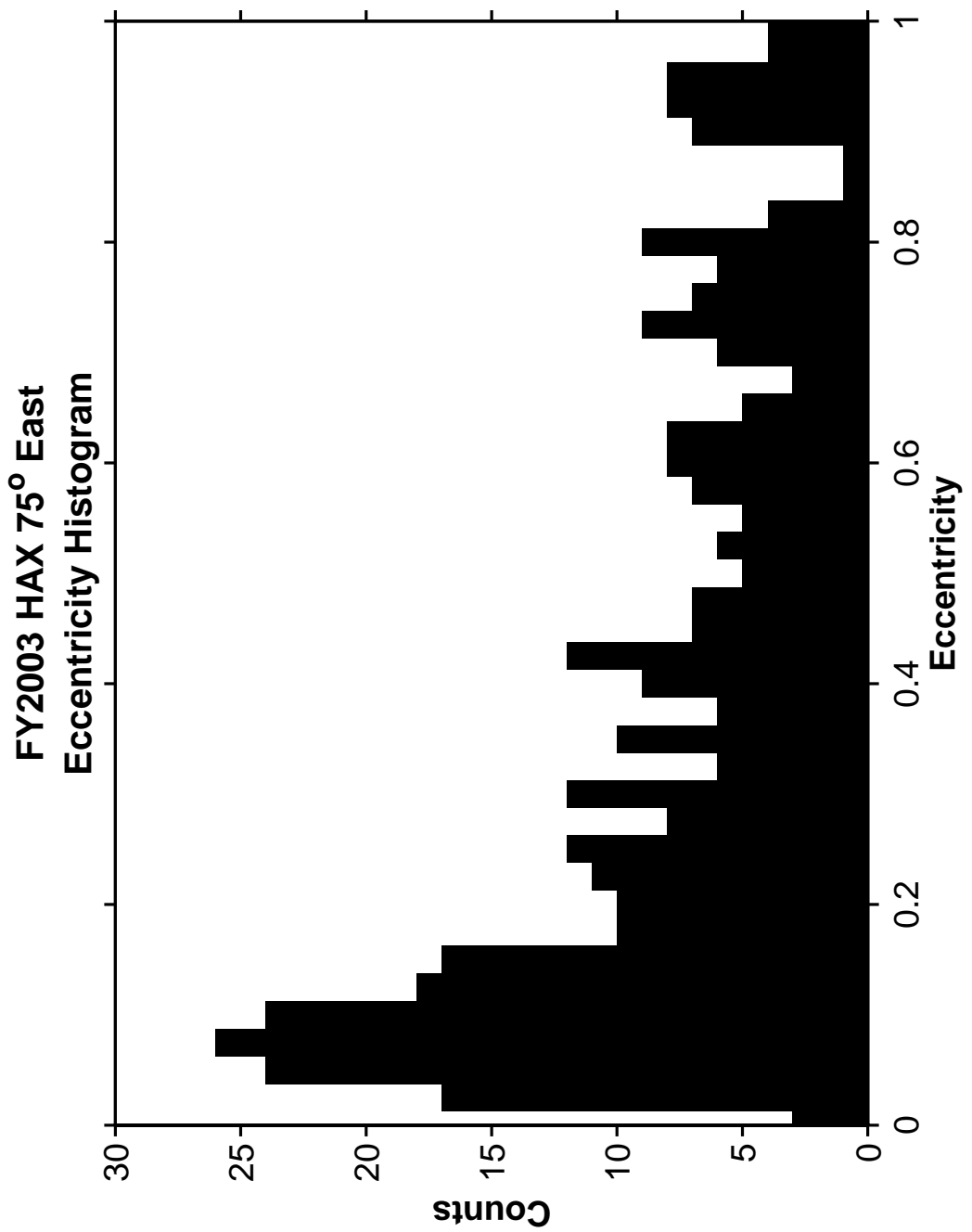


Figure 124. HAX Eccentricity Histogram.

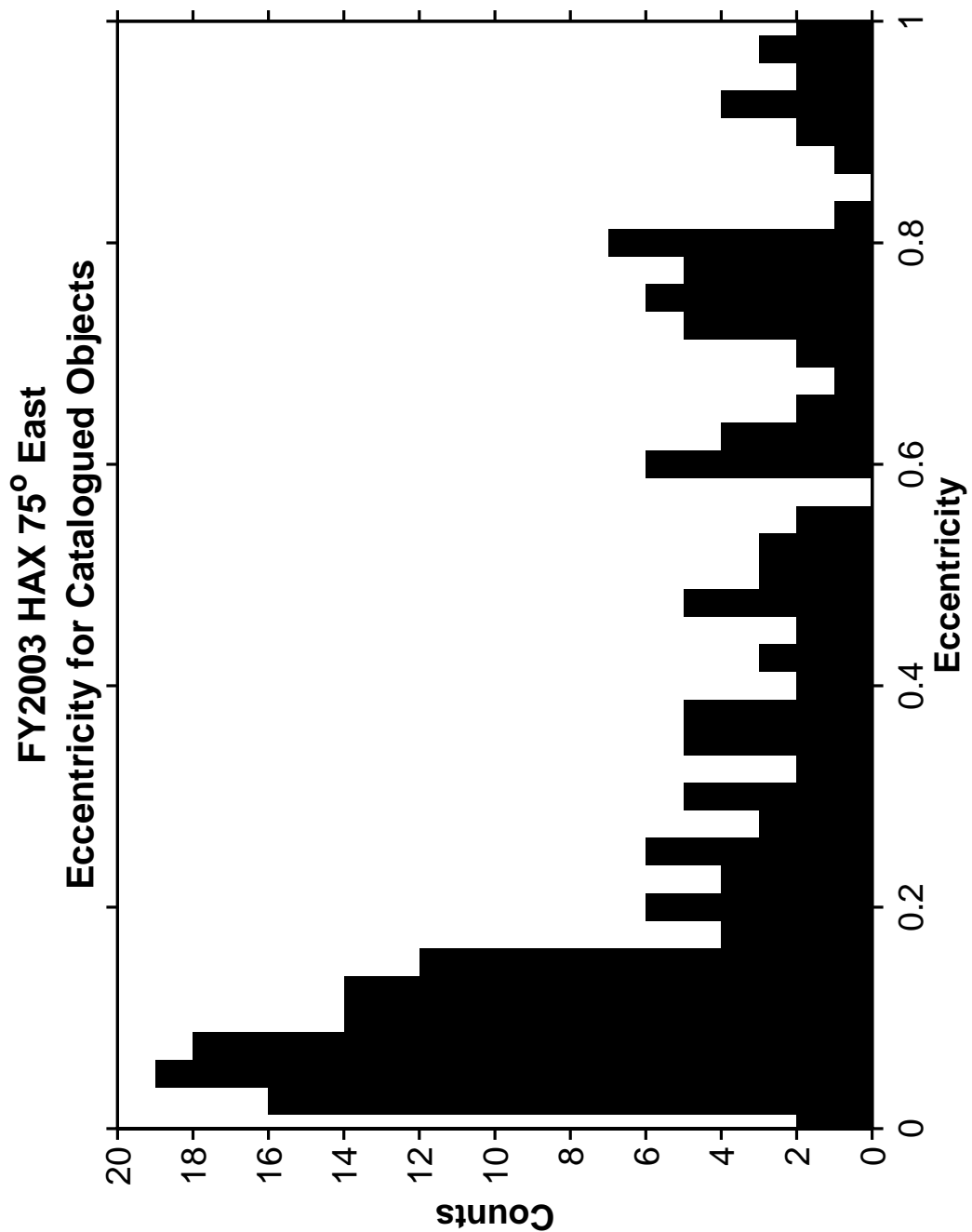


Figure 125. HAX Eccentricity Histogram for Catalogued Objects.

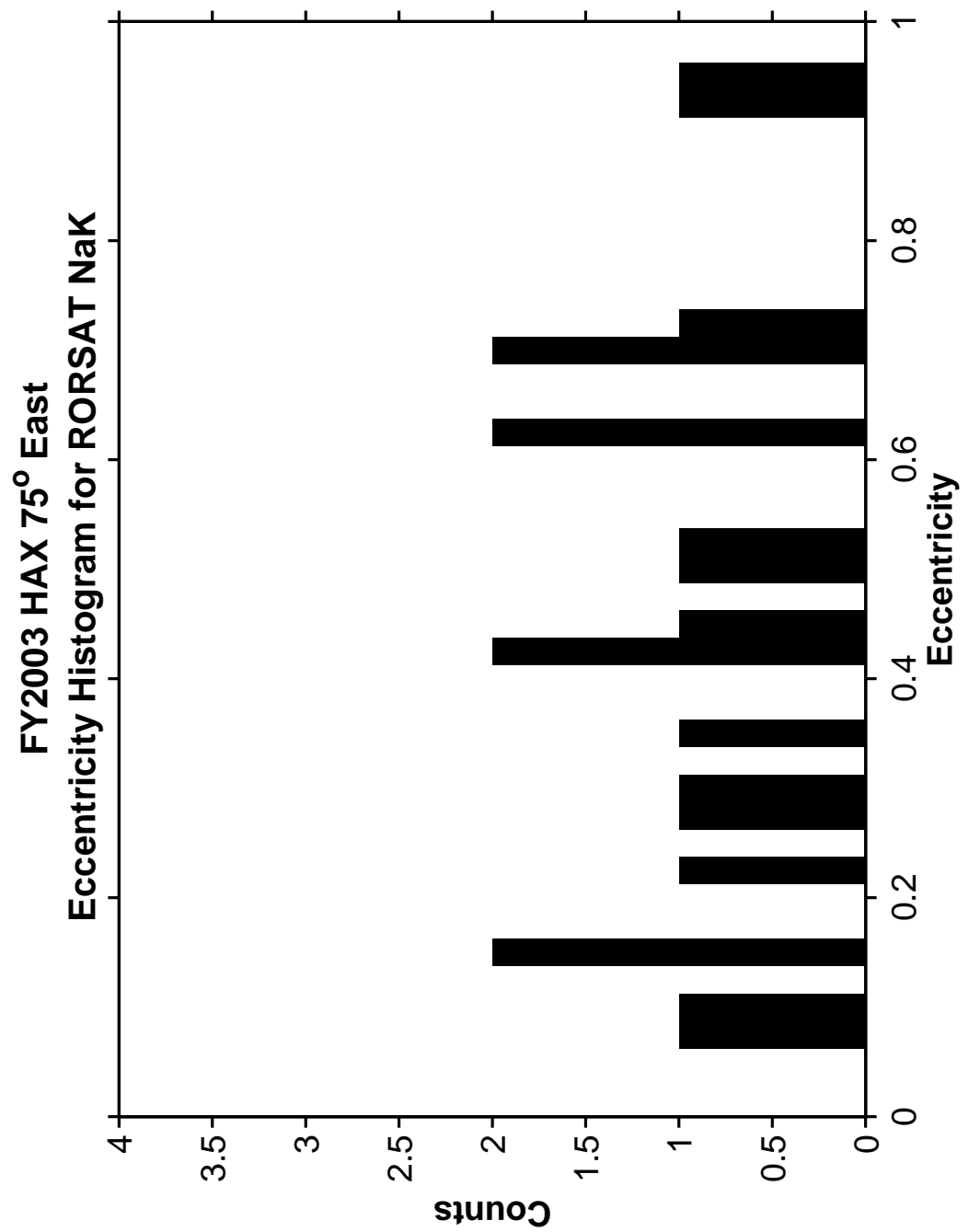


Figure 126. HAX Eccentricity Histogram for RORSAT NaK Debris.

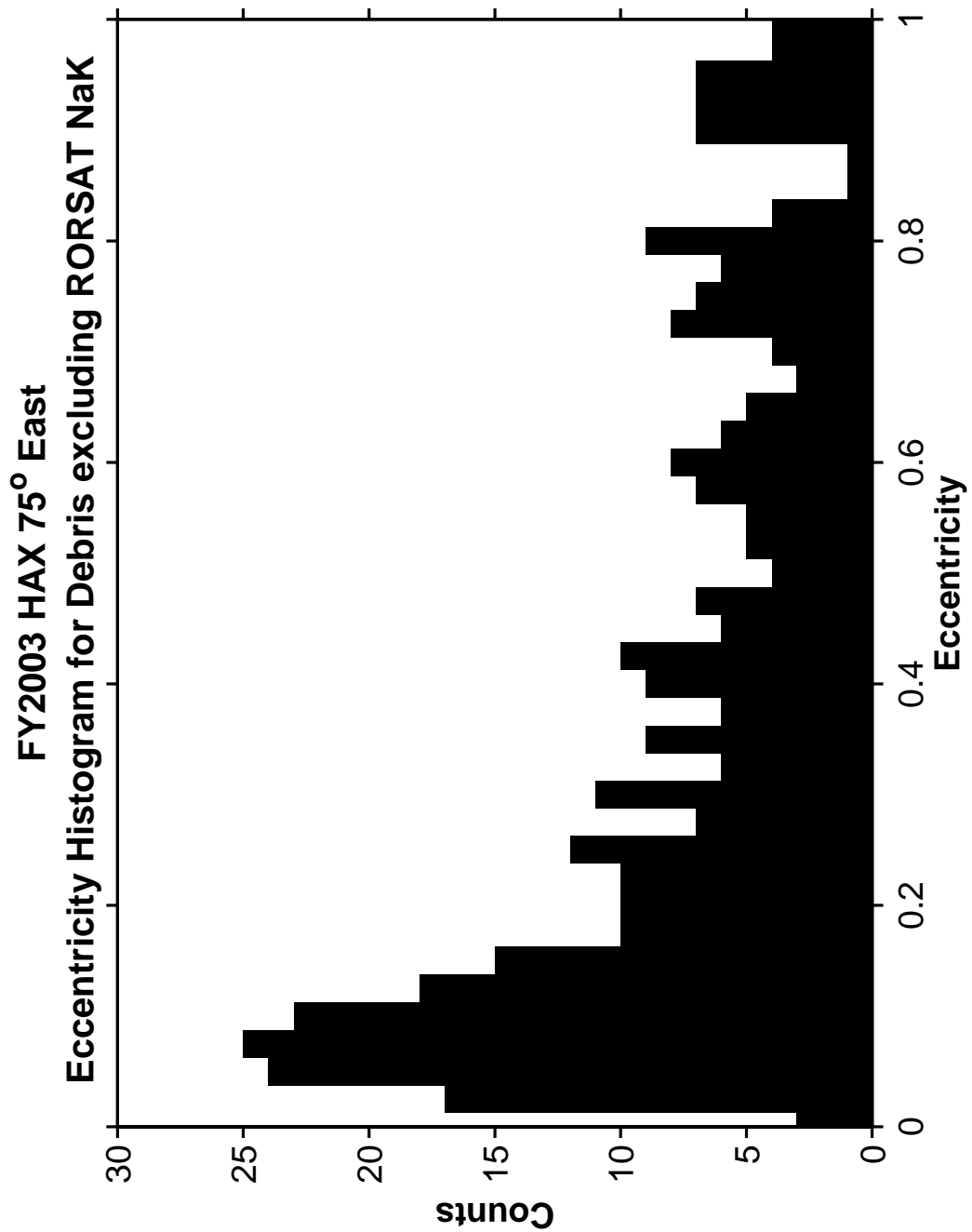


Figure 127. HAX Eccentricity Histogram excluding RORSAT Nak Debris.

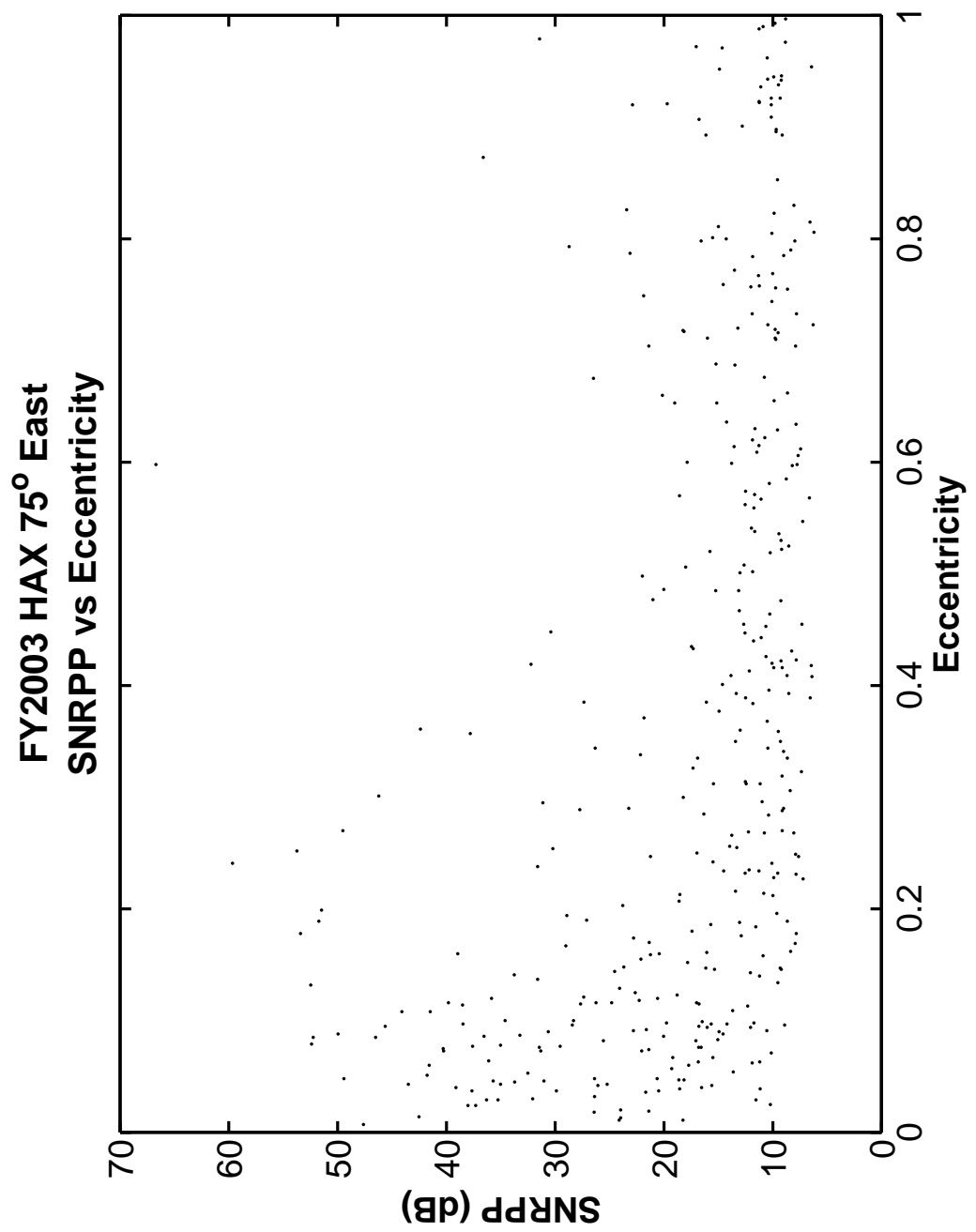


Figure 128. HAX Principal Polarization SNR versus Eccentricity.

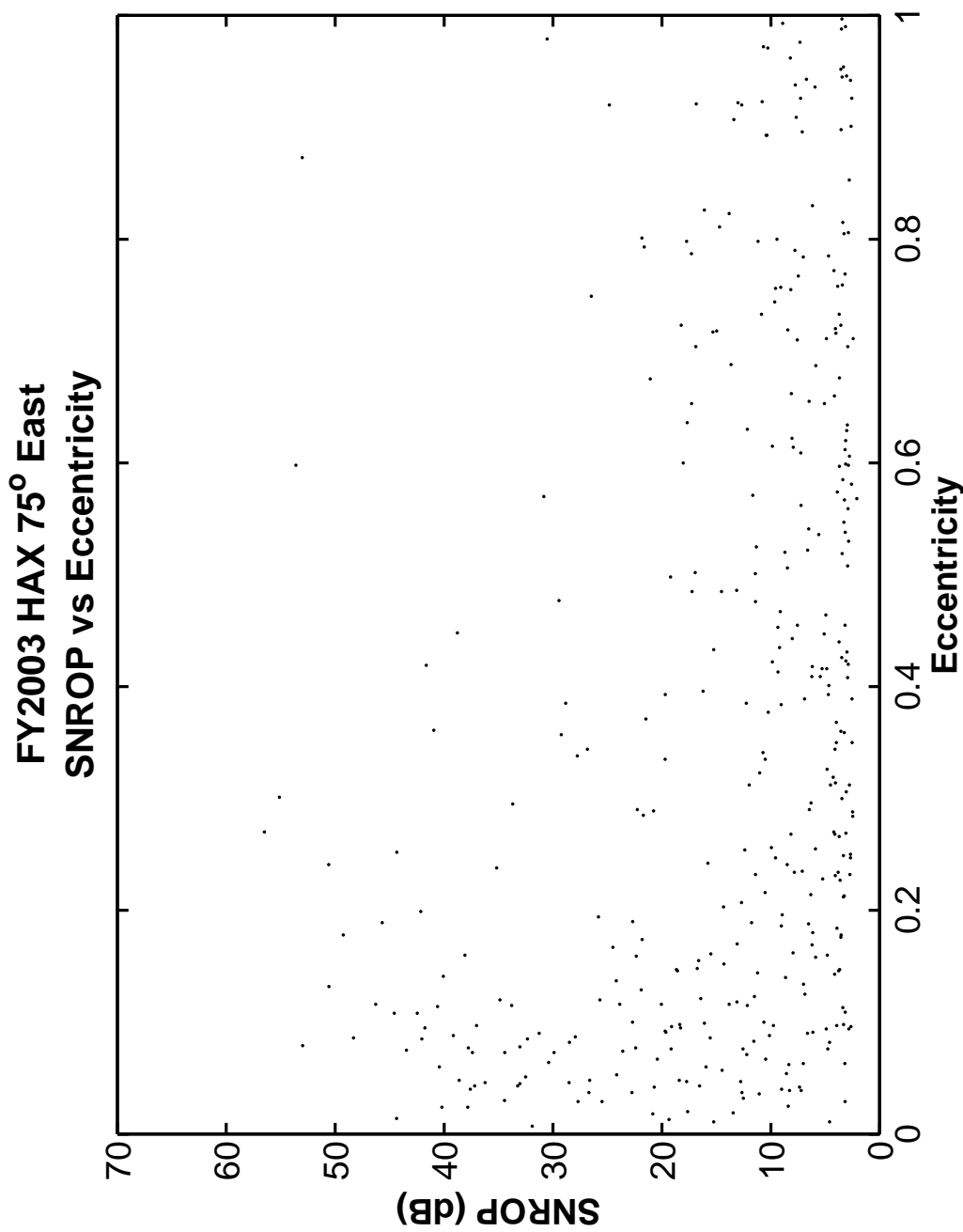


Figure 129. HAX Orthogonal Polarization SNR versus Eccentricity.

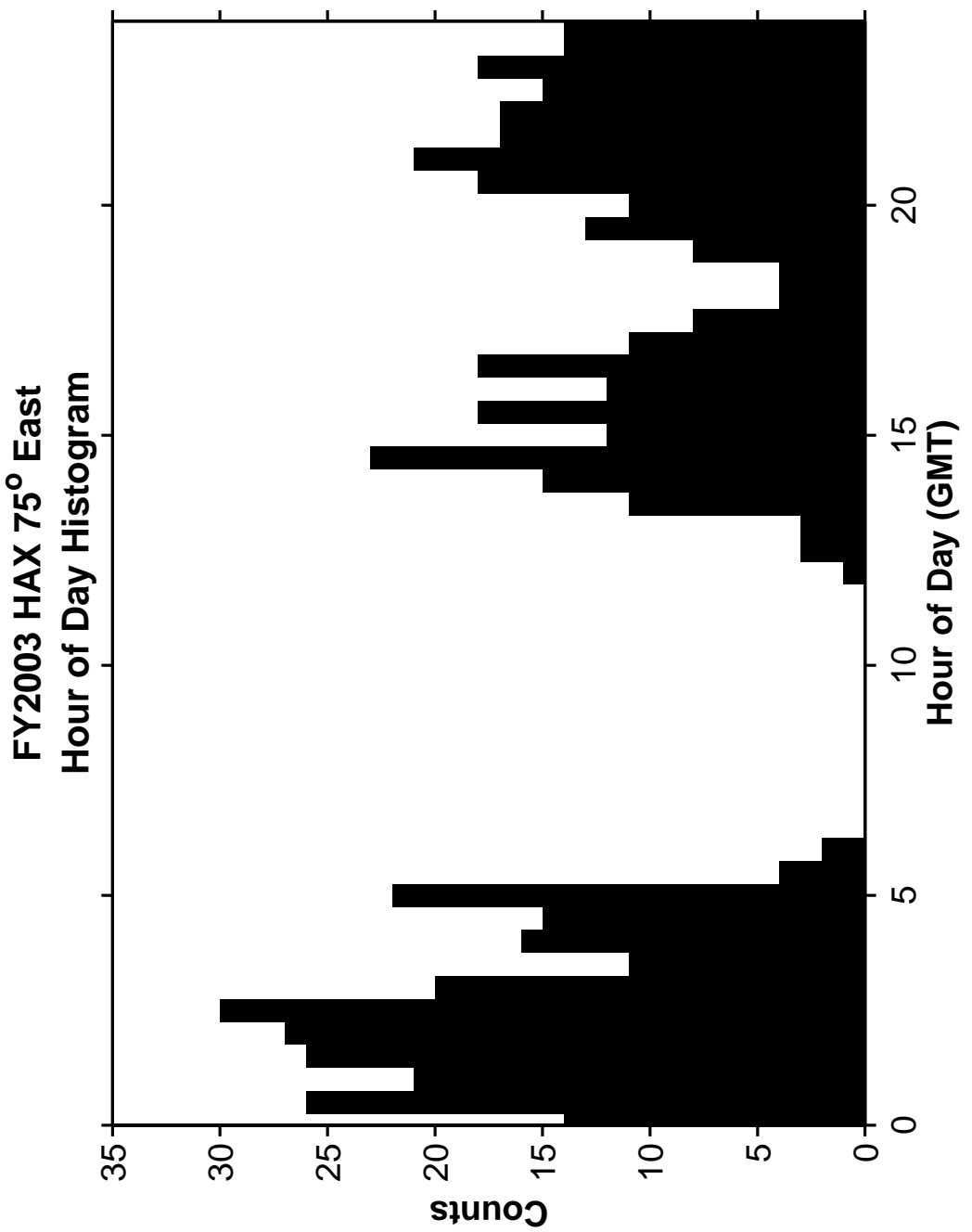


Figure 130. Histogram of the Daily Time of HAX Detections.

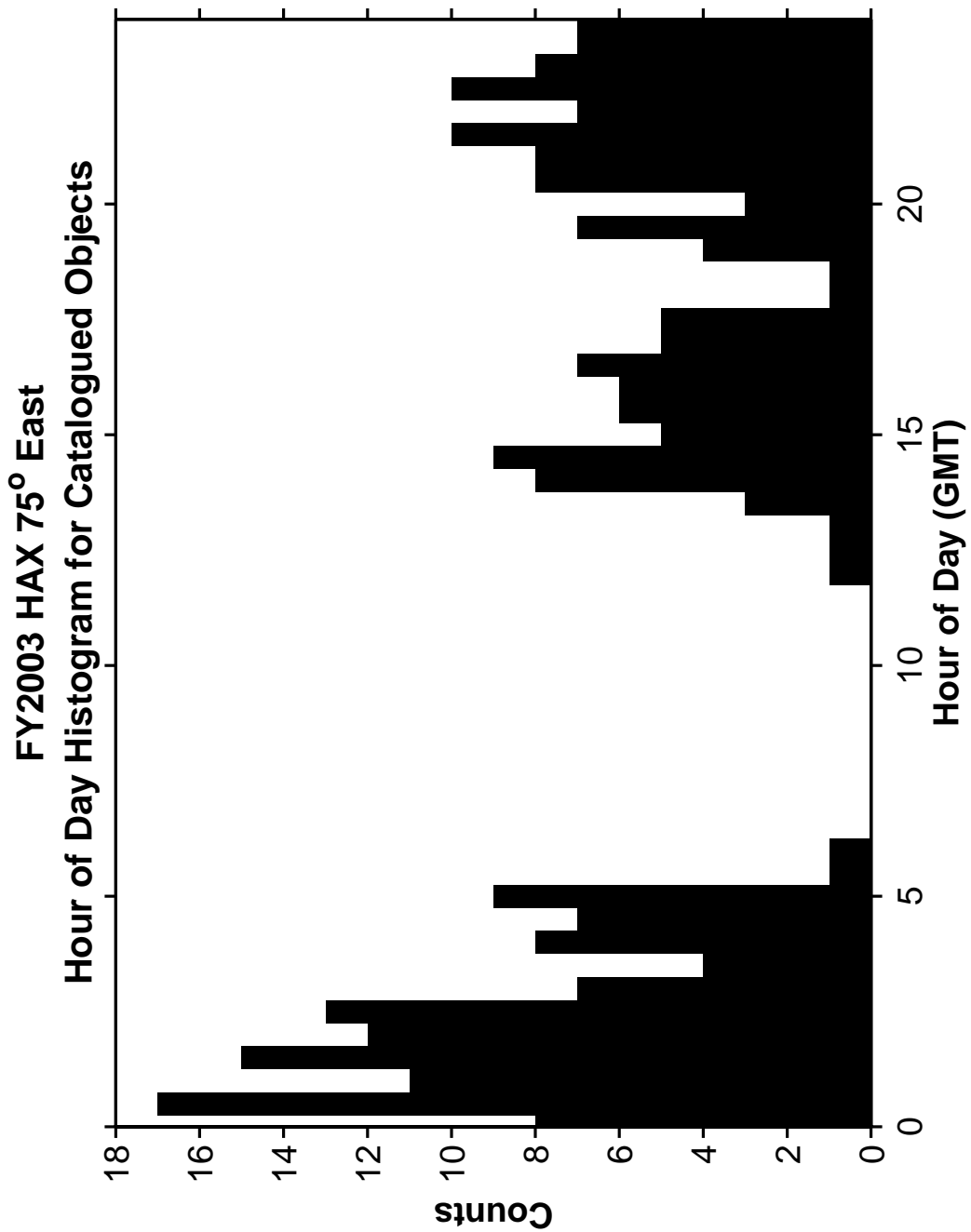


Figure 131. Histogram of the Daily Time of Catalogued HAX Detections.

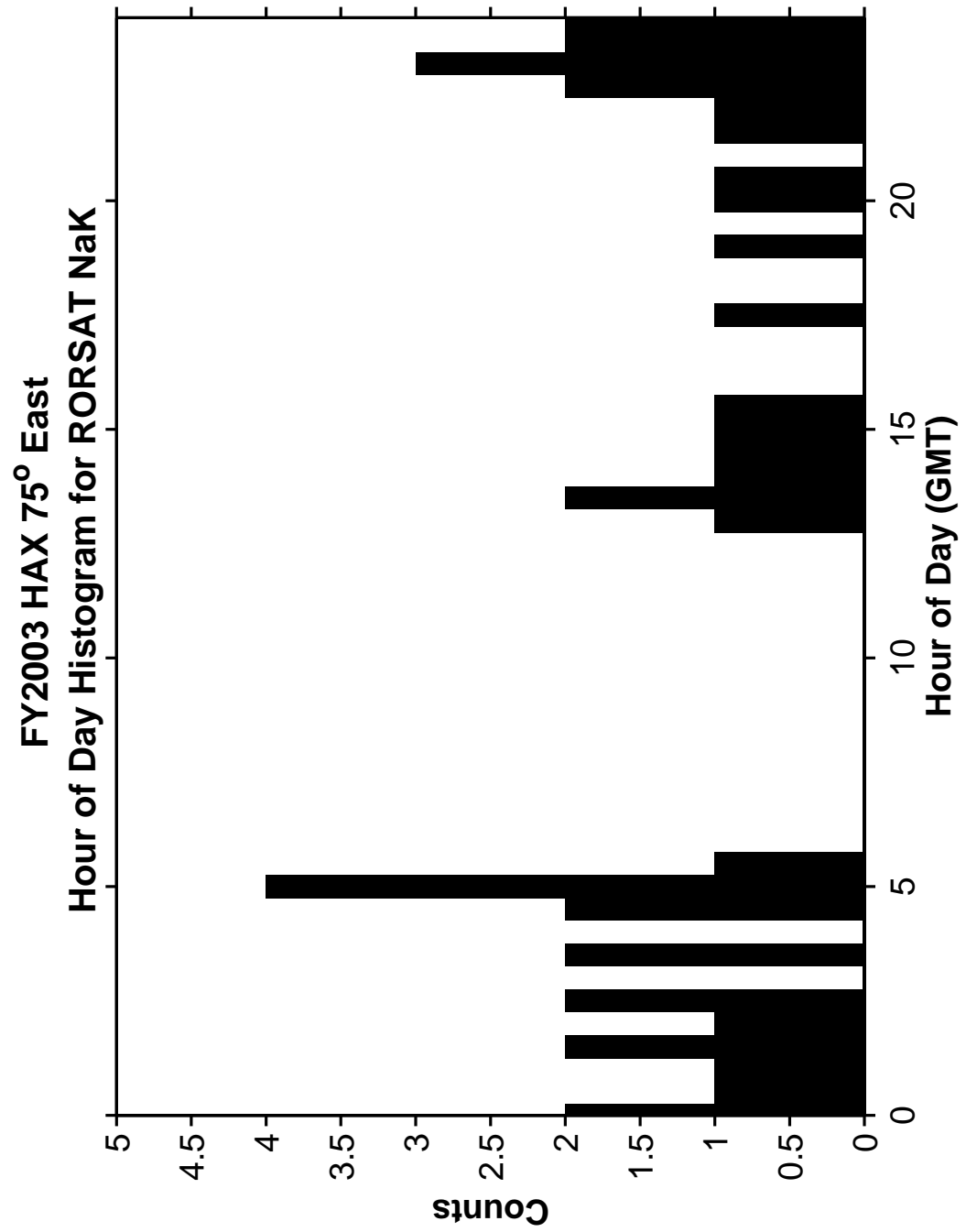


Figure 132. Histogram of the Daily Time of RORSAT NaK Detections.

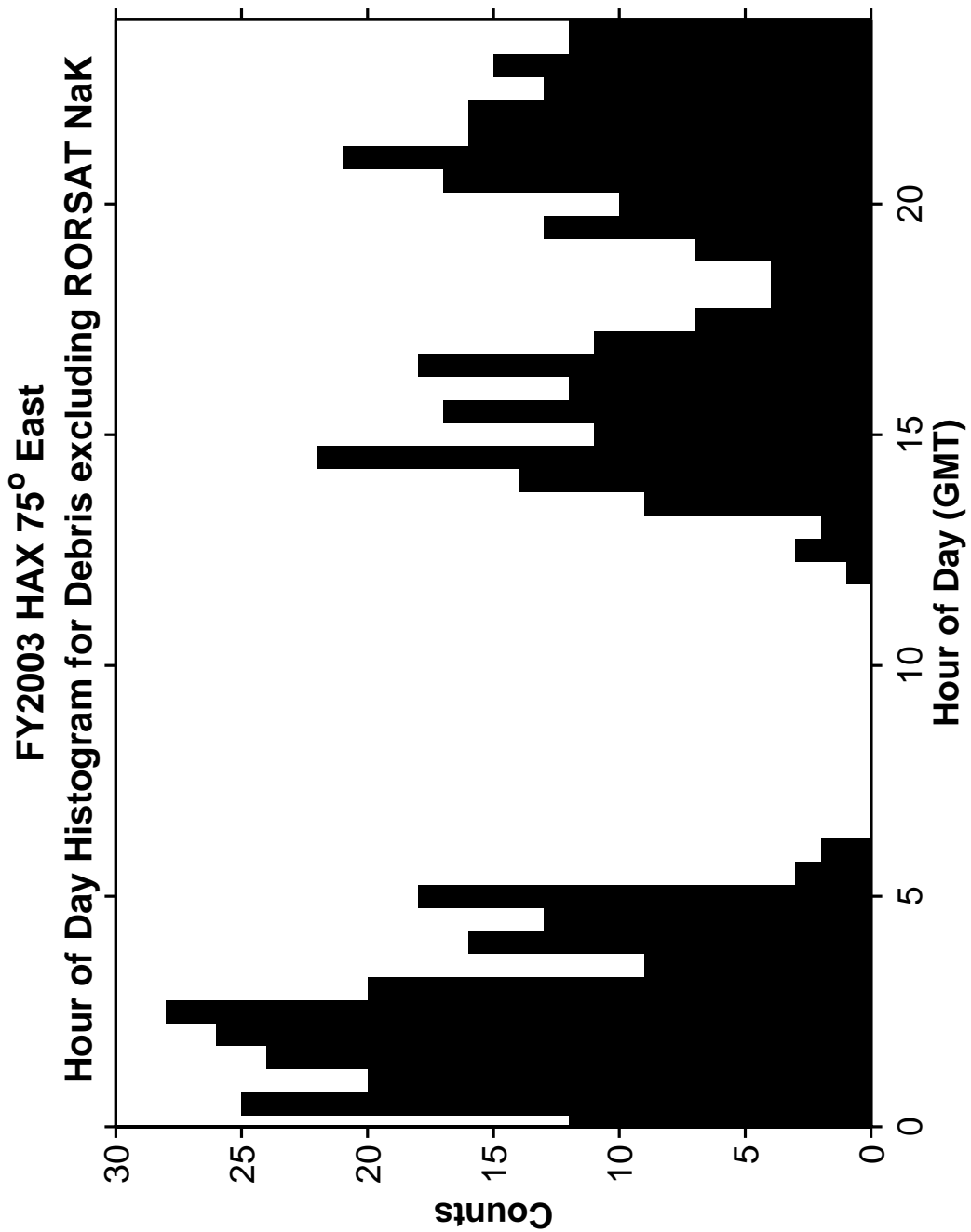


Figure 133. Histogram of the Daily Time of Detections excluding RORSAT NaK Debris.

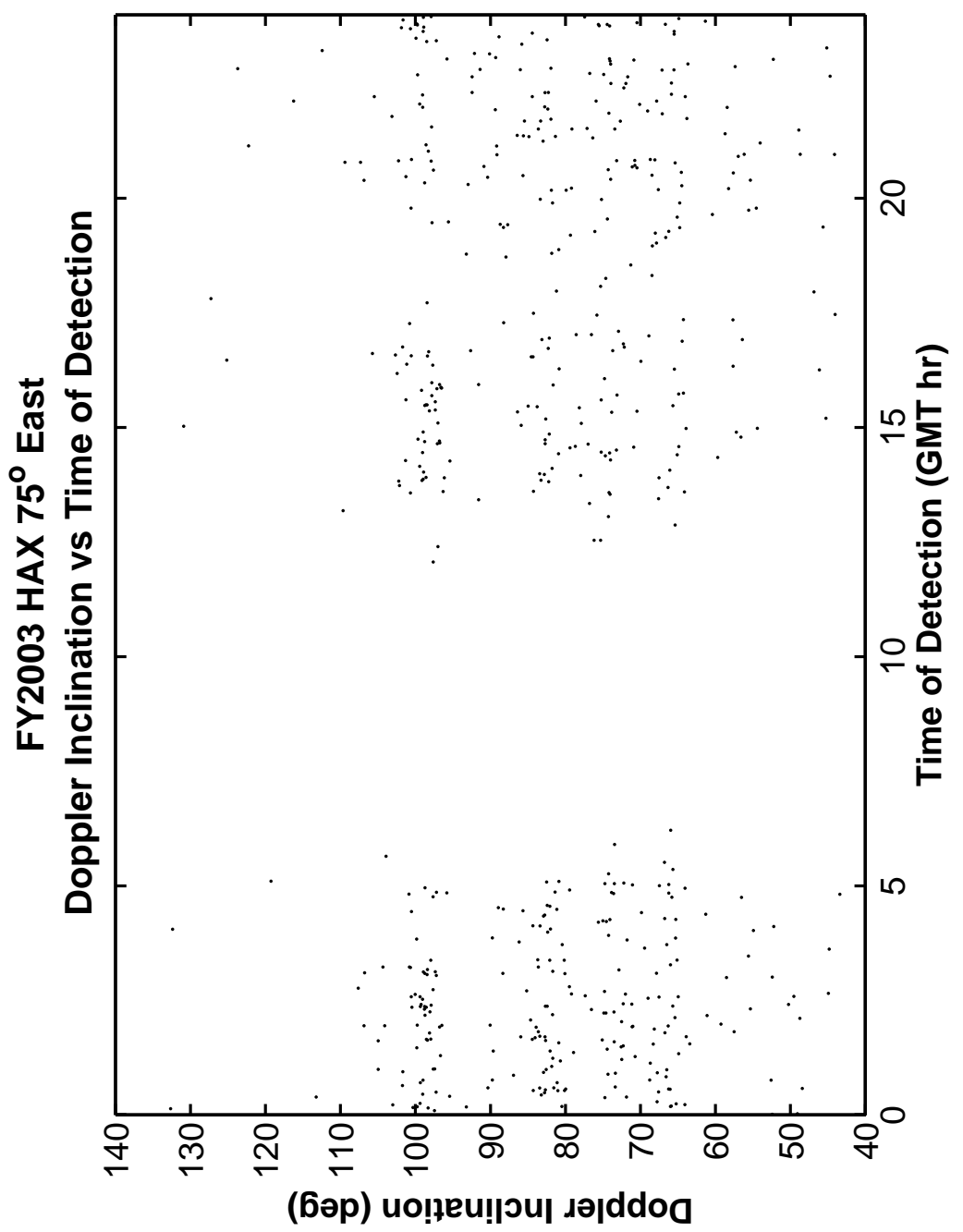


Figure 134. HAX Doppler Inclination versus the Daily Time of Detections.

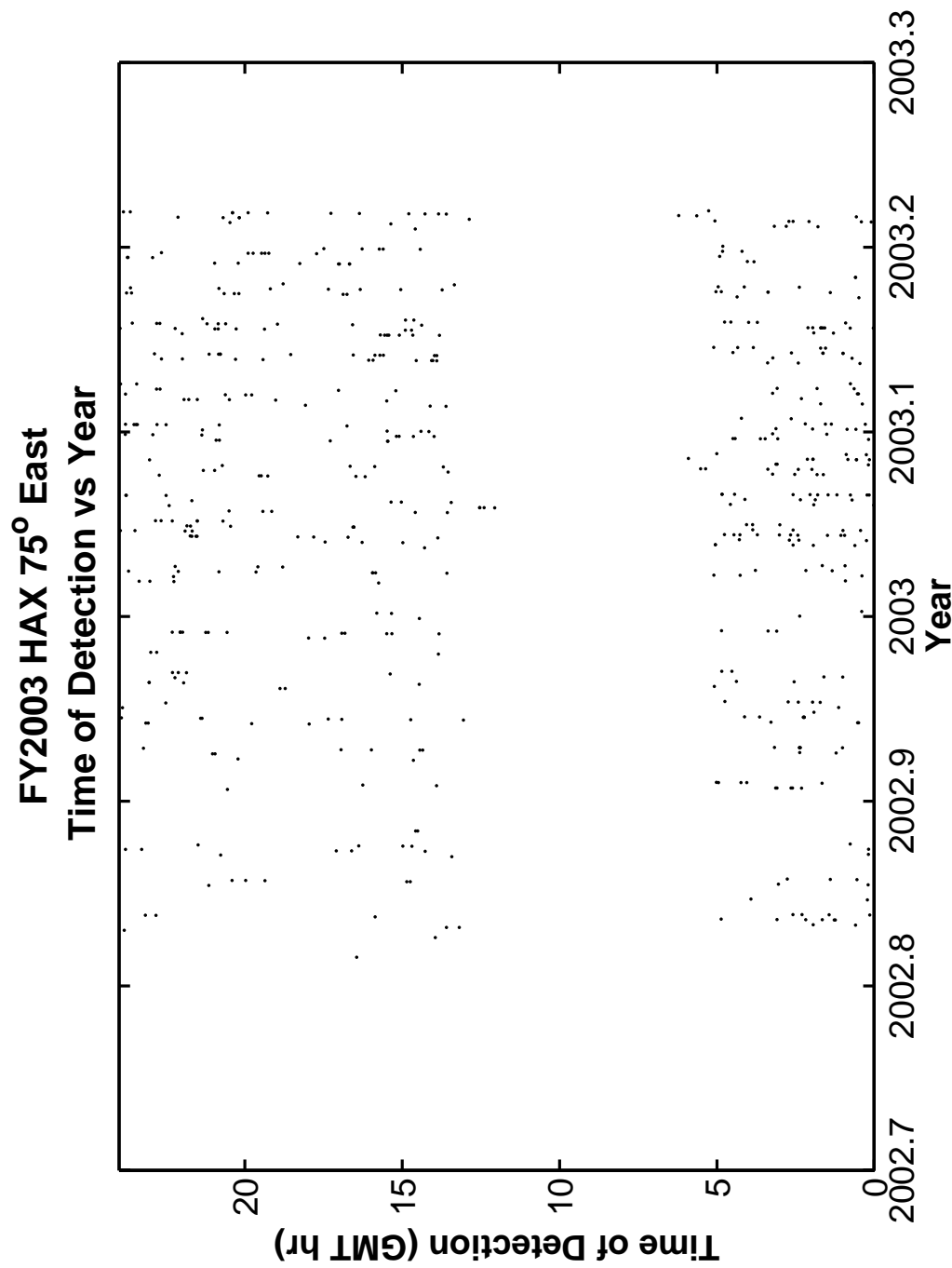


Figure 135. HAX Time of Detection versus Observation Schedule throughout the Year.

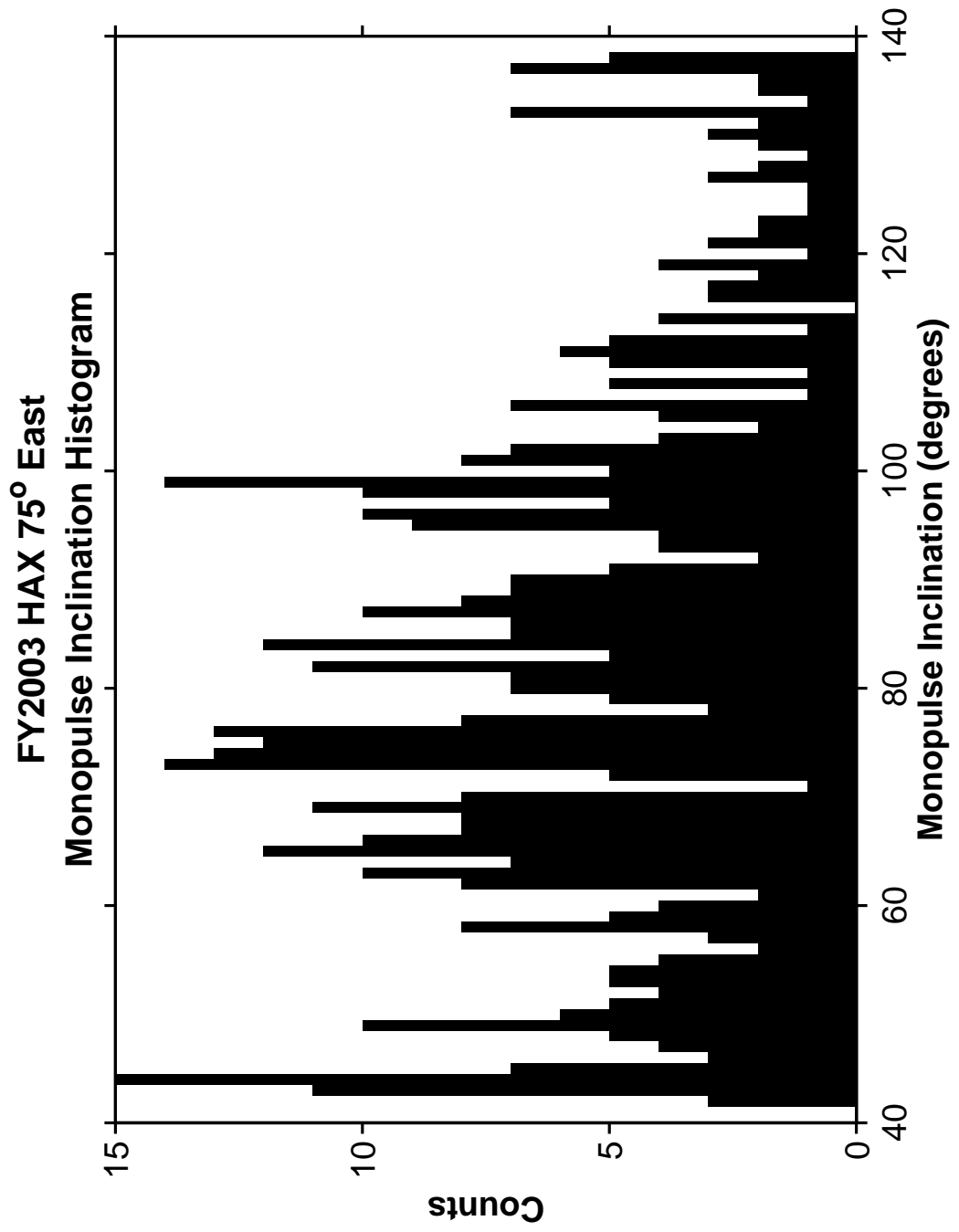


Figure 136. HAX Monopulse Inclination Histogram.

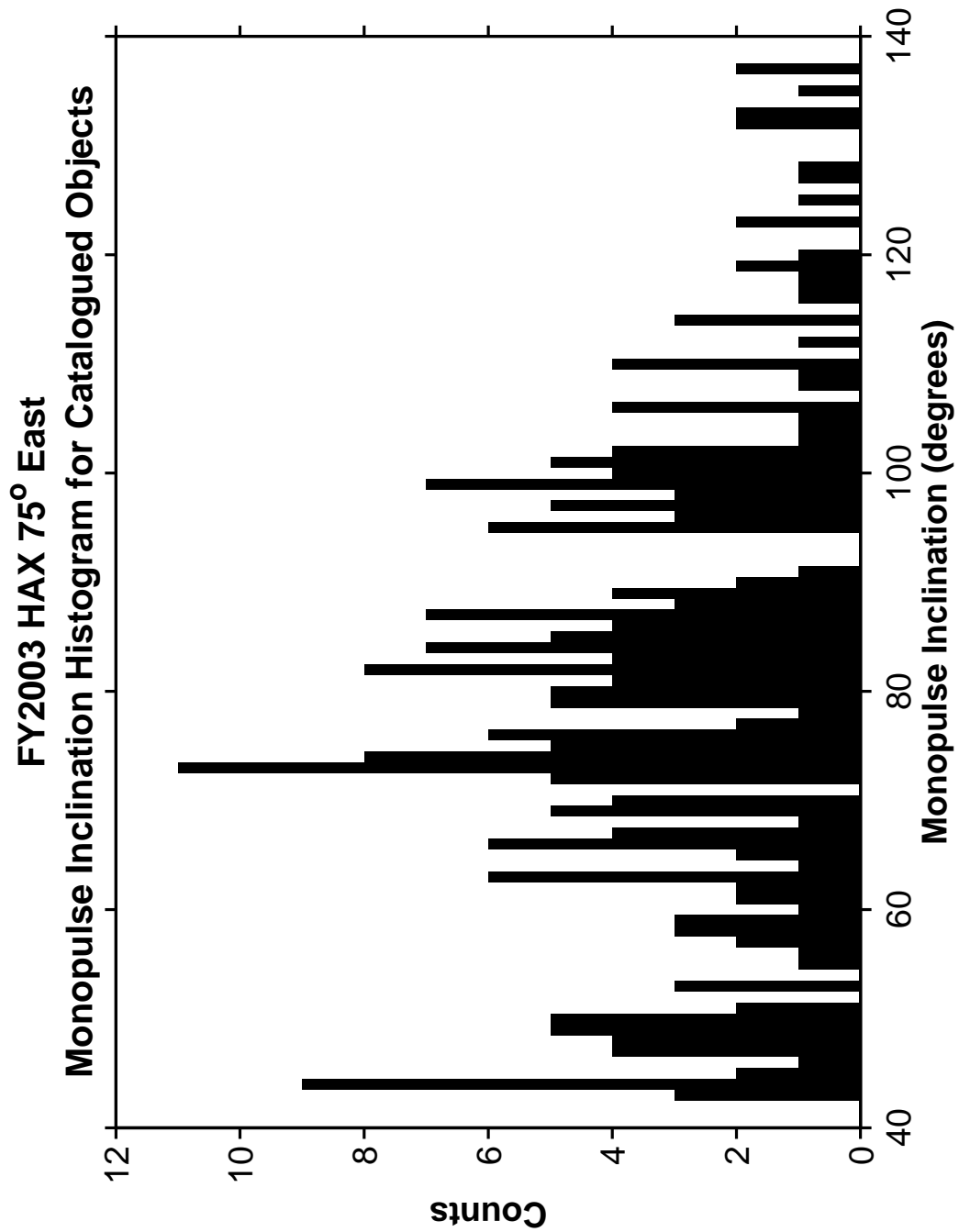


Figure 137. HAX Monopulse Histogram for Catalogued Objects.

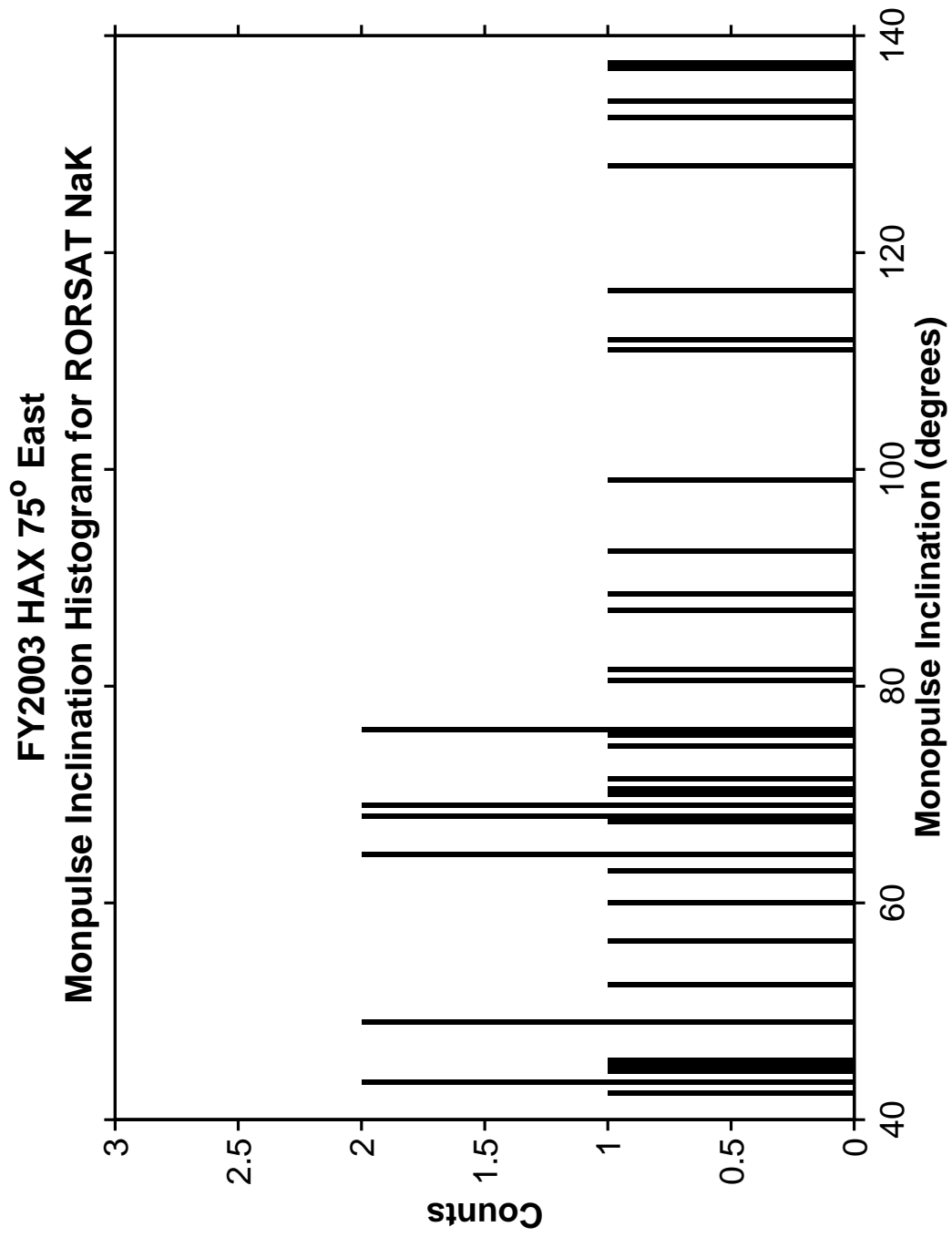


Figure 138. Haystack Monopulse Histogram for RORSAT Nak Debris.

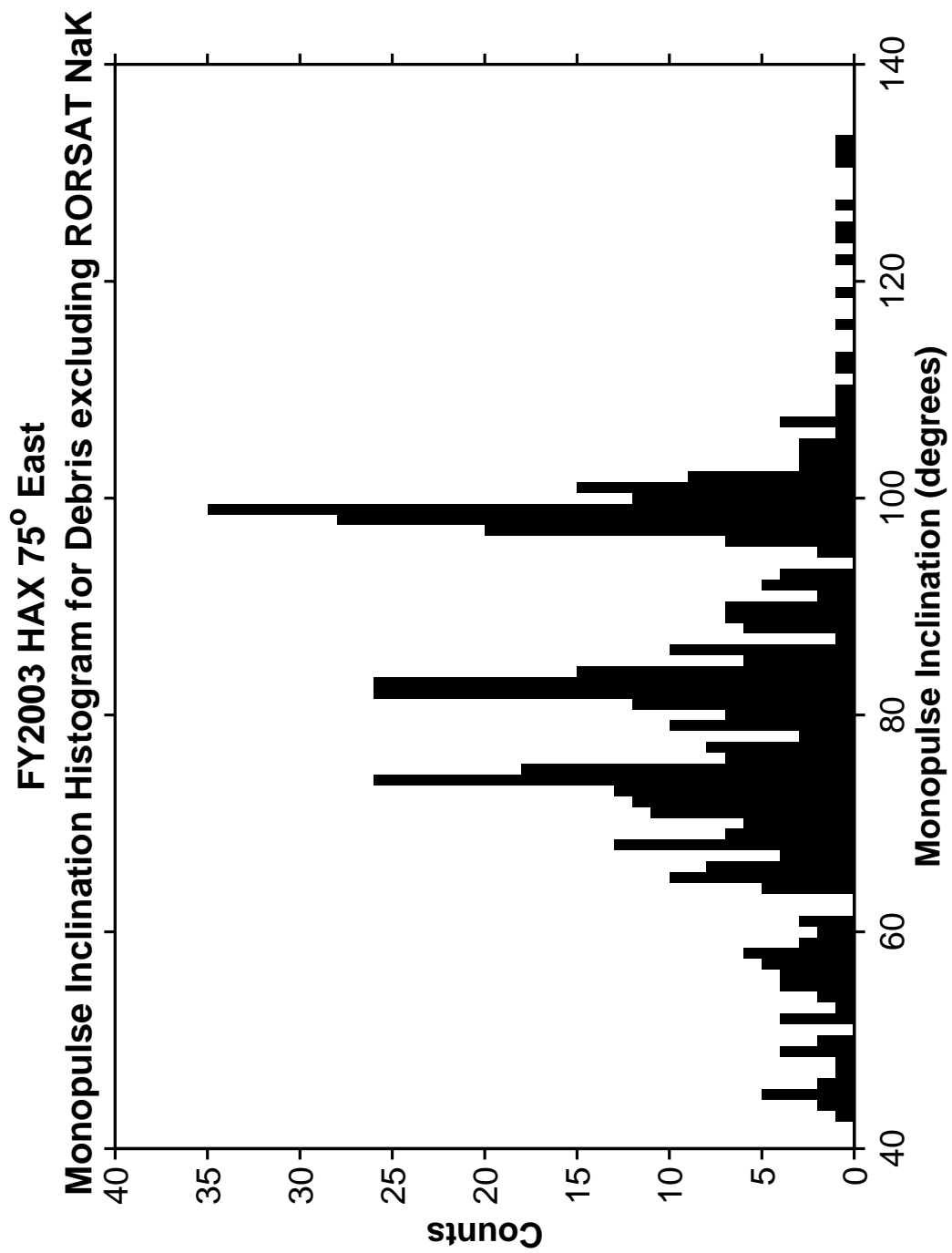


Figure 139. Haystack Monopulse Histogram excluding RORSAT Nak Debris.

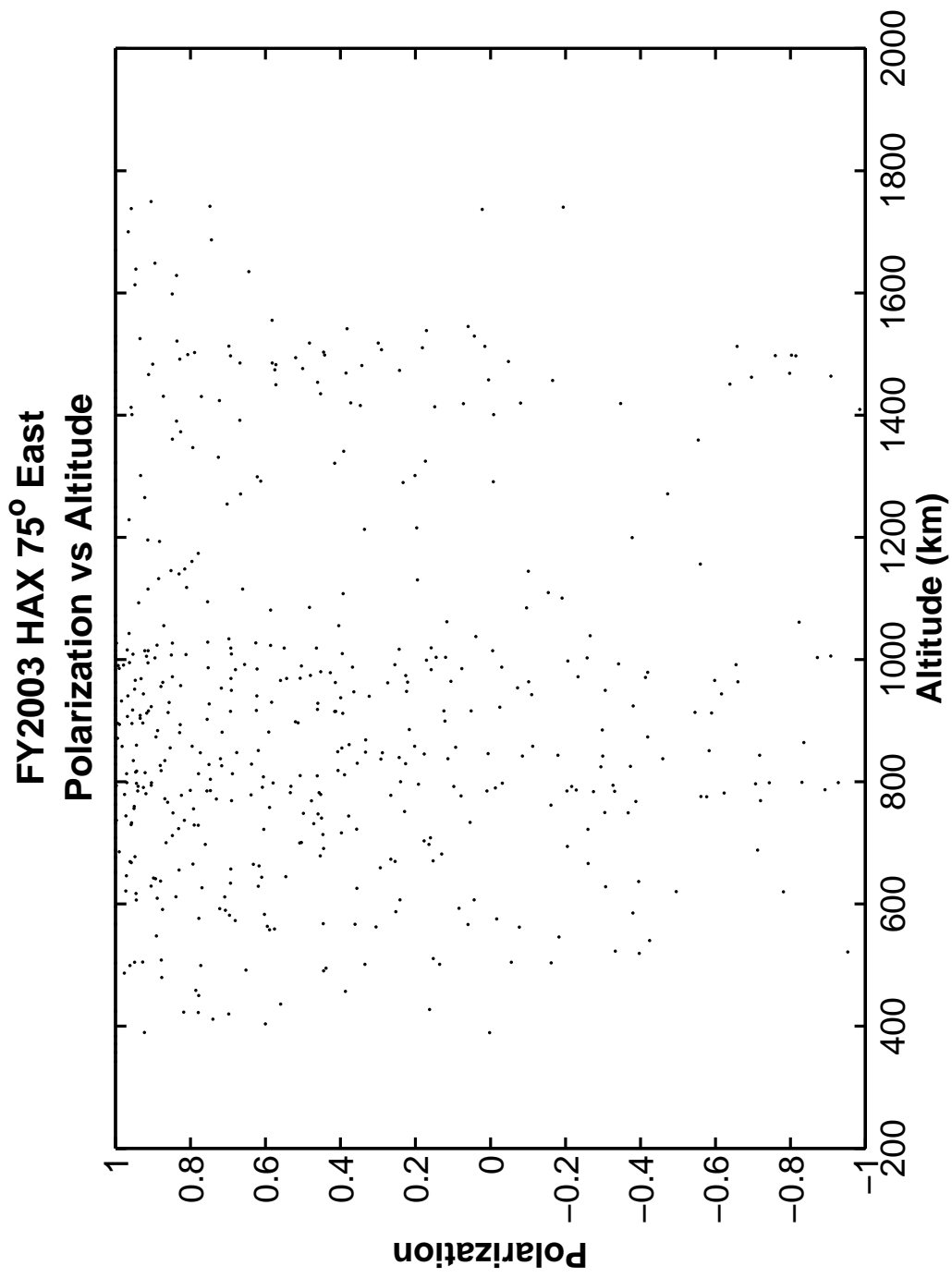


Figure 140. HAX Polarization versus Altitude.

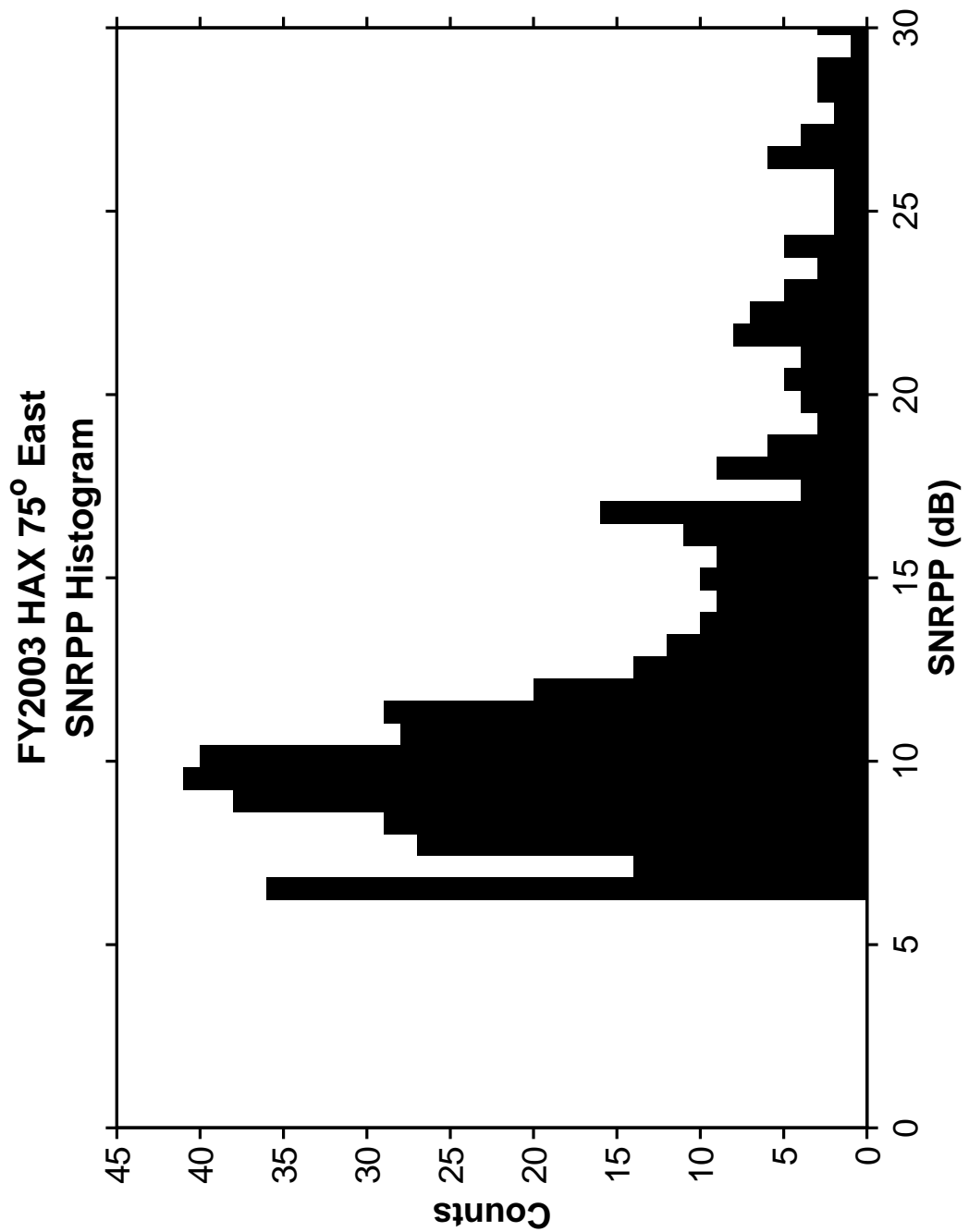


Figure 141. HAX Principal Polarization SNR Histogram.

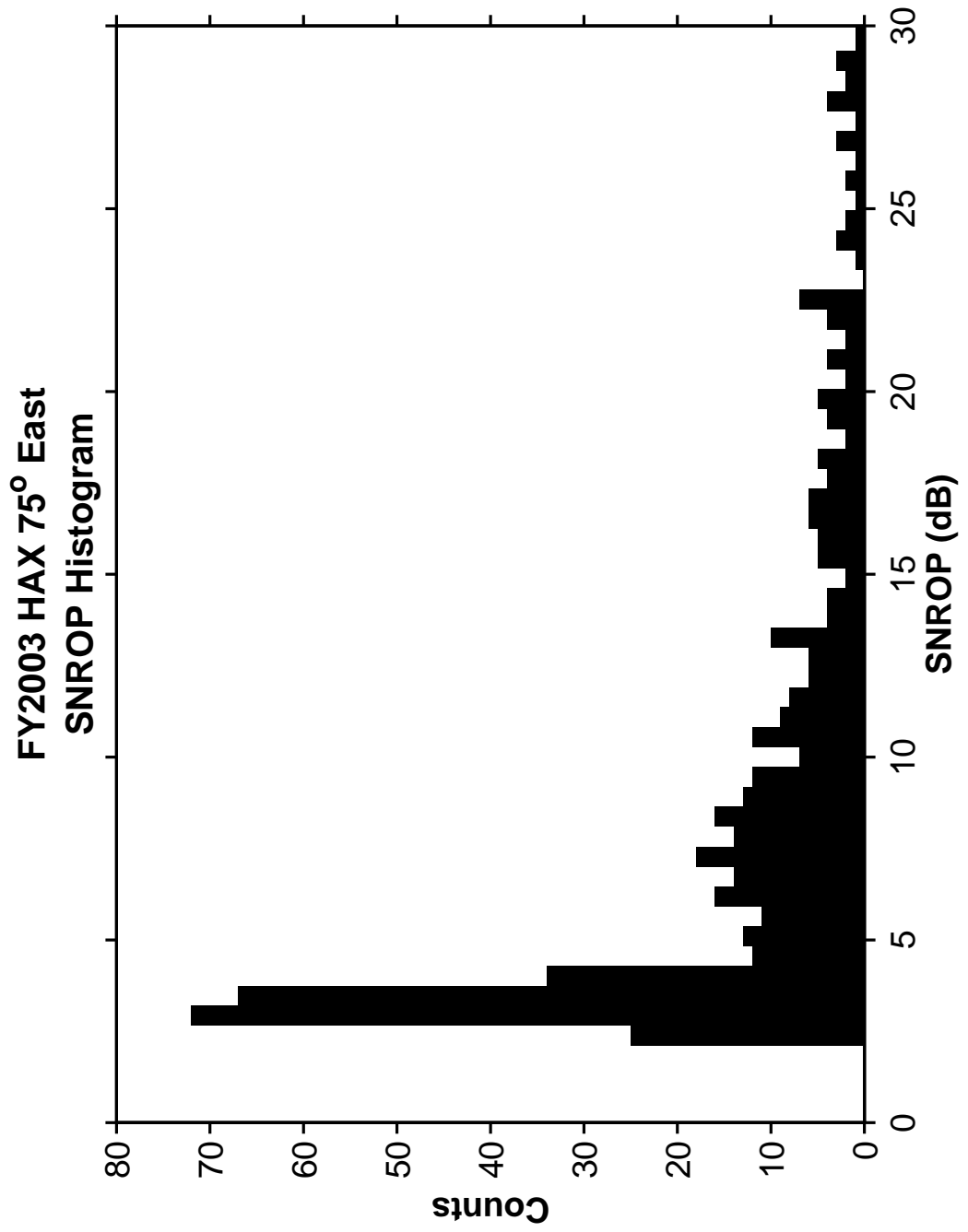


Figure 142. HAX Orthogonal Polarization SNR Histogram.

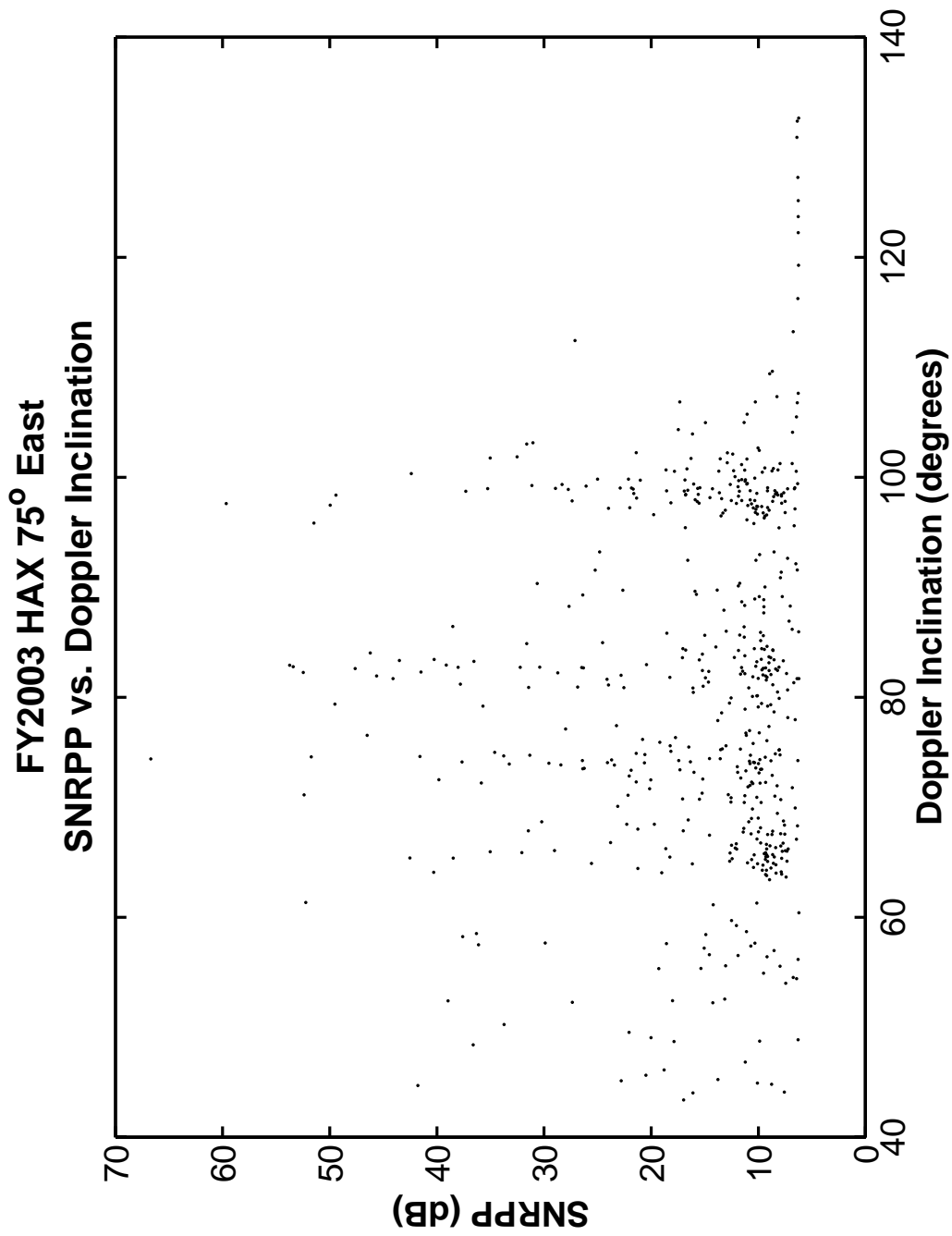


Figure 143. HAX Principal Polarization SNR versus Doppler Inclination.

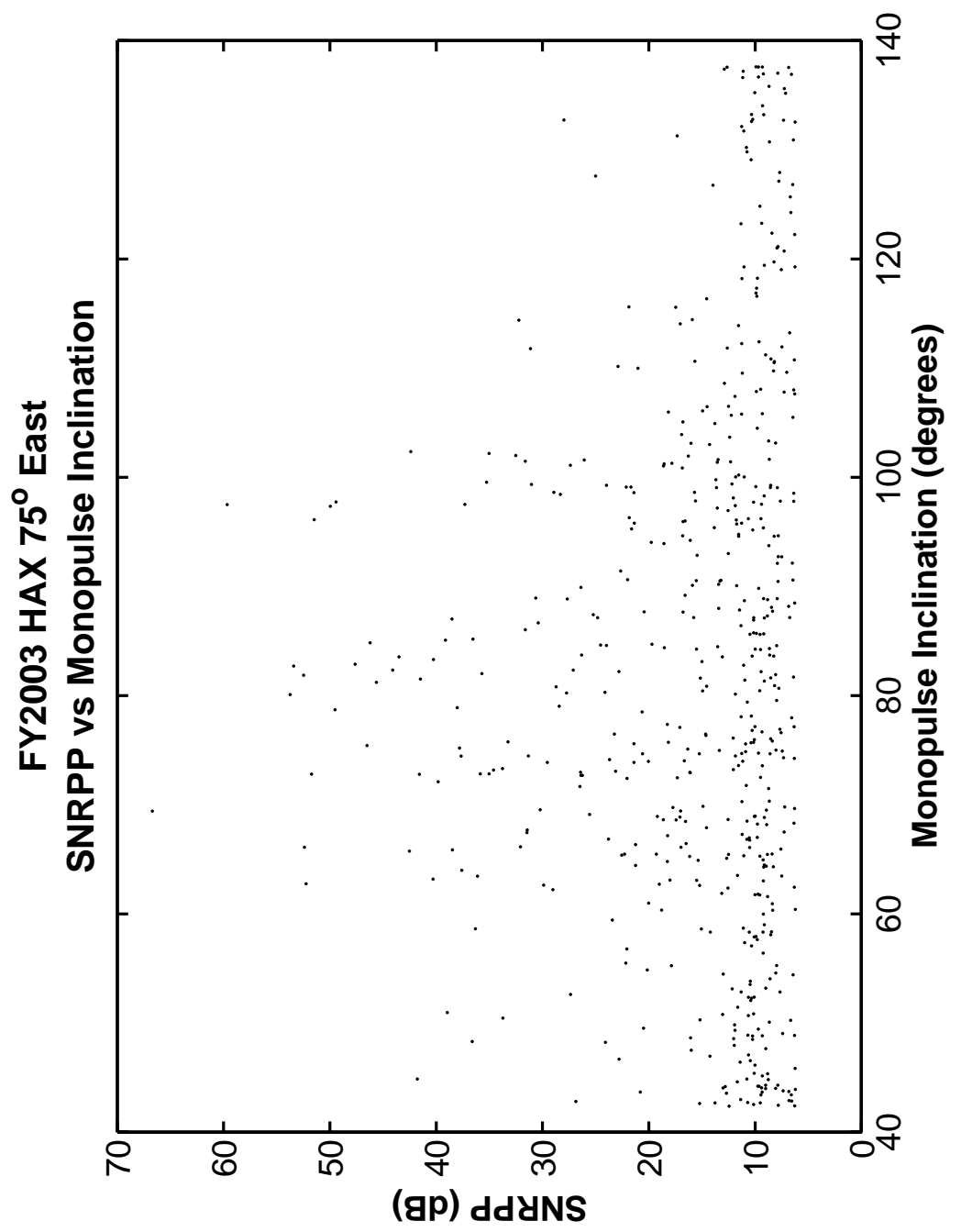


Figure 144. HAX Principal Polarization SNR versus Monopulse Inclination.

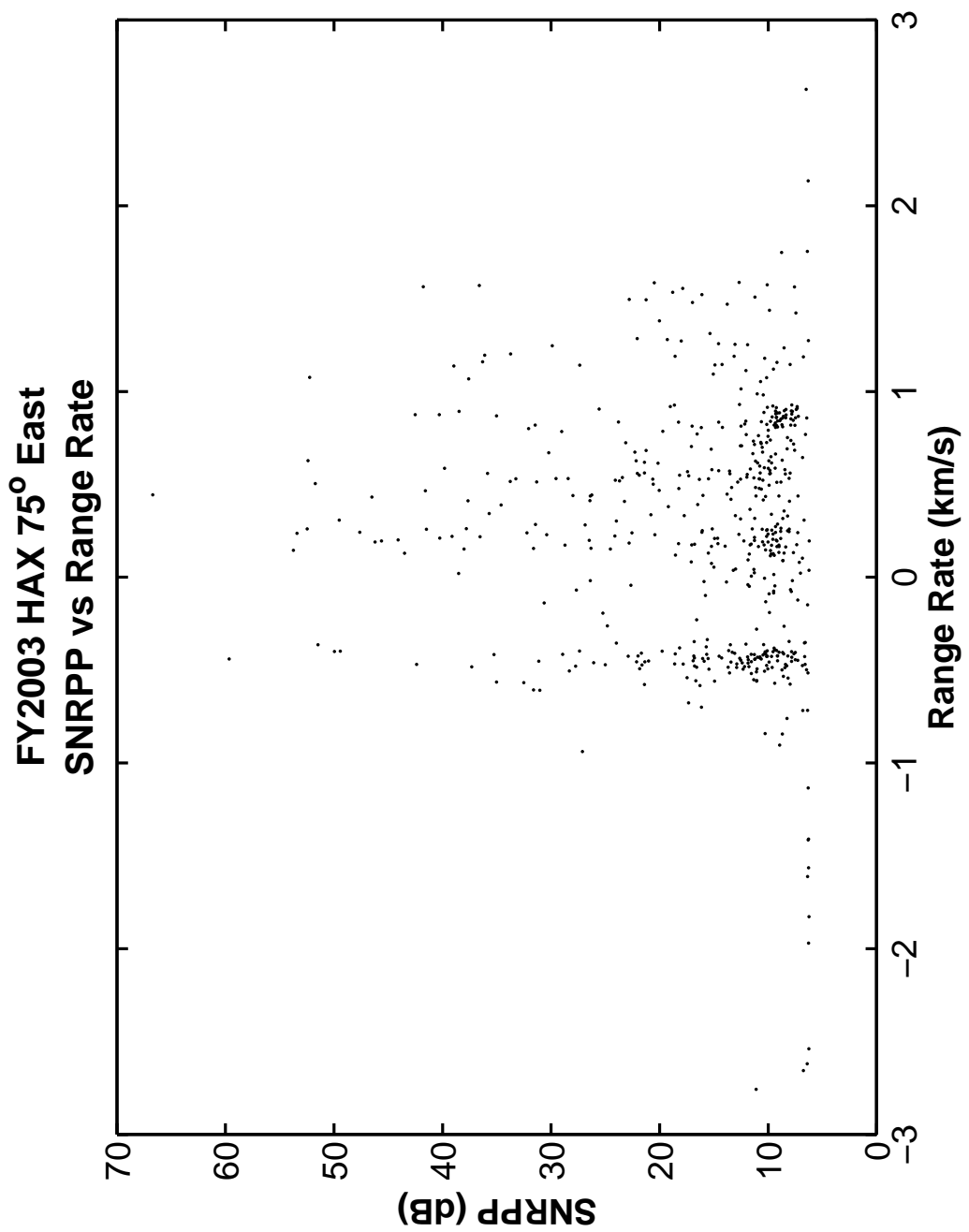


Figure 145. HAX Principal Polarization SNR versus Range Rate.

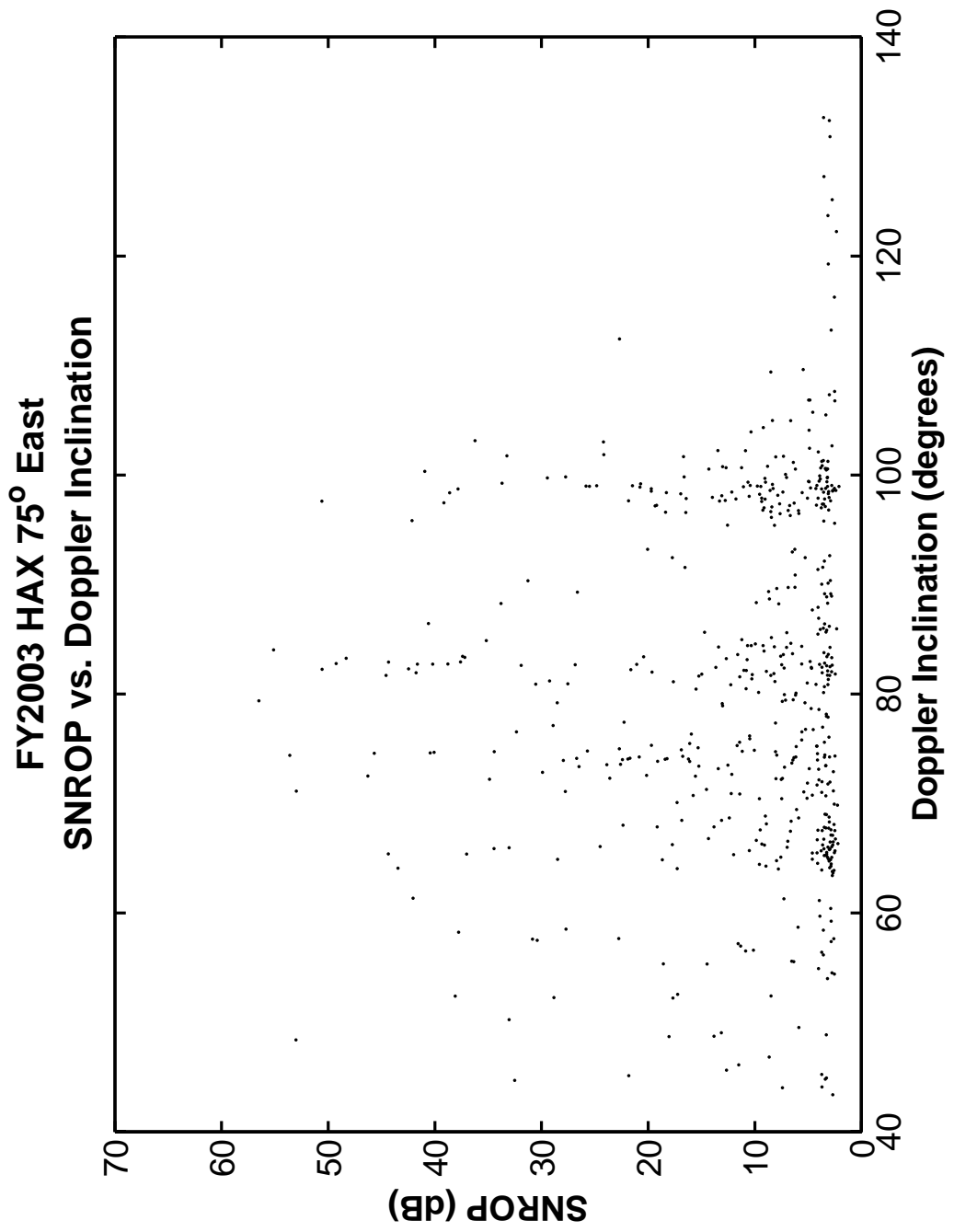


Figure 146. HAX Orthogonal Polarization versus Doppler Inclination.

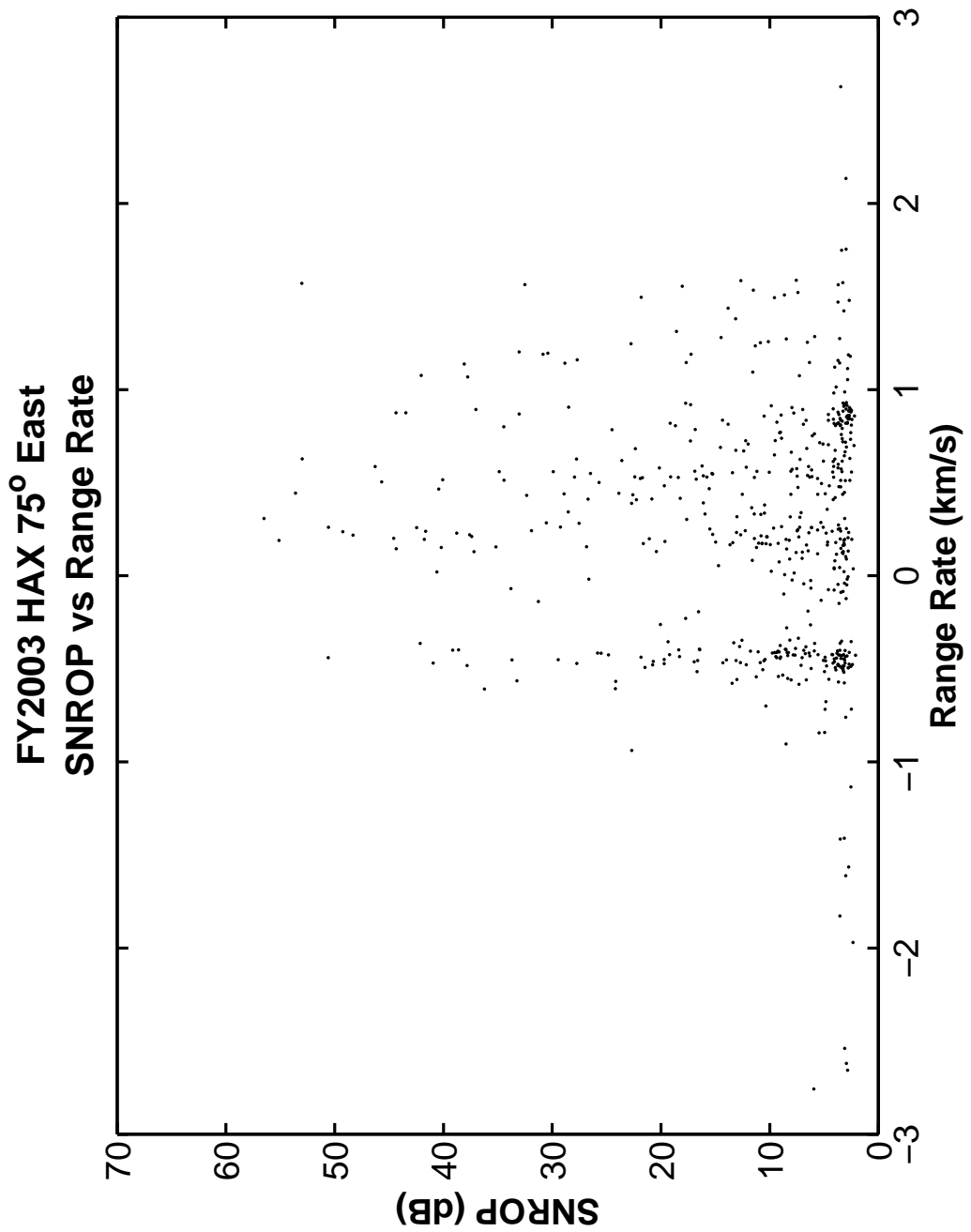


Figure 147. HAX Orthogonal Polarization versus Range Rate.

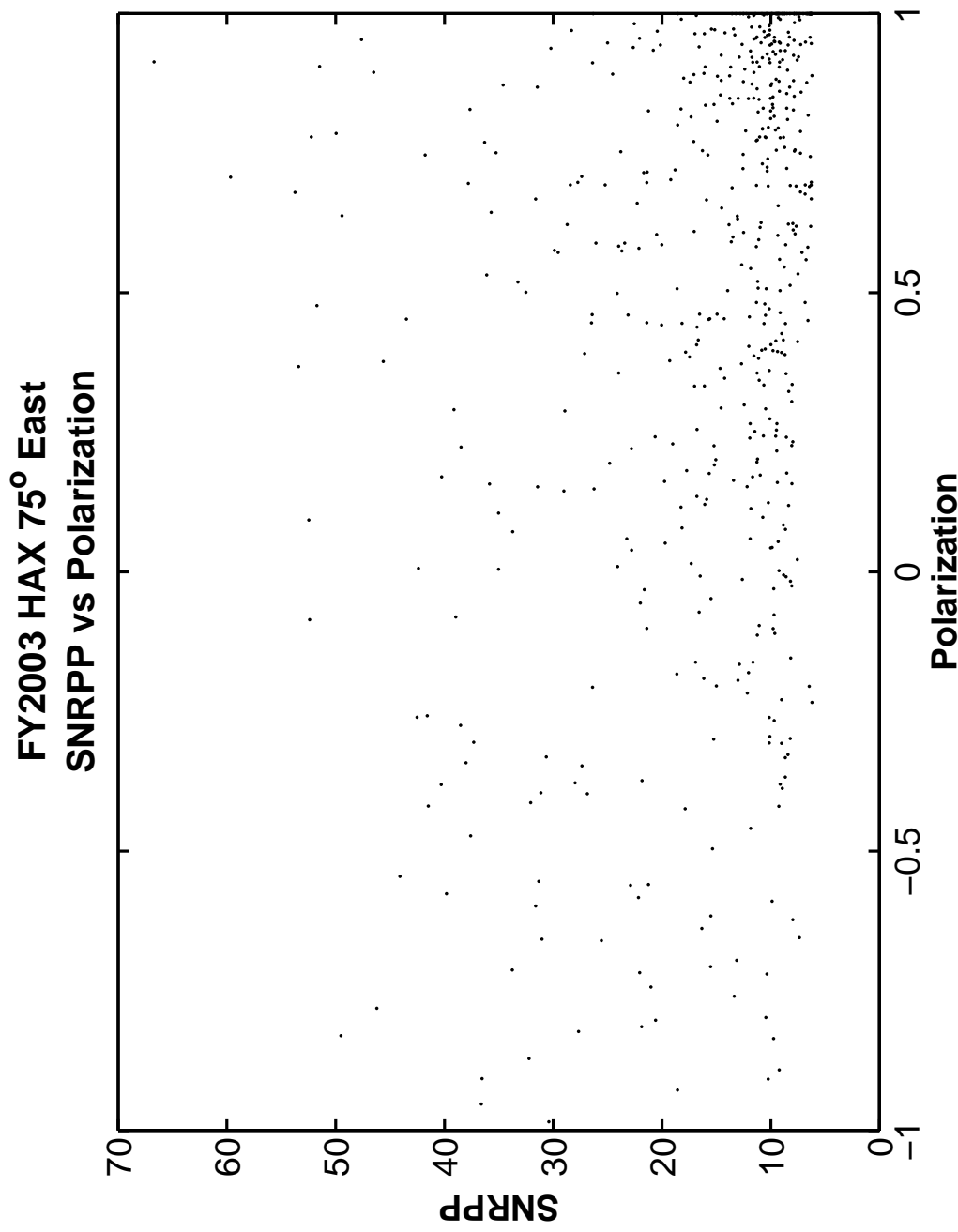


Figure 148. HAX Principal Polarization SNR versus Radar Return Signal Polarization.

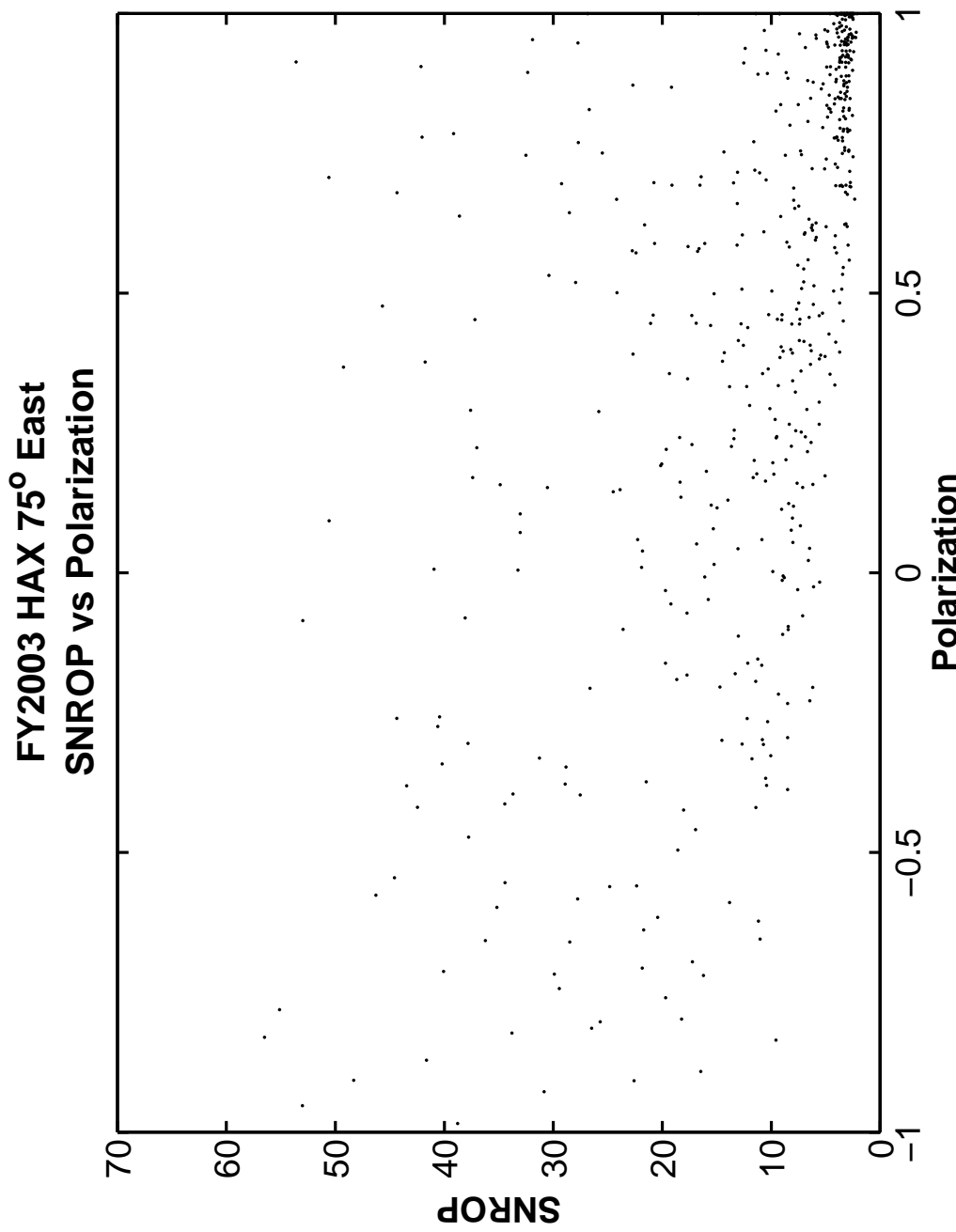


Figure 149. HAX Orthogonal Polarization SNR versus Radar Return Signal Polarization.

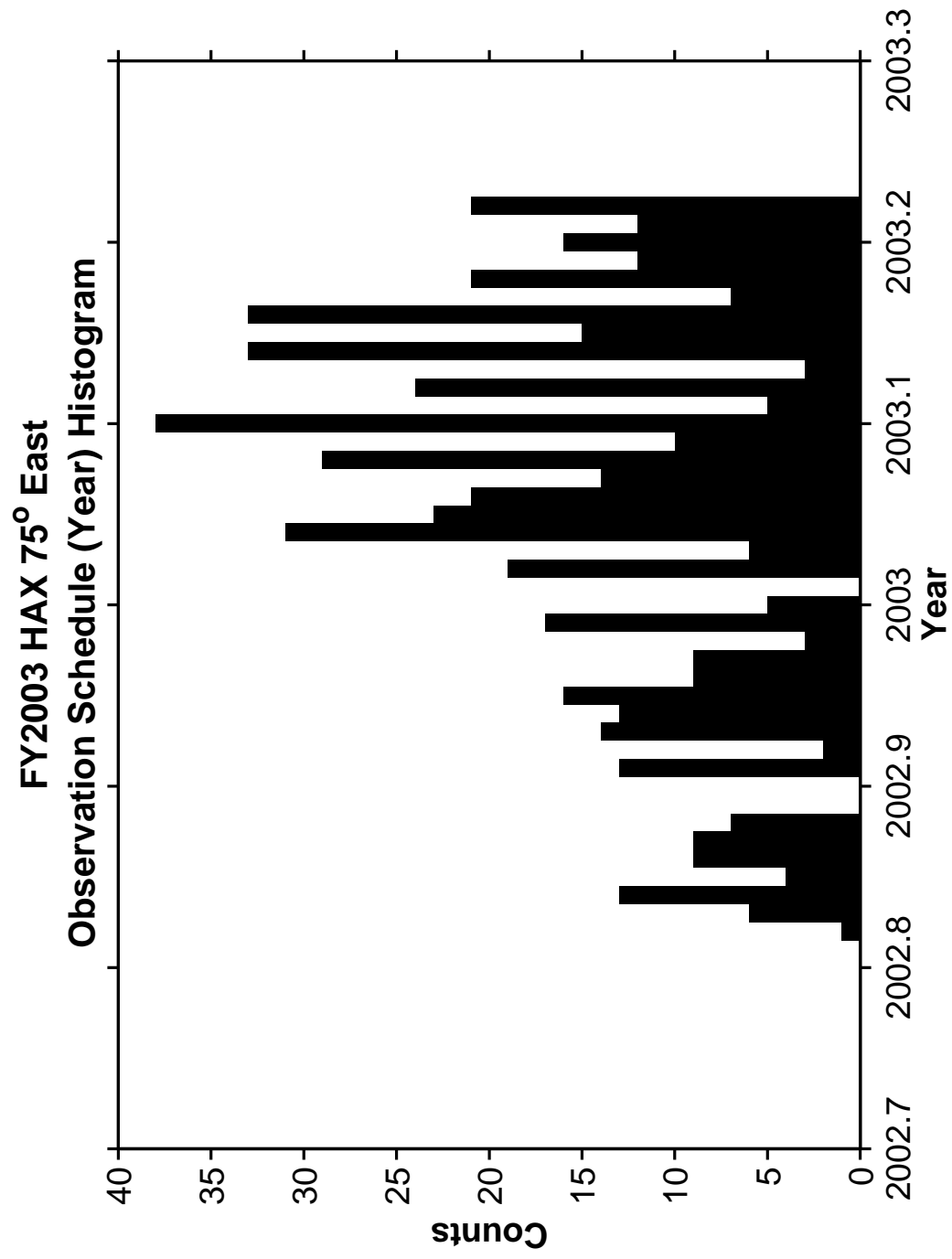


Figure 150. HAX Histogram of Observation Schedule throughout the Year.

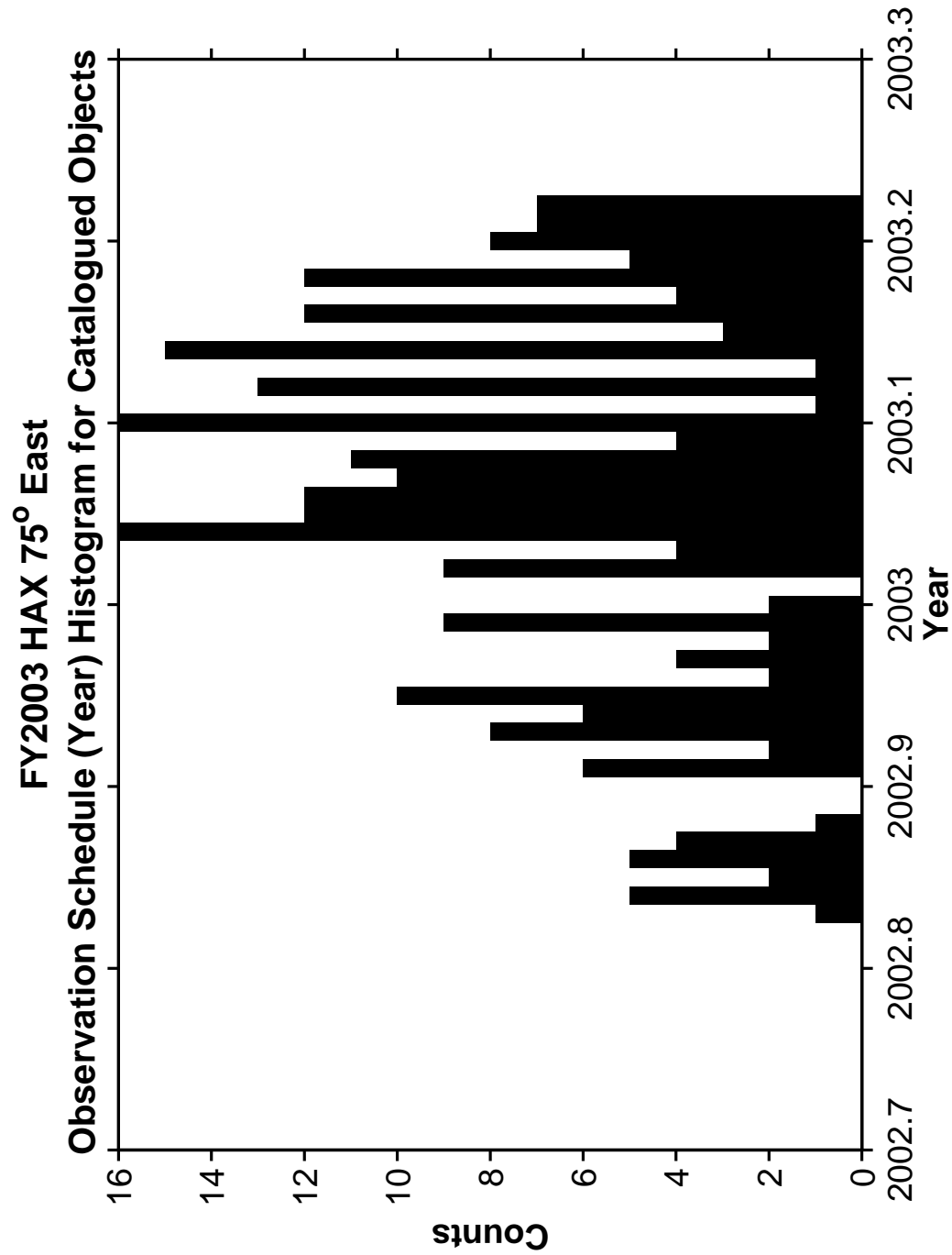


Figure 151. HAX Histogram of Observation Schedule of Catalogued Objects throughout the Year.

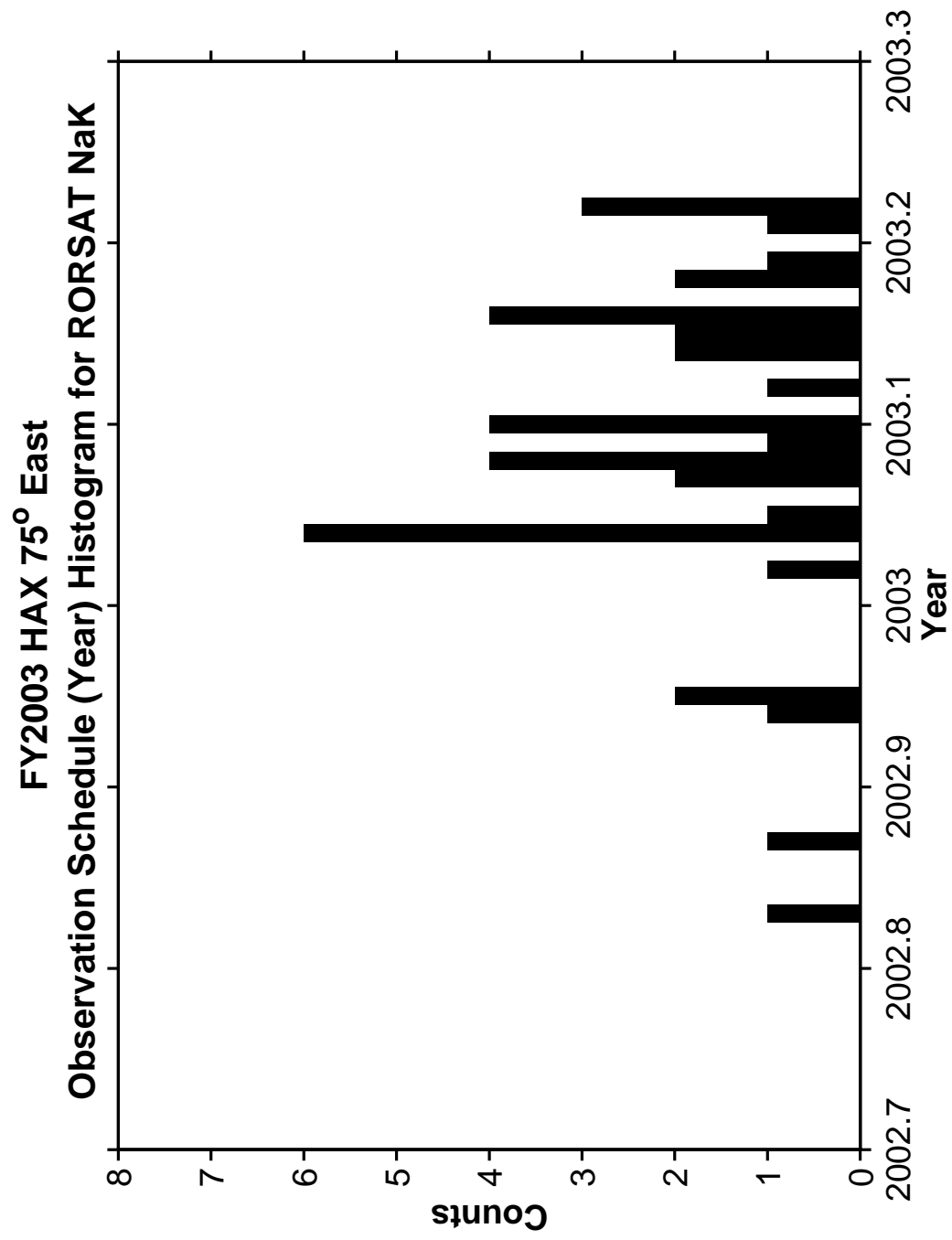


Figure 152. HAX Histogram of Observation Schedule of RORSAT NaK throughout the Year.

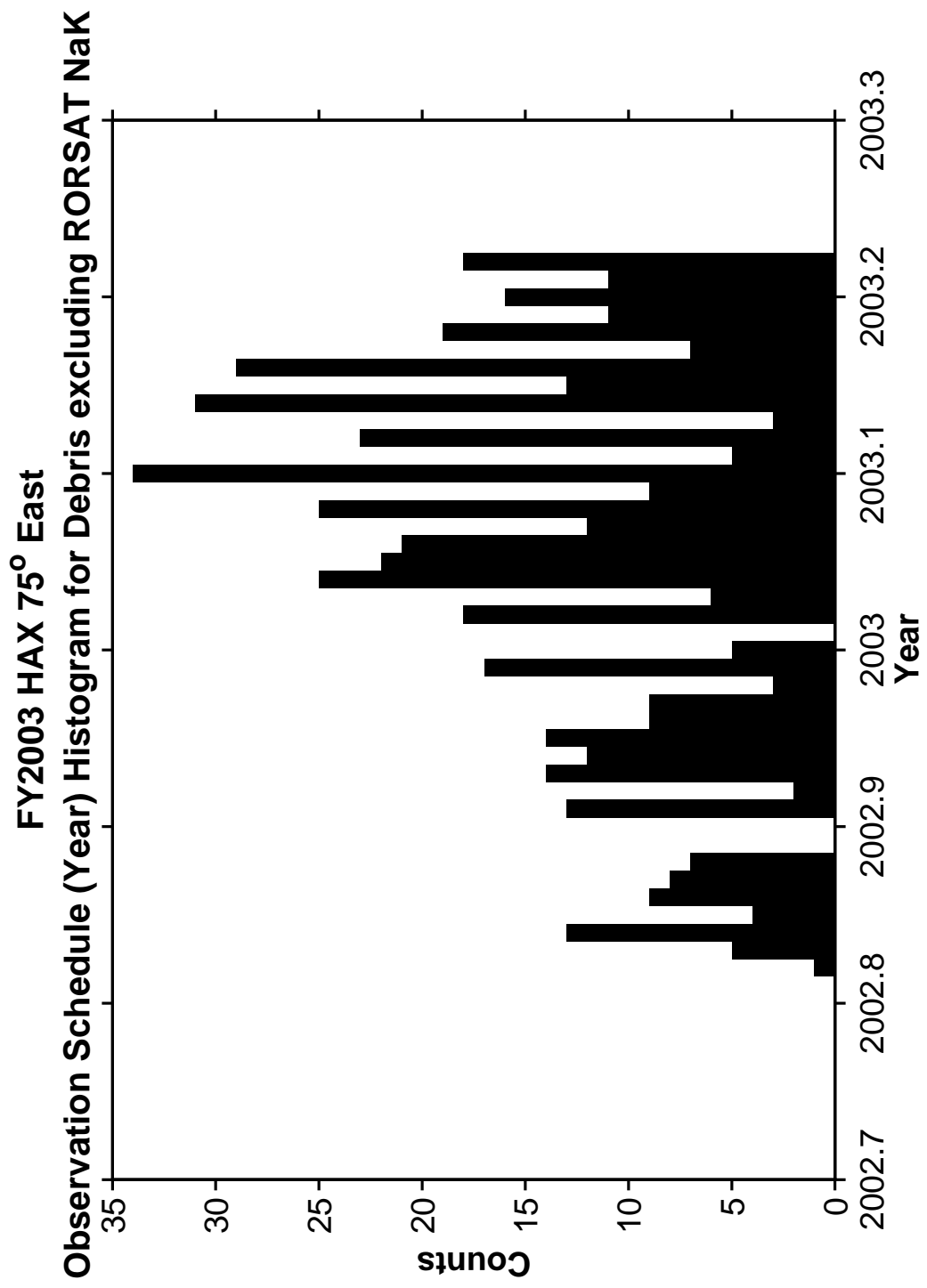


Figure 153. HAX Histogram of Observation Schedule excluding RORSAT NaK Debris throughout the Year.

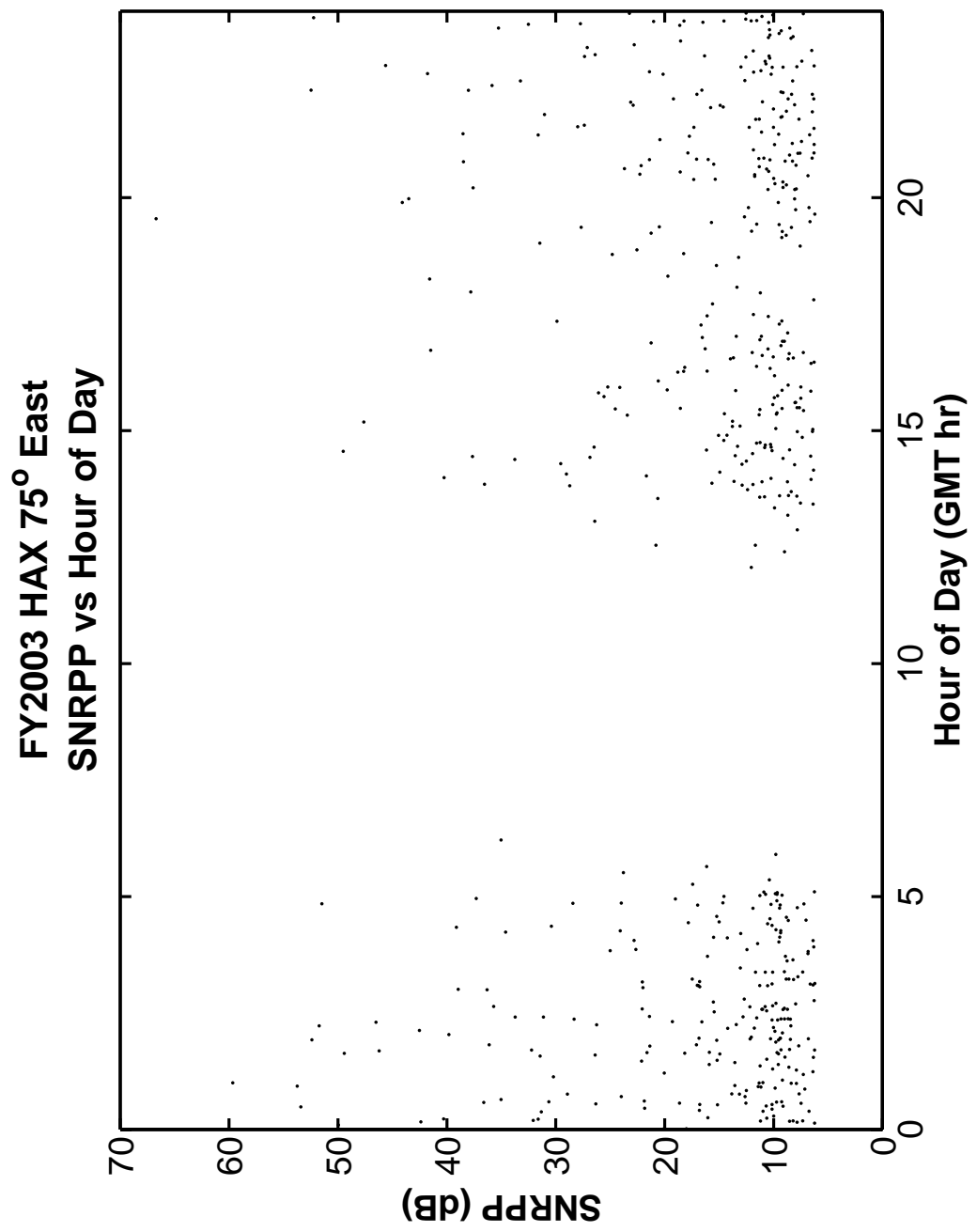


Figure 154. HAX Principal Polarization versus Hour of Day of Detections.

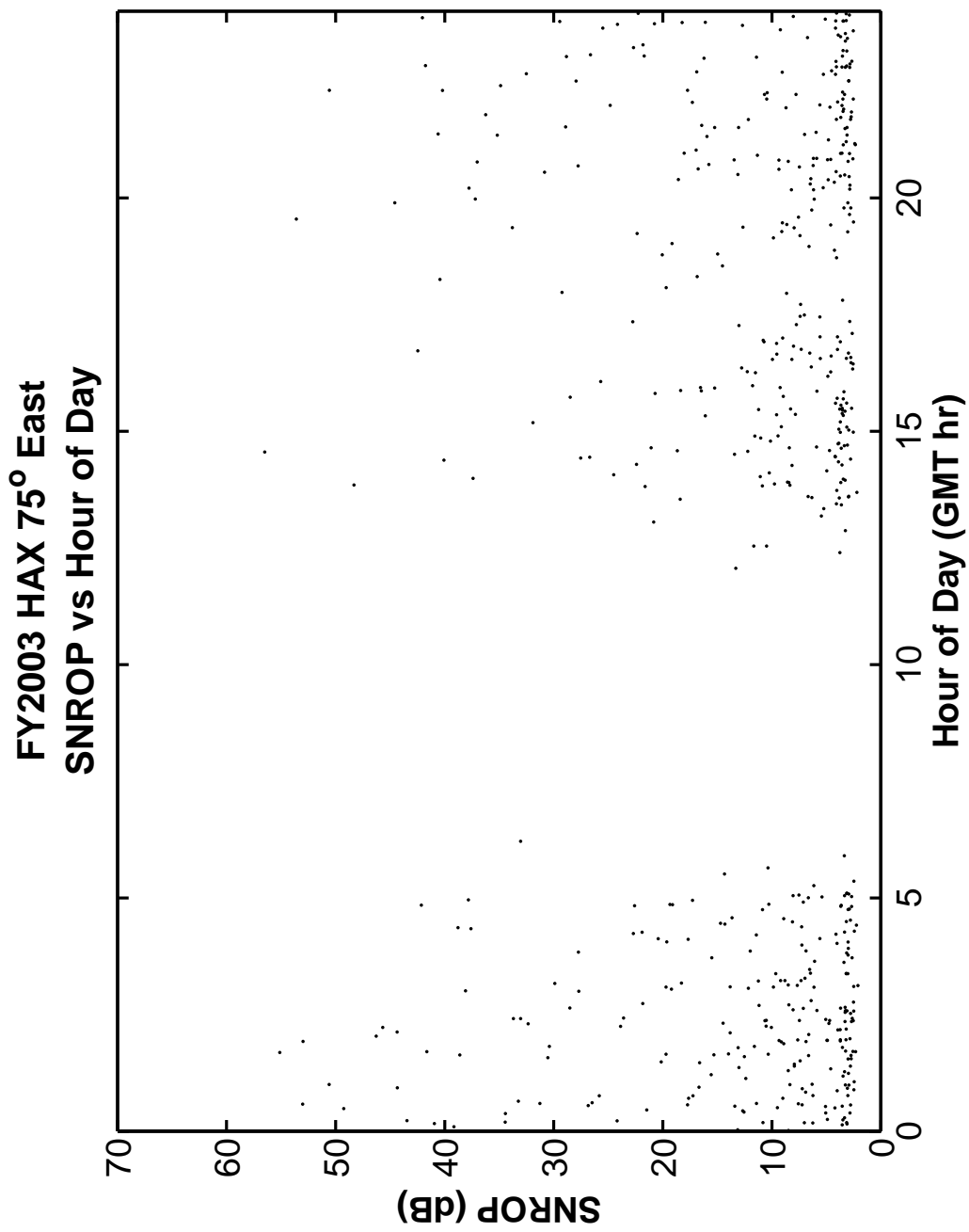


Figure 155. HAX Orthogonal Polarization versus Hour of Day of Detections.

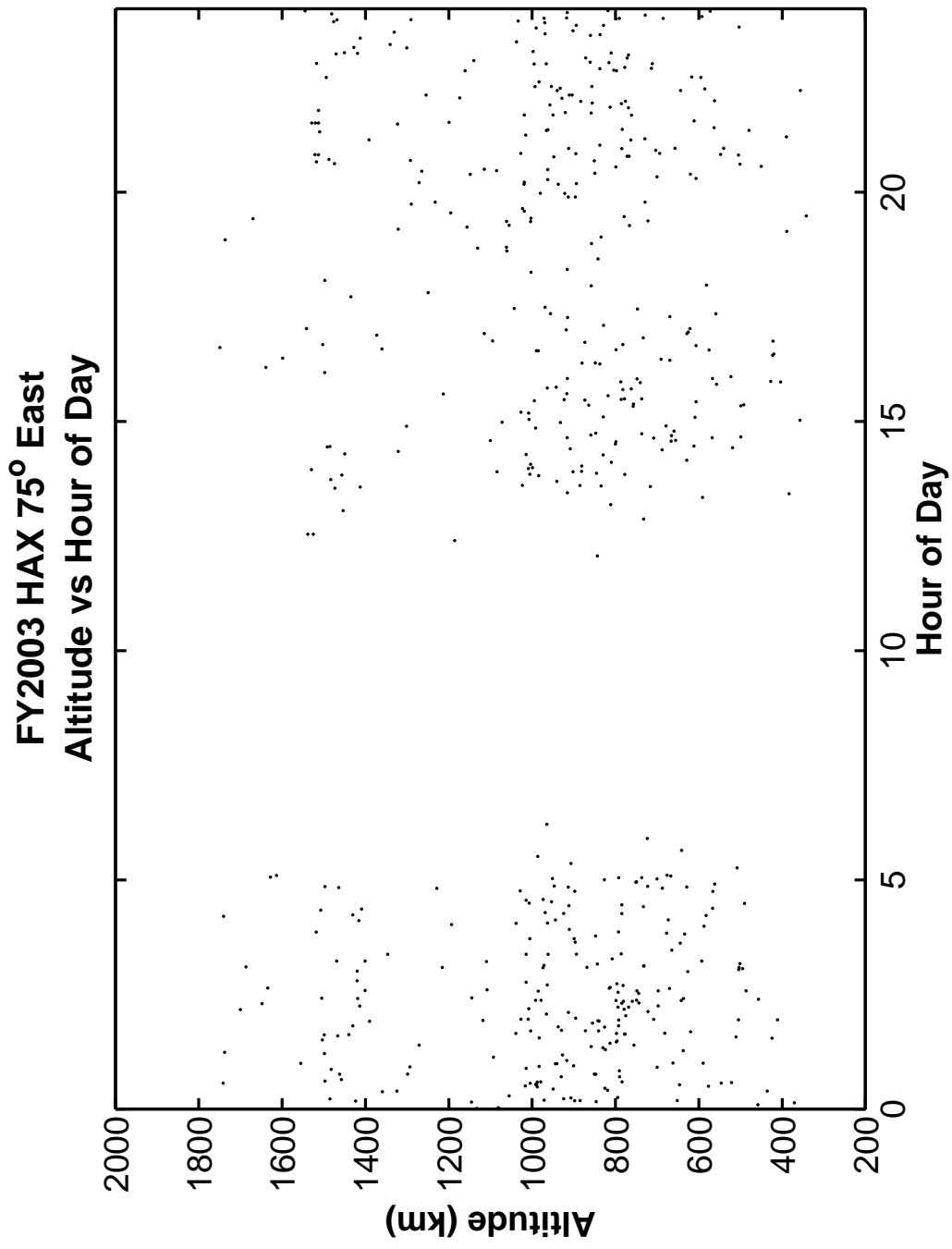


Figure 156. HAX Altitude versus Hour of Day of Detections.

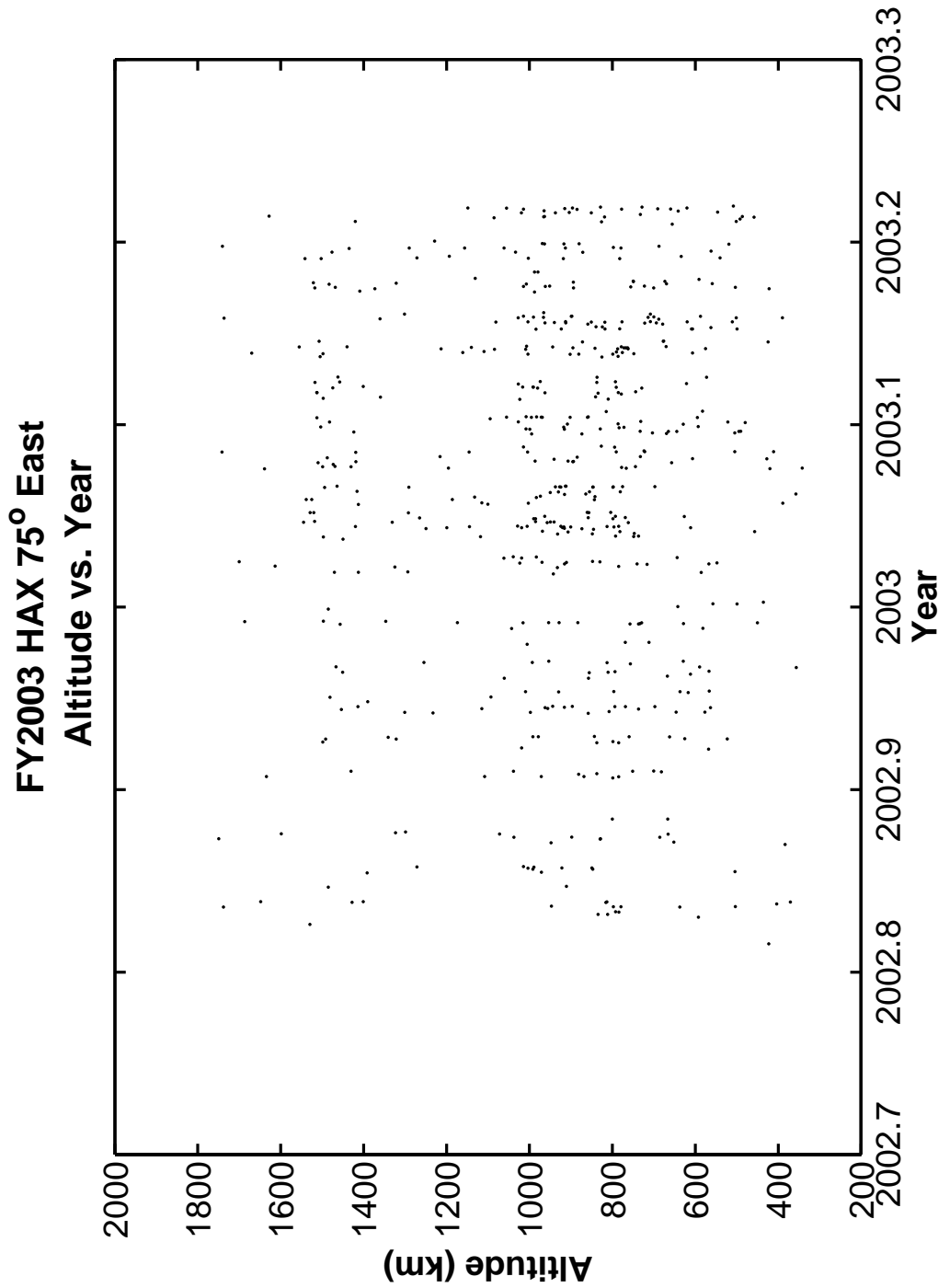


Figure 157. HAX Altitude versus Observation Schedule throughout the Year.

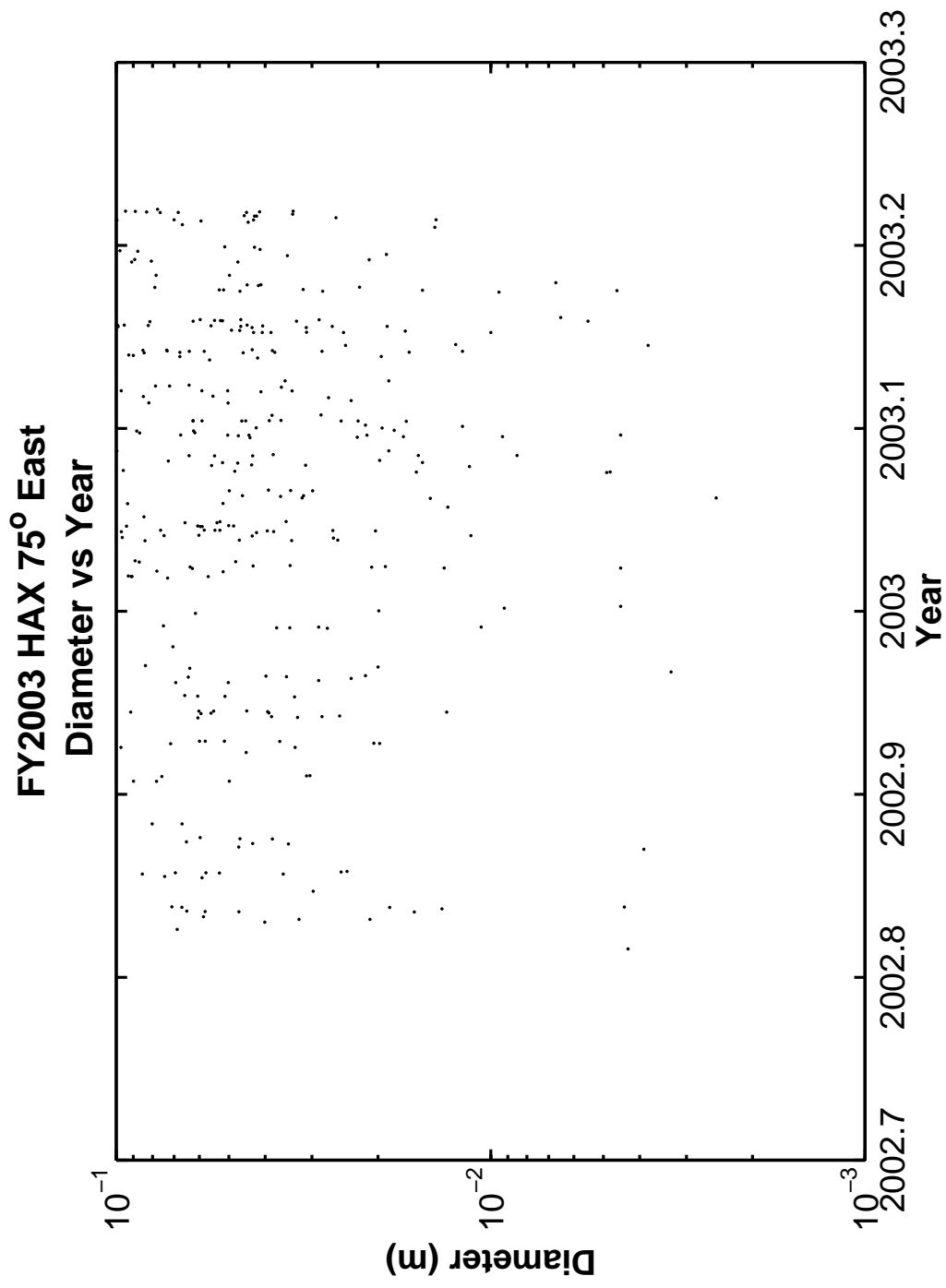


Figure 158. HAX Diameter versus Observation Schedule throughout the Year.

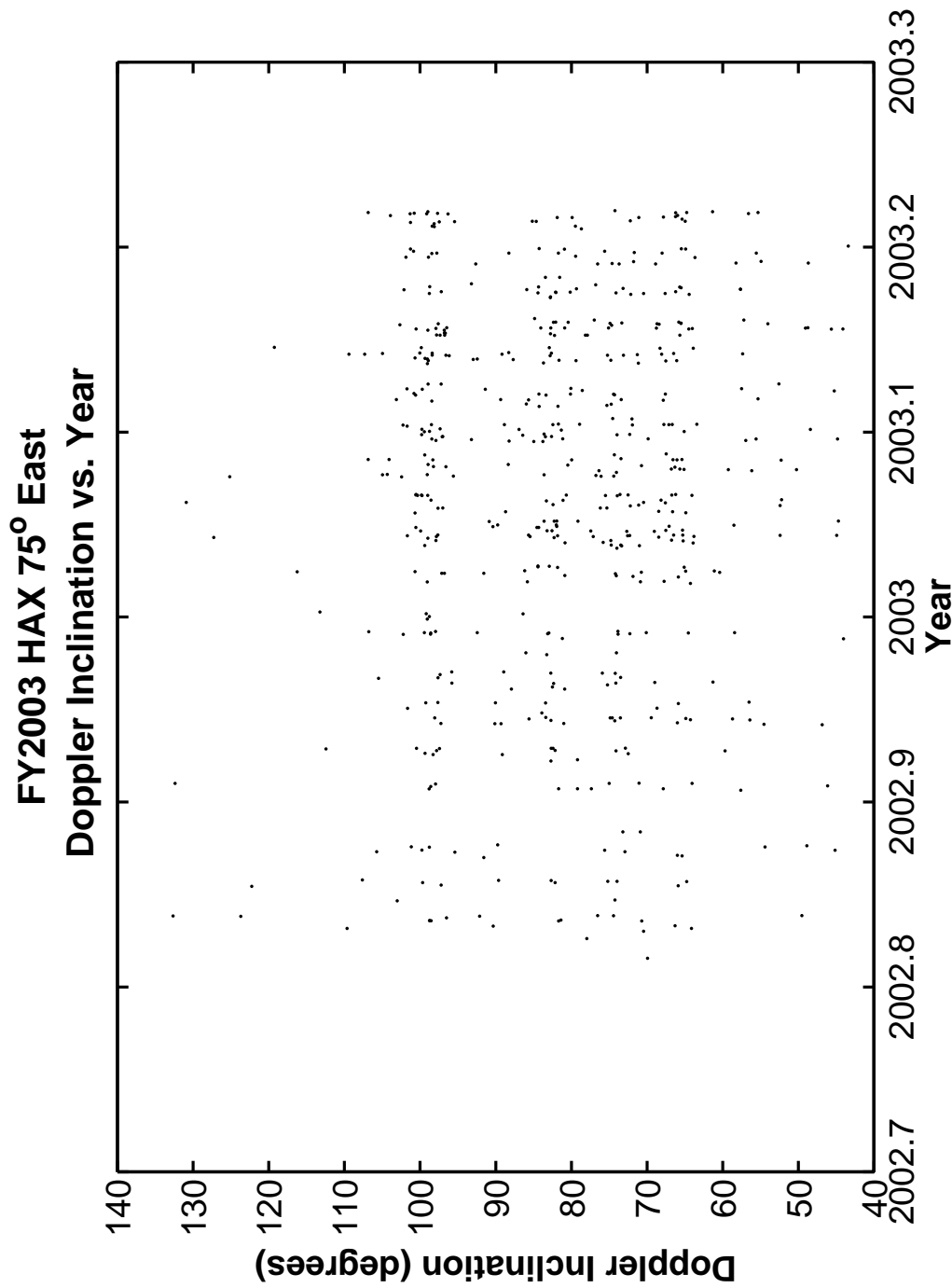


Figure 159. HAX Doppler Inclination versus Observation Schedule throughout the Year.

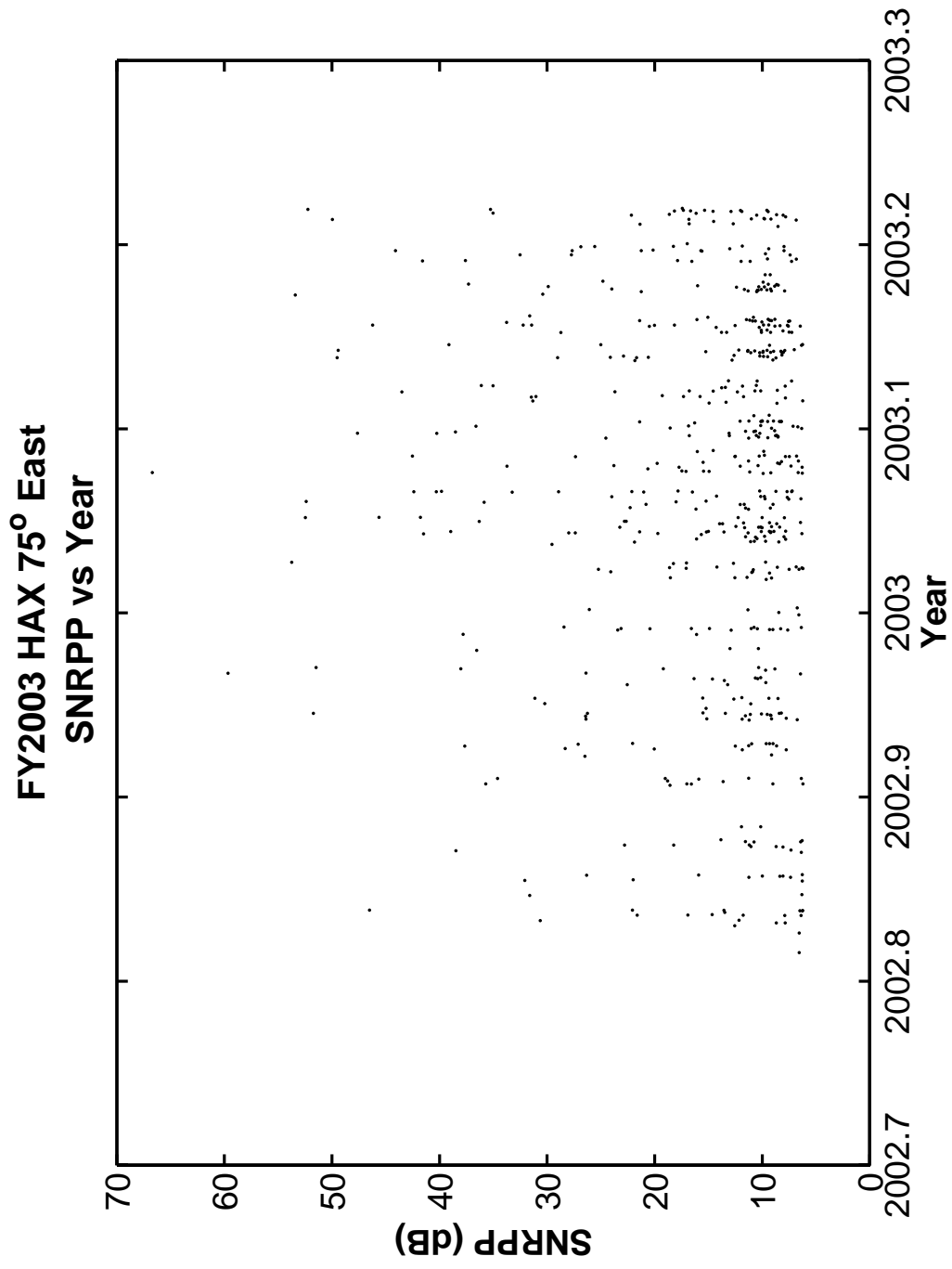


Figure 160. HAX Principal Polarization SNR versus Observation Schedule throughout the Year.

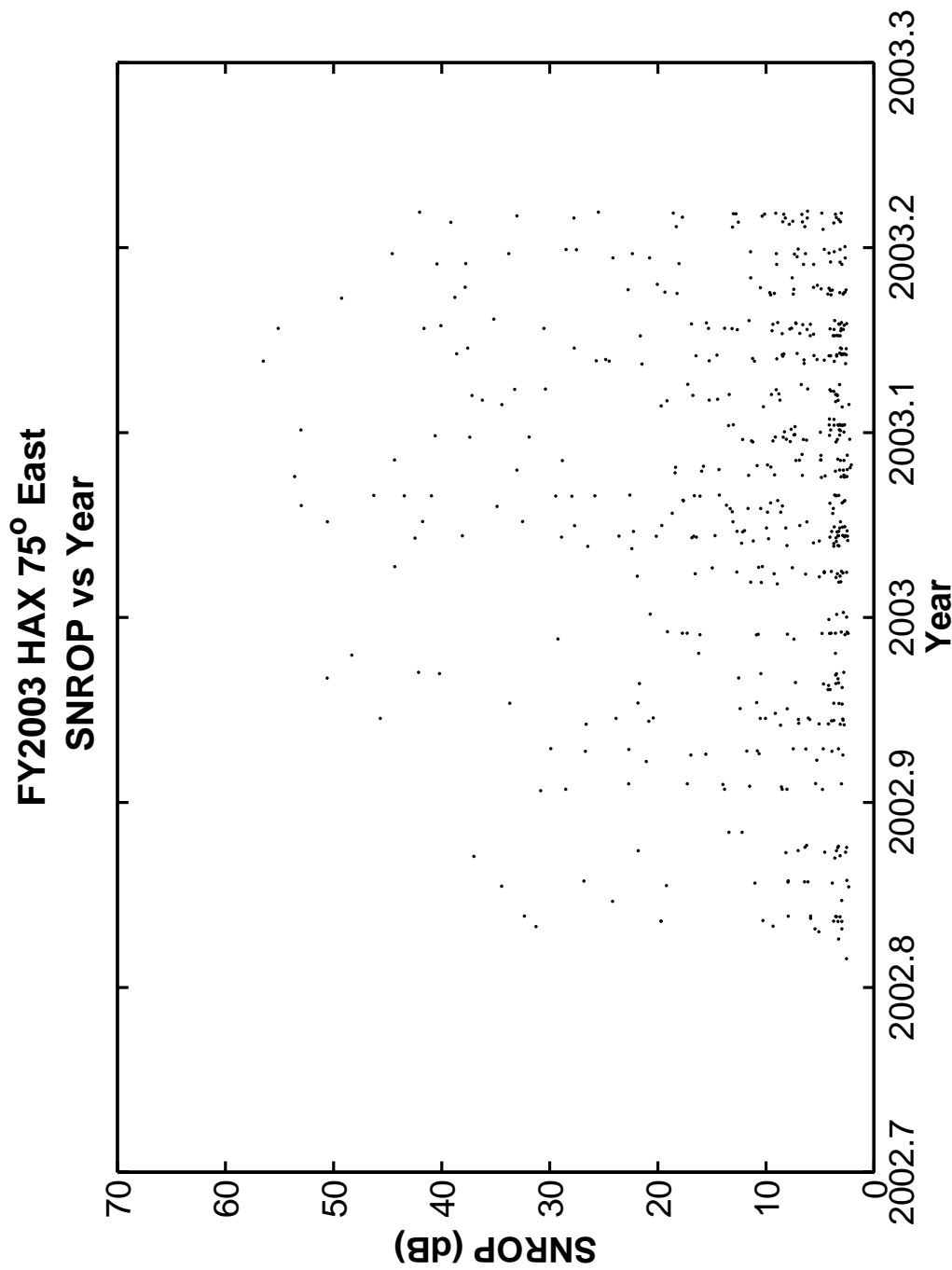


Figure 161. HAX Orthogonal Polarization SNR versus Observation Schedule throughout the Year.

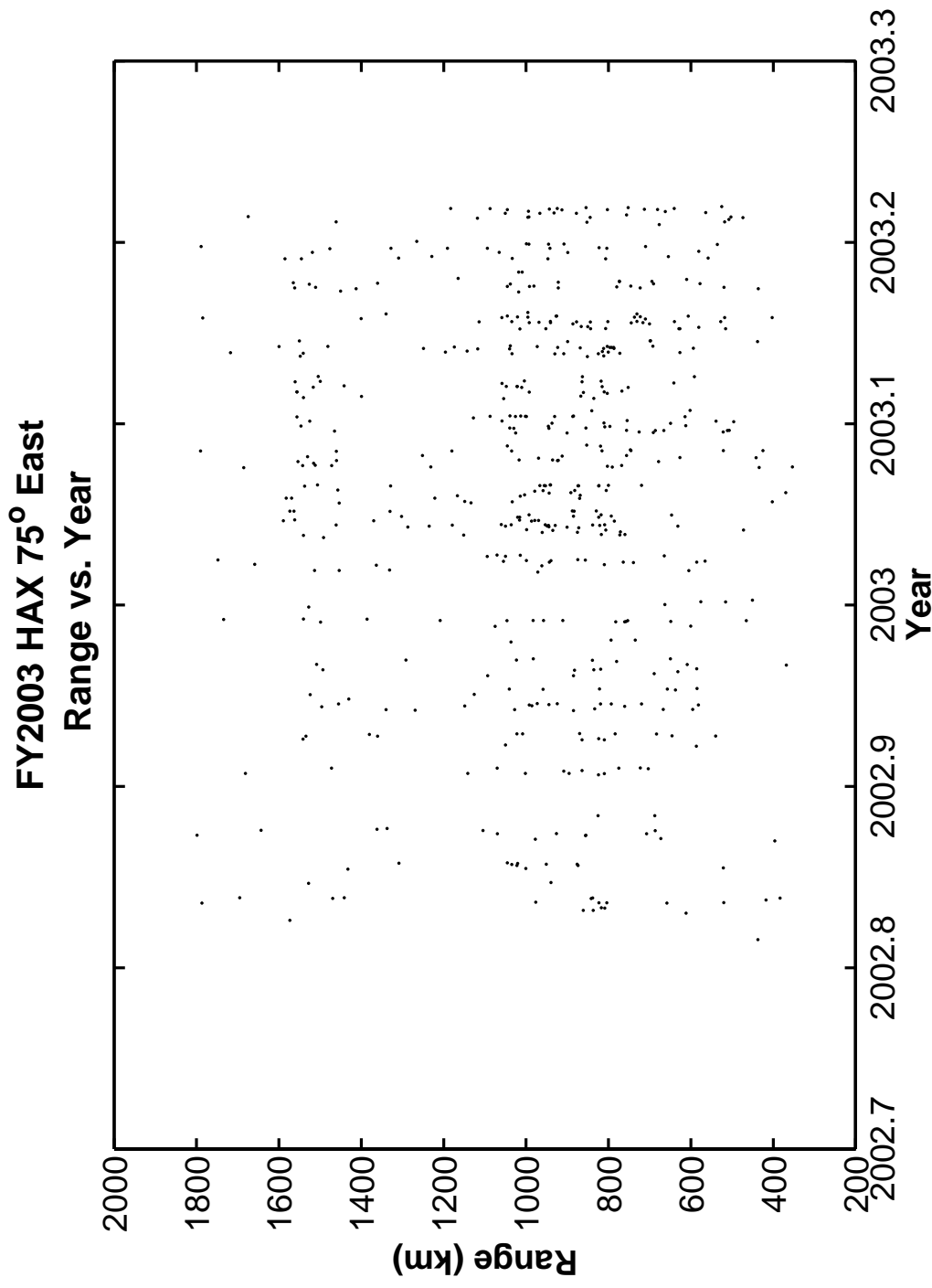


Figure 162. HAX Range versus Observation Schedule throughout the Year.

FY2003 HAX 75° East
Polarization vs Year

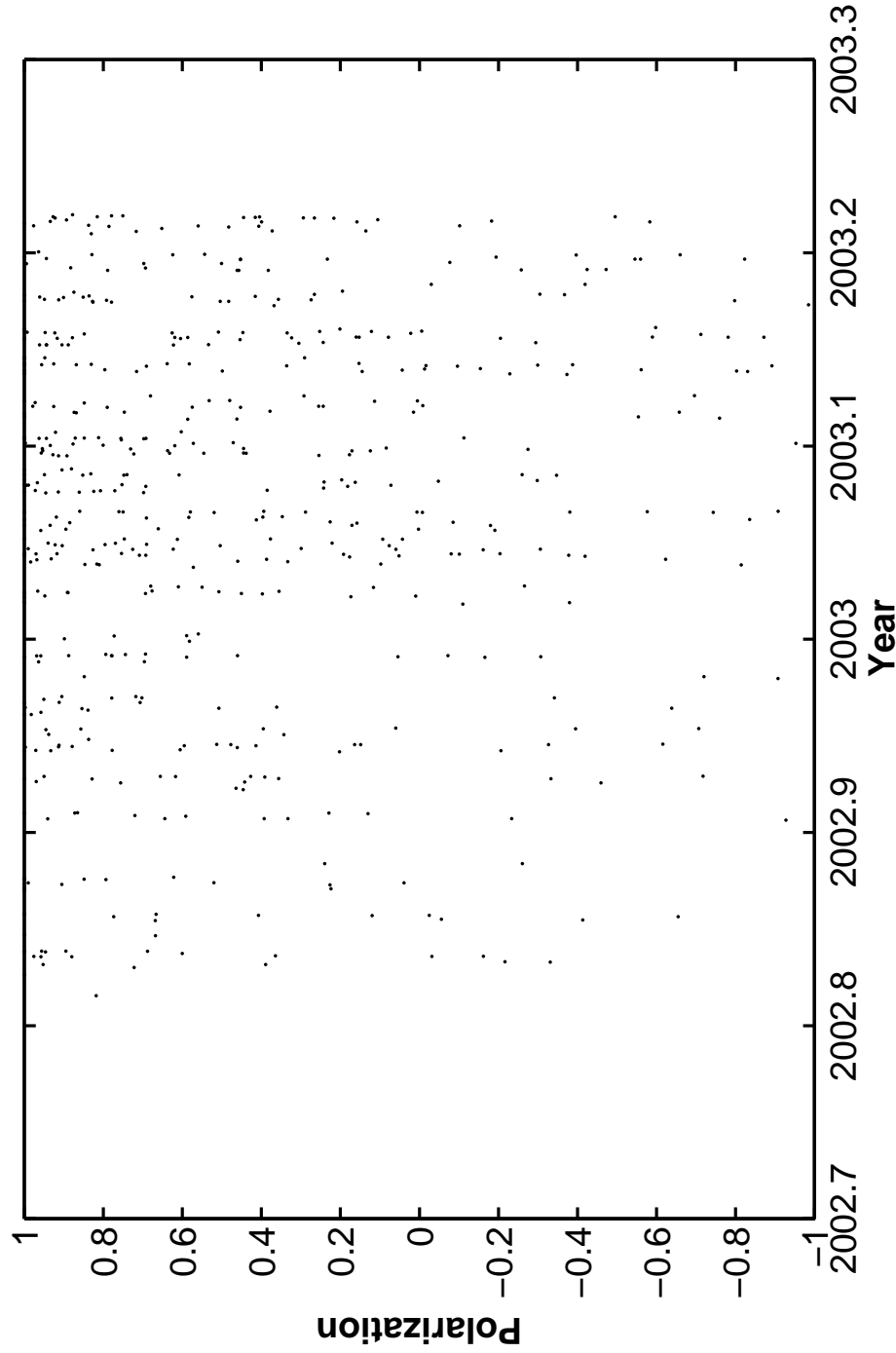


Figure 163. HAX Radar Return Signal Polarization versus Observation Schedule throughout the Year.

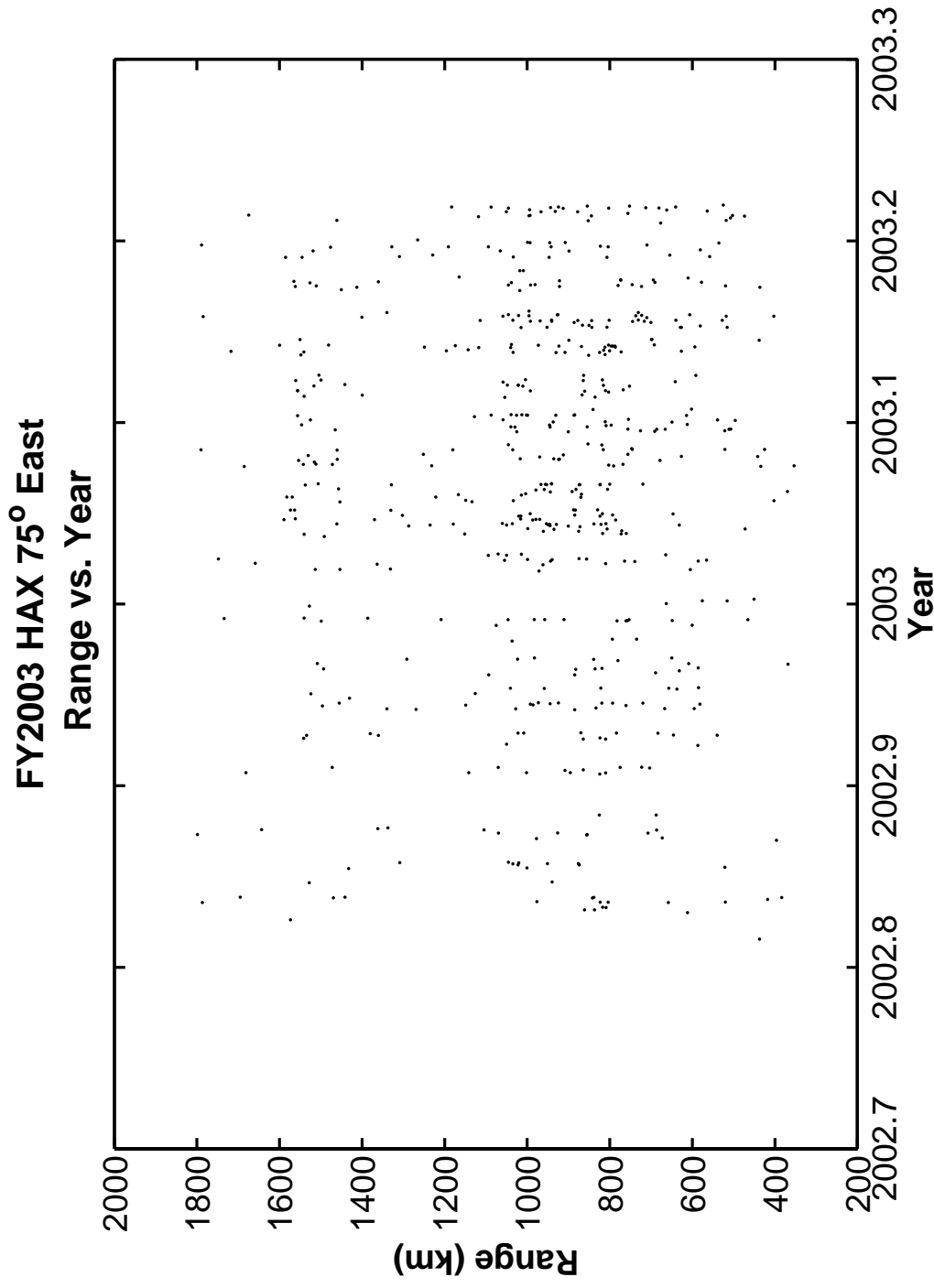


Figure 164. HAX Range versus Observation Schedule throughout the Year.

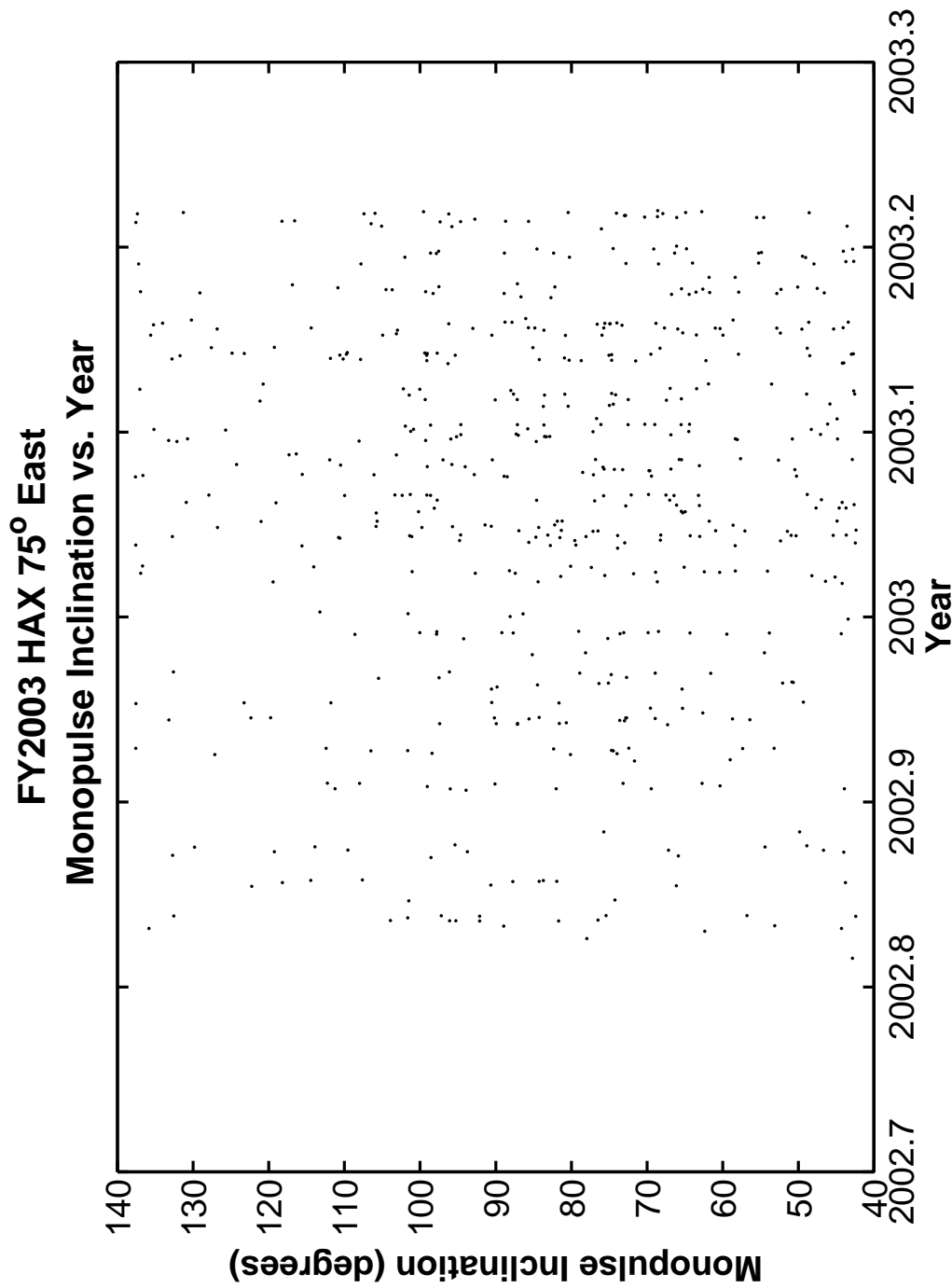


Figure 165. HAX Monopulse Inclination versus Observation Schedule throughout the Year.